

Effects of Waterjet Treatment on Surface
Integrity of Metals and its Optimization

Mohd Azmir Mohd Azhari –

Band 11

Mohd Azmir Mohd Azhari

**Effects of Waterjet Treatment on Surface
Integrity of Metals and its Optimization**

ISBN 978-3-943995-60-2
ISSN 1614-6220

**KIMA Schriftenreihe
Band 11**

Herausgeber: Univ. Prof. Dr.-Ing. C. Schindler

Mohd Azmir Mohd Azhari

Effects of Waterjet Treatment on Surface Integrity of Metals and its Optimization

KIMA Schriftenreihe

Band 11

Herausgeber: Univ. Prof. Dr.-Ing. C. Schindler

Bibliografische Information der Deutschen Nationalbibliothek

Die Deutsche Nationalbibliothek verzeichnet diese Publikation in der Deutschen Nationalbibliografie; detaillierte bibliografische Daten sind im Internet über <http://dnb.d-nb.de> abrufbar.

Herausgeber: Fachbereich Maschinenbau und Verfahrenstechnik
Lehrstuhl für Konstruktion im Maschinen- und Apparatebau
Univ. Prof. Dr.-Ing. C. Schindler
Postfach 3049
Technische Universität Kaiserslautern, Gebäude 42
67653 Kaiserslautern

Verlag: Technische Universität Kaiserslautern

Druck: Technische Universität Kaiserslautern
Hauptabteilung 5
Abteilung 5.6 Foto-Repro-Druck

D-386

© Fachbereich Maschinenbau und Verfahrenstechnik, Kaiserslautern 2014

Alle Rechte vorbehalten, auch das des auszugsweisen Nachdrucks, der auszugsweisen oder vollständigen Wiedergabe (Photographie, Mikroskopie), der Speicherung in Datenverarbeitungsanlagen und das der Übersetzung.

Als Manuskript gedruckt. Printed in Germany.

ISSN 1614-6220

ISBN 978-3-943995-60-2

Effects of Waterjet Treatment on Surface Integrity of Metals and its Optimization

Vom Fachbereich Maschinenbau und Verfahrenstechnik
der Technischen Universität Kaiserslautern
zur Verleihung des akademischen Grades

Doktor-Ingenieur (Dr.-Ing.)

genehmigte Dissertation

von

M.Sc. Mohd Azmir Mohd Azhari
aus Perak, Malaysia

Vorsitzender: Prof. Dr.-Ing. Siegfried Ripperger
Berichterstatter: Prof. Dr.-Ing. Christian Schindler
Prof. Dr.-Ing. Eberhard Kerscher
Dekan: Prof. Dr.-Ing. Bernd Sauer

Tag der Einreichung: 18. September 2013
Tag der Mündlichen Prüfung: 11. Dezember 2013

Kaiserslautern, Mai 2014

D 386

Acknowledgement

First of all, I would like to express my deepest gratitude to the Almighty God, for His blessings, I am finally able to complete this work. I would like to take this opportunity to wish my sincere thanks to my ‘*Doktorvater*’, Prof. Dr.-Ing. Christian Schindler, for his support and encouragement. I would also like to express my appreciation to Prof. Dr.-Ing. Eberhard Kerscher for being able to examine this work as well as giving me the opportunity to work under him during the last 3 months of my stay in Germany.

I would like to give credits to those who are directly or indirectly involved in the completion of this work especially colleagues from ‘*Lehrstuhl für Konstruktion im Maschinen- und Apparatebau (KIMA)*’ and ‘*Arbeitsgruppe Werkstoffprüfung (AWP)*’, Technische Universität Kaiserslautern. The technical support from *Lehrstuhl für Fertigungstechnik und Betriebsorganisation (FBK)* and *Lehrstuhl für Messtechnik und Sensorik (MTS)*, Technische Universität Kaiserslautern, is gratefully acknowledged.

I would also like to take this opportunity to thank Universiti Malaysia Pahang and Government of Malaysia in providing financial support during my stay in Germany. Last but not least, my most heartfelt gratitude is reserved to my mom and family for their undying patience, trust and belief in my endeavour.

To Fauzana, Afeef, Fatini and Aleena

Table of contents

List of symbols and abbreviations.....	VII
Kurzfassung.....	X
Zusammenfassung.....	XII
1 Introduction	1
2 State of the art	3
2.1 Methods of mechanical surface treatment.....	3
2.1.1 Shot peening process	4
2.1.2 Laser shock peening process	12
2.1.3 Waterjet peening process	15
2.2 Mechanics of waterjet impact	17
2.2.1 Liquid erosion mechanisms	20
2.2.2 Strengthening mechanisms	24
2.3 Effect of waterjet impact on surface.....	26
2.3.1 Roughness.....	26
2.3.2 Erosion.....	29
2.4 Effect of waterjet impact on sub-surface.....	33
2.4.1 Hardness	33
2.4.2 Microstructures	36
2.5 Effect of waterjet impact on fatigue life	38
2.6 Summary of state of the art	42
3 Problem specification and scientific approach	45
4 Research methodology	48
4.1 Materials.....	48
4.2 Experimental setup.....	52
4.2.1 Equipment.....	52
4.2.2 Experimental design	53
4.2.3 Experimental procedure	54
4.3 Analysis of test samples	55
4.3.1 Surface roughness measurement.....	55
4.3.2 Hardness measurement.....	56

4.3.3	Microstructural analysis	57
4.4	Fatigue test.....	58
5	Results and discussions	61
5.1	Effect of waterjet peening on surface	61
5.1.1	Roughness.....	61
5.1.2	Erosion.....	65
5.1.3	Comparisons of surface effects between both materials.....	77
5.2	Erosion mechanisms	79
5.3	Effect of waterjet peening on sub-surface	94
5.3.1	Hardness	94
5.3.2	Microstructures	101
5.4	Effect of waterjet peening on fatigue life.....	108
5.4.1	Fatigue life performance	108
5.4.2	Surface fracture analysis	112
6	Optimization of the waterjet peening process.....	116
6.1	Design of experiment.....	116
6.2	Response surface methodology	117
6.3	Analysis of results.....	120
6.3.1	Roughness.....	120
6.3.2	Hardness	124
6.3.3	Optimization	134
6.3.4	Fatigue results	135
7	Conclusions.....	140
7.1	Evaluation of surface effects	140
7.2	Evaluation of sub-surface effects	141
7.3	Evaluation of fatigue effects	141
7.4	Optimization of waterjet peening process.....	142
8	Summary and outlook	143
	Literature	145

List of symbols and abbreviations

Latin symbols

<i>Symbols</i>	<i>Units</i>	<i>Definition</i>
a	mm	Radius of the solid contact zone
c_l	m/s	Shock velocity of the liquid
c_s	m/s	Shock velocity of the solid
c_w	m/s	Acoustic velocity of the liquid
D_c	mm	Coverage diameter of the waterjet
D_n	mm	Nozzle diameter
D_s	mm	Average diameter of the shot
D_{spot}	mm	Laser spot diameter
E_{pulse}	J	Laser pulse energy
E_s	J	Kinetic energy of the shot
f_A	μm	Arc height on A-strip
h	mm	Standoff distance
I_{laser}	GW/cm	Laser intensity
I_{shot}		Almen intensity
m_s	kg	Mass of the shot
n_{impact}		Number of laser impacts
n_j		Number of waterjet passes
n_{shot}		Number of shot treatment times
N_{pulse}	pulse/mm ²	Laser pulse density
p_0	MPa	Waterjet supply pressure
p_i	MPa	Waterjet impact pressure
p_s	MPa	Central stagnation pressure
r	mm	Radius of curvature of the liquid drop
R_a	μm	Average surface roughness
R_p	μm	Maximum peak height of the roughness profile
R_v	μm	Maximum valley depth of the roughness profile
R_t	μm	Total height of the roughness profile
v_i	m/s	Impact velocity of the liquid
v_n	mm/min	Feedrate of the waterjet nozzle
v_r	m/s	Velocity of the liquid radial flow

v_s	m/s	Velocity of the shot
t_p	min	Peening duration
z	μm	Depth of the residual stress below the surface
z_0	μm	Assumed value of the residual stress depth

Greek symbols

<i>Symbols</i>	<i>Units</i>	<i>Definition</i>
α	$^\circ$	Contact angle of the liquid drop
Δt	s	Duration of the water-hammer pressure
ε		Strain
θ	$^\circ$	Inclination angle of the nozzle
ρ_l	kg/m^3	Density of the liquid
ρ_s	kg/m^3	Density of the solid
σ_r	MPa	Residual stress
$\sigma_{r,s}$	MPa	Residual stress at the surface
$\sigma_{r,max}$	MPa	Maximum residual stress
σ_{UTS}	MPa	Ultimate tensile strength
σ_{YS}	MPa	Yield strength

Abbreviations

AWJP	Abrasive waterjet peening
CAD/CAM	Computer-aided design/ computer-aided manufacturing
CEMS	Conversion electron Mössbauer spectroscopy
CJA	Cavitating jet in air
CJW	Cavitating jet in water
KIMA	Chair of Design in Mechanical Engineering
LASIK	Laser in situ keratomileusis
LSP	Laser shock peening
NC	Numerical control
OJP	Oil jet peening
PC	Personal computer
RCW	Rounded cut wire
Ref.	Reference
TEM	Transmission electron microscopy

WCP	Water cavitation peening
WJP	Waterjet peening
WWJ	Water-waterjet
XRD	X-ray diffraction
3D	Three dimensional

Kurzfassung

Die Arbeit befasst sich mit den Auswirkungen des mehrfachen Überfahrens der Werkstückoberfläche mit dem Wasserstrahl und anderen Einflussfaktoren, wie Vorschub, Wasserdruck und Düsenabstand auf die Wasserstrahlbehandlung von Metalloberflächen. Hierzu wurde die Oberflächenbeschaffenheit vor und nach der Wasserstrahlbearbeitung herangezogen. Eine Erhöhung der Anzahl der Überfahrten mit dem Wasserstrahl und eine Erhöhung des Drucks führen zu einer höheren Rauheit, einer größeren Erosion, sowie einer höheren Härte. Die Vorschubgeschwindigkeit hat eine gegenteilige Wirkung auf die genannten Oberflächeneigenschaften. Es lässt sich ein bestimmter Düsenabstand finden, bei dem die maximale Oberflächenrauheit, Erosion und Härte entsteht. Durch Untersuchungen der Mikrostrukturen der bearbeiteten Oberflächen wurden Erkenntnisse über den Mechanismus des Materialabtrags sowie den Beginn und die Weiterentwicklung von Schädigungen gewonnen. Basierend auf der Methode der statistischen Versuchsplanung wurde außerdem die Oberflächenbehandlung mit Wasserstrahl optimiert. Ebenfalls entwickelte Empirische Modelle zeigen eine sehr gute Korrelation zwischen gemessenen und erwarteten Ergebnissen. Eine geeignete Auswahl der Parameter zur praktischen Anwendung kann darauf basierend erfolgen.

Abstract

The study addresses the effect of multiple jet passes and other parameters namely feedrate, water pressure and standoff distance in waterjet peening of metallic surfaces. An analysis of surface integrity was used to evaluate the performance of different parameters in the process. An increase in the number of jet passes and pressure leads to a higher roughness and more erosion and also a higher hardness. In contrast, the feedrate shows a reverse effect on those surface characteristics. There exists a specific value of standoff distance that results in the maximum surface roughness, erosion as well as hardness. Analysis of the surface microstructure gave a good insight into the mechanism material removal process involving initial and evolved damage. Also, the waterjet peening process was optimized based on the design of experiment approach. The developed empirical models had shown reasonable correlations between the measured and predicted responses. A proper

selection of waterjet peening parameters can be formulated to be used in practical works.

Zusammenfassung

Für die Wasserstrahl-Technologie gibt es verschiedene Anwendungen, wie zum Beispiel Trennen, Oberflächenbehandlung, Reinigung, Entfernung von Beschichtungen und Randschichtverfestigung (Waterjet peening, WJP). WJP ist eine relativ neue Anwendung der Wasserstrahl-Technologie. Es handelt sich hierbei um eine mechanische Verstärkung der Oberfläche, welche durch hochfrequente Stöße der Wassertropfen mit der Werkstück-Oberfläche und der daraus bedingten lokalen plastischen Verformung bewirkt wird. Dadurch werden hohe Druckeigenspannungen in die Oberfläche induziert, was eine größere Oberflächenhärte und längere Lebensdauer der Komponenten bedingt. Es ist bekannt, dass Hochdruckwasserstrahlen in der Lage sind, eine starke Beschädigung der Oberfläche des Werkstoffs durch Erosion zu verursachen. Diese ist durch den Stoß der sich mit hoher Geschwindigkeit bewegende Flüssigkeitsmasse mit der Werkstückoberfläche bedingt. Die vorliegende Arbeit befasst sich mit den Auswirkungen des mehrfachen Überfahrens der Werkstückoberfläche mit dem Wasserstrahl und anderen Einflussfaktoren, wie Vorschub, Wasserdruck und Düsenabstand auf den WJP Prozess für Edelstahl X5CrNi18-10 (Werkstoffnummer 1.4301) und Stahl C45 (Werkstoffnummer 1.0503). Eine Analyse der Oberflächenbeschaffenheit in Bezug auf die Oberflächenrauheit, Abtragung, Härte und Mikrostrukturen wird verwendet, um den Einfluss verschiedener Parameter auf den WJP zu bewerten.

Eine Erhöhung der Anzahl der Überfahrten mit dem Wasserstrahl führt zu einer höheren Rauheit und Erosion auf der Oberfläche durch die wiederholte Belastung der Oberfläche mit dem Strahl. Ein hoher Wasserdruck bewirkt aufgrund der höheren kinetischen Energie der Wassermoleküle ebenfalls eine größere Oberflächenrauheit und verstärkte Erosion. Dahingegen zeigt eine Steigung des Vorschubs eine umgekehrte Wirkung auf Oberflächenrauheit und Erosionsrate. Für den Düsenabstand existiert ein bestimmter Abstand, bei dem der Strahl hauptsächlich aus Wassertröpfchen besteht, wodurch sich eine maximale Oberflächenrauheit und Erosion ergibt. Die Erosion und der Materialabtrag sind bei Stahl C45 (UNS G10450) höher als bei Edelstahl X5CrNi18-10 (UNS S30400), was in der geringeren Härte des Stahls C45 begründet ist. Die Mikrostruktur gibt Aufschluss über den Mechanismus des Materialabtrags, der anfänglichen und sich entwickelnde Beschädigung.

Die Härte sinkt mit steigendem Abstand der Düse zur Oberfläche. Ein mehrfaches Überfahren der Oberfläche mit dem Strahl und eine Erhöhung des Drucks führen zu einer größeren Härte und einer größeren Tiefenwirkung. Im Gegensatz dazu hat eine Erhöhung des Vorschubs eine geringere Härte zur Folge. Für einen bestimmten Düsenabstand wird die Härte maximal. Die wassergestrahlten Proben weisen eine geringere Schwingfestigkeit als die unbearbeiteten Proben auf, was wahrscheinlich durch die erhöhte Oberflächenrauheit bzw. Kerbwirkung bedingt wird. Für die Dauerfestigkeit spielt die Oberflächenrauheit eine größere Rolle als die Erhöhung der Härte.

In der Arbeit wurde zudem die Wasserstrahl-Randschichtverfestigung basierend auf der Methode der statistischen Versuchsplanung optimiert. Diese basiert auf den Response-Surface-Methoden unter Verwendung des experimentellen Ansatzes nach Box-Behnken. Dabei wurde die Aluminiumlegierung AlMg1 (Werkstoffnummer 3.3315) als Probenmaterial gewählt. In diesem Zusammenhang wurden empirische Modelle entwickelt, um die Oberflächenrauheit und die Härte vorherzusagen. Die empirischen Modelle zeigen eine sehr gute Korrelation zwischen den gemessenen und erwarteten Ergebnissen. Eine geeignete Auswahl der Parameter zur praktischen Anwendung kann darauf basierend erfolgen.

This page is intentionally left blank.

1 Introduction

The technology and applications of high pressure waterjet have been studied for many decades (as early as 1960s) [1]. It has been used extensively in various industry-related applications including machining, surface preparation, cleaning, coating removal and surface treatment like waterjet peening (WJP). In general, water is compressed to an ultrahigh pressure up to about 700 MPa and discharged from a small orifice typically between 0.2 to 0.4 mm in diameter [1, 2]. If abrasive is used, it is then mixed with the stream of high-velocity water in a chamber before entering the nozzle. The system produces a high velocity water stream up to 900 m/s, with or without abrasive particles causing damage to materials by shearing, cracking, erosion, cavitation, delamination and plastic deformation [2].

In a machining process, high-pressure waterjet is used to cut a workpiece. With an addition of abrasive particles, the machining capability of the waterjet is significantly improved. Various machining processes can be performed including cutting, drilling, milling, etc. A wide range of materials and thicknesses can be cut with good cutting quality and small taper. However, different processing parameters and material properties have to be carefully assessed as to produce the desired cutting qualities. Using only water at a relatively low pressure, cleaning of surfaces from dirt or coats can be achieved [3]. High pressure waterjet also is used successfully to mill coal into powders [4].

Waterjet peening (WJP) is a relatively new application of the waterjet technology [5]. It is a mechanical surface strengthening process where high-frequent impact of water drops on the surface of metal components, which causes local plastic deformation. As a result, high compressive residual stresses are induced in the surface-near layer of the workpiece, which leads to enhanced surface hardness and fatigue life [6]. With an addition of abrasive particles, a higher amount of compressive residual stresses is induced but with a significant increase in roughness of metal surfaces [1].

In the Chair of Design in Mechanical Engineering (KIMA), University of Kaiserslautern, there were a few research projects conducted in the field of waterjet technology. Several studies were carried out on the simulation and performance of the cutting jet [7, 8, 9, 10, 11]. The waterjet technology has also been introduced in a

medical-related application. Few studies were reported about its potential application [12, 13, 14, 15].

The present study attempts to investigate the effect of the waterjet peening process on the material surfaces. The work consists of eight chapters. The present chapter briefly introduces the waterjet technology in general. Chapter 2 reviews the current state of the art on several mechanical surface treatment processes including shot, laser shock and waterjet peening. However, the basic concept of the waterjet peening process is discussed in detail. Also, some results from the previous literatures on the effect of the waterjet peening process are reported. The motivation and the scope of the present study are explained in Chapter 3. Chapter 4 describes the experimental and analytical procedures in conducting the study. Chapter 5 presents the main results in the characterization of the waterjet peening process. The effects of the process on the materials surface, sub-surface and the fatigue performance are discussed. The optimization of the waterjet peening process is presented in Chapter 6. Chapter 7 discusses the conclusions based on the results and the recommendations for future works. Lastly, a summary and outlook for future research is presented in Chapter 8.

2 State of the art

In today's practice, mechanical surface treatments have been widely applied particularly in the spring-manufacturing, automotive and aerospace industries. Furthermore, these processes are known to be well established in ancient times concerning metallic materials where evidently hammering was the first mechanical method used to make particular components to final shape and strength [16]. It was realized that the failure due to fatigue depends on many factors, and very often it develops from particular surface areas of engineering parts. So, it seems possible to improve the fatigue strength of metallic components by the application of suitable mechanical surface strengthening processes [16].

2.1 Methods of mechanical surface treatment

Various mechanical treatment processes can be applied to enhance the surface characteristics of engineering components. These treatments use physical processes to determine the resulting surface condition. The compressive stresses are mainly induced into ductile metals mechanically by localized plastic deformation within the outer surface region [17]. Mechanical surface treatment processes usually available in today's industry can be roughly divided into cutting and non-cutting methods [18]. However, the main focus of cutting methods is on producing a final shape of a product, while achieving optimal surface layer states is only a secondary objective. Therefore, the present study is confined to describing the non-cutting methods which serve to primarily enhance the surface layer state. A summary of these methods is shown in [Table 2-1](#). The methods are generally divided into groups based on the movement between the tools and the workpiece and also the nature of the impacting force, i.e. either a static or an impulsive tool impact. In the present study, the description of methods without relative movement is limited to impulsive impact, which has a repetitive irregular pattern as in shot and waterjet peening as well as a repetitive regular pattern as in laser shock peening process.

Table 2-1: Overview of the principal non-cutting processes of mechanical surface treatment [18]

Tool input	No. of treatments	Without relative movement	With relative movement			
			Rolling		Sliding	
			Without slip	With slip	Solid medium	Liquid medium
Static	Singular	smooth embossing, flat embossing, size embossing	deep rolling, finish rolling, size rolling		spinning, drawing, spinning	autofretting, stressing
	Repetitive regular					
Impulsive	Singular					
	Repetitive regular	hammering, laser shock peening, waterjet peening				
	repetitive irregular	shot peening, needle peening, ultrasonic peening			brushing	

2.1.1 Shot peening process

Shot peening is a cold working process generating a high plastic strain on the surface of metals. In general, it has been applied to the metal parts that require a high level of surface hardness and an elevated resistance to fatigue failure in service [19]. Shot peening is widely used as a mechanical surface treatment method in the automotive and aerospace industries [20]. In the process, peening balls or ‘shots’ which are normally made of hard materials such as steel, ceramic or glass spheres, strike a surface of metal at high velocity as illustrated in [Fig. 2-1](#). After the strike, the elastically stressed region tends to recover to the fully unloaded state, while the plastically deformed region sustains some permanent deformation. A compressive residual stress region is introduced due to these inhomogeneous elasto-plastic deformations [21].

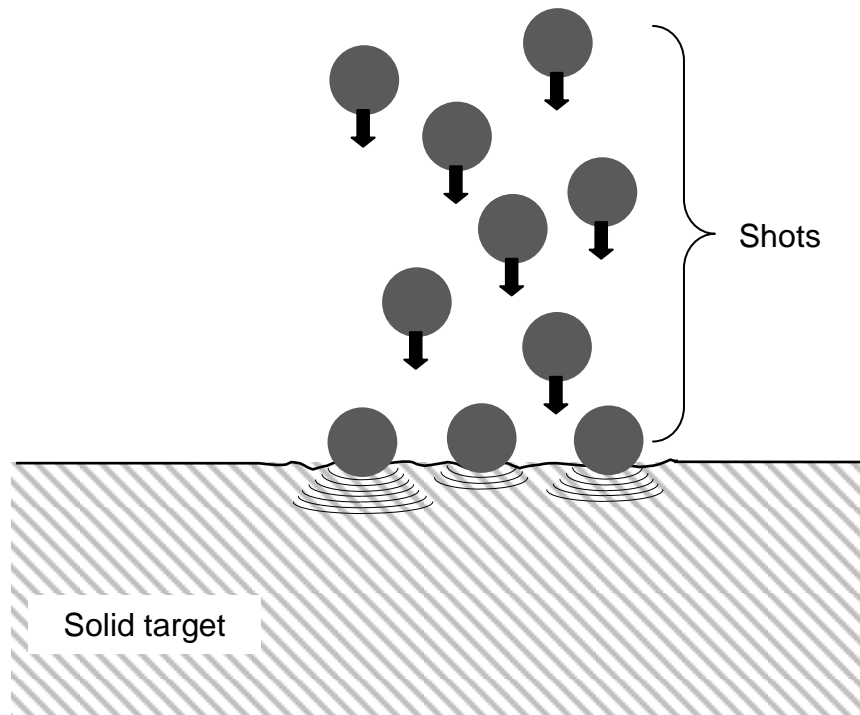


Fig. 2-1: Illustration of shot peening process [22]

Wohlfahrt [23] explained about the two competitive residual stress (σ_r) generating processes in the shot peening as illustrated in [Fig. 2-2](#). The first process is the direct plastic elongation of layers very close to the surface as a consequence of tangential forces due to numerous shot indentations as shown in [Fig. 2-2 \(a\)](#). As the deformed region tends to expand, it is restrained by adjacent material which has not been plastically deformed by the shot impact. The plastic zones are joined up to form a uniform layer when the whole of the surface is covered by impinging shots. Since the plastically deformed surface layer seeks to occupy more space, it is progressively compressed. It is comparable to the hammering of the surface and is indicated in an increase of surface roughness. The elastic-plastic elongation of the surface layers yields the maximum magnitude of compressive residual stresses at the very surface as indicated in the bottom of [Fig. 2-2 \(a\)](#).

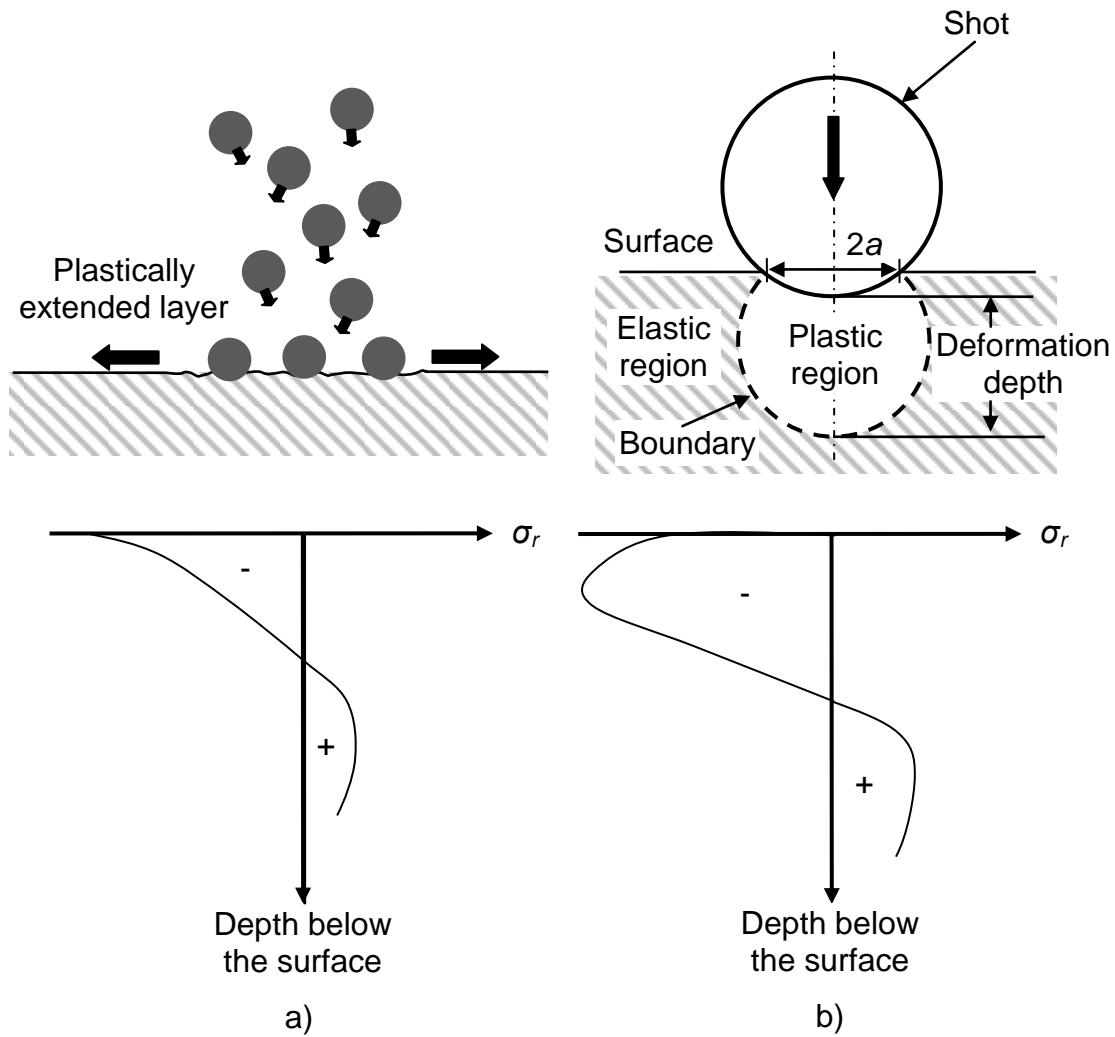


Fig. 2-2: Schematic illustration of the formation of residual stresses due to the two residual stress generating processes in shot peening, a) direct stretching of a surface layer and, b) Hertzian pressure [23, 24, 25]

The second residual stress generating process can be explained as Hertzian pressure which arises as a consequence of the vertical force connected with the impact of each shot ball as illustrated in [Fig. 2-2](#) (b) [23, 24]. The resulting shear stress has a maximum value at a distance of $0.47a$ below the surface (where a is the radius of the contact zone) [23]. The residual stress distribution is illustrated in the bottom of [Fig. 2-2](#) (b). If the Hertzian pressure becomes high enough, the maximum shear stress can exceed the flow stress in the depth of $0.47a$ and the resulting plastic deformation will generate compressive residual stresses in this depth [23]. In practice, the distribution of compressive residual stress after the shot peening process is the result of the combined effect of these two competing processes, direct plastic surface deformation and plastic deformation of deeper layers [25]. The depth

of the induced compressive residual stress may be up to a few hundred micrometers below the treated surface [24, 26, 27].

The introduction of compressive residual stress by surface plastic deformation is usually regarded as the major factor in increasing the fatigue strength. The magnitude and depth of the compressive stress depends upon the kinetic energy of the impacting particles, the yield strength of the peened material and the relative hardness of the shots and the peened material [26]. Since, the kinetic energy of the shots, E_s , is given by Eq. (2-1).

$$E_s = \frac{1}{2} m_s v_s^2 \quad (2-1)$$

where m_s and v_s are the mass and velocity of the shot particle respectively. Thus, the velocity of the shots is regarded as one of the most significant parameters in the shot peening process [28].

In the shot peening process, the kinetic energy transferred by a shot stream can be measured based on a standard procedure called Almen Intensity Test developed and patented by John O. Almen [28]. The intensity is obtained by using Almen strips and an Almen gauge as shown in Fig. 2-3. The Almen strips are made from cold-rolled spring steel (SAE 1070 – Material no. 1.1231) in three different thicknesses and denoted as *N*, *A* and *C* strips for different intensity measurement levels but all have the same dimensions [28]. The strip is exposed to the shot stream for a specified time and it bends because of plastic deformations induced by the shot peening as shown in Fig. 2-3 (a) Then, the strip is removed and placed on the Almen gauge as shown in Fig. 2-3 (b). The value of the arc deflection at the centre of the Almen strip is recorded as the Almen intensity (I_{shot}). A higher intensity (i.e. higher arc deflection) means that a higher amount of kinetic energy has been transferred to the treated components [25].

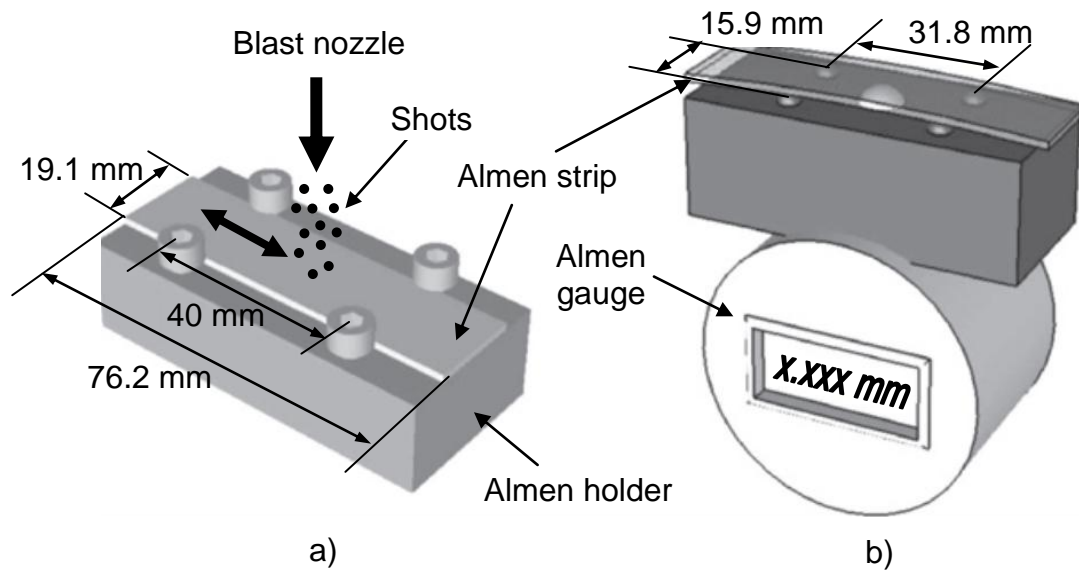


Fig. 2-3: a) The Almen strip is peened on an Almen holder, b) the Almen arc height is measured using the Almen gauge [29]

A lot of investigations have been conducted to study the effect of shot peening in the formation of a residual stress field and its effect to the fatigue life. Lee et al. [19] investigated the effect of the cementite phase on the surface hardening of carbon steel with three different carbon contents, i.e. 0.1 %C, 0.45 %C, and 0.8 %C, under the shot peening process. All specimens were treated at different peening durations (t_p) using rounded cut wire (RCW) hardened steel shots with an average diameter (D_s) of 250 μm . The results show that the surface hardness increases with an increase in carbon content of the steels as shown in [Fig. 2-4](#). They concluded that the surface hardening of the carbon steels in the shot peening is achieved through both the grain refinement and carbon dissolution following the spheroidization of the cementite phase. They observed a higher degree of the grain refinement and also a higher amount of dissolved cementite into the ferrite in the steels with higher carbon contents. This renders the ferrite supersaturated with carbon, upon which the degree of surface hardening markedly increases.

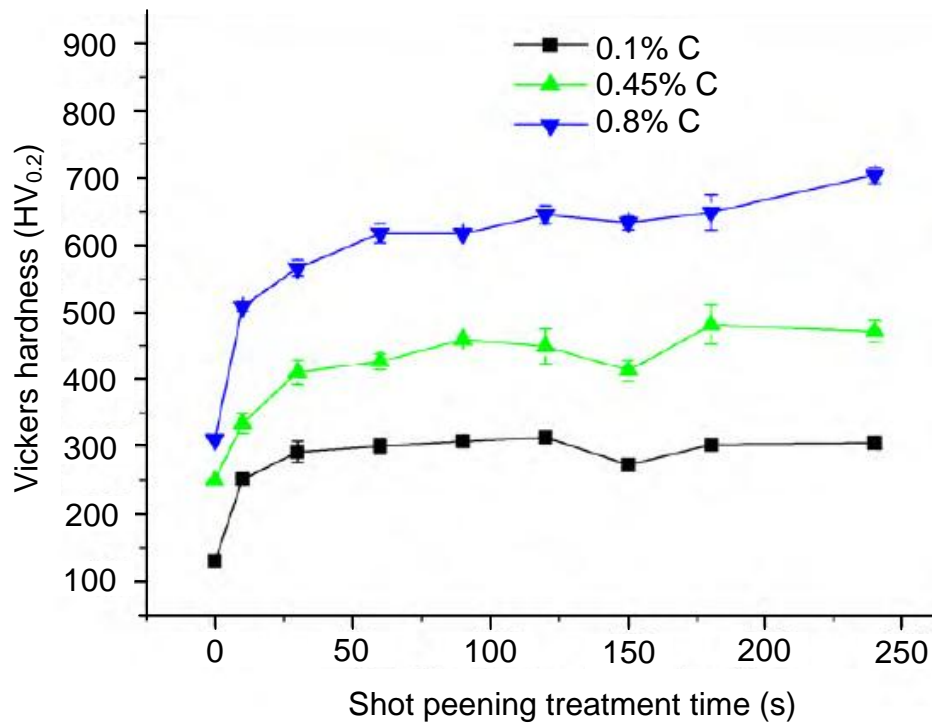


Fig. 2-4: Surface hardness profiles of the three carbon steels [19]

Sanjurjo et al. [20] investigated the effects of the shot peening process on a duplex stainless steel AISI 2205 (Material no. 1.4462). They have treated the material using the shot peening process in a controlled condition where a significant higher intensity peening was developed. The cast steel S-230 shots were used. The results were compared with the same material treated by an industrial shot peening process but produced a lower intensity peening. As expected, the controlled shot peening treatment was much more effective in inducing a higher compressive residual stress up to 631 MPa as compared to 367 MPa in the case of the industrial peening. In addition, the total thickness of the compressive layer generated by the controlled peening treatment was more than 350 μm deeper than the one generated by the industrial peening.

Wang et al. [26] studied the compressive residual stress field for several shot-peened metals namely 20Cr, 30CrMo, 40Cr, GC4, 45 steels and LC9 aluminium alloy in different states systematically and quantitatively. They developed empirical models for measuring the compressive residual stress at the surface, $\sigma_{r,s}$, maximum compressive residual stress, $\sigma_{r,max}$, and the depth of the compressive residual stress field, z , as shown in Eq. (2-2) to Eq. (2-4) respectively.

$$\sigma_{r,s} = 120 + 0.5\sigma_{YS}(\pm 30) [MPa] \quad (2-2)$$

$$\sigma_{r,max} = \begin{cases} 70 + 0.667\sigma_{UTS} (\sigma_{UTS} < 1000 \text{ MPa}) [MPa] \\ 430 + 0.323\sigma_{UTS} (\sigma_{UTS} \geq 1000 \text{ MPa}) [MPa] \end{cases} \quad (2-3)$$

$$z = z_0 + f_A \left(1.392 - \left(0.611 \times \frac{\sigma_{UTS}}{1270 \text{ MPa}} \right) \right) [\mu m] \quad (2-4)$$

where σ_{YS} is the yield strength, σ_{UTS} is the ultimate tensile strength, f_A is the peening intensity (i.e. arc height on A-strip) and z_0 is the assumed value of z which equals to 0.01 mm for Ti-alloy and Al-alloy, 0.09 mm for steel with $\sigma_{UTS} = 870 - 1000$ MPa and 0.04 mm for other steels.

The effect of hardness, fatigue strength and surface roughness of nitrogen austenitic stainless steel in primary shot peening and double shot peening was investigated by Singh et al. [30]. Initially, both specimens were peened with glass shots however zirconium micro-shots were used for double shot peening. They found that a double shot peening process reduces the surface roughness without significant change in the residual stress. As a result, the fatigue life increases mainly due to the improvement in surface finish from the double shot peening process. Furthermore, Torres and Voorwald [31] evaluated the fatigue life of AISI 4340 steel, used for aircraft landing gears, under four different peening intensities (i.e four different peening pressures were applied from 8 to 45 psi). Steel shots (S 230) with an average diameter of 0.7 mm were used. They found that at the highest stress there is no change in the number of cycles until failure except in the specimen treated with the lowest peening intensity as shown in [Fig. 2-5](#). However, there is an increase in the fatigue life for medium and high cycles. They also found that the best fatigue life conditions were found in the intermediate peening intensities. Perhaps, a lower fatigue life at the highest intensity was due to an effect of overpeening. The surface experiences some defects in the form of microcracks which may act as crack initiation in the fatigue test.

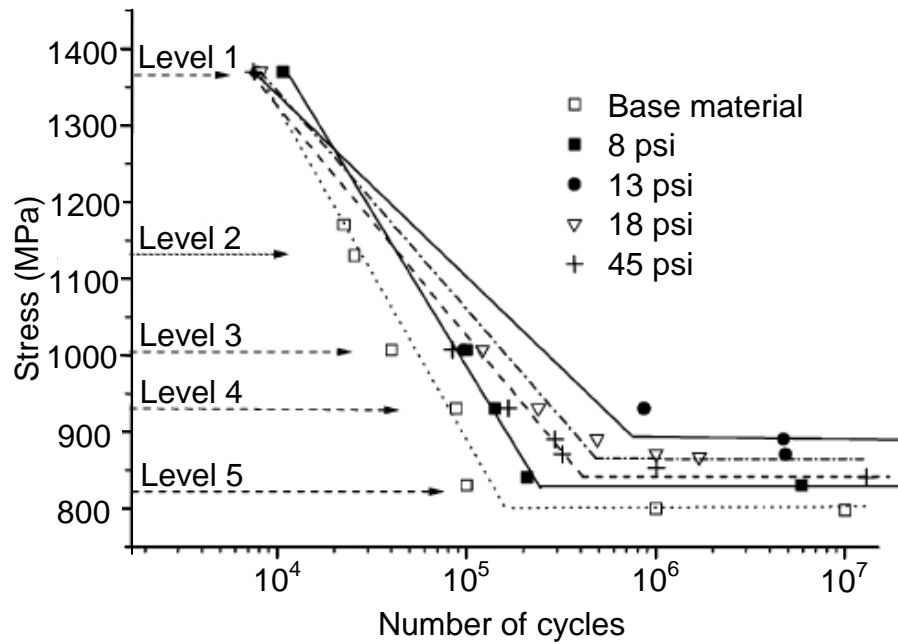


Fig. 2-5: S-N curves on the base and shot peened specimens [31]

Zhang et al. [32] investigated the influence of different shot peening media namely Zirblast B30, Ce-ZrO₂ and glass beads on the fatigue performance of the high-strength wrought magnesium alloy AZ80. They found that peening with Ce-ZrO₂ shots resulted in the fewest surface defects, lowest roughness, highest maximum compressive residual stress and highest improvement of the fatigue strength. The different responses in surface integrity of the peened magnesium alloy are possibly due the different properties of the peening media. Since Ce-ZrO₂ has a higher density and size than Zirblast B30 and glass beads, thus it has to travel at a significantly lower velocity in order to achieve a similar peening intensity. Consequently, less surface damage was produced from a lower kinetic energy of Ce-ZrO₂ shots.

Lee et al. [33] studied the influence of shot peening on the microstructure, surface roughness and corrosion resistance of AISI 304 stainless steel. Based on microstructures at the surface, they found the formation of nano-sized grains, multi-directional mechanical twins and strain-induced martensite. Also, the plastically deformed region with multi-directional mechanical twins and slip bands on the surface layer was formed to a depth of 200–250 μm . The hardness was increased by about 40 % with respect to the as-received specimen up to a depth of 300 μm . However, the surface roughness was increased significantly after the shot peening

treatment which leads to a lower corrosion resistance mainly because the practical area for corrosion per unit area also increases with increasing surface roughness.

Shen et al. [34] studied the effect of plasma nitriding of AISI 304 austenitic stainless steel with a pre-shot peening process. The material was peened with industrial steel shots having a diameter of 0.8 mm. They found that the substrate suffered severe deformation and the grain boundary became obscure within the outmost layer below 20 μm in depth. Beyond that depth, a huge change in the substructure within the grains and different systems of slip bands were observed for most of the grains as illustrated in [Fig. 2-6](#).

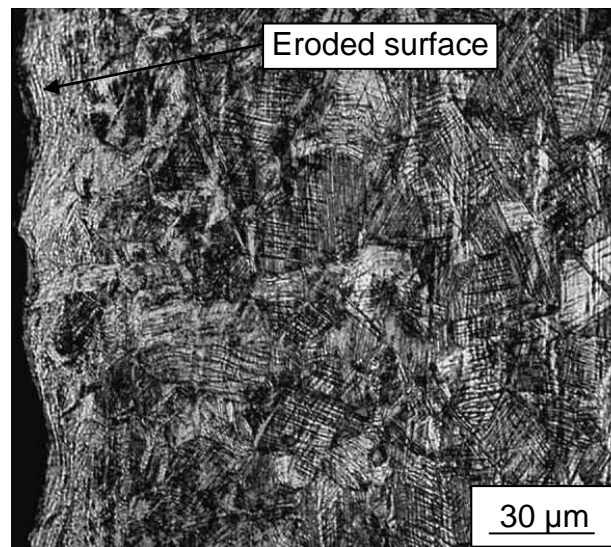


Fig. 2-6: Cross-sectional morphologies of shot-peened austenitic stainless steel 304 sample [34]

2.1.2 Laser shock peening process

In principle, laser shock peening (LSP) is similar to other peening processes with the aim of enhancing the fatigue life of engineering components. It is the latest peening technology initially introduced in the aerospace industry [22]. In the process, a laser beam is directed toward the surface of a metal component coated with an ablative layer (e.g. paint or tape) and covered with a thin layer of transparent material, usually water as illustrated in [Fig. 2-7](#). This creates high energy plasma that generates a pressure shock wave and propagates the compressive stress through the material [22]. The material will experience an extensive plastic deformation when the magnitude of the shock wave exceeds its dynamic yield strength. After the flow of the

shock wave, the elastically stressed subsurface layer tends to recover to its original condition but the continuity of the material in the elastic and plastic zone prevents this to happen. As a result, it develops a compressive residual stress at the surface thus contributing to the improvement of yield strength and hardness of laser peened material [35, 36, 37].

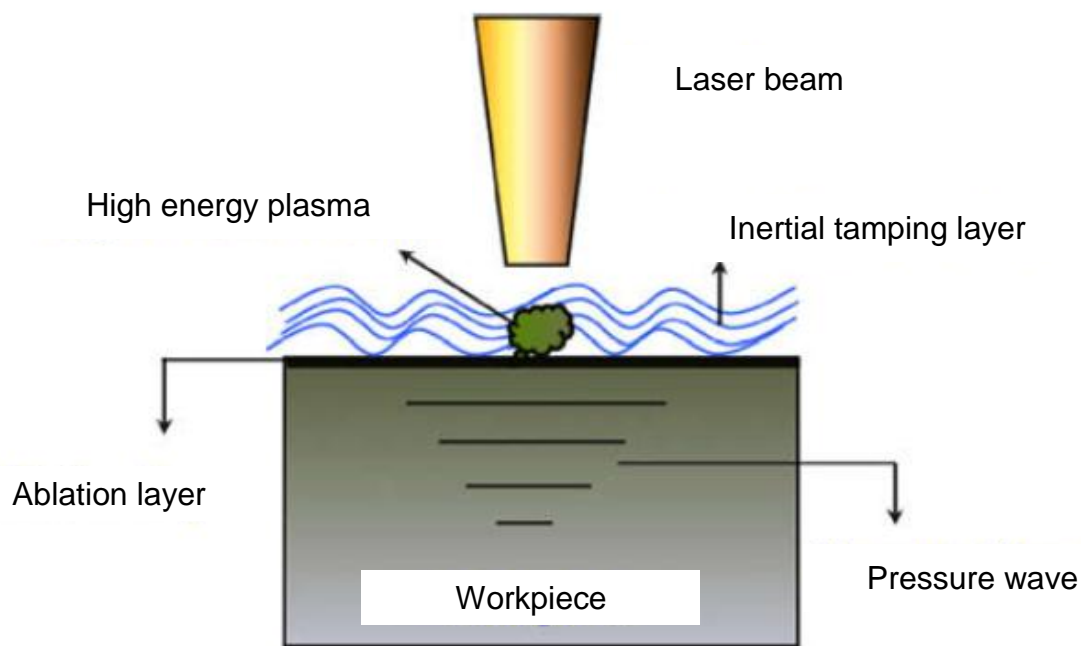


Fig. 2-7: Illustration of laser peening process [35]

There are two distinctive aspects of the laser peening as compared to the shot peening process [22]. Firstly, the surface to be peened is immersed in a thin layer of water which prevents the high energy plasma from expanding, thus driving the energy into the workpiece surface. Secondly, the ablative layer is used as a sacrificial layer to prevent a possible burning of the surface from high energy plasma.

In general, a depth of laser peening induced stresses between 0.5 to over 1 mm can be attained depending on processing conditions and material properties [37]. In some cases, laser peening induces higher residual stresses as well as deeper depths [38]. The fatigue life enhancement of metallic components may be accomplished with the inducement of the compressive residual stresses in surface layers. Gao [38] determined the improvement of fatigue property in 7050-T7451 aluminium alloy by laser and shot peening. Laser peening was done under different treatment times, n_{shot} (i.e. 2, 4, 6 and 8 times). While, shot peening was done using different

shots (i.e. glass beads, ceramic beads and cast steel shots). The author found that the laser peening had produced the depth of compressive residual stress layer up to 1200 μm compared to only 250 μm for shot peening. Moreover, the fatigue strength of the laser peened specimen was increased by 42 % with respect to the as-machined specimen, while there was an increase of 35 % in fatigue strength for the shot peened specimen.

Other researchers reported the effect of laser shock peening without a coat or ablation layer in the workpiece material [39, 40]. The laser beam is directly in contact with the workpiece surface, thus requiring the use of a smaller output power as to avoid severe melting of the surface. Maawad et al. [39] investigated the high cycle fatigue performance of titanium alloy after a laser shock peening process without coating. They varied few parameters in the laser shock peening process namely the laser pulse energy (E_{pulse}), laser spot diameter (D_{spot}) and laser pulse density (N_{pulse}). They also compared the results with a similar material treated by a shot peening process. The outcomes indicated that the laser shock peening process without coating produced a better performance of high cycle fatigue than the conventional shot peening process due to a larger amount of compressive residual stress and a deeper strengthening layer. However, the laser shock peening process without coating produced a higher surface roughness caused by easily induced surface vaporization and later on re-solidification of the molten droplets. Furthermore, Sathyajith [40] reported the effect of laser peening without coating on aluminium alloy 6061-T6. Their results show that the laser peening without coating had significantly improved the surface compressive stress and hardness with a little increase in surface roughness.

Lim et al. [41] investigated the enhancement of abrasion and corrosion resistance of duplex stainless steel using a pulsed Nd:YAG laser in the laser shock peening process. They treated the surface at a condition which may result in the maximum increase of surface hardness because a higher abrasion resistance may be achieved for metals with a higher surface hardness. They found that the compressive residual stress at the laser peened sample was enhanced by about three times from that of unpeened material with the depth profile extended up to about 0.8 mm. They also found that at the optimal process parameters, wear volume and corrosion rate of duplex stainless steel were reduced by 39% and 74.2%, respectively which a lower

density and size of corrosion pits were produced on wear track as a result of laser shock peening.

Peyre et al. [42] compared the performance of laser and shot peening in surface modifications of 316L stainless steel. In the laser peening process, the laser intensities (I_{laser}) as well as number of laser impacts (n_{impact}) were varied accordingly. The results show that the work hardening levels consistently increase with higher laser intensities and number of laser impacts. Furthermore, the microstructures of laser peened specimens show a lot of deformation twins and persistent slip bands especially for specimens treated with higher laser intensities and numbers of impacts as shown in Fig. 2-8. They also found that the laser peening treatment generated lower residual stresses and work hardening levels than shot peening treatment possibly due to the nature of laser peening process which involves no contact.

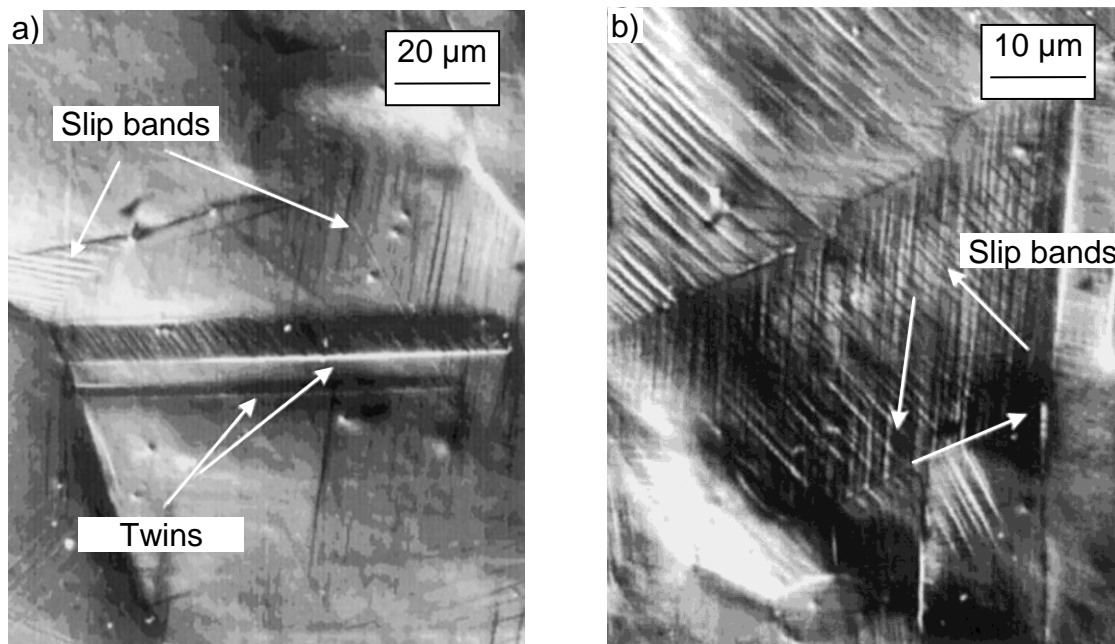


Fig. 2-8: Microstructures of laser peened surfaces show a) deformation twins and slip bands (one activated system) at 4 GWcm^{-2} laser intensity and 3 number of laser impacts, b) a presence of three deformation systems in the same grain at 8 GWcm^{-2} laser intensity and 6 number of laser impacts [42]

2.1.3 Liquid peening process

In the liquid peening process, high impacts of water droplets are used to impinge a metal surface thus causing local plastic deformation. Mostly water is used but some researchers performed experiments with oil. Others used a water-oil emulsion. A

basic principle of water jet peening is shown schematically in [Fig. 2-9](#). The nozzle is moved at a desired feedrate (traverse speed), v_n , in the linear direction across the surface to be peened. The process parameters that may influence the residual stress formation and coverage area are the traverse speed of the nozzle, v_n , the water pressure p_o , at the nozzle entrance, the nozzle to specimen's surface distance (i.e., standoff distance, h), the nozzle diameter, D_n and the inclination angle of attack, θ . p_i is the impact pressure that strikes the metal surfaces. Water pressure (or jet flow rate) at the nozzle entrance, nozzle geometry (e.g. nozzle diameter), inclination angle of attack and pitch are the main parameters influencing the jet coherence as well as the peening power. Whereas, standoff distance and traverse speed of the nozzle are the main parameters affecting the interaction between the jet and the workpiece surfaces [8].

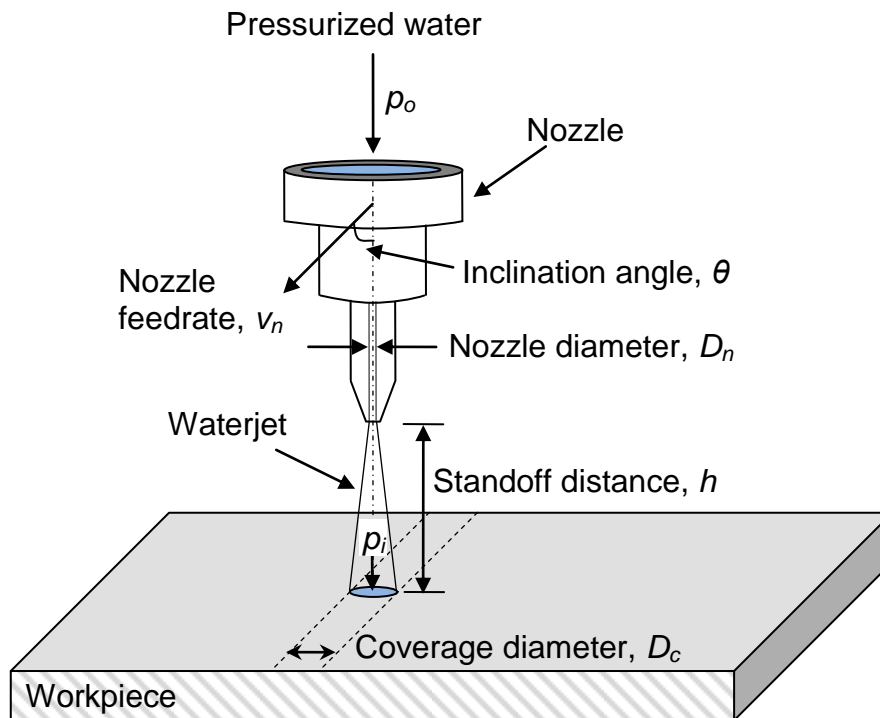


Fig. 2-9: Basic principle of water jet peening

Quite a number of research in WJP process has been conducted to study its potential applications and associated sciences. Chillman et al. [43] explored the effects of high pressure WJP at 600 MPa on the surface finish and integrity of the titanium alloy (Ti-6Al-4V). They varied the traverse rates (v_n) and the standoff distance (h). They found that WJP at 600 MPa induces a plastic deformation to higher depths in the subsurface layer and also a higher degree of plastic

deformation. Grinspan and Gnanamoorthy [44] substituted water with oil in a peening process (OJP) of aluminium alloy where the depth of residual stress was noticed to be more than 250 μm below the surface.

Ju and Han [45] investigated the influence of water cavitation peening (WCP) treatment on the microstructure of pure titanium. WCP refers to a technique in the waterjet peening process in which suitable air can be inserted into the extra high-velocity flow in the nozzle as shown in [Fig. 2-10](#). The combined high pressurized water with air can generate a uniform bubbles cloud which then collapse on the surface of the components thus producing a high impact of water cavitation [46]. Normally, the same nozzle arrangement in abrasive waterjet treatment is used for WCP. The air is led into the inlet instead of the abrasive particles. Ju and Han [45] observed that a longer peening duration (t_p) of WCP produces higher residual stresses. Qin et al. [47] investigated the influence of the inclination angle (θ) on the process capability of water cavitation peening. They found that the impact pressure and residual stresses obtained at various inclination angles were almost equal to each other within the effective process area.

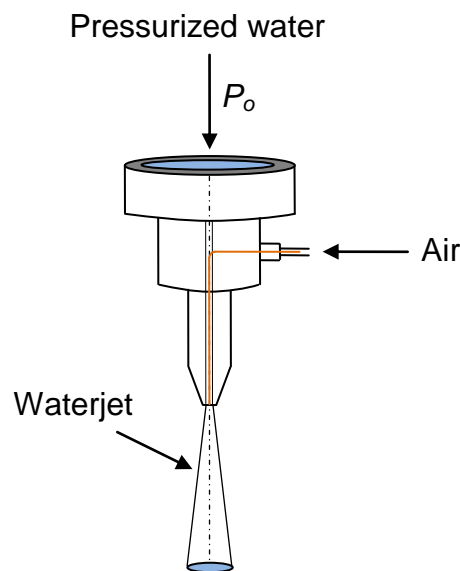


Fig. 2-10: Schematic of jet nozzle with aeration

2.2 Mechanics of waterjet impact

The mechanism of waterjet impact is determined from how the waterjet stream hits the surface of the material. The physical characteristics of the waterjet stream may affect the response of treated surfaces. Therefore, it is important to understand the

physical representation of the waterjet stream as it exits from the nozzle until it hits the workpiece.

A stream of high-pressurized water consists of three different regions namely, the initial region, the transition region and the final region [48, 49]. These regions can be explained with the help of a diagram as shown in Fig. 2-11 (a). The stagnation pressure is assumed to be the same as that at the nozzle exit within the initial region. Also, the jet is considered as a solid continuous beam with a high axial dynamic pressure and almost no air content. The approximate length can be determined from extrapolation of the decrease in the stagnation pressure [50]. A typical flow of the waterjet is shown in Fig. 2-11 (b).

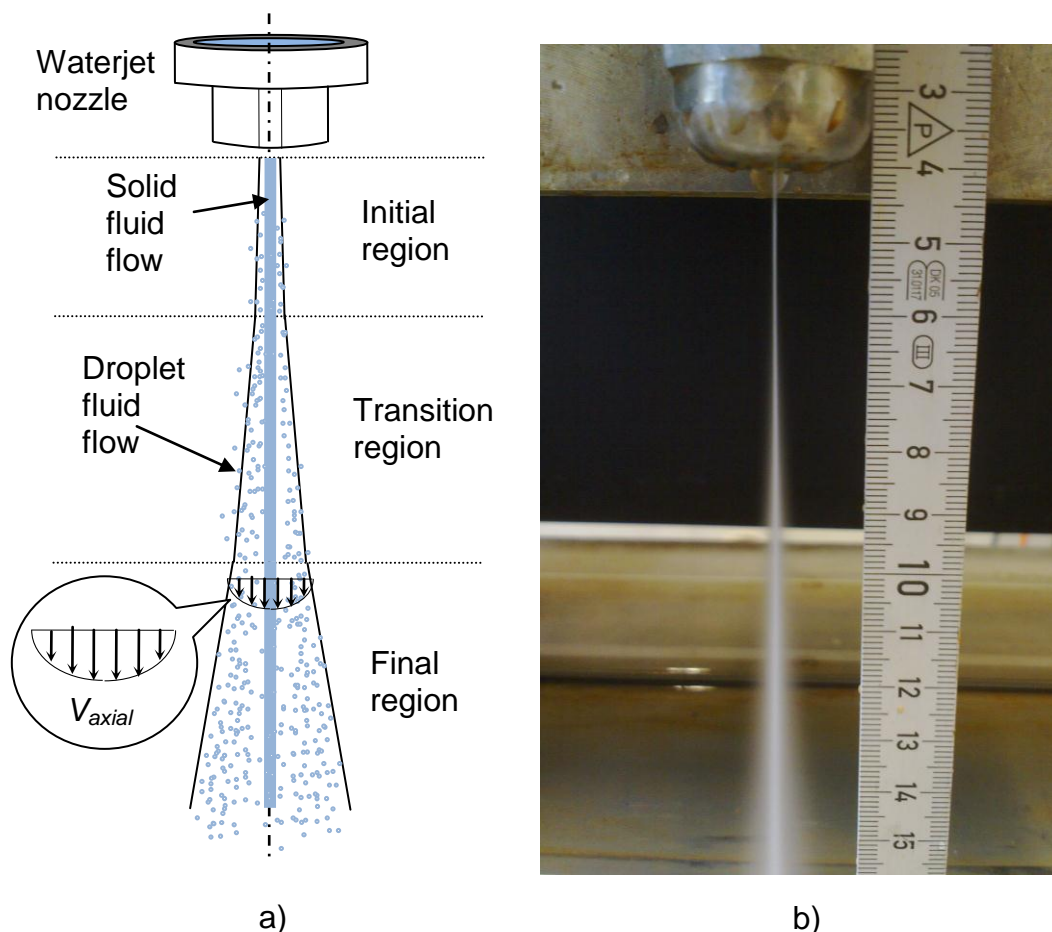


Fig. 2-11: a) Physical characteristics of waterjet stream [48, 49], b) a typical flow of waterjet

At the end of the initial region, the continuous structure of the waterjet starts to disintegrate and becomes a droplet beam consisting of water lumps and droplets surrounded by fine droplets. This is considered to be the beginning of the transition

region. The breakup of the waterjet stream into droplets is mainly due to the interaction of the waterjet with the surrounding air. The velocities of the water lumps and droplets remain largely unchanged within this region. However, continuous interactions between the waterjet and surrounding air result in more disintegration of the droplets as the jet travels further in the transition region. This will lead to a reduction in droplets velocities and also a widening of the effective flow field i.e. a diverging of water stream. It is also believed that the size of droplets becomes smaller as it is closer to the outer boundary between the jet and the ambient air. This is due to the fact that the outer boundary contains a higher concentration of air and the jet is in constant friction with it. As a result, the axial velocity of the jet reduces as it moves away from the centre of the nozzle to the extent it exhibits almost zero velocity as shown in [Fig. 2-11](#) (a). In other words, within this region there exists a mist zone where the droplets show a zero velocity [51]. Finally, the waterjet enters the final region where there is a noticeable decrease in the droplets velocities as the droplets break up into finer droplets. Within this region, the jet has dissipated most of the energy to effectively modify the features of material surfaces.

The velocity of the jet exiting from the nozzle can be estimated based on the Bernoulli's equation in fluid dynamics. It is assumed that the water exits the nozzle as in ideal case which there is a rotationally symmetric flow with a constant speed over the cross sectional pipe. This assumption will neglect the pipe and nozzle friction for an incompressible flow. According to the Bernoulli equation, the equilibrium equation (the inlet is indexed as 0, and the outlet is 1) can be established as Eq. (2-5).

$$p_0 + \rho gh_0 + \frac{1}{2}\rho_0 v_0^2 = p_1 + \rho gh_1 + \frac{1}{2}\rho_1 v_1^2 + \Delta p_{loss} \quad (2-5)$$

Δp_{loss} is a pressure loss in the nozzle due to the friction in the nozzle. In order to calculate the theoretical maximum possible energy conversion in the nozzle, the pressure drop is neglected as in ideal case, i.e. $\Delta p_{loss} \approx 0$. The height difference between the inlet and outlet can be neglected especially if the nozzle's standoff distance is very small or in a case of horizontal arrangement, i.e. $h_0 = h_1$. The outlet pressure can be neglected since the water flows freely in the ambient air at the end of the nozzle, i.e. $p_1 \approx 0$. Also, inlet velocity can be considered zero since it is within a closed system. Then after simplification and rearranging of (Eq. 2-5), the outlet velocity, v_1 can be estimated as in Eq. (2-6).

$$v_1 = \sqrt{\frac{2p_0}{\rho}} \quad (2-6)$$

This is the theoretical maximum possible velocity. In actual case due to the friction, the rate may be somehow lower. In this case due to the very low pressure at the outlet, the water can be assumed to be incompressible. The velocity, v_1 , can be considered as the water impact velocity, v_i , when it hits the material surface [52, 53]. However, the fluid flow associated with high-speed impinging droplets is rather complicated and still not fully understood [54].

2.2.1 Liquid erosion mechanisms

It is known that highly pressurized water is able to cause severe damage to the surface of target materials by means of erosion. This is caused by the collision of a high-velocity liquid mass with a solid target that generates short high-pressure transients. An extensive review on the liquid impact was summarized by Field [55] from his own works and that of other researchers [52, 56, 57, 58, 59, 60]. The impact of liquid on a solid target consists of two main stages as illustrated in [Fig. 2-12](#).

In the first stage, the liquid behaves in a compressible manner generating the so-called ‘water-hammer’ pressure or impact pressure [61]. At the moment when the droplet hits the solid surface, a high compressive pressure region is generated at the shock front of the jet due to the compression of water. This pressure is the main reason for most of the damage resulting from liquid impact on the solid surface.

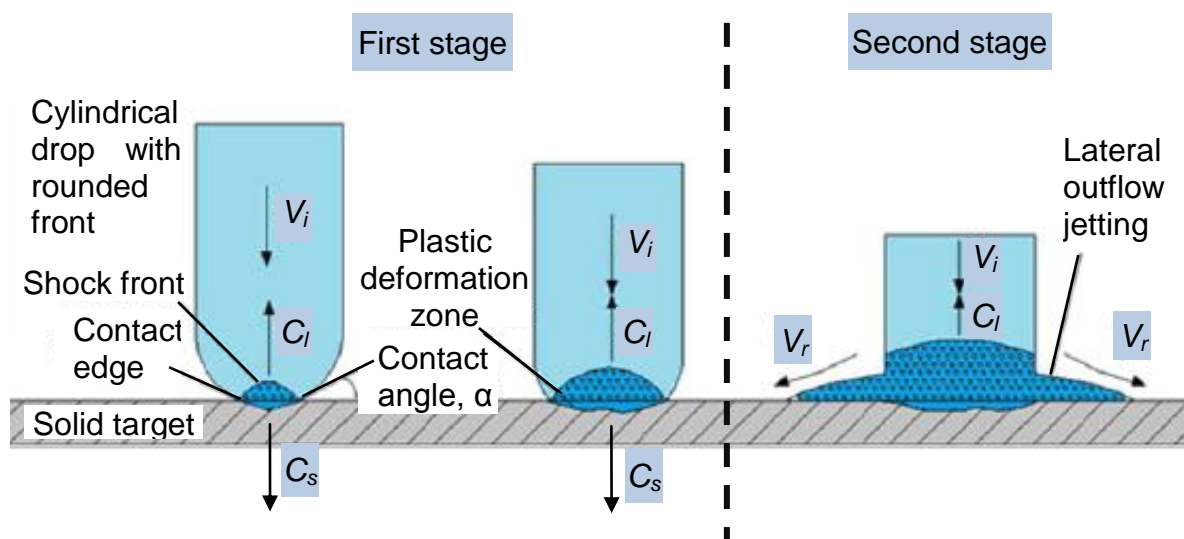


Fig. 2-12: Schematic illustration of liquid impact on solid target [56, 62]

The second stage of liquid impact begins after the release of the impact pressure as illustrated in Fig. 2-12. At this stage there is a rapid fall in pressure along the contact periphery. The outward flow becomes possible when the limit of compressible deformation of the drop is exceeded as given in Eq. (2-7).

$$\frac{v_i}{c_l} \leq \sin \alpha \quad (2-7)$$

where α is the contact angle.

The outward flow continues while the water-hammer compression at the centre of impact is relieved as well. The maximum pressure acting on the surface will then occur along the central stagnation line. The central stagnation pressure, p_s for incompressible flow is given in Eq. (2-8).

$$p_s = \frac{1}{2} \rho_l v_i^2 \quad (2-8)$$

In this stage of impact, a large shear stress is generated due to the high-speed radial flow, v_r across the surface after the jet impact as indicated in the second stage of Fig. 2-12. As a result, local shear fractures may happen even in high strength materials [57].

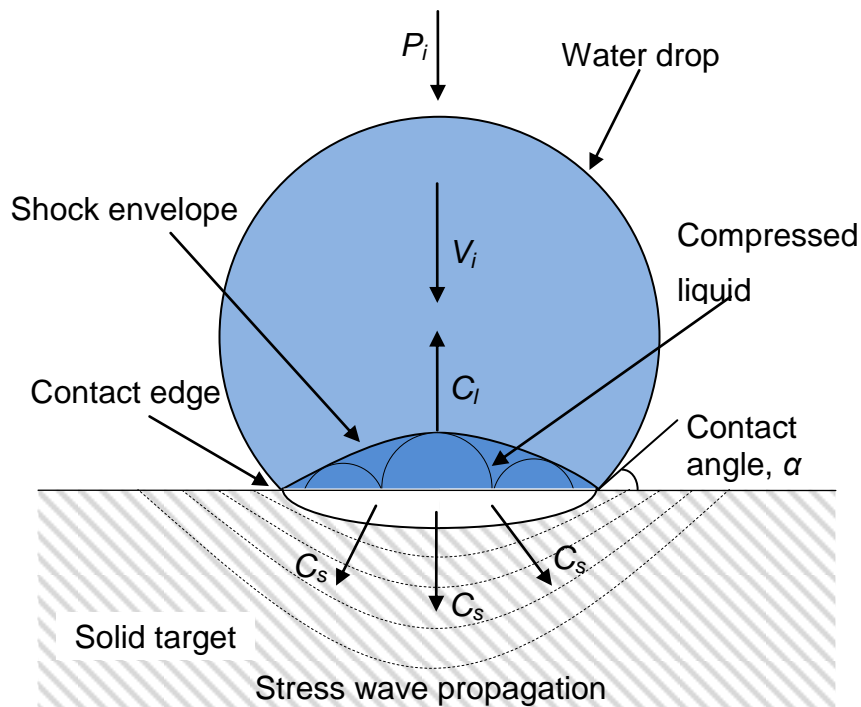


Fig. 2-13: The situation a short time after a droplet impact [55]

The situation a short time just after the impact is illustrated in [Fig. 2-13](#). The shock envelope is made up of many wavelets. The liquid behind the envelope is compressed and the solid target beneath this area is subjected to a high pressure. This high pressure impact is maintained while the shock wave moves supersonically from the edge of the contact area between the impacting droplet and the solid target into the material with respect to the shock speed [55, 56, 57, 60].

The contact zone of the impact begins to expand with the non-uniform pressure distribution reaching a maximum value thus leading to the generation of a dilatational compression wave, a distortional shear wave and a Rayleigh surface wave [56, 63, 64]. These waves are illustrated in [Fig. 2-14](#). The Rayleigh wave travels in the longitudinal direction of the wave velocity of the material. This surface wave interacts with small surface cracks which are located an extended distance from the primary impact zone thus leading to additional crack growth [56, 63].

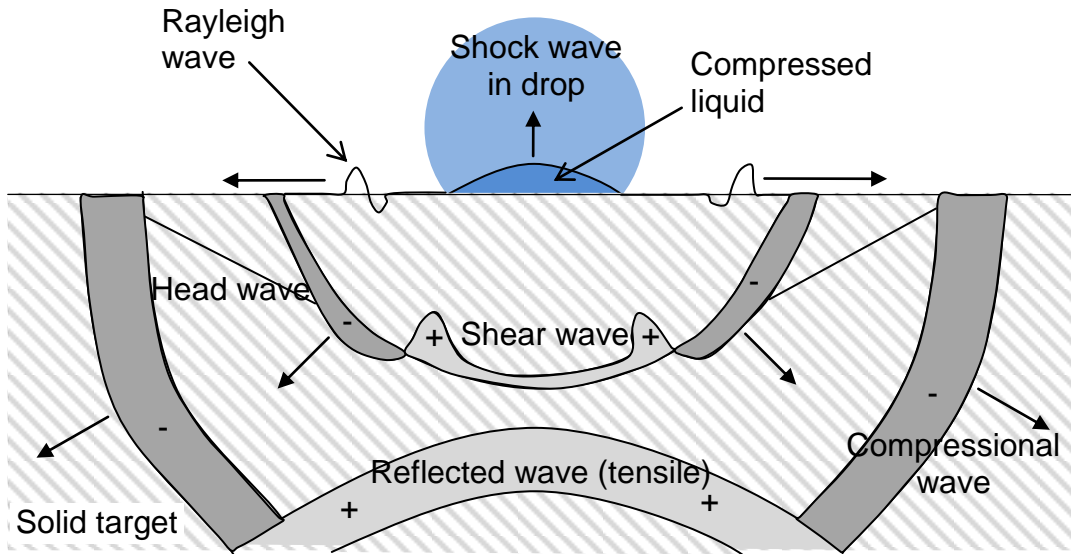


Fig. 2-14: Impact of a spherical drop on a material showing the shock wave in the drop and the stress waves in the material. The shaded width of the shear and compressional waves represent the relative amplitudes of the particle motion [64]

The most commonly used approximations to the pressure developed in the liquid-solid impact are based on the one-dimensional elastic impact theory. The water-hammer pressure or impact pressure, p_i can be calculated as in Eq. (2-9).

$$p_i = \frac{v_i \rho_l c_l \rho_s c_s}{\rho_l c_l + \rho_s c_s} \quad (2-9)$$

where v_i is the impact velocity of the liquid. ρ_l, ρ_s and c_l, c_s are the densities and the shock velocities of the liquid and the solid, respectively. For an impact on a rigid target which is true for most metals, the values of $\rho_s c_s$ is an order of magnitude larger than $\rho_l c_l$ for water. Therefore, the impact pressure can be sufficiently approximated as in Eq. (2-10).

$$p_i = \rho_l c_l v_i \quad (2-10)$$

In case of a high velocity liquid impact, an appropriate shock velocity can be used to calculate the impact pressure. This can be expressed with the term of the acoustic velocity, c_w as shown in Eq. (2-11).

$$c_l = c_w + k v_i \quad (2-11)$$

where the acoustic velocity, c_w for water is about 1500 ms^{-1} . While, k is a constant which has a value close to 2 for water in the high impact velocity range (v_i up to 1000 ms^{-1}).

The duration of its impact depends on the time taken by the released waves to pass through the compressed liquid. The very short duration of the water-hammer pressure pulse, Δt can be calculated as in Eq. (2-12).

$$\Delta t = \frac{3r v_i}{2c_l^2} \quad (2-12)$$

where r is the radius of curvature of the drop (liquid mass) in the region of contact.

Therefore, it can be summarized that the erosion of material surface results from both stages of liquid impact. During the initial stage, the maximum compressive stress acts along the central line of impact thus producing a central depression crater as well as various cracks. Later, the compressive stress diminishes and the outward flow begins to exert a tensile stress at some critical value of the liquid/solid contact angle. The erosion of the material surface by an impacting liquid may result from the impact pressure, or from the shearing effects of high-velocity outward flow, or from the both [52, 56, 57, 58, 59, 60, 61].

2.2.2 Strengthening mechanisms

The properties of metal are directly related to its dislocation motions. The strengthening mechanism of metal depends on this relationship. Dislocations are defects in the orderly arrangement within an atomic structure of a metal. The plastic deformation of a metal corresponds to the motion of dislocations. In other words, a metal is able to plastically deform if the dislocations inside it are able to move. Therefore, the mechanical strength may be improved by reducing the ability of dislocations to move. It is because hardness and strength are related to the ease with which plastic deformation can be made to occur. That is to say that a larger mechanical force will be required to initiate plastic deformation. On the contrary, a higher ability of dislocation to move results in a larger tendency of a metal to deform, as a result it becomes softer and weaker. In general, it can be said that all strengthening techniques rely on this simple principle which is to restrict the dislocation motion thus producing a harder and stronger material [17, 65, 66].

The strengthening of metals can be achieved through a few mechanisms for example by grain size reduction, solid-solution alloying and strain hardening [17, 65, 66]. However, these are the strengthening mechanisms for single phase metals and may require some increase in temperature. The strengthening of multiphase alloys is more complex wherein the mechanical properties are dependent on the characteristics of the microstructure. The development of a microstructure generally involves some type of phase transformation which is a change in the number and/or character of the metallic phases [17]. Since the materials used in the present study are both ferrous alloys (i.e. austenitic stainless steel 304 and ferritic carbon steel 1045), therefore the discussion is limited to the strengthening mechanism based on phase transformations particularly martensitic transformation as it happens principally in Fe-C alloys systems. However, the strain hardening mechanism is also discussed here since it happens in the peening processes. Of course, in the real sense the alloys are deformed and strengthened in conjunction with one another, for example, an alloy may be collectively strengthened based on strain hardening and phase transformation [17].

The strain hardening is sometimes called work hardening or cold working because the temperature during the deformation process occurs at a much lower temperature

relatively to the melting temperature of the metal and in most cases at room temperature [17]. It is the strengthening process of a metal by plastic deformation. When a material is permanently deformed, the dislocation motion moves until it is stopped by something else in the crystalline lattice. The dislocation motion can be effectively restricted by another dislocation since they cannot pass through each other [65]. As a result, the dislocations will be mounted up against each other and became interlocked. This may prevent any further permanent deformation without the use of significantly higher energy thus considerably enhancing the strength of the material under subsequent loading.

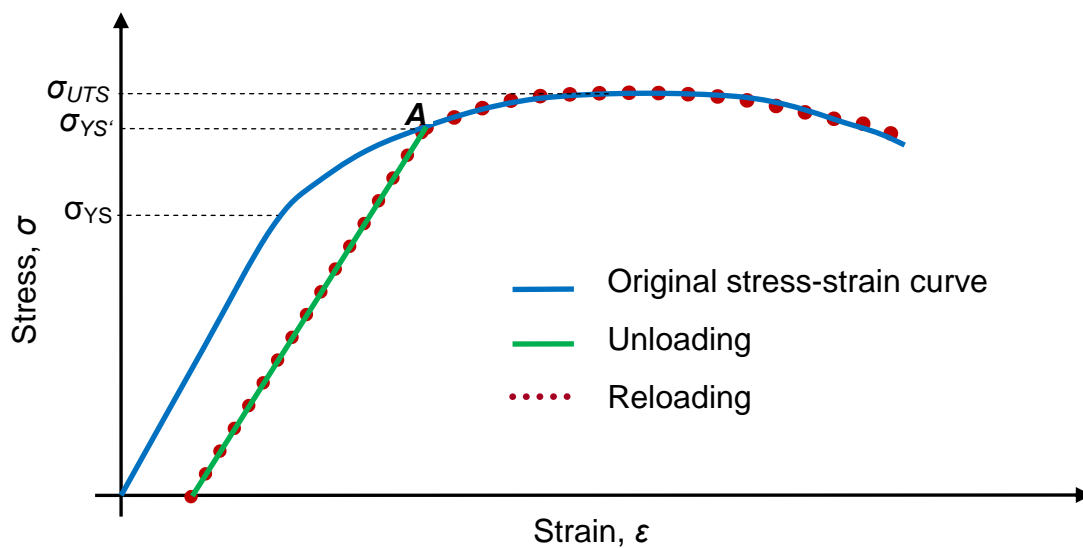


Fig. 2-15: The typical stress-strain diagram of a metal [17, 65]

Theoretically, strain hardening can be explained based on a typical stress-strain diagram of a metal as shown in Fig. 2-15. The original stress-strain behaviour is shown as a blue line. Its original yield strength is indicated as σ_{YS} . Initially, a certain amount of stress is applied beyond its original yield strength to point A. When the stress is released, the material returns to a state of zero stress along a path parallel to the elastic loading line (green line) due to elastic strain recovery. Upon reloading, the material follows the same path up to the original stress-strain curve (red dotted line). However, the material's elastic limit has been increased to $\sigma_{YS'}$. Therefore, the material becomes stronger during the process since its new yield strength, $\sigma_{YS'}$ is now substantially higher than the original yield strength, σ_{YS} . However, the total elongation available has now diminished thus decreasing its ductility and formability.

Martensitic transformation involves a change in the crystal structure by shear movements of atoms [67]. This reaction is found in many alloy systems, but the principal and most important system is the Fe-C alloy. Martensite is a metastable phase which has the same composition as the austenite from which it forms [17]. Martensite forms without a change in composition, therefore diffusion is not required for the transformation to occur. It is for this reason that martensite can form at such a low temperature by adequate loadings. The most important characteristic of martensite is its potential of very high hardness. In some way, this hardness is directly related to the fundamental characteristic of martensite, but somehow it is caused by the severe distortions that accompany the formation of the martensite.

2.3 Effect of waterjet impact on surface

2.3.1 Roughness

It is widely known that the surface roughness plays a critical role in determining the fatigue life of engineering components. Thus, a lot of studies have been conducted to investigate the effect of waterjet impact on material surfaces. Arola et al. [68] studied the effect of waterjet peening (WJP) and abrasive waterjet peening (AWJP) on the surface topographies of commercially pure titanium and a titanium alloy (Ti6Al4V). Based on a comparison of the standard roughness parameters for each material, they found that the surface texture resulting from AWJP was primarily dependent on the treatment conditions, not the material. However, a minimal increase in roughness occurred in the treatment of the pure titanium as expected from its comparatively lower yield strength than the titanium alloy. There were also changes of roughness through WJP of both materials, however the changes were far less significant than those resulting from AWJP. This is to be expected as AWJP invokes a combination of erosion and localized plastic deformation as a result of abrasive particle impact thus increasing the surface roughness. On the effect of peening parameters, they found that the increase in kinetic energy achieved with the use of large abrasives and high jet pressures resulted in more substantial erosion of the surface.

Arola and Hall [69] further investigated the effect of parameters on particle deposition in abrasive waterjet surface treatment of commercially pure titanium. Based on the results, they found that the surface texture was mostly influenced by the level of the

jet pressure and the abrasive particle size. As expected, the surface roughness increased linearly with the jet pressure and the abrasive particle size. They explained that an increase in kinetic energy of the jet resulting from the mass and/or velocity of the abrasives increased the potential for material removal. Furthermore, some of the abrasive particles remain embedded in the surface upon jet impact which may cause a change in surface roughness. Arola and McCain [70] explored the feasibility of using AWJP as a new method of surface preparation for metal orthopaedic implants. The surface roughness resulting from AWJP of the titanium alloy (Ti6Al4V) was significantly lower than the surface of titanium with plasma spray coating used for cementless fixation in metal orthopaedic implants.

Kunaporn et al. [71] studied the effect of different nozzles on surface preparation of 6061-T6 aluminium alloy. They used three different nozzles namely a fuzzy jet (i.e. air is aerated into the nozzle similar to a WCP jet), a fan jet (i.e. the water is spread upon exiting the nozzle), and a round jet (plain waterjet) as shown in [Fig. 2-16](#). They found that under the same treatments, the specimens treated with the fan jet produced the same order of surface roughness to those specimens treated with the round jet. Whereas the specimens treated with the fuzzy jet yielded a roughness value about five times higher than the other two types of nozzles. They explained that the fuzzy jet produced a higher level of the kinetic energy than the fan jet and the round jet. The high jet energy in the fuzzy jet is due to the air that is directed into the mixing tube.

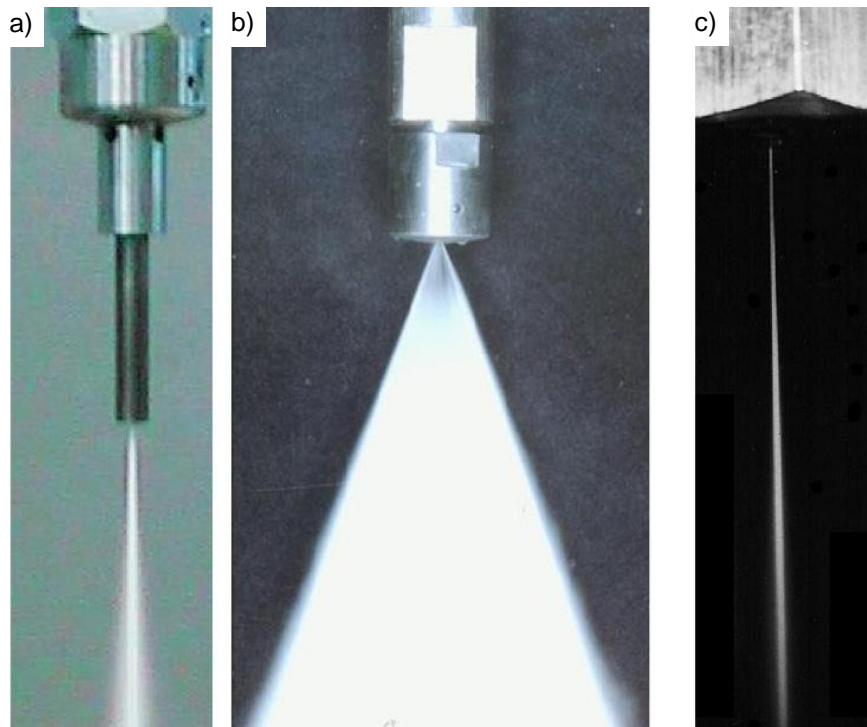


Fig. 2-16: The stream of waterjet exiting the, a) fuzzy jet, b) fan jet, and c) round jet nozzles [71]

Kunaporn et al. [72] also investigated the effect of peening parameters on the surface texture using only a fan jet and round jet nozzles. However, a different aluminium alloy was used (7075-T6). Generally, the removal characteristics within the impact zone are found to predominantly dependent on the standoff distance [73]. The water peening using the round jet nozzle caused a rougher surface than those using the fan jet nozzle for standoff distance higher than 36 mm. However, the fan jet nozzle had a significant effect on the surface roughness at a standoff distance less than 30 mm. Little changes of surface finish were noticed in the specimens waterpeened at the standoff distance higher than 44 mm using both nozzles. While, increasing the peening duration by lowering the nozzle traverse rate yielded an increase in surface roughness [74]. Furthermore, the waterjet treatment under the same peening duration yielded a similar surface roughness although the nozzle traverse rate was different [72]. Possibly, under the same peening duration, the resulting kinetic energy of the jet on those specimen surfaces is equal. The surface roughness may also not change if the materials are under an elastic pre-stress condition during an abrasive waterjet peening process [75].

2.3.2 Erosion

It is understood that the surface erosion is directly related to the surface roughness. High erosion of the surface tends to produce a high roughness as well since more material has been removed. Therefore, it is not surprising to see surfaces subjected to waterjet treatment producing high roughness values while generating more erosion of the surface.

Chillman et al. [43] conducted a preliminary investigation on the effect of different types of jets in waterjet peening on the surface finish of a titanium alloy (Ti6Al4V). Three types of jets were used namely plain waterjet (only water), water-air jet (or water cavitation jet) and water-water jet (WWJ) (i.e. water was entrained instead of air). They observed that the WWJ was violently vibrating and produced a pattern that was not uniform. Meanwhile based on the erosion volume rate, the water cavitation jet produced higher erosion than the plain waterjet. They further investigated the effect of various peening parameters using only the plain waterjet and water-air jet [51]. In general, for both types of jets they found that a decrease in the traverse rate led to an increase in the degree of erosion as shown in [Fig. 2-17](#). It became clear that the erosion mechanism is dependent on the jet exposure time which increases by decreasing the traverse rate.

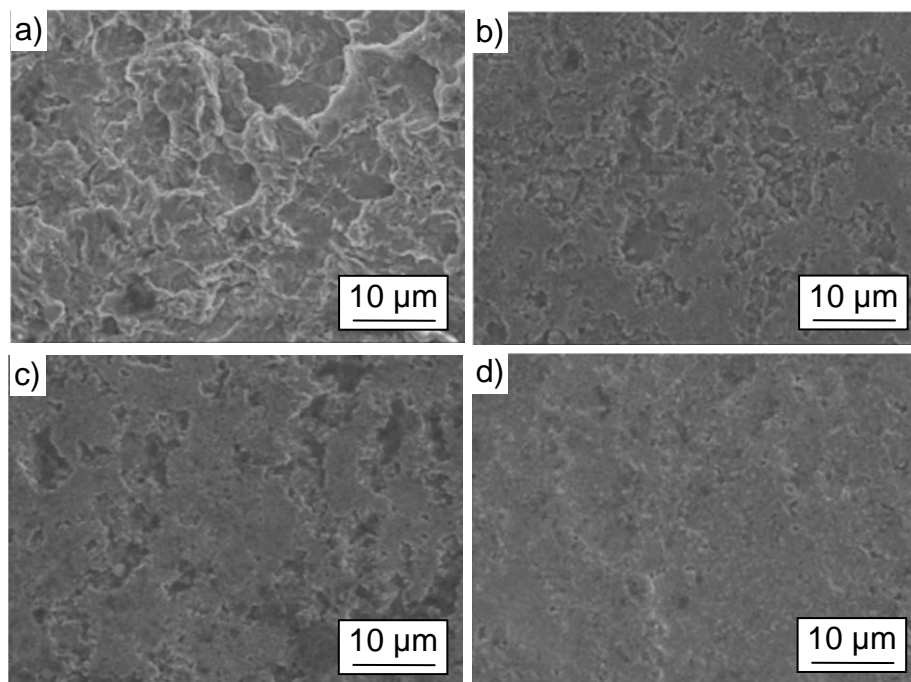


Fig. 2-17: Surface erosion images of titanium alloy at different traverse speed, a) 1272 mm/min, b) 1902 mm/min, c) 2538 mm/min and d) 10158 mm/min [51]

With respect to the standoff distance, the two types of jets gave a different effect on the erosion. For the case of plain waterjet, no erosion was evident at small standoff distances (< 38 mm). However, the erosion rate continued to increase up to a distance of 100 mm and continued to decrease beyond that. For the case of water-air jet with a low air flow rate, the erosion became much more uniform regardless of standoff distances [51]. While, a high air flow rate led to a decrease in the erosion for standoff distances higher than 38 mm. They explained the relationship between the standoff distance and the erosion from the jet structure point of views. The amount of air flow rate aerated into the jet flow had a direct impact on the ability of the jet to remove material. The injection of a low air flow rate produced an increase in erosion rate (about 2 - 4 times) compared with the plain waterjet. It is due to an increase in the erosive nature of the jet by accelerating the breakdown of water into droplets. However, too much air may saturate the jet thus leading to a loss of velocity droplet particularly at increased standoff distance.

In contrast, Oka et al. [76] found that the maximum damage rates were commonly observed for standoff distances from 120 to 200 mm in waterjet peening of aluminium alloy 5083 regardless of pressures. Again, they pointed to the nature of the jet structure. A very short standoff distance causes a low material removal possibly because of a formation of water column instead of water droplets. The water column only presses the specimen without imposing cyclic stresses onto it. Therefore, its impact frequency is too low to cause large erosion at the very short standoff distance. The impact frequency increases as the standoff distance increases thus inducing a proportional increase in the damage rate. However, the standoff distance at the maximum damage rate did not coincide with the maximum impact frequency. They speculated that the droplet velocity might as well influence the damage rate of a material under waterjet impingement. The calculated droplet velocity was constant at the maximum value up to a standoff distance of 200 mm and it gradually decreased beyond that. Therefore, a combination of maximum droplet velocity and medium impact frequency produces the highest damage rate. Although, the maximum impact frequency was found at a standoff distance more than 200 mm, but the droplet velocity was reduced thus decreasing the damage rate.

The effect of a pulsating waterjet impact on aluminium surface using a fan jet nozzle has been investigated by Foldyna et al. [77]. An acoustic generator of pressure

pulsations was attached to the machine thus producing the pulsating jet as shown in [Fig. 2-18](#). Understandably, the pulsating jet breaks up into smaller droplets at a standoff distance shorter than is necessary for development of pulses in the jet. Therefore, the optimum standoff distance with the maximum erosion of aluminium surface was found to be shorter in the range of 20 to 40 mm depending on the excitation amplitude. They also found that the optimum standoff distance decreased with a larger excitation amplitude due to the fact that the break up length of the pulsating jet was inversely proportional to the excitation amplitude.

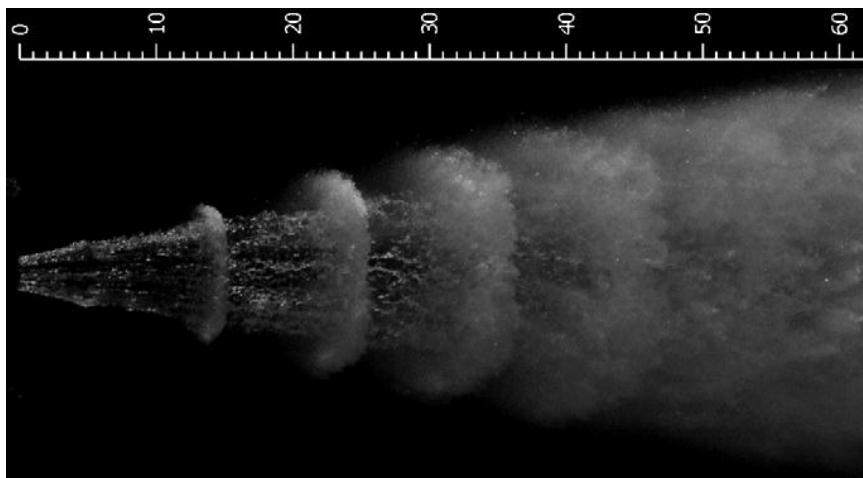


Fig. 2-18: Pulsating jet generated at 20 MPa (scale represents standoff-distance in mm) [77]

Barriuso et al. [78] investigated the effect of the traverse rate in roughening of stainless steel 316 LVM and titanium alloy (Ti6Al4V) by abrasiveless waterjet peening. Using the scanning electron microscope (SEM) to examine the microstructure of the eroded surfaces, they observed that both specimens treated with a lower traverse rate produced more erosion manifested by a larger number of pits with deeper undercuts. Also, they noticed that within similar machining conditions, the steel specimens had coarser erosion than the Ti6Al4V ones as shown in [Fig. 2-19](#). It is to be expected since the hardness of the steel specimen ($\sim 210 \text{ HV}_{0.01}$) is lower than the Ti6Al4V ($\sim 320 \text{ HV}_{0.01}$).

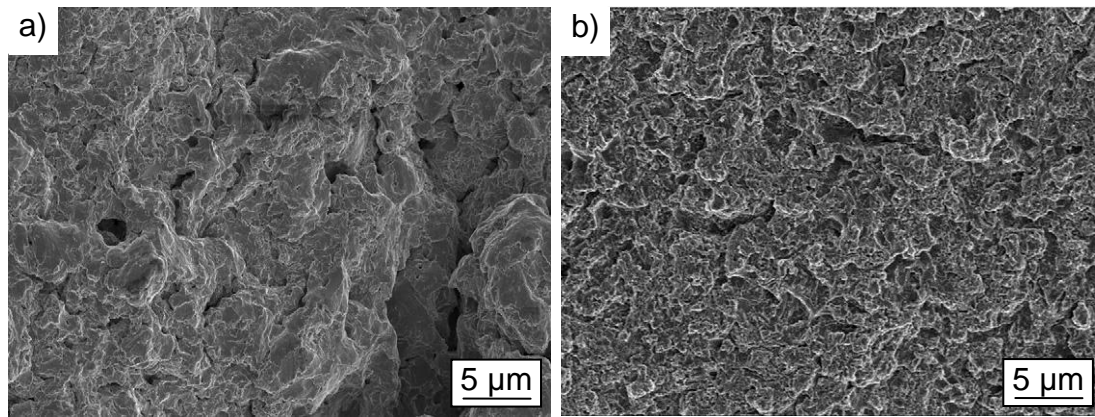


Fig. 2-19: SEM images of eroded surfaces, a) stainless steel (316 LVM) and b) titanium alloy (Ti6Al4V) [78]

A similar observation was also made by Taylor [79] in surface roughening of nickel-chromium alloy (Inconel 718) which revealed more erosion at a lower traverse rate. Taylor [79] also studied the effect of pressure on the erosion. He found that more erosion was noticed at a higher pressure. The same study notices a clear threshold pressure required for measurable erosion which is above 207 MPa. It is interesting to note that upon examination of the eroded surface using SEM at a higher magnification, the waterjet erosion produces a fractal surface. Furthermore, there is no indication of ductile fracture or brittle fracture as indicated by the absence of long-running cleavage facets. Since the waterjet erosion feature size is 10 times smaller than its grain size, as a consequence there is no feature evident that relates to the erosion structure.

Islam et al. [80] discussed the effect of waterjet surface treatment on tribological properties of aluminium-silicon alloy. They reported that the optical microscopy examination revealed the mechanisms for material removal during waterjet treatment which consisted of ploughing of grains as well as transgranular and intergranular propagation of cracks. Nevertheless, the microscopic features of the eroded surfaces are similar in nature regardless of the parametric conditions used for the treatment [70]. Further examination using SEM revealed that the impact of waterjet caused a collapse of porosity underneath the surface.

The aspects of the material removal mechanism in plain waterjet milling on gamma titanium aluminide (γ -TiAl) have been discussed by Kong et al. [81]. Their study focuses on in-depth surface observations from macro and microscopic point of view.

Based on macroanalysis of jet footprint, they found that at a low water-hammer pressure the jet did not form continuous erosion traces onto the workpiece and thus its erosion was inhomogeneous. Whereas, at higher water hammer pressure the erosion became significantly continuous. At microscopic features, they observed two different levels of material removal mechanism. Firstly, the initial damage or low level surface damage occurred through few stages namely a plastic deformation, stress wave propagation and generation of micropits. Secondly, the evolved damage or subsequent combined erosion stages resulted in mainly granular cracking and fracture as well as lamellar fracture of the material. Furthermore, Huang et al. [62] looked at the mechanisms of damage initiation in a titanium alloy (Ti6Al4V) subjected to water droplet impact. On the macroscopic scale of the damage, they observed similar erosion features as explained by Kong et al. [81]. However, under microscopic view, they found some distinct erosion features where the damage initiation was achieved through grain tilting and preferential grain boundary damage.

2.4 Effect of waterjet impact on the sub-surface

2.4.1 Hardness

It is known that the waterjet peening process causes an increase in the strength on the material sub-surface due to work hardening and phase transformation. The increase in material strength can be measured through the amount of induced residual stresses and hardness. Although, the hardness value represents only the surface resistance of the material against plastic deformation, it is widely employed mainly because of its simple test method. Furthermore, the value of hardness and residual stress induced from a peening process can be correlated. Under peening processes, the material surface shows an increase in the hardness as well as in the compressive residual stress. Although the profile and the magnitude are not similar between the hardness and the compressive residual stress, however the depth of the hardening and the strengthening layers shows a little difference. [30, 39, 82]

The effect of waterjet peening conditions on the improvement of residual stress on the surface of stainless steel 304 has been investigated by Hirano et al. [83]. Using a surface layer removal technique, they measured the residual stresses by X-ray diffraction from the surface to a depth of 250 μm . They found that the initial residual

stress at the surface was tensile in nature from 60 to 100 MPa. After WJP, the residual stresses were compressive in nature with the maximum stress at the surface of about 500 MPa and decreased with an increase in surface depth. They also found that the residual stress was still compressive at a depth of about 250 μm . In terms of the influence of various WJP conditions, they found that the residual stress increased with the peening duration. Whereas, increasing the pressure induced a higher amount of residual stress on the material surface. While, the maximum residual stress improvement was achieved at a standoff distance of about 30 mm.

Tönshoff et al. [5] measured the amount of induced compressive residual stresses on case hardened steel 16MnCr5E under waterjet peening impact. With increasing peening duration, they observed that the amount of compressive residual stress increased up to a maximum level of about 560 MPa. However, for longer peening durations, a distinct decrease of compressive residual stress was noticed. Interestingly, they also observed that somehow the water pressure had no influence on the level of the maximum compressive residual stress, but higher water pressures shifted the maximum to shorter peening durations. The increase in surface hardness was also related to longer peening durations [5]. In contrast, Arola et al. [68] noted that the induced compressive residual stresses resulting from waterjet peening of titanium alloy Ti6Al4V and pure titanium increased with the water pressure. However, the amount of residual stresses resulting from WJP of the pure titanium was higher than the Ti6Al4V. They explained that the lower yield strength of the pure titanium enabled more extensive near-surface deformation and resulted in a larger compressive residual stress.

In water cavitation peening (WCP) of steel 1045, the maximum compressive stress induced was up to 215 MPa with a depth of strengthening layer up to 110 μm [84]. Whereas, in WCP of steel 1070, Qin et al. [47] observed an increase in compressive stress of around 600 MPa from the original compressive stress of 350 MPa. By varying the inclination angles of the nozzle, they however found that the induced residual stresses were almost uniform and equibiaxial as shown in [Fig. 2-20](#). In contrast Daniewicz and Cummings [85] found a higher increase in compressive residual stresses measured in parallel to the rolling direction than those measured transversely to the rolling direction. They argued that it might be a result of crystallographic texture influences on the measurements. They further found that a

decrease in the magnitude of the compressive residual stress with an increase in the water pressure which is in disagreement with the trend observed by Arola et al. [68]. This decrease in surface compressive residual stress was potentially the result of a higher surface roughness due to an increase in the water pressure which eventually reduces the accuracy of X-ray diffraction (XRD) residual stress measurements.

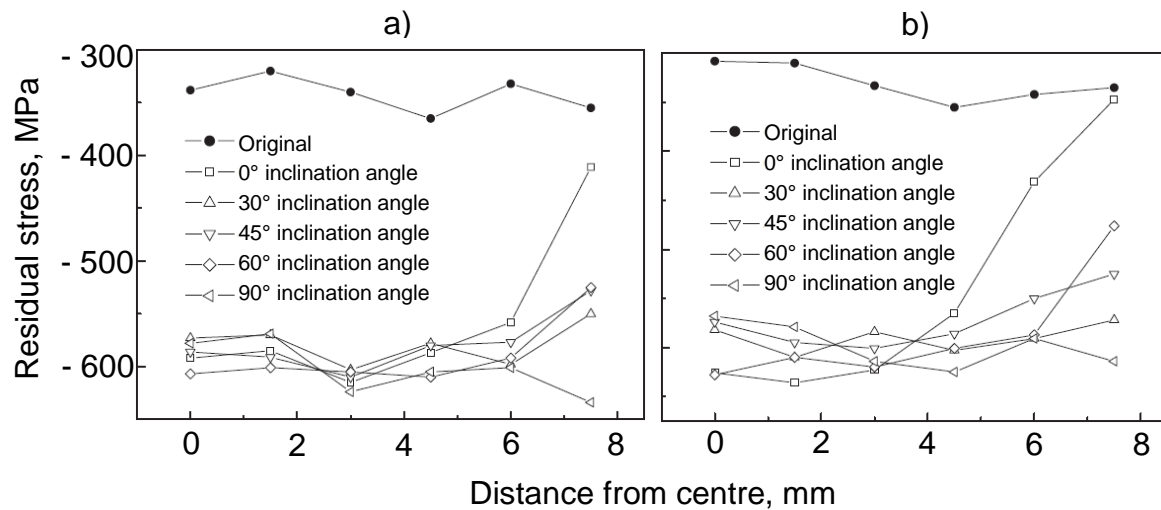


Fig. 2-20: The relationship between the inclination angle of WCP and residual stress in, a) X direction, and b) Y direction [47]

Grinspan and Gnanamoothy [82] treated aluminium alloys 6063-T6 and 6061-T4 with oil jet peening. They found the magnitude of induced surface compressive residual stress decreased with increasing in standoff distance in both materials possibly due to reduction in impact pressure with increasing standoff distance. The increase of compressive residual stress was higher in 6063-T6 than 6061-T4 due to the former higher yield strength. The depth of induced compressive residual stress in both samples was more than 200 μm . In case of hardness, they found that the surface hardness increased by 34 - 44% compared to unpeened material hardness. While the hardened layers extended up to a depth of approximately 350 and 400 μm for both materials respectively. In oil jet treatment of another material steel 1040, they found the surface compressive residual stress increased with decreasing nozzle traverse rate with a depth of the strengthening layer of about 50 μm [86]. While, the increase in hardness was about 14 - 22% of the base material hardness. Kunaporn et al. [71] found that the hardness increased in some conditions by about 10-15% from the base material hardness during waterjet treatment of aluminium alloy 6061-T6. The degree of surface hardening was extended to a depth of about 200 μm .

Islam et al. [80] also observed a similar increase in hardness of about 15% during waterjet treatment of Al-Si alloy.

2.4.2 Microstructures

The phase transformation in a surface layer of 304 stainless steel induced by the shot peening process has been discussed by Ni et al. [87]. It is understood that the surface of metal experiences a severe plastic deformation due to continuous collision with the shots. Therefore, the plastic deformation at high strain rates results in a phase transformation from the austenitic phase to the martensitic phase [87]. They used conversion electron Mössbauer spectroscopy (CEMS) and X-ray diffraction (XRD) methods to characterize the phase structures in the shot peened surface layer. They found that the amount of martensite increased remarkably with an increase in shot peening treatment time until a maximum value was reached after 15 min of treatment time as illustrated in Fig. 2-21. However, upon longer treatment time, the amount of martensite decreased slightly due to a reversion of martensite possibly from the effect of temperature rise at the surface.

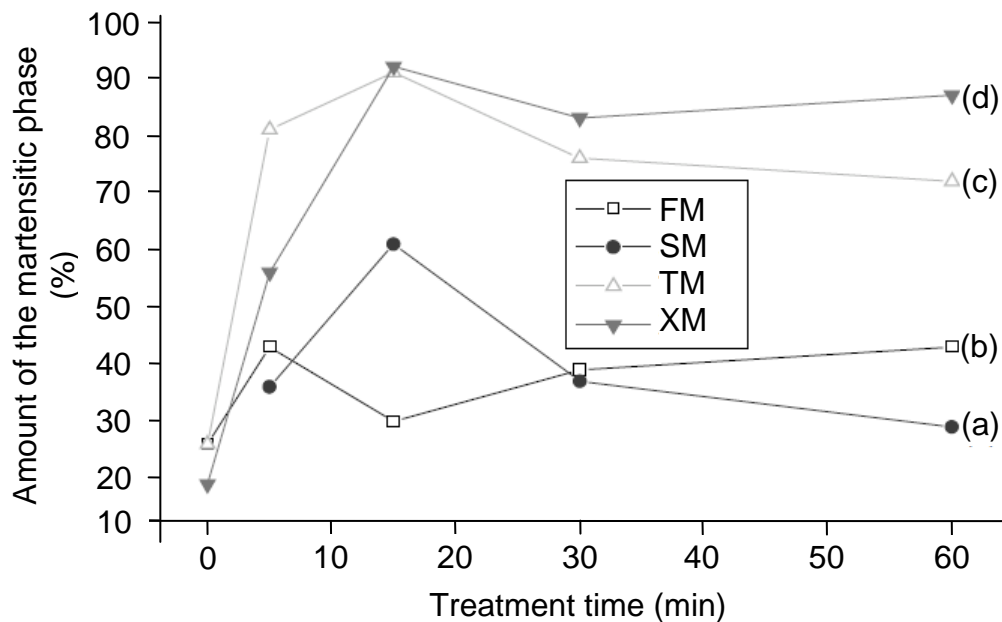


Fig. 2-21: The amount of martensitic phase as a function of treatment duration in stainless steel 304, (a) the second type of martensite (SM), b) the first type of martensite (FM), c) total martensite (TM) determined from CEMS, and (d) total amount of martensite determined from XRD (XM) [87]

Whereas, Wang et al. [88] investigated the formation of martensite in the surface layer of medium-manganese austenitic steel caused by shot peening treatment. Using the XRD and transmission electron microscopy (TEM), they found the formation of nanograined microstructures mainly composed of strain induced α martensite grains with the average size of about 8 nm. The volume fraction of α martensite decreases with an increase in the depth of shot-peened surface which most likely reduces its hardness as well. Ju and Han [45] reported on the effect of WCP duration on the microstructural changes in the near-surface layer of pure titanium. They observed that the density and quantity of deformation twinning increased gradually with increasing peening duration and decreased gradually with increasing layer depth from the treated surface. The SEM analysis revealed that several deformation twinings formed in a single crystal grain, while others interlaced with the different slip systems as depicted in [Fig. 2-22](#).

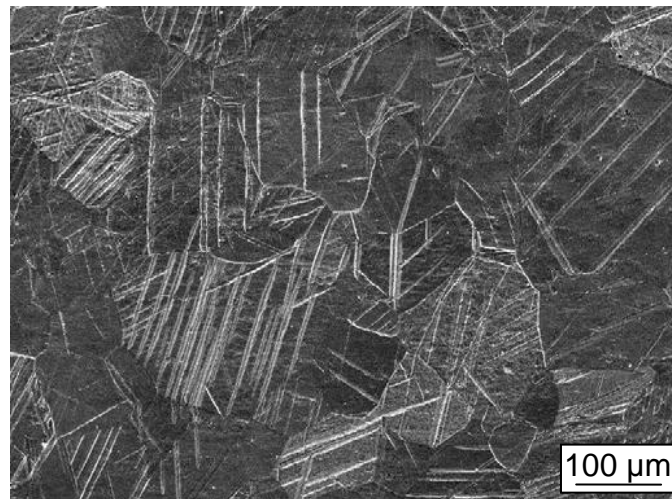


Fig. 2-22: SEM microstructure at a depth of 30-40 μm [45]

Barriuso et al. [78] found severe plastically deformed grains up to a depth of 20 μm beneath the eroded surface during waterjet peening of stainless steel 316 LVM. Further on, the grains progressively increased to achieve a grain size of the bulk up to a distance of 70 - 100 μm as shown in [Fig. 2-23](#) (a). Interestingly, these distances coincided approximately with regard to the distance of the hardness gradient. Upon detailed examination at a higher magnification, they also observed some cracks just below the eroded surface as shown in [Fig. 2-23](#) (b).

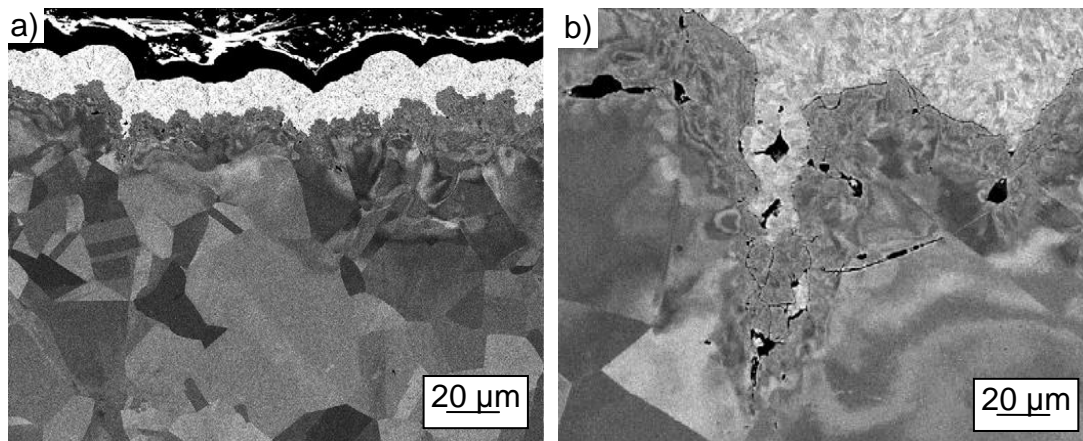


Fig. 2-23: SEM images of stainless steel 316 LVM at different magnifications, a) 500 X and, b) 3000 X [78]

Tsujikawa et al. [89] treated stainless steel 304 samples using a shot peening process at different particle injection pressures. They noticed that the sample shot peened at a higher injection pressure generated more deformed grains in the forms of slip bands and twins as shown in [Fig. 2-24](#). Also, the deformed grains were found at a deeper distance from the peened surface.

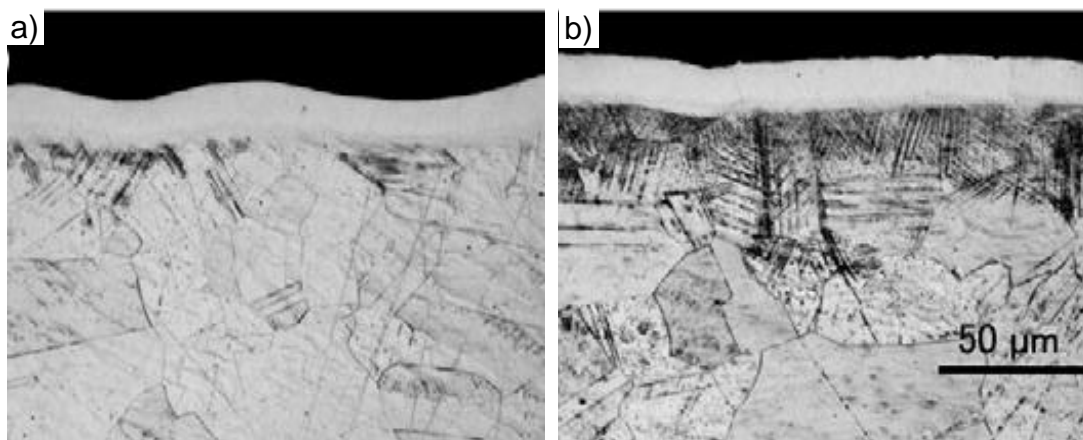


Fig. 2-24: Cross-sectioned views of shot peened specimens at different injection pressures, a) 0.1 MPa and, b) 0.9 MPa [89]

2.5 Effect of waterjet impact on fatigue life

Fatigue is one of the main criteria in the design of engineering components. It is simply because it has been estimated that it contributes to approximately 90% of all mechanical service failures [90]. It is the failure due to the application of fluctuating stress that is much lower than their yield stress limit. A few studies have reported that the waterjet peening process is employed to modify material surfaces by introducing

compressive residual stresses which consequently may increase the fatigue life of the materials.

The improvement of fatigue strength in abrasive waterjet peening of stainless steel 304 and titanium alloy Ti6Al4V has been reported by Arola et al. [91]. They compared the fatigue strength of both specimens treated with two parametric conditions that gave a high and low induced compressive residual stresses respectively. They found a rather limited increase in the fatigue strength for both materials ($< 10\%$) as shown in Fig. 2-25 (a). They further treated a new set of Ti6Al4V specimens at a higher intensity (peening duration) as to produce a higher level of induced residual stresses. Apparently, the endurance strength increased to nearly 25% as shown in Fig. 2-25 (b).

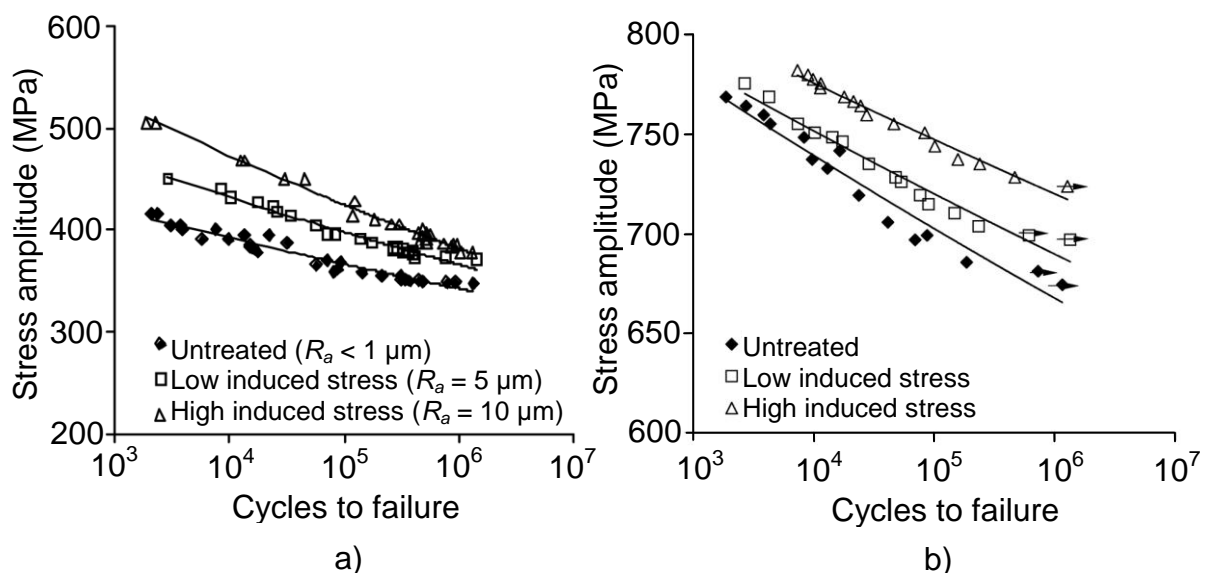


Fig. 2-25: The Wöhler diagrams of the AWJ peened and untreated specimens (Arrows indicate specimens that did not fail). a) stainless steel 304, and b) titanium alloy Ti6Al4V [91]

While, Kunaporn et al. [92] reported a maximum increase in the fatigue strength by 20-30 % in waterjet peening of aluminium alloy 7075-T6. However, they also noted that the degree of fatigue improvement was strongly dependent on the peening conditions. They observed that increasing the pressure and the peening time might yield an increase in surface hardness, but the fatigue limit would rapidly decline due to an increase in surface erosion as well. It is well known that surface irregularities may encourage fatigue crack initiation at the specimen surface [93].

During oil jet peening of carbon steel 1040, an improvement of fatigue strength by about 19 % was reported [86]. They further reported that the fatigue life was higher in specimens peened at a higher pressure probably because of the difference in magnitude of the induced compressive residual stress at the surface as well as of the hardening effect. In contrast as shown in [Fig. 2-26](#), they found that the fatigue strength of peened specimens seemed to be almost similar regardless of the nozzle traverse rate since the residual stress and hardening showed also not much difference.

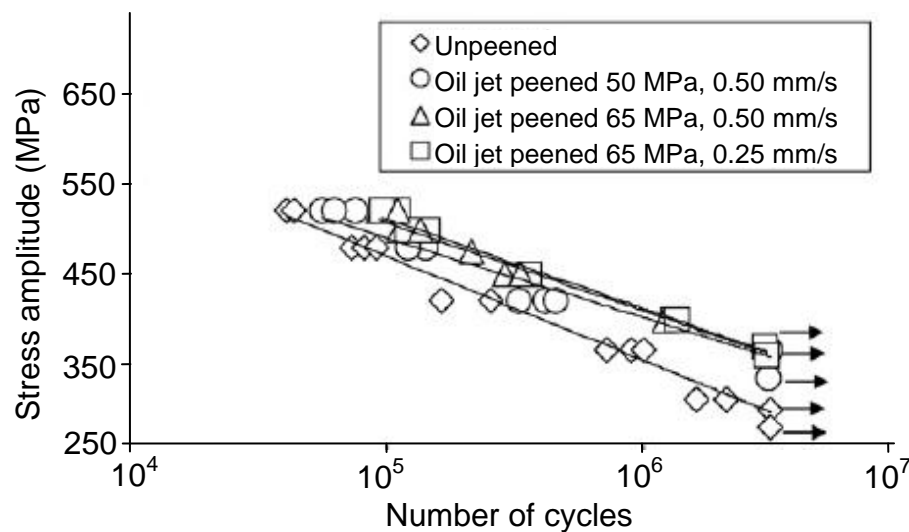


Fig. 2-26: The wöhler diagrams of the oil jet peened and unpeened specimens (Arrows indicate specimens that did not fail) [86]

Han et al. [84] reported an increase of fatigue life of about 15-20 % in water cavitation peening of carbon steel 1045. They compared the fatigue life of peened and unpeened specimens of original as well as oil quenched carbon steel 1045. They also noticed that the improvement of fatigue life was obviously apparent at higher cycles as shown in [Fig. 2-27](#) (a). The typical fracture surface with fatigue striation patterns is shown in [Fig. 2-27](#) (b).

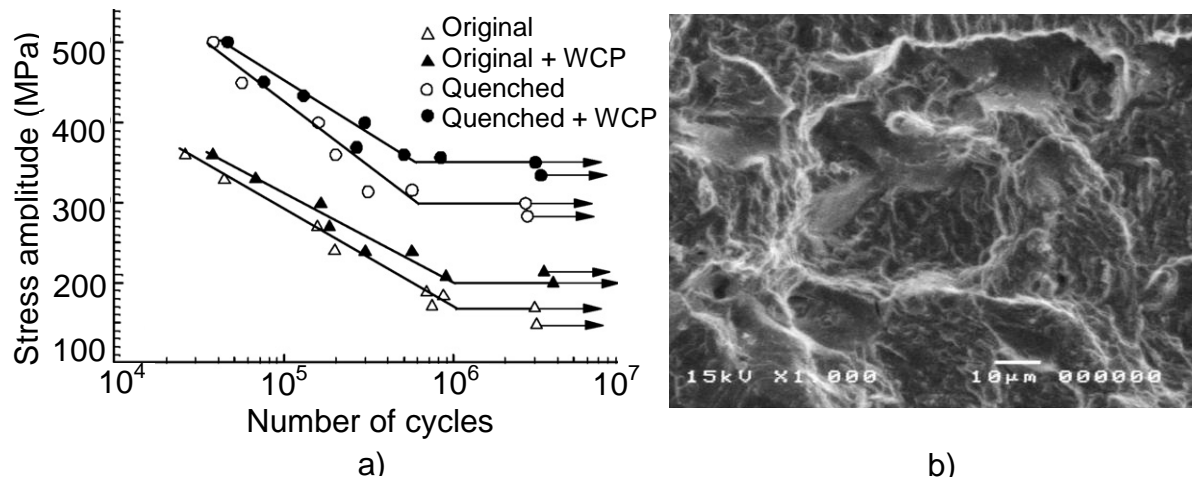


Fig. 2-27: a) The wöhler diagrams of the different test specimens (Arrows indicate specimens that did not fail), b) the typical fracture surface [84]

The fatigue strength of stainless steel 316 under cavitating jets in air (CJA) and water (CJW) has been investigated by Soyama [94]. The cavitation peening in water takes place inside a water-filled chamber. It is obvious that the improvement of the fatigue strength using the cavitating jet is better in air than in water as shown in Fig. 2-28. The lower fatigue strength of CJW is possibly due to the interference between the jet and water. Interestingly, although he found the induced residual stress in CJW at two different standoff distances were nearly the same, but the fatigue strength was barely improved for the specimens treated at lower standoff distance as shown in Fig. 2-28. This could be due to some cracks occurred in the peened area of specimens treated with a lower standoff distance.

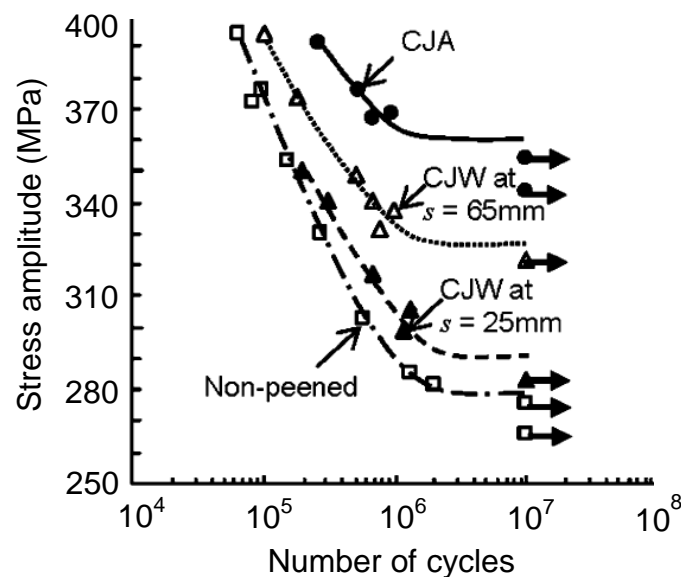


Fig. 2-28: The wöhler diagrams of the different test specimens (Arrows indicate specimens that did not fail) [94]

2.6 Summary of state of the art

The basic concepts of peening processes namely the shot peening, laser shock peening and waterjet peening process are presented in this chapter. However, the literatures on the waterjet peening process are discussed in details since it is the main focus of the present study. The various studies on the peening processes are summarized in Table 2-2, Table 2-23 and Table 2-24 respectively for shot, laser shock and liquid peening.

Table 2-2: Summary of the various studies on shot peening process

Ref.	Process	Conditions	Material	Topic of study
[19]	Shot peening	shot: steel D_s : 250 μm t_p : 0 - 250 s	AISI 1010 AISI 1045 AISI 1080	Surface hardness
[20]	Shot peening	shot: cast steel S-230 I_{shot} : 5 - 13 A	AISI 2205	Residual stress Strengthening depth Fatigue strength
[26]	Shot peening	shot: cast steel D_s : 0.8 mm f_A : 0.3 – 0.6 mm	20Cr, 30CrMo, 40Cr, GC4, C45 steel, AA LC6	Residual stress Strengthening depth Empirical models
[30]	Shot peening	single shot: glass double shot: Zi D_s : 0.05 – 0.15 mm I_{shot} : 1 – 6 A	RS561	Residual stress Strengthening depth Fatigue strength
[31]	Shot peening	shot: steel 230 D_s : 0.7 mm I_{shot} : 0.0027 – 0.0141 A	AISI 4140	Residual stress Strengthening depth Fatigue strength
[32]	Shot peening	shot: Zirblast B30, Ce- ZrO ₂ , glass beads D_s : 0.3 – 0.8 mm	Mg alloy AZ80	Surface roughness Residual stress Strengthening depth Fatigue strength
[33]	Shot peening	shot: cast steel D_s : 0.8 mm	AISI 304	Surface roughness Microstructure Hardness Hardening depth Corrosion resistance
[38]	Shot peening	shot: glass beads, ceramic beads, cast steel shots D_s : 0.15 – 0.28 mm	AA 7050	Surface roughness Residual stress Strengthening depth Fatigue strength

Table 2-3: Summary of the various studies on laser shock peening process

Ref.	Process	Conditions	Material	Topic of study
[38]	LSP	N_{shot} : 2 – 8	AA 7050	Surface roughness Residual stress Strengthening depth Fatigue strength
[39]	LSP without coating	E_{pulse} : 48 – 52 mJ D_{spot} : 0.4 ± 0.03 mm N_{pulse} : 127 ± 0.1 pulse/mm ²	Ti-2.5Cu, Ti-54M, LCB	Surface roughness Residual stress Strengthening depth Fatigue strength
[40]	LSP without coating	low energy laser (< 300 mJ)	AA 6061 T6	Surface roughness Hardness Hardening depth Fatigue strength
[41]	LSP	N_{pulse} : 25 – 75 pulse/mm ²	SS 2205	Residual stress Strengthening depth Wear resistance Corrosion resistance
[42]	LSP	I_{laser} : 8 – 20 GW cm ⁻² N_{impact} : 2 - 12	AISI 316L	Surface roughness Hardness Residual stress Microstructure

Table 2-4: Summary of the various studies on liquid peening process (Part 1)

Ref.	Process	Conditions	Material	Topic of study
[43]	WJP	v_n : 84.7 – 169.3 mm/s h : 12.7 – 63.5 mm	Ti6Al4V	Surface roughness Hardness Hardening depth
[44]	OJP	h : 15 – 40 mm	AA6063	Surface roughness Hardness Hardening depth
[45]	WCP	t_p : 15 – 60 min	Pure Ti	Hardness Hardening depth Residual stress
[46]	WCP	h : 30 -120 mm t_p : 5 – 30 min	SAE 1070	Impact pressure Residual stress Strengthening dept
[47]	WCP	θ : 0 - 90°	SAE 1045	Impact pressure Residual stress
[68]	WJP	p_o : 140 – 280 MPa	pure Ti, Ti6Al4V	Surface roughness Residual stress
[71]	WJP	v_n : 102 – 2752 mm/s h : 12.7 – 38.1 mm nozzle type: fuzzy, fanjet, roundjet	Ti6Al4V	Surface texture Hardness Hardening depth

Table 2-5: Summary of the various studies on liquid peening process (Part 2)

Ref.	Process	Conditions	Material	Topic of study
[74]	WJP	n_j : 2 – 6 v_n : 1000 – 3000 mm/min p_o : 100 – 300 MPa	AISI 304	Surface roughness Hardness Hardening depth Microstructure
[75]	AWJP	p_o : 103 – 262 MPa grit size: 54 – 120 mesh #	Ti6Al4V, spring steel, Inconel	Surface roughness Residual stress Strengthening depth
[76]	WJP	p_o : 10 – 70 Mpa h : 30 – 500 mm	Al alloy 5083	Erosion Impact force
[77]	WJP	pulsating jet p_o : 20 -40 MPa h : 10 – 90 mm	Al 99.5	Erosion Surface roughness Microstructure
[78]	WJP	v_n : 0.05 – 0.1 m/min	AISI 316 Ti6Al4V	Surface roughness Hardness Hardening depth Microstructure
[79]	WJP	p_o : 207 – 345 MPa v_n : 30.5 – 127 cm/min	Inconel 718	Erosion Microstructure
[80]	WJP	p_o : 34 – 70 MPa h : 25 – 76 mm v_n : 25 – 250 mm/s	Al-Si alloy	Erosion Hardness Hardening depth Microstructure
[85]	WJP	h : 6 – 11.4 mm p_o : 100 – 140 MPa	Al 1100 H14	Surface roughness Residual stress
[86]	OJP	v_n : 0.25 – 0.5 mm/s	AISI 1040	Surface hardness Surface morphology Fatigue strength
[91]	AWJP	h : 152 – 254 mm p_o : 103 – 262 MPa v_n : 1.02 – 2.03 m/min grit size: 54 – 120 mesh #	AISI 304 Ti6Al4V	Surface roughness Residual stress Fatigue strength
[92]	WJP	p_o : 103 – 310 MPa v_n : 454 – 787 m/s h : 24 – 64 mm	Al 7075-T6	Surface roughness fatigue strength
[94]	WCP	cavitation in air and water	JIS SUS316L	Residual stress Fatigue strength
[95]	WJP	n_j : 1 - 3 p_o : 50 – 150 MPa v_n : 500 – 1500 mm/min h : 20 – 60 mm	Al 5005	Surface roughness Hardness Hardening depth Process optimizatrion
[96]	WCP	h : 55 – 85 mm	JIS SCM420	Residual stress Surface roughness Process optimization
[97]	WJP	p_o : 175 – 225 MPa h : 5 – 10 mm n_j : 2 – 4 v_n : 20 – 40 mm/min	Al 6063-T6	Residual stress Hardness Surface roughness Process optimization

3 Problem specification and scientific approach

The material surface plays an important role in the response of the engineering components. Surfaces are often subjected to various surface treatment processes to achieve certain qualities that are not available from the primary manufacturing processes [98]. The process is conducted for various reasons including to improve the performance of materials, change physical properties, vary appearance and alter dimensions. A diverse range of thermal, mechanical and chemical treatments has been developed to modify the surface characteristics [99]. Various surface treatment processes have been used for a wide range of materials from semiconductors to metals, ceramics, polymers, bio and nanomaterials [100].

The quality and performance of a product is directly related to its surface integrity produced from different surface treatment processes. Surface integrity comprises the topography (e.g. roughness, erosion), the mechanical properties (e.g. residual stress, hardness), metallurgical states (e.g. phase transformation, microstructure) and other related property variations of the work material during surface processing procedures [101]. Therefore, alteration of the surface integrity especially in the mechanical related applications has a significant effect on fatigue strength and lifetime of engineering components.

A fatigue failure under cyclic loads is most commonly originated at the near-surface area where it has the highest stress concentrations and tensile stresses resulting from production processes. A major method of increasing fatigue performance is by imposing compressive residual stresses within a thin outer surface layer. As a result, the possibility of crack initiation leading to fatigue failure is reduced. The method may offer some positive effects by enhancing the fatigue strength of the components than the usage of highly alloyed and more expensive materials [5].

The shot peening and the laser shock peening processes are widely established in the industry. However, there are possible disadvantages of the shot peening process including defects and rough peened surfaces which have shown to be detrimental to fatigue crack initiation [102]. While in the laser shock peening, there are possibilities of thermal effects such as melting of the metal surface, especially for alloys of a low

melting point [103]. The waterjet peening process may overcome the limitations of other peening processes, particularly leaving a clean and smooth surface with low surface roughness as well as the absence of thermal effects [44]. Over the past decade, the WJP process has shown to be a promising method in the mechanical surface strengthening process. A lot of research has been conducted to study its potential applications and associated sciences. However, a detailed knowledge in this process is not comprehensively reported in the literature. Therefore, there is a need to widen the knowledge in the field of the waterjet peening process by conducting more research.

Considerable works have been done in investigating the effect of various WJP process parameters on the inducement of residual stresses on metallic surfaces. However, all the works were carried out in a single-pass treatment. There is a possibility that the residual stress can be introduced in a higher amount and/or deeper below the surface if the metallic surfaces are treated repeatedly with multiple passes. As shown in studies on traditional machining processes, particularly grinding, it became clear that there is a variation in magnitude of residual stress with respect to the depth of the residual stress distribution in multiple passes grinding technique [104]. It was also revealed that as the number of grinding passes increases, the normal grinding force increases as well, which resulted in a higher amount of compressive residual stresses being induced [105]. Furthermore, a study on multipass abrasive waterjet cutting has shown its superiority over a single-pass cutting where it produces better surface quality and penetration depth [106]. It is thus essential to investigate the effect of multiple passes treatment in the WJP process. The main objective of the present study is to evaluate the response of different materials namely, stainless steel 304 and carbon steel 1045 when they are subjected to multiple passes treatment in the WJP process. Additionally, the effect of other parameters in WJP such as feedrate, standoff distance and water pressure is also discussed.

Furthermore, little attention has been paid to the optimization of the waterjet peening process. It is known that increasing the energy and frequency of water drops may lead to a higher increase in hardness as well as a deeper hardening layer [74]. Unfortunately, it may also increase the roughness of the material surfaces which is detrimental to its fatigue life. Therefore, it is important to find a balance between the

increase in hardness and also roughness of the material surfaces. In order to have good increase in hardness within acceptable roughness of the peened surfaces, it is necessary to employ optimization techniques to find the optimal waterjet peening conditions. Also, workable models between the hardness as well as the roughness and the peening parameters can be developed in order to plan the process in advance with high rates of reproducibility. For this reason, the response surface methodology can conveniently be employed. Therefore, a special chapter in the present thesis is specifically dedicated to discuss about the optimization of WJP parameters on aluminium alloy 5005 as an example and also the development of workable empirical models for surface roughness (R_a) and hardness.

4 Research methodology

4.1 Materials

A total of three different materials was selected in the present work. Both ferrous and non-ferrous materials were chosen namely austenitic stainless steel 304, carbon steel 1045 and aluminium alloy 5005. These materials were primarily chosen because of their wide usage as mentioned in the literatures and also their availability in the laboratory. Both ferrous alloys were used for extensive investigations on the effect of waterjet peening parameters mainly due to their relatively higher strength compared to aluminium. Furthermore, both materials were treated using a similar set of parametric levels in order to make an appropriate comparison of their responses under the waterjet peening process. The non-ferrous alloy was used for the study of optimization in the waterjet peening process because of its much lower strength than the ferrous alloys. Therefore, the aluminium alloy 5005 was treated with a different set of parametric levels so that a proper assessment on the optimization of its performance could be done. The details about the experimentation and optimization in the waterjet peening process of aluminium alloy 5005 are explained in Chapter 6.

The austenitic stainless steel 304 (X5CrNi18-10, material no. 1.4301) was selected as the first test material. Austenitic steels are commonly used for stainless applications because of their excellent formability even at room temperature [107]. Stainless steel 304 is the most common of austenitic grades which is used in chemical processing equipments and heat exchangers for food, dairy, and beverage industries. Austenitic stainless steel is also used in medical applications. In fact, Arola et al. [91] studied the influence of abrasive waterjet peening on austenitic stainless steel (AISI 304). With the use of abrasive particles, the treated surfaces produced quite high values of R_a up to 14 μm even with a single jet pass [91]. It is known that rough surfaces are expected to encourage fatigue crack initiation thus accelerating the failure of a component. Therefore, it is of interest to treat the same material but without the use of abrasives in the waterjet peening process so that smoother surfaces can be produced. The typical chemical composition and mechanical properties of austenitic stainless steel 304 are given in [Table 4-1](#) and [Table 4-2](#) respectively.

Table 4-1: Chemical composition (weight-%) of austenitic stainless steel 304 [108]

C	Mn	Si	P	S	Cr	Ni	Others	Fe
0.07	2.00	1.00	0.045	0.015	17.00-19.50	8.00-10.50	N 0.11	Balance

Table 4-2: Mechanical properties of austenitic stainless steel 304 [108]

Yield strength (MPa)	Tensile strength (MPa)	Elongation (%)
230	540-750	45

The surfaces of the received specimens were already smoothened and film coated from the production process through the rolling method. It had an average surface roughness, R_a of 0.15 μm . Therefore, no necessary smoothing of the surfaces was needed prior to the experiments. Fig. 4-1 (a) shows the surface microstructure of the austenitic stainless steel 304 sample as received. Some rolled grains from the manufacturing process can be clearly seen. Fig. 4-1 (b) shows the equiaxed grain structures of the cross-sectioned surface.

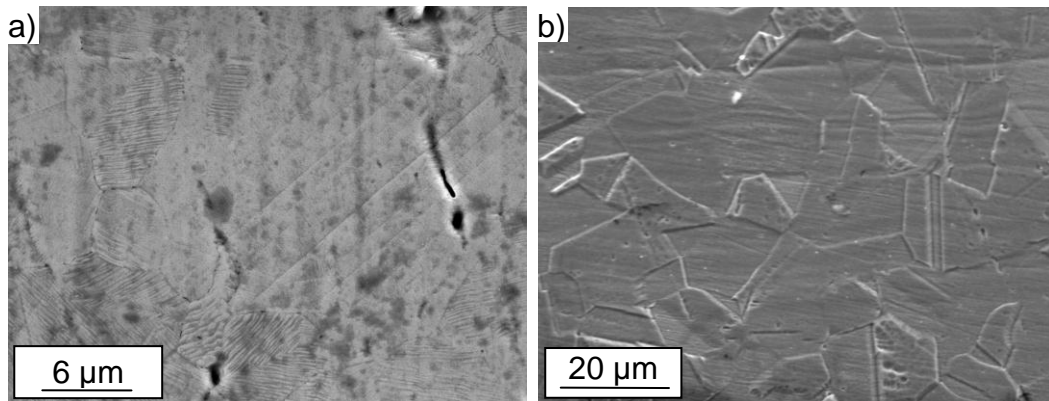


Fig. 4-1: Microstructures of austenitic stainless steel 304 specimen, a) at surface of received specimen, b) at cross-sectioned after etched

The second test material used for the experiments of this work was carbon steel 1045 (C45, material no. 1.0503). It is a plain carbon steel containing 0.45 wt% C. It is widely available in the market. Carbon steels in general are known to be able successfully undergoing heat treatment processes. These heat-treated alloys are stronger and their applications include railway wheels and rails, gears, crankshafts, and other machine parts and high-strength structural components calling for a combination of high strength, wear resistance and toughness [17]. The surface hardness of carbon steel 1045 can be improved through a shot peening process [19].

Furthermore, its strength can also be improved using a water cavitation peening process (WCP) [84]. In case of WCP, the cavitating bubbles which collapse on the surface of the component produced a higher amount of compressive stress [84]. However, a higher level of the kinetic energy produced in the cavitating jet had also yielded a significantly high value of roughness on the material surface [71]. Therefore, it is an interesting topic to study the response of the same material when it is subjected to a pure waterjet peening process. A smoother surface can be expected since the plain waterjet produces a lower level of the kinetic energy than the cavitating jet [71]. The typical chemical composition and mechanical properties of carbon steel 1045 are given in [Table 4-3](#) and [Table 4-4](#) respectively.

Table 4-3: Chemical composition (weight-%) of carbon steel 1045 [108]

C	Mn	Si	P	S	Cr	Ni	Mo	Others	Fe
0.42-0.50	0.50-0.80	0.40	0.045	0.045	0.40	0.40	0.10	Cr+Mo+Ni 0.63	Balance

Table 4-4: Mechanical properties of carbon steel 1045 [108]

Yield strength (MPa)	Tensile strength (MPa)	Elongation (%)
230-305	530-580	15-16

The microstructures of carbon 1045 are shown [Fig. 4-2](#). The surface has been polished up to a level of mirror surface as shown in [Fig. 4-2](#) (a) using a lapping machine. As a result, it has a very low average surface roughness, R_a of 0.07 μm . The cross-sectioned microstructures show the ferrite and pearlite constituents as seen in [Fig. 4-2](#) (b).

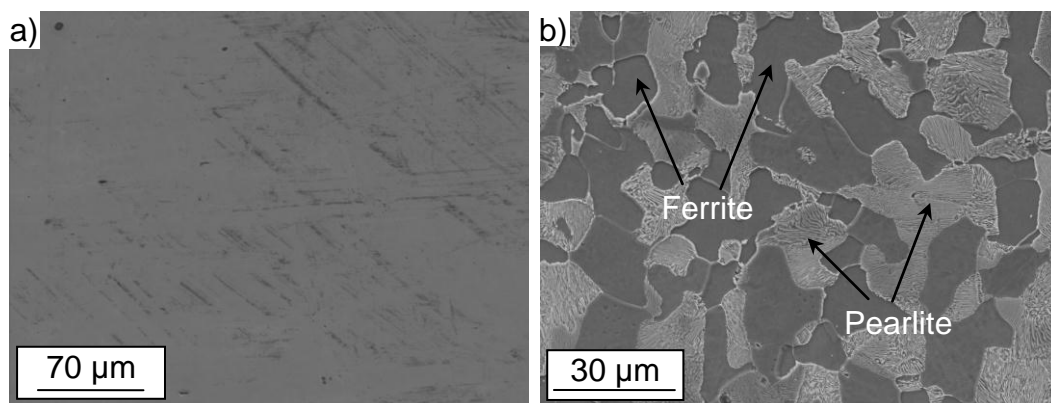


Fig. 4-2: Microstructures of carbon steel 1045 specimen, a) at surface of received specimen, b) at cross-sectioned after etched

The third tested material was aluminium alloy 5005 (AlMg1 G15, material no. 3.3315) which was mainly used to elaborate the optimization method of the waterjet peening process. Aluminium alloys in general are well known to possess a high strength to weight ratio. This advantage makes them suitable to be used in many industrial applications. Some of the more common applications of aluminium alloys include railway car bodies, automotive parts (e.g. engine blocks, pistons and manifolds), cooking utensils, low pressure vessels and piping, and fuel tanks [17]. In the present study, aluminium alloy 5005 was used largely because it is readily available on the market. Its typical chemical composition and mechanical properties are given in [Table 4-5](#) and [Table 4-6](#) respectively.

Table 4-5: Chemical composition (weight-%) of aluminium alloy 5005 [109]

Mg	Si	Fe	Cu	Mn	Cr	Zn	Al
0.70-1.10	0.30	0.45	0.05	0.15	0.10	0.20	Balance

Table 4-6: Mechanical properties of aluminium alloy 5005 [110]

Yield strength (MPa)	Tensile strength (MPa)	Elongation (%)
110-175	145-185	8

The surfaces of the received specimens were also already smoothened and film coated from the production process through rolling method as shown in [Fig. 4-3](#) (a). The sample had an average surface roughness (R_a) of 0.50 μm . Again, no necessary smoothing of the surfaces was needed prior to the experiments. [Fig. 4-3](#) (b) shows the cross-sectioned surface of the specimen.

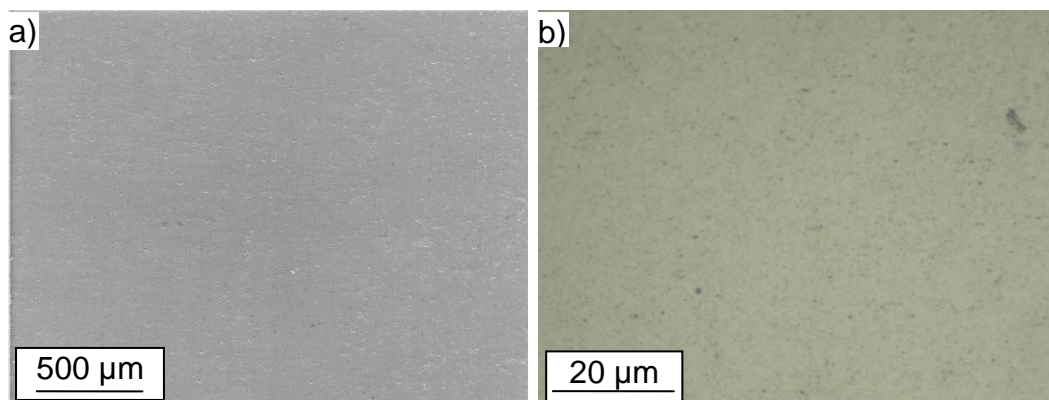


Fig. 4-3: Microstructures of aluminium alloy 5005 specimen, a) at surface of received specimen, b) at cross-sectioned

4.2 Experimental setup

4.2.1 Equipment

The equipment used for machining all the samples was an UHDE high pressure waterjet machine at the KIMA Chair as shown in [Fig. 4-4](#). The UHDE pump is capable generating a water pressure up to 6000 bars with a maximum flow rate of about 2 l/min. The incidence angle was set at 90° (i.e. the nozzle head was perpendicular to the specimen surface). It produces a width of treated surface of approximately 0.8 mm. The process was done without the use of abrasives where surfaces free of embedded abrasive particles could be expected. The movement of the nozzle is done through a PC based NC controller with CAD/CAM interface. The nozzle moves in two axes with a maximum working area of 900 x 1200 mm.

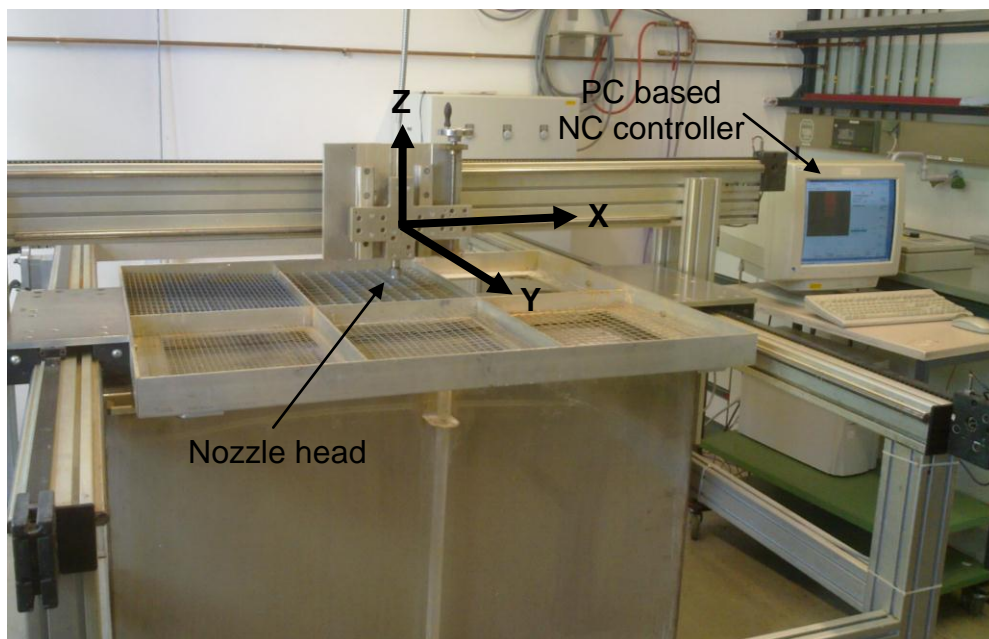


Fig. 4-4: Waterjet machine at KIMA

The machine is equipped with a nozzle made of stainless steel, brass seal and sapphire stone produced by Quick-Ohm Küpper & Co GmbH. The nozzle has a diameter of 0.3 mm. The nozzle and its cross-sectional view are shown in [Fig. 4-5](#) [111].

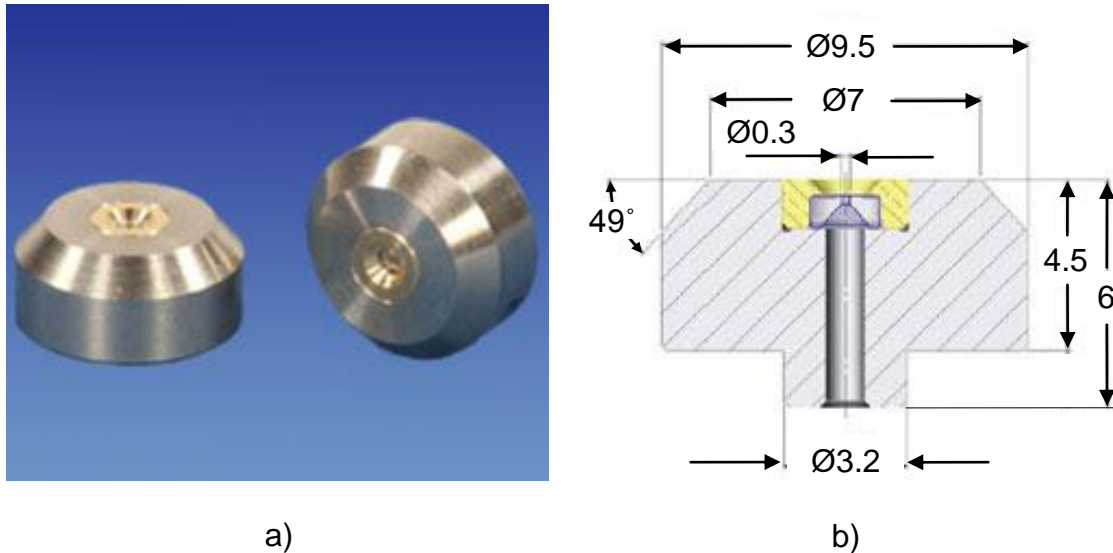


Fig. 4-5: a) the nozzle, and b) its cross-sectional view (all dimensions are in millimetres)

4.2.2 Experimental design

In WJP, there is a vast number of parameters affecting the quality of the results. Therefore, only a few parameters were selected to ensure the feasibility of the multipass treatment and its influence can be properly assessed. The machining parameters and their respective ranges were carefully selected based on preliminary trial runs as well as on literature reviews [43, 44, 51]. These machining parameters were easily managed by adjusting those parameters into the desired levels. The effect of WJP treatment was clearly observed within these ranges of parameters. The machining parameters and their ranges are shown in [Table 4-7](#). Some of the parameters were kept constant during the entire experiments such as nozzle diameter, D_n , (0.3 mm) and inclination angle, θ , (90°). A full factorial experiment was conducted which gave a total of 27 experimental runs. For each experimental run, the machining parameters were set to a pre-defined level accordingly.

Table 4-7: Machining parameters and their respective ranges

No.	Machining parameters	Range		
		Low	Medium	High
1.	Number of jet passes, n_j	2	4	6
2.	Feedrate, v_n (mm/min)	1000	2000	3000
3.	Pressure, p_0 (MPa)	100	200	300

It is known that, the standoff distance plays an important role in determining the response of the material under the waterjet peening process. However, its effect covers a wide range of distances as to constitute the different zones of waterjet structure [48, 49]. Therefore, a set of distances were selected for a systematic investigation on the effect of standoff distance within the present study. The distances were selected primarily based on initial trial runs and literature reviews [51, 76]. The levels of standoff distance are given in [Table 4-8](#).

Table 4-8: Range of standoff distances

Standoff distance, h (mm)					
30	60	90	120	150	180

4.2.3 Experimental procedure

The square test plates had the dimension of 150 mm × 30 mm in surface area and 3 mm of thickness. The specimen was laid on the workpiece table of the waterjet machine as shown in [Fig. 4-6](#). It was properly clamped to ensure that the specimens would not move and remain in the horizontal position during the treatment process.

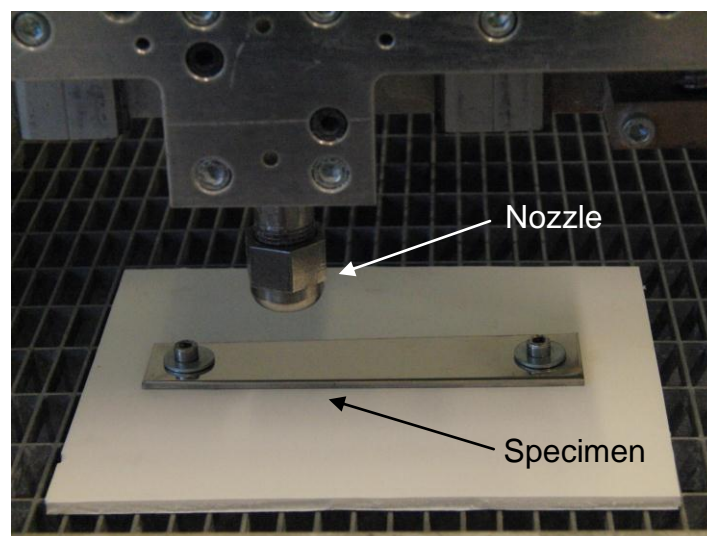


Fig. 4-6: The test specimen during the treatment process

For each experimental run, the machining parameters were set to the intended levels according to the experimental design. Once all the parameters were set to their respective levels, the test samples were treated as programmed into a CNC

programme. With that programme, the nozzle was moved along the width direction as illustrated in Fig. 4-7. The nozzle moved in a reverse direction repeatedly according to the set number of jet passes. There was a gap of 2 mm left between each experimental run. The gap ensures that no interference occurs between the exposed tracks of the jets.

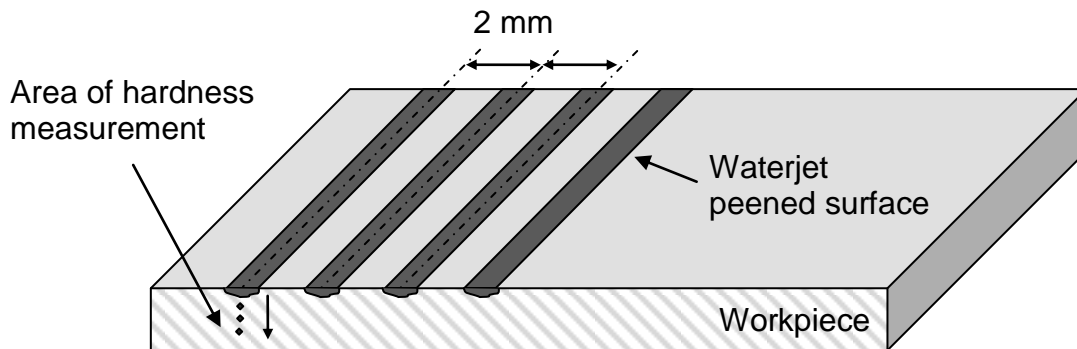


Fig. 4-7: Illustration of the treated specimen

4.3 Analysis of test samples

All the treated surfaces were analyzed accordingly. First of all, a portion of the treated surface was used for roughness measurements. Another portion of the treated surface was used for hardness measurements and microstructural analyses as to avoid any interference from the roughness measurement since the stylus of the roughness tester has to be in contact with the surface. The microstructures on the treated surfaces were captured using an optical and a scanning electron microscope (SEM). A three dimensional (3D) measuring instrument, Nanofocus μ Surf was also used to capture 3D images of the surfaces. Later, the specimens were sectioned for sub-surface analyses namely hardness measurement as well as sub-surface microstructure measurement. A Vickers hardness indenter was used for hardness measurement. Finally, a new set of specimens were treated for fatigue test analysis.

4.3.1 Surface roughness measurement

The roughness was measured on the treated surface. A computer-based surface roughness measuring device (Hommel T8000) available at the Institute for Measurement and Sensor-Technology (MTS), University of Kaiserslautern, was used

in the present investigation. The machine is equipped with a ball-shaped ruby stylus tip having a diameter of 5 μm and tip angle of 90° . The stylus was traversed along the direction of treated surface at a constant speed of 0.05 m/s. The transverse surface roughness profiles for each treated surface were taken in the middle of treated lines. All measurements were acquired using a cut-off length of 0.8 mm. The machine provides most values of the standard roughness parameters such as R_a (average arithmetic roughness), R_v (maximum valley depth of the roughness profile), R_p (maximum peak height of the roughness profile) and R_t (total height of the roughness profile) according to the ISO 4287 [112]. However, the result of R_a will be discussed in the present study since it is the most widely used parameter in roughness profile. R_a is defined as the arithmetic average of the vertical deviations from the nominal surface over a specified length. The R_a values were taken at least four times for each sample so that averages could be calculated in order to minimize the variability.

4.3.2 Hardness measurement

The treated specimens were prepared for hardness measurement and microstructural analysis based on standard procedures as described by Buehler Ltd. [113]. The treated samples were sectioned into smaller pieces using an abrasive wheel cutter with a sufficient flow of coolant. After that, the sectioned specimens were hot mounted with the edge of the treated specimen exposed on the polishing surface. This method uses pressure and heat to encapsulate the specimens. A commonly mounting material for metallographic specimens, ProbeMet (supplied by Buehler Ltd) was used. It contains conductive filler particles (copper) and thermosetting epoxy resin as to obtain electrical conductivity for the SEM analysis purpose later.

The mounted specimens were then grinded using silicon carbide abrasive papers with successive particle grit sizes (P120, P240, P400, P600 and P1200) in wet condition. Finally, the specimens were mechanically polished as to produce a flat and mirror-like in appearance. Polishing was firstly conducted with 6 and 1 μm diamond abrasives suspended onto napless canvas cloth. Final polishing was done in sequence with 0.3 μm (alpha alumina) and 0.05 μm (gamma alumina) suspensions using medium nap cloths. In the end, subsurface hardness measurement was

conducted on the polished specimens using a computer-controlled Buehler OmniMet MHT hardness tester available at the Institute for Manufacturing Technology and Production Systems, University of Kaiserslautern. The Vickers hardness was obtained as a function of depth with 10 gf load over a 15 s indentation period. An average of at least four hardness data was recorded at every depth. It was acquired on the cross-section of the specimen at different depths starting from roughly 25 μm beneath the eroded surface as shown in Fig. 4-8. The measurements were continued at 10 different depths until a far distance of 1000 μm (i.e. 25, 50, 75, 100, 150, 200, 300, 500, 750 and 1000 μm).

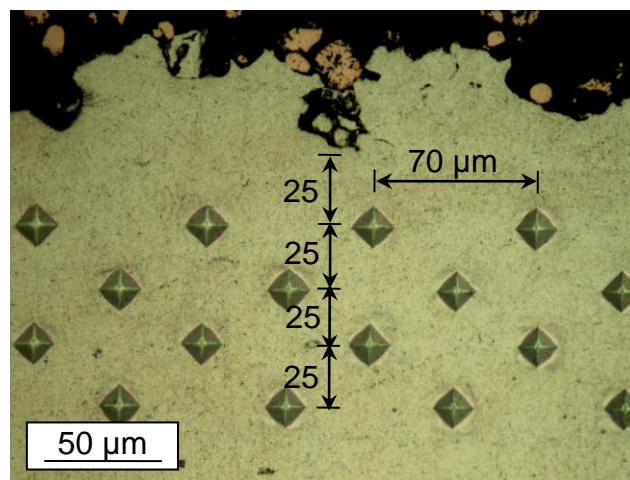


Fig. 4-8: Hardness measurement on a cross-sectioned specimen

4.3.3 Microstructural analysis

A microstructural analysis is divided into two parts. A scanning electron microscope was used to characterize both the surface and the sub-surface microstructures. A Philips - XL 40 scanning electron microscope available at the MTS Institute, was used with an accelerating voltage of 20 kV. A secondary electron image (SEI) was primarily employed for the characterization of the microstructures. The image magnifications were adjusted accordingly as to capture both macro and micro scales of the microstructures. While, a non-contact optical 3D measurement (Nanofocus μSurf) explorer also available at the MTS Institute, was used for the measurement and analysis of surfaces. The 3D structures of the surfaces were acquired using a 10x objective lens which covered a measuring field of about 1600 $\mu\text{m} \times 1600 \mu\text{m}$.

The specimens from the hardness measurement were reused for the sub-surface microstructure investigation. However, the specimens were prepared again as to avoid the effect of material deformation from the hardness indentation. After final polishing of the specimens, etching was conducted using the recommended chemical solutions. Etching is mainly conducted to reveal particular structural characteristics of metals. V2A etchant (supplied by Buehler Ltd.) was used to etch the polished specimens of austenitic stainless steel 304. It was done by immersing the specimens in the solution for about 30 seconds at 50° C. While, for carbon steel 1045, the most common etchant, 3% Nital (also supplied by Buehler Ltd.) was used. The specimens were immersed in the solution for duration about 50 seconds at room temperature.

4.4 Fatigue test

The final test was conducted to analyze the fatigue performance after treatment under different waterjet peening conditions. Its objective is to measure the effectiveness of the waterjet peening process in improving the fatigue strength of the metallic samples. Due to some constraints, only the austenitic stainless steel 304 and the aluminium alloy 5005 were used for the fatigue test. Though the fatigue performance for the other material (i.e. carbon steel 1045) is not expected to be the same, it is believed that the general trend of the results may somehow show a similarity under the waterjet peening treatment. Furthermore, the fatigue test results for the same materials under other peening processes from the work of previous researchers are reported in Chapter 5.4.

The fatigue test specimens were prepared according to the dimensions as shown in [Fig. 4-9 \(a\)](#). The plate has a thickness of 3 mm. Three different conditions were used in the waterjet treatment of the fatigue specimens. The conditions were selected based on three different numbers of jet passes i.e. 2, 4 and 6. The rest of the parameters were kept constant i.e. pressure = 200 MPa, feedrate = 2000 mm/min, nozzle diameter = 0.3 mm and standoff distance = 30 mm. The waterjet peening was conducted on both sides of the specimens in the region where it experienced the highest stress (i.e. in the middle of the specimen) up to a length of 15 mm as shown in [Fig. 4-9 \(b\)](#). The effective coverage width of waterjet peening on the surface was about 0.4 mm. Therefore, for a complete coverage of the surface, the nozzle was moved in a gap distance of 0.4 mm over the length of 15 mm. A minimum of 14

specimens for each treatment condition was used for the investigation. The specimens were tested at different stress levels with an interval of about 25 MPa. The original specimens were also tested so that the fatigue strength performance could be compared between the treated and non-treated specimens.

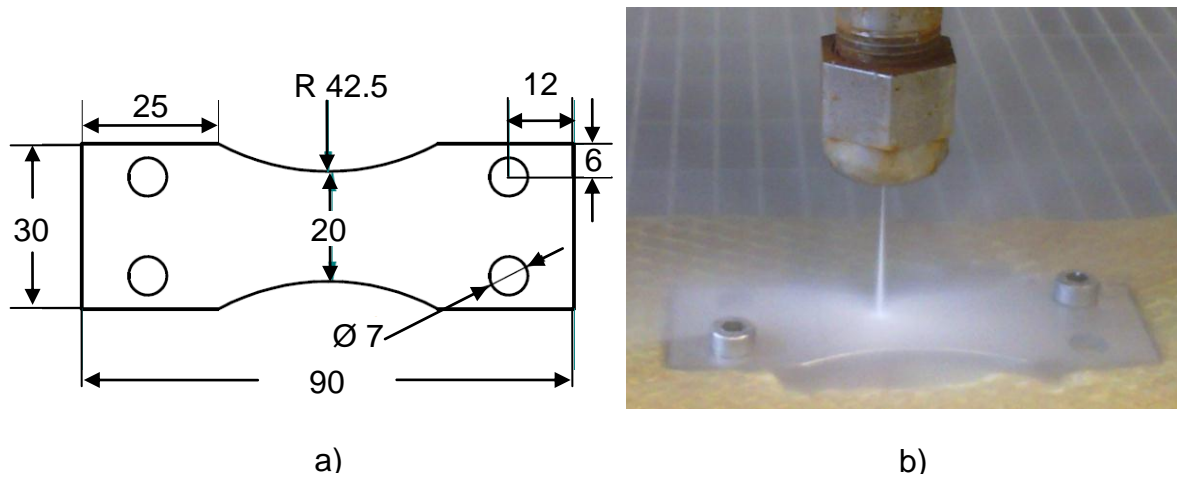


Fig. 4-9: a) Schematic drawing of the fatigue test specimen (all dimensions are in millimetres), b) waterjet peening of fatigue specimen

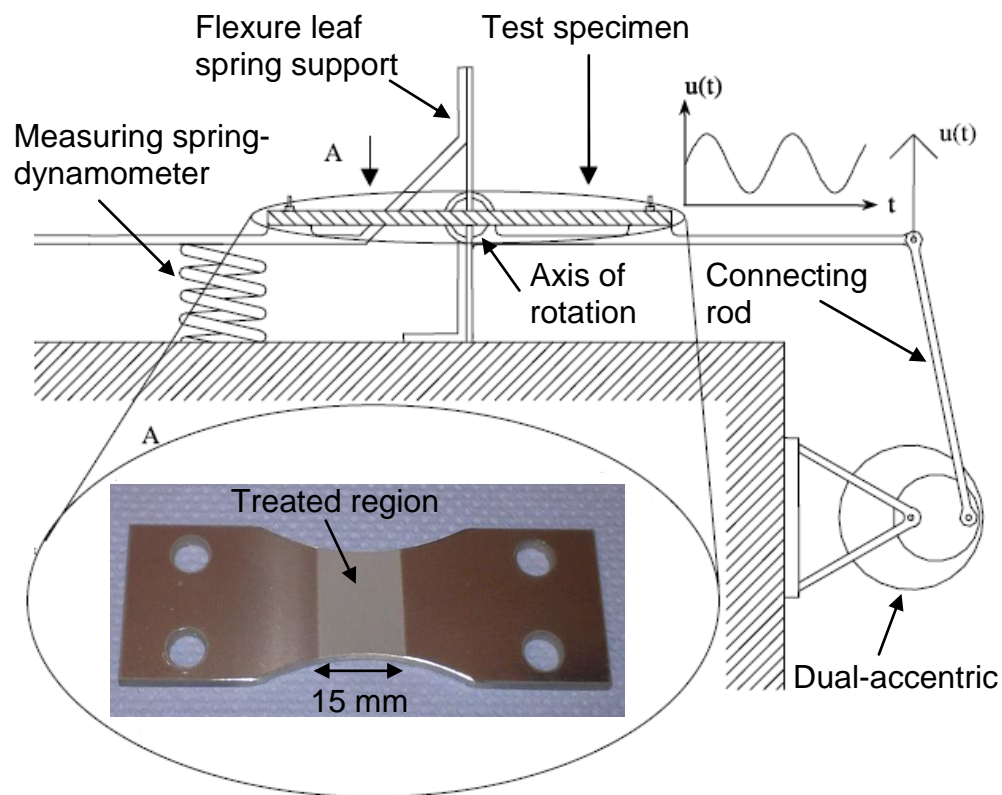


Fig. 4-10: Schematic of an alternating bending fatigue tester (Inset is the treated test specimen) [114, 115]

The fatigue tests were conducted at room temperature on an alternating bending fatigue test machine type PWO (manufactured by Schenck GbmH) available at the Working Group of Material Testing, University of Kaiserslautern. It is an alternating bending fatigue machine which is able to perform dynamic fatigue test in accordance with the German standard DIN 50142 [114]. The machine displacement is controlled through a crank-linkage mechanism as illustrated in [Fig. 4-10](#). This produces a sinusoidal waveform with a frequency of 23 Hz. The test was conducted at various bending stress levels. The test was continuously run up to failure or 10×10^6 cycles, depending on whichever occurred first. The fatigue life responses of the treated and non-treated specimens were achieved by plotting the number of cycles to failure versus the maximum applied bending stress. Later, the fracture surfaces of the specimens were examined using SEM to characterize the failure features.

5 Results and discussions

This chapter discusses the main results about the effect of the waterjet peening process on the stainless steel 304 and the carbon steel 1045. The results are explained based on the surface and sub-surface characteristics as well as the fatigue behaviour. Also, the erosion mechanisms involving both materials are discussed.

5.1 Effect of waterjet peening on surface

The discussion on the effect of the waterjet peening process on material surfaces is divided into two sections. The first section of the investigations discusses the effect of various waterjet peening parameters on the surface roughness. The surface erosion generated by the waterjet peening process parameters is discussed in the second part of the section. Both macro and micro scales of surface erosion are considered in this section.

5.1.1 Roughness

The effect of the number of passes on the surface roughness of both peened specimens for different feedrates is shown in [Fig. 5-1](#). Generally, it can be clearly seen that increasing the number of jet passes produces a higher surface roughness for both specimens. Unlike a through cut in the waterjet machining process where a smoothing action is expected on the kerf walls of workpiece by subsequent passes to remove the 'peaks' left by precedent passes [106]. However, in the waterjet peening process, rougher surfaces are expected due to repeated bombardment of waterjet onto the surface [74]. This implies the roughening of the surface by the subsequent passes which make the surface rougher. In other words, the subsequent passes do not remove the peaks left by precedent passes, but introduce new peaks on the surface of the workpiece thus increasing their surface roughness. Furthermore, rougher surfaces were also produced at lower feedrates as illustrated in [Fig. 5-1](#). This effect which can be explained as decreasing the traverse rate allows additional overlap machining action and more water molecules to impinge on the surface thus producing a higher surface roughness.

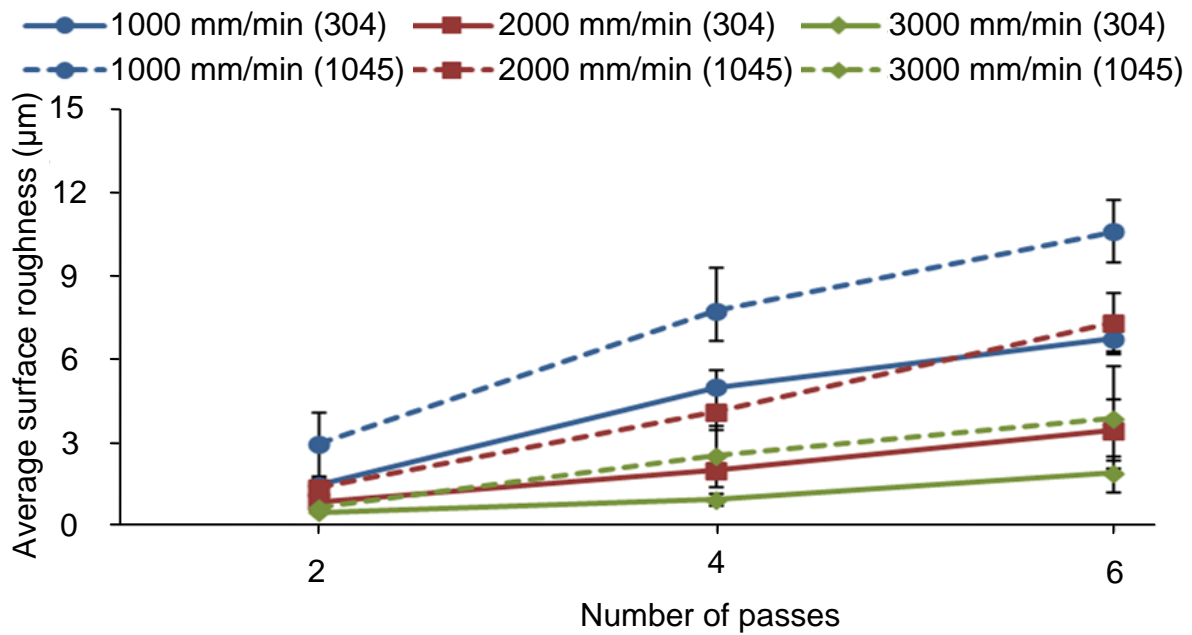


Fig. 5-1: Effect of number of passes on surface roughness for different feedrates at a pressure of 200 MPa and a standoff distance of 30 mm (Stainless steel 304 and carbon steel 1045 are represented by solid and dashed lines respectively)

The effect of the number of passes on the surface roughness for different pressures is shown in [Fig. 5-2](#). It is obvious that the effect of the number of passes shows a similar trend like the previous case where a higher number of jet passes results in a rougher surface. Furthermore, it is clear that the surface roughness increases with an increase in the water supply pressure as illustrated in the diagram. It is known that the water supply pressure is directly proportional to the impingement velocity of the water droplet [116]. Therefore, it can be anticipated that a higher water supply pressure increases the kinetic energy of the water molecules and enhances their capability for material removal thus increasing the surface roughness. In comparison with Arola et al. [68], but utilizing a single pass treatment in abrasiveless WJP of a pure titanium and titanium alloy (Ti6Al4V), they found only a mild increase in surface roughness with an increase in WJP pressure. This is also true for the present case but only at a minimum of 2 jet passes as shown in the diagram. At a higher number of jet passes, there are significant changes of surface roughness for different pressures.

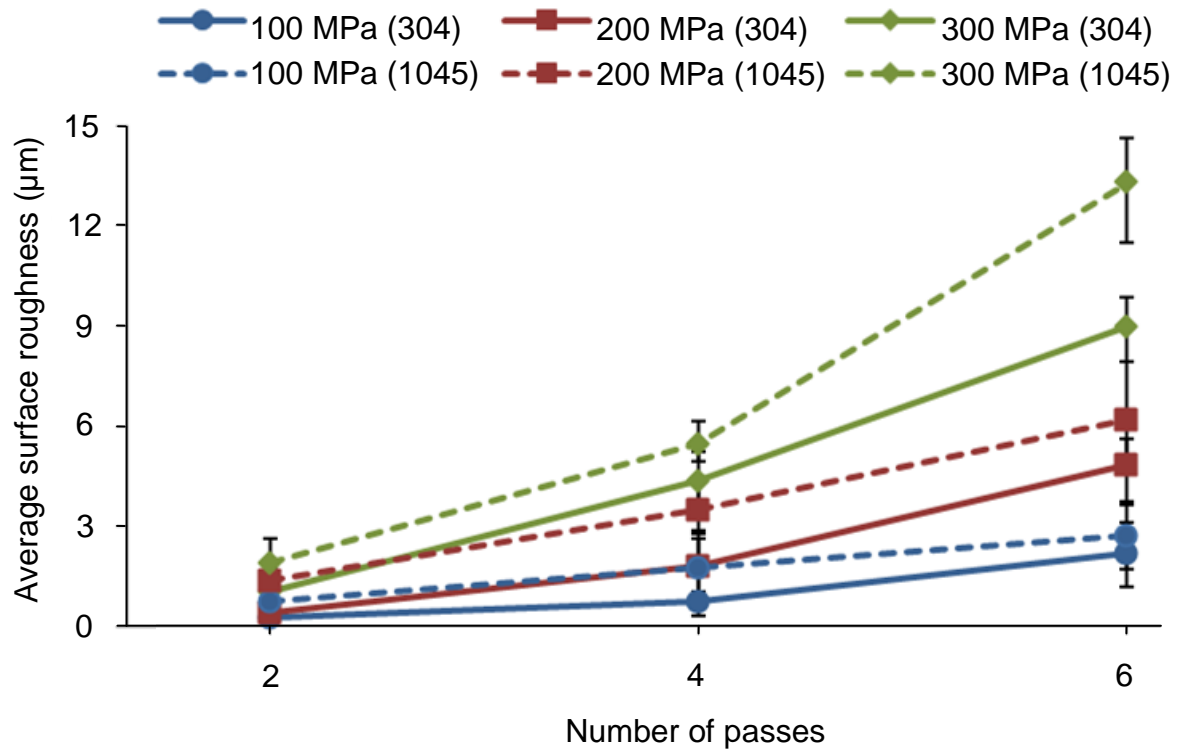


Fig. 5-2: Effect of number of passes on surface roughness for different pressures at a feedrate of 2000 mm/min and a standoff distance of 30 mm (Stainless steel 304 and carbon steel 1045 are represented by solid and dashed lines respectively)

It is of interest to compare the present results with those obtained by Arola et al. [91] with the same alloy of austenitic stainless steel 304 but treated with abrasive WJP. They recorded an average surface roughness ranging from approximately 5 to nearly 14 μm by utilizing pressures between 103 and 262 MPa and feedrates between 1020 and 2030 mm/min which are about the same as in the present case, i.e. 100 to 300 MPa and 1000 to 3000 mm/min respectively. However, the surface roughness values for austenitic stainless steel 304 were recorded less than 10 μm as in the present case. Therefore, it can be said that the abrasiveless WJP may produce a lower surface roughness even if it is treated with more jet passes.

The effect of the standoff distance on the surface roughness for a different number of jet passes in the waterjet peening process is shown in [Fig. 5-3](#). Initially, the surface roughness increases with an increase in the standoff distance until it reaches a maximum roughness at a standoff distance of 90 mm. Beyond that, it decreases and approaches the original surface roughness. A lower standoff distance causes very little removal of material. Probably, water droplets were not generated but rather a water column or a continuous beam of waterjet [76]. The continuous water column

only presses the surface of the specimen without imposing the cyclic stresses. Therefore, the impact frequency of the water column is too low to cause significant erosion at the short standoff distance [76]. Moreover, there is a high possibility that at a shorter standoff distance, the reflection of water droplets after hitting its target disturbs the new incoming water droplets from the nozzle [8, 95]. However, at a relatively high standoff distance due to the divergence of waterjet, the effect of waterjet reflection is drastically reduced.

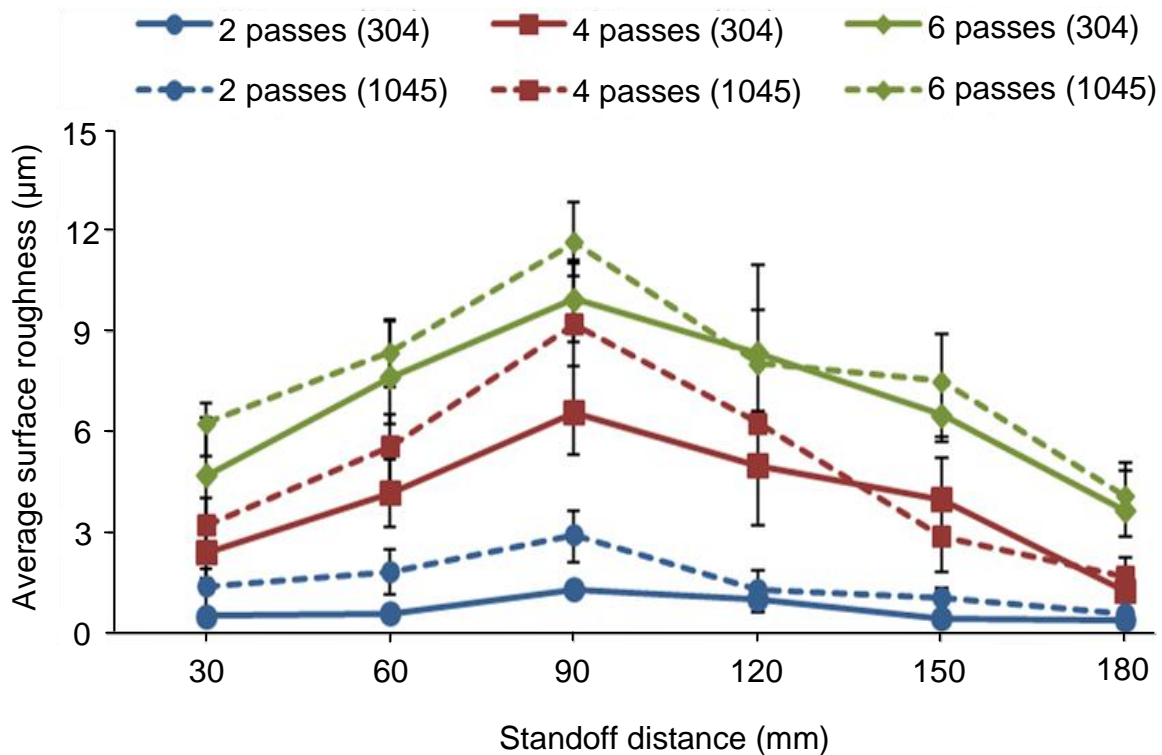


Fig. 5-3: Effect of standoff distance on surface roughness for different number of passes at a pressure of 200 MPa and a feedrate of 2000 mm/min (Stainless steel 304 and carbon steel 1045 are represented by solid and dashed lines respectively)

Also in the present study, the standoff distance between 60 to 120 mm can be said as a transition region of the jet structure from a flow to mainly water droplets [48, 49]. Interestingly, Han et al. [84] found that the maximum impact pressure due to the waterjet cavitation peening occurred in the range of standoff distances between 70 to 95 mm. This explains higher erosion within these distances with the maximum erosion at a standoff distance of approximately 90 mm. Oka et al. [76] found that the maximum damage depth was observed for a standoff distance between 120 and 200 mm at all water pressures in the waterjet treatment of aluminium alloy 5083. Whereas, Chillman et al. [51] found that the distance of 100 mm produces the

highest erosion in the waterjet surface processing of the titanium alloy Ti6Al4V. A further increase in standoff distance results in a lower surface roughness. This is said to be the final region of waterjet structures where there is a noticeable decrease in the droplet velocities as the droplets break up into finer ones. Within this region, the jet has dissipated most of the energy to effectively modify the features of material thus lowering the amount of surface erosion.

It is also interesting to note that the effects of feedrate and pressure in the surface roughness are more prominent at a higher number of jet passes. As shown in [Fig. 5-1](#) to [Fig. 5-3](#), there are significant changes of surface roughness at a higher number of jet passes for different feedrates, pressures and standoff distances respectively. It is possible that during the initial jet passes, the impact of the jet only resulted in initiating some cracks without significantly sheared the material at the surface. The cracks did not considerably change the value of roughness since most materials were not removed. However, at subsequent jet passes, besides initiating some new cracks, the previous cracks might easily propagate leading to removal of more fragments of material. As a result, a noticeable increase in roughness could be observed since most materials at the surface were removed. Furthermore, in the cavitation erosion test, the erosion rates typically exhibit two different regimes based on the cavitation exposure time [117]. The erosion rate is almost negligible within the first regime or the incubation period. While, there is an accelerated erosion rate within the second regime. It is to note that a lower number of jet passes represents a lower exposure time. Beyond that, there were accelerated surface erosion particularly at the highest number of jet passes which constituted the highest exposure time. Based on the surface roughness, it can be suggested that 2 - 4 jet passes is the incubation period of the surface erosion in the present study. Furthermore, Oka et al. [76] reported that the incubation period decreases with an increase in water pressure. It means that the slope of the surface roughness increases rapidly with an increase in water pressure as shown in [Fig. 5-2](#).

5.1.2 Erosion

A further analysis of the peened surfaces is based on SEM images. A lower magnification of SEM images was used so that macroscale erosion of jet tracks could be observed. The SEM images were taken at a magnification of about 70 times. The

erosion tracks on the austenitic stainless steel 304 workpiece surface produced by different feedrates are shown in [Fig. 5-4](#) to [Fig. 5-6](#). The arrows indicate the direction of the jet nozzle feedrate. It is clear that the erosion decreases with an increase in the nozzle feedrate.

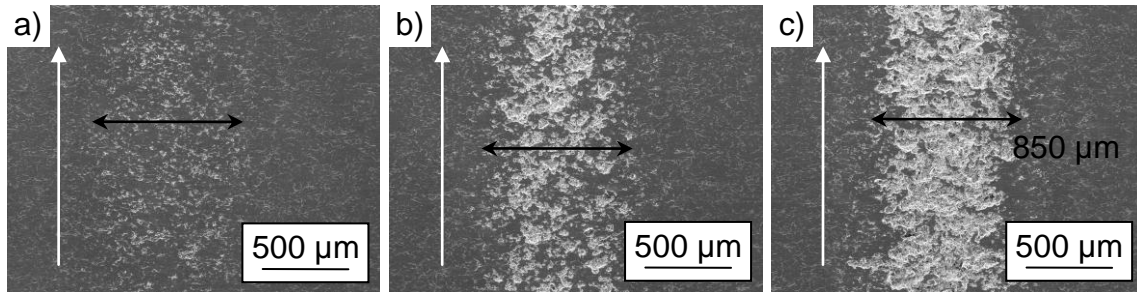


Fig. 5-4: Erosion tracks of austenitic stainless steel 304 for different number of passes, a) 2 passes, b) 4 passes and c) 6 passes, at a feedrate of 1000 mm/min, a pressure of 200 MPa and a standoff distance of 30 mm

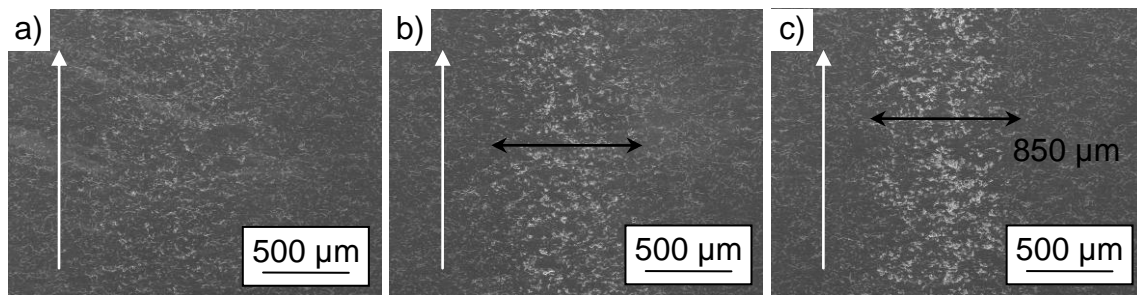


Fig. 5-5: Erosion tracks of austenitic stainless steel 304 for different number of passes, a) 2 passes, b) 4 passes and c) 6 passes, at a feedrate of 2000 mm/min, a pressure of 200 MPa and a standoff distance of 30 mm

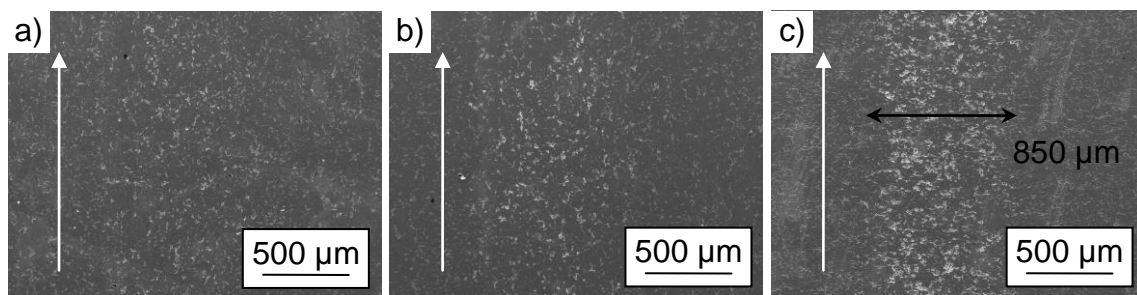


Fig. 5-6: Erosion tracks of austenitic stainless steel 304 for different number of passes, a) 2 passes, b) 4 passes and c) 6 passes, at a feedrate of 3000 mm/min, a pressure of 200 MPa and a standoff distance of 30 mm

At higher feedrates, there exists limited erosion with small isolated pockets as shown in [Fig. 5-5](#) and [Fig. 5-6](#). Moreover, the erosion tracks were discontinuous and almost negligible particularly for erosion tracks at a higher feedrate and a lower number of

passes as seen in [Fig. 5-5](#) (a), [Fig. 5-6](#) (a) and [Fig. 5-6](#) (b). Generally, it can be said that the erosion tracks are very stochastic in nature. However, at a higher number of passes particularly at the lowest feedrate as shown in [Fig. 5-4](#) (c), the erosion track becomes significantly continuous thus indicating a repeated removal of material at subsequent jet passes.

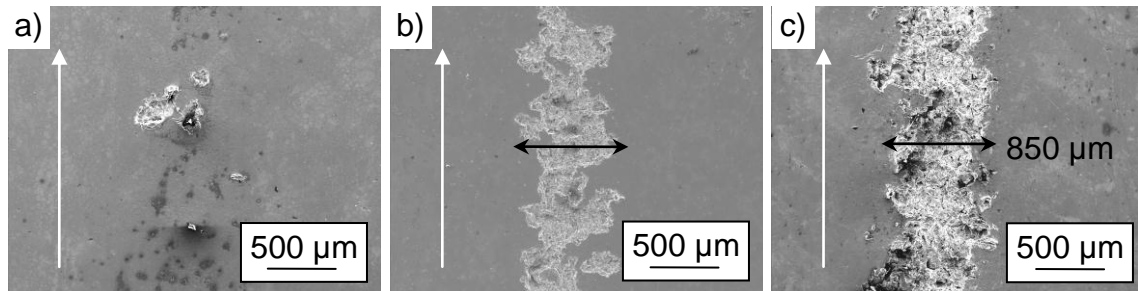


Fig. 5-7: Erosion tracks of carbon steel 1045 for different number of passes, a) 2 passes, b) 4 passes and c) 6 passes, at a feedrate of 1000 mm/min, a pressure of 200 MPa and a standoff distance of 30 mm

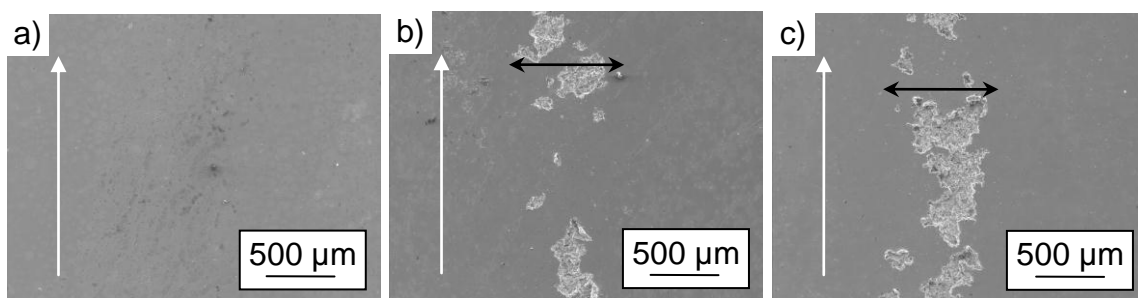


Fig. 5-8: Erosion tracks of carbon steel 1045 for different number of passes, a) 2 passes, b) 4 passes and c) 6 passes, at a feedrate of 2000 mm/min, a pressure of 200 MPa and a standoff distance of 30 mm

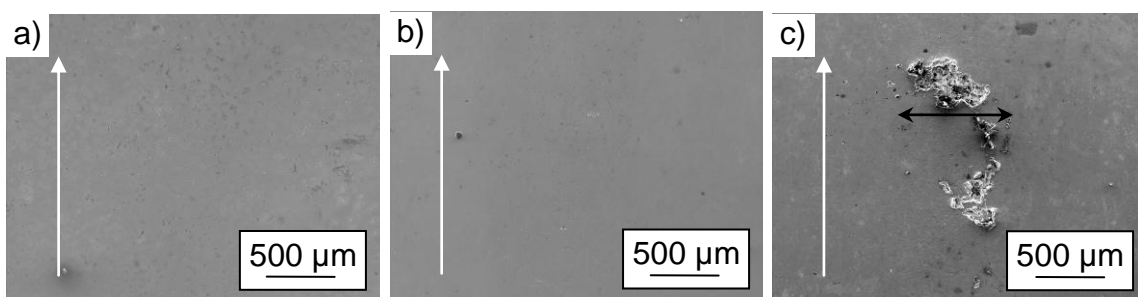


Fig. 5-9: Erosion tracks of carbon steel 1045 number of passes, a) 2 passes, b) 4 passes and c) 6 passes, at a feedrate of 3000 mm/min, a pressure of 200 MPa and a standoff distance of 30 mm

The erosion tracks on the carbon steel 1045 workpiece surface produced by different feedrates are shown in [Fig. 5-7](#) to [Fig. 5-9](#). The arrows indicate the direction of the jet

nozzle feedrate. Again, a general trend as observed previously for the workpiece surfaces of austenitic stainless steel 304 was found here. The SEM images show that the erosion increases with a decrease in nozzle feedrate as well as with an increase in the number of jet passes. At higher feedrates and lower numbers of jet passes, there exists limited erosion in isolated regions with small pockets as shown in [Fig. 5-7 \(a\)](#), [Fig. 5-8 \(a\)](#) and [Fig. 5-9](#). A clearer trace of jet tracks was revealed under jet impingement at a lower feedrate and a higher number of jet passes as seen in [Fig. 5-7 \(b\)](#), (c) and [Fig. 5-8 \(b\)](#), (c). Furthermore, at the lowest feedrate and the highest number of jet passes as shown in [Fig. 5-7 \(c\)](#), the erosion track becomes significantly continuous.

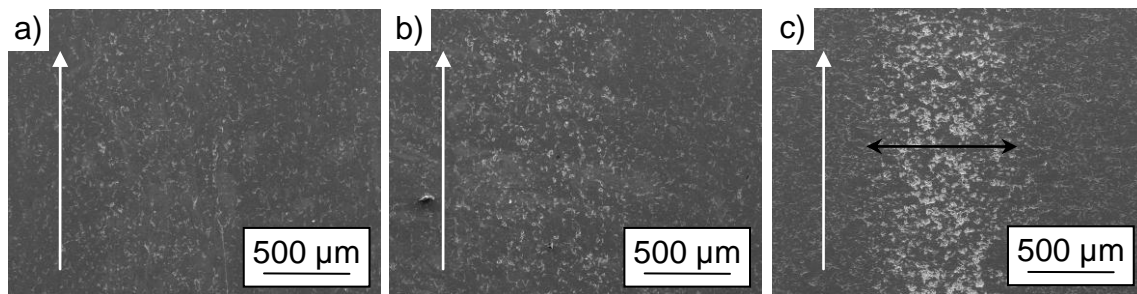


Fig. 5-10: Erosion tracks of austenitic stainless steel 304 for different number of passes, a) 2 passes, b) 4 passes and c) 6 passes, at pressure = 100 MPa

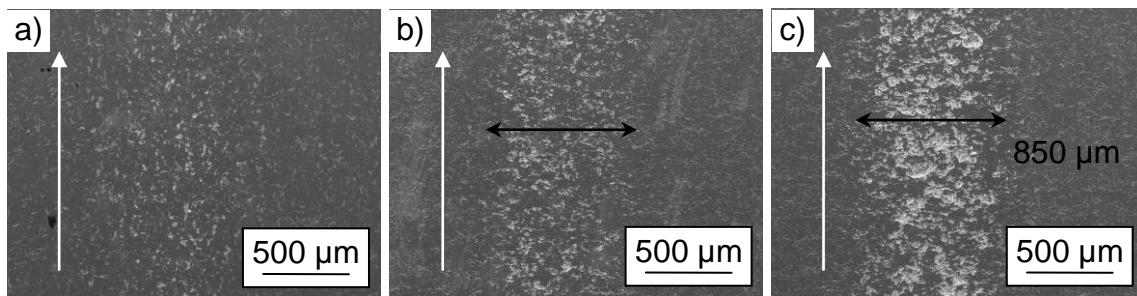


Fig. 5-11: Erosion tracks of austenitic stainless steel 304 for different number of passes, a) 2 passes, b) 4 passes and c) 6 passes, at pressure = 200 MPa

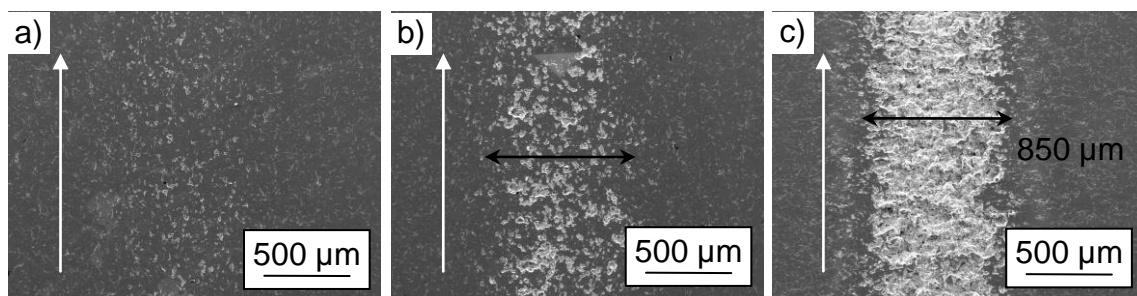


Fig. 5-12: Erosion tracks of austenitic stainless steel 304 for different number of passes, a) 2 passes, b) 4 passes and c) 6 passes, at pressure = 300 MPa

The erosion tracks on the austenitic stainless steel 304 workpiece surface produced by different pressures are shown in [Fig. 5-10](#) to [Fig. 5-12](#). The arrows indicate the direction of the jet nozzle feedrate. From the figures, it is clear that the erosion increases with an increase in the water pressure. At lower pressures, there exists limited erosion with small isolated pockets as shown in [Fig. 5-10](#) and [Fig. 5-11](#). Moreover, the erosion tracks were discontinuous and almost negligible particularly for erosion tracks at a lower pressure and number of passes as seen in [Fig. 5-10](#) (a), (b) and [Fig. 5-11](#) (a). The erosion tracks are also very stochastic in nature. However, the erosion track becomes significantly continuous at the highest number of jet passes and the highest pressure as shown in [Fig. 5-12](#) (c), thus indicating a higher energy of jet as well as a repeated action of material removal at subsequent jet passes.

The erosion tracks of ferritic steel 1045 subjected to waterjet treatment at different pressures are shown in [Fig. 5-13](#) to [Fig. 5-15](#). The arrows indicate the direction of the jet nozzle feedrate. Overall, all surfaces examined show different degrees of damage. It is obvious that the pressure as well as the number of jet passes demonstrate a similar effect on the surface erosion as seen in the waterjet peening of austenitic stainless steel 304. The erosion increases with an increase in the water pressure and also the number of jet passes.

Furthermore, it is to notice that every surface micrograph treated with 2 jet passes regardless of feedrates and pressures produces a very small amount of erosion. Also the value of surface roughness is very low with less than 3 μm in every case as shown in [Fig. 5-1](#) and [Fig. 5-2](#). Almost all the original surfaces remain intact since the erosion was inhomogeneous and discontinuous hence they were not detrimental to the original surface. This shows that 2 jet passes may not really produce considerable erosion to the surface in spite of different feedrates and pressures. This indicates that in the present study a threshold number of jet passes for the material erosion can be considered at about 2 jet passes. Also this can be said as the incubation period of the surface erosion in the present study.

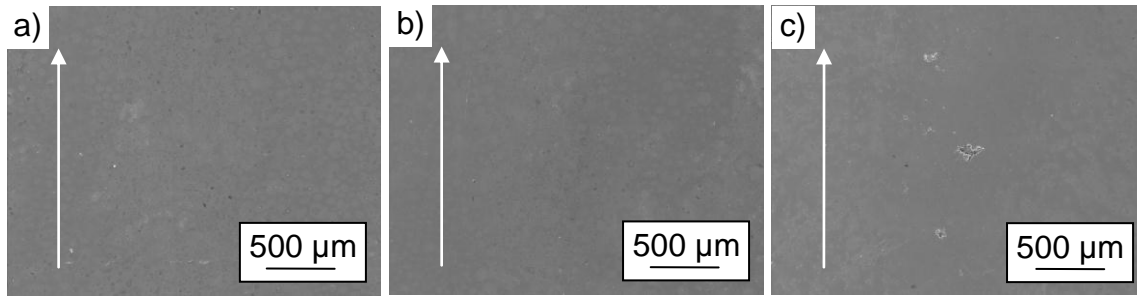


Fig. 5-13: Erosion tracks of carbon steel 1045 for different number of passes, a) 2 passes, b) 4 passes and c) 6 passes, at a pressure of 100 MPa, a feedrate of 2000 mm/min and a standoff distance of 30 mm

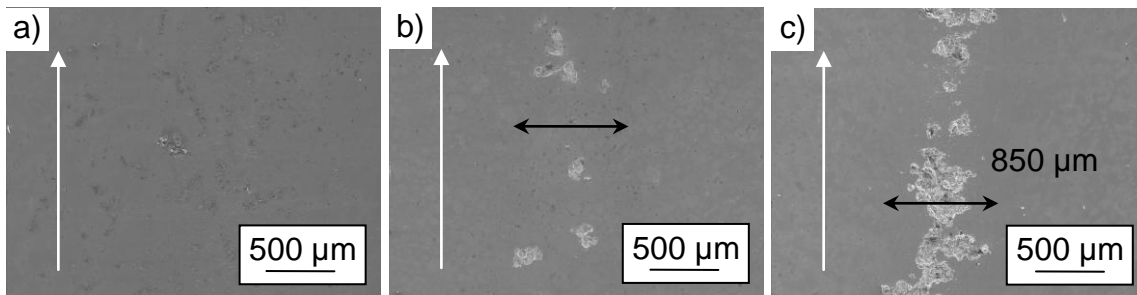


Fig. 5-14: Erosion tracks of carbon steel 1045 for different number of passes, a) 2 passes, b) 4 passes and c) 6 passes, at a pressure of 200 MPa, a feedrate of 2000 mm/min and a standoff distance of 30 mm

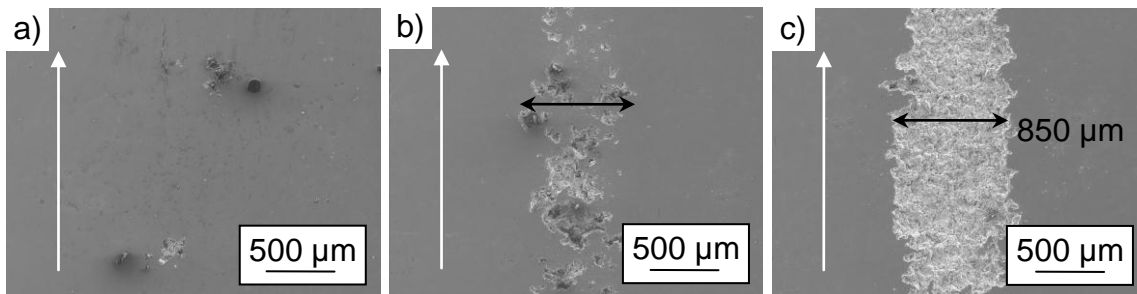


Fig. 5-15: Erosion tracks of carbon steel 1045 for different number of passes, a) 2 passes, b) 4 passes and c) 6 passes, at a pressure of 300 MPa, a feedrate of 2000 mm/min and a standoff distance of 30 mm

As previously discussed, increasing the number of jet passes only increases the surface roughness slightly for specimens treated at either higher feedrates or lower pressures as illustrated in [Fig. 5-1](#) and [Fig. 5-2](#) respectively. Also, their surfaces experience only minimal erosion with small craters as shown in [Fig. 5-6](#) and [Fig. 5-10](#) as well as [Fig. 5-9](#) and [Fig. 5-13](#) respectively for the stainless steel 304 and the carbon steel 1045. This could be possibly due to the shock absorption of a water film formed on the bottom of the crater from previous jet passes [76]. As a result, these water films absorb the water impact from subsequent jet passes and minimize the

total damage to the surface. However, the effectiveness of these water films in absorbing shock is significantly reduced if the exposure duration (i.e. feedrate) is too low or the energy (i.e. pressure) is too high as in the present case when the feedrate is 1000 mm/min or the pressure is 300 MPa. It is clear that within these regions the material is sufficiently exposed to the waterjet impact and/or the water droplets carries enough energy to remove the material at the surface as indicated in [Fig. 5-4](#) and [Fig. 5-12](#) as well as [Fig. 5-7](#) and [Fig. 5-15](#) for the stainless steel 304 and the carbon steel 1045 respectively. This is confirmed by a study of Barriuso et al. [78] in roughening another type of austenitic stainless steel AISI 316 LVM with a single jet pass but with much lower feedrates between 50 to 100 mm/min and a higher jet pressure of 360 MPa produced rougher surfaces of about 11 - 13 μm . This is possible since a higher water pressure as well as much lower feedrates were utilized although the specimens were treated with only a single jet pass. This shows that multiple jet passes treatment may not produce substantial erosion if the pressure and the feedrate are within the threshold limit.

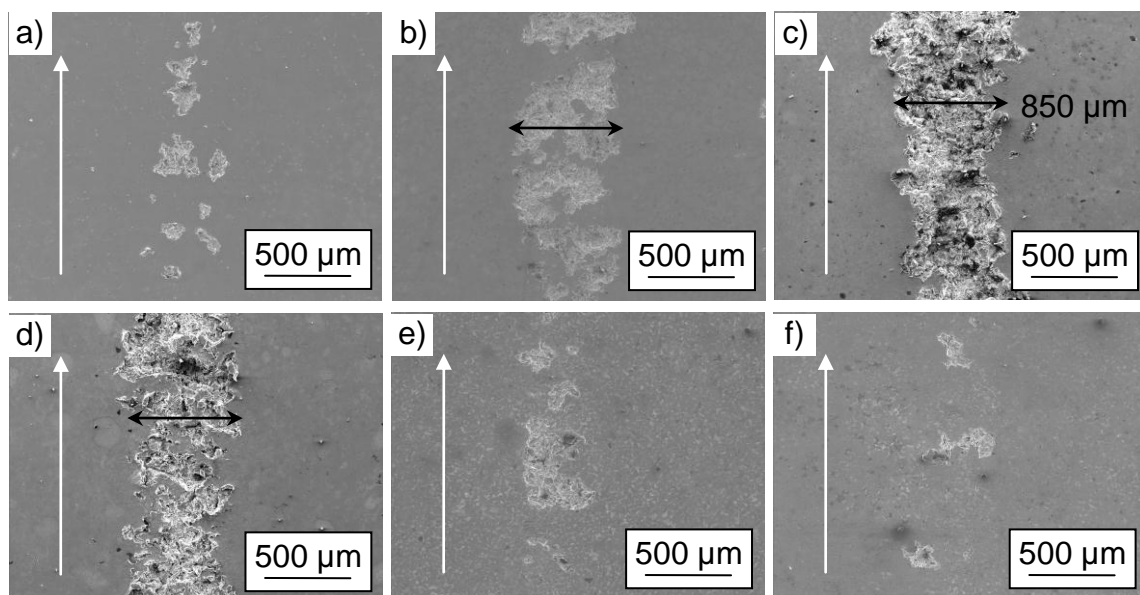


Fig. 5-16: Erosion tracks of carbon steel 1045 for different standoff distances, a) 30 mm, b) 60 mm, c) 90 mm, d) 120 mm, e) 150 mm and f) 180 mm, at a pressure of 200 MPa, a number of jet passes of 4 and a feedrate of 2000 mm/min

An example on the effect of the standoff distance on the surface erosion is shown [Fig. 5-16](#). It is clear that the erosion increases with an increase in the distance between the nozzle and the workpiece until it reaches the maximum at a distance of 90 mm ([Fig. 5-16 \(c\)](#)). A further increase in the standoff distance results in lower

erosion. As expected, the erosion was the least at the highest standoff distance of 180 mm as the case of the present study. Furthermore, based on the trend of the surface roughness as shown in [Fig. 5-3](#), it can be clearly seen that beyond this maximum distance the roughness approaches the original roughness of the specimens. So, the distance perhaps about 200 mm, can be considered as a critical effective standoff distance while beyond it the waterjet is unable to remove the materials. Based on a mathematical model developed in a coating removal experiment, Leu et al. [118] approximated the optimal standoff distance (i.e. the distance where the most material was removed) to be about half of the critical effective standoff distance. This is about 100 mm for the present study which is in agreement as the maximum erosion occurred at a distance of 90 mm as indicated in [Fig. 5-3](#) as well as [Fig. 5-16](#).

As discussed above, a high velocity of waterjet can cause damage to the target materials by means of erosion. The structure and velocity of the jet change based on the different regions of the waterjet. The loss of jet velocity begins once the jet leaves the nozzle exit due to aerodynamic interaction, turbulence and cavitation [62]. It can be expected that the initially coherent jet breaks up to form droplets as air is entrained into the jet [118]. Sohr and Thorpe [119] suggested that this breakdown into droplets occurred at a critical standoff distance which is approximately 175 times of the orifice diameter. Comparing this to the present work, the critical standoff distance where the jet breaks up to form droplets is about 52.5 mm with the nozzle diameter of 0.3 mm. This is somehow in agreement with the present study where the standoff distance between 60 to 120 mm is said as the main transition region of the jet structure consisting of mainly water droplets as found from [Fig. 5-3](#). This may also explain higher erosion within these distances with the maximum erosion at a standoff distance of approximately 90 mm as shown in [Fig. 5-16](#).

Since the SEM images only show the surface features in 2 dimensions, it is difficult to assess the depths of the erosion tracks. It would be interesting to discuss the extent of the erosion especially their depths. Therefore, a 3D profilometer was used to capture the 3D features of the surfaces. Based on 3D images of waterjet treated surfaces for both materials at different parameters, there was little difference in the characteristics and the extent of the observed erosion tracks other than their depths. Hence, only a few representations of 3D images are presented in this section as to

describe the effect of peening parameters on the erosion depths. 3D images of the surface structures treated at different numbers of jet passes are shown in [Fig. 5-17](#). These are the surface 3D images for the same specimens as presented in [Fig. 5-15](#). It is obvious that the erosion tracks in 3D show similar features as previously characterized by SEM. However, it is clear that the erosion depths are higher in the specimens treated with a higher number of jet passes as indicated by high values of valley depths as indicated in [Fig. 5-17](#) (b) and (c).

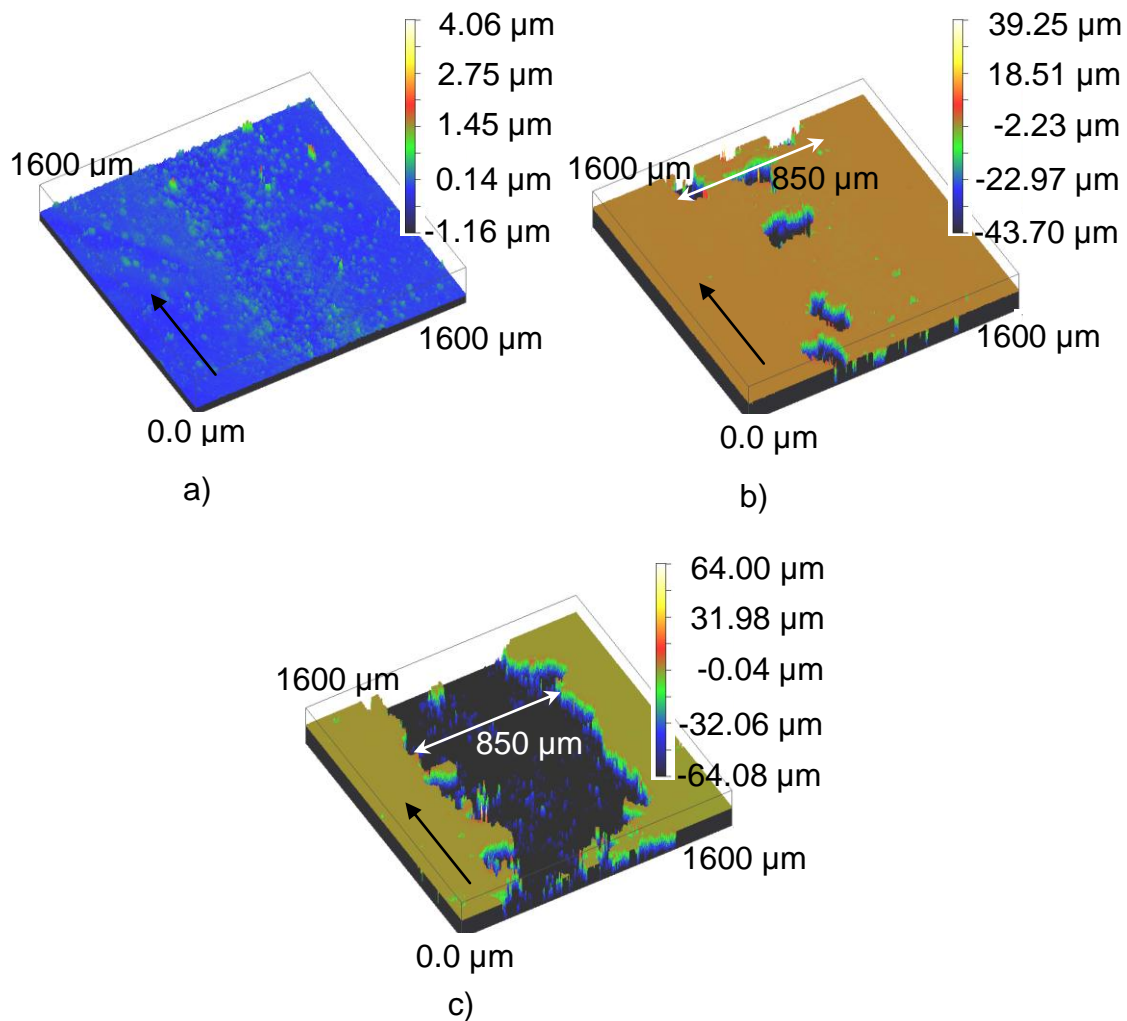


Fig. 5-17: 3D images of surface erosion at different jet passes, a) 2 passes, b) 4 passes and c) 6 passes, at a pressure of 200 MPa, a feedrate of 2000 mm/min and a standoff distance of 30 mm (black arrows indicate the traverse direction of the nozzle)

Whereas, 3D images of the surface structures treated at different feedrates are shown in [Fig. 5-18](#). The surface 3D images are for the same specimens as presented in [Fig. 5-7](#) (c), [Fig. 5-8](#) (c) and [Fig. 5-9](#) (c) respectively. It seems that the erosion tracks in 3D show similar features as previously characterized by SEM.

Basically, the erosion becomes less continuous as the feedrate increases. It is interesting to note that the depth of the valley are about the same for the specimen treated at lower feedrates of 1000 and 2000 mm/min as shown in [Fig. 5-18 \(a\)](#) and [Fig. 5-18 \(b\)](#) respectively. However, the high of the peak is higher for the specimen treated with the lowest feedrate. Perhaps, this feature contributes to a higher value of the roughness in the specimen treated with a lower feedrate. In addition, it is good to note that the depth of the craters under waterjet impingement at particularly lower feedrates may be the same but its erosion is not homogeneous over the treated surface.

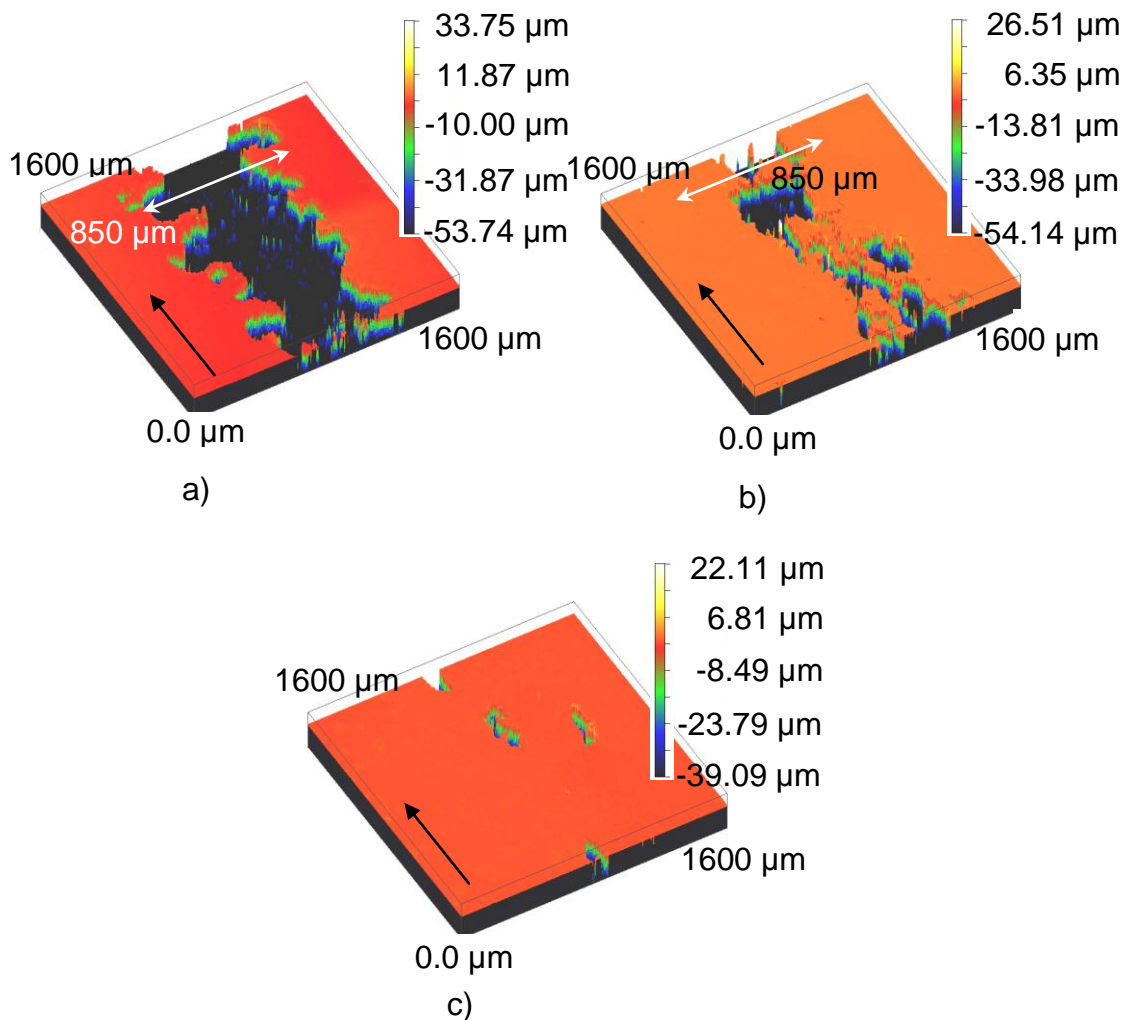


Fig. 5-18: 3D images of surface erosion at different feedrates, a) 1000 mm/min, b) 2000 mm/min c) 3000 mm/min, at a pressure of 200 MPa, a number of jet passes of 4 and a standoff distance of 30 mm (black arrows indicate the traverse direction of the nozzle)

3D images of the surface structures for the same specimens treated at different pressures are shown in [Fig. 5-19](#). The images were taken on the same erosion

tracks as presented in [Fig. 5-13 \(c\)](#), [Fig. 5-14 \(c\)](#) and [Fig. 5-15 \(c\)](#) respectively. Again, the erosion tracks in 3D show similar features as previously characterized by SEM. Generally, the surface erosion is more continuous as the pressure increases. Also, the erosion depths are higher in the specimens treated with a higher pressure as indicated by high values of valley depths.

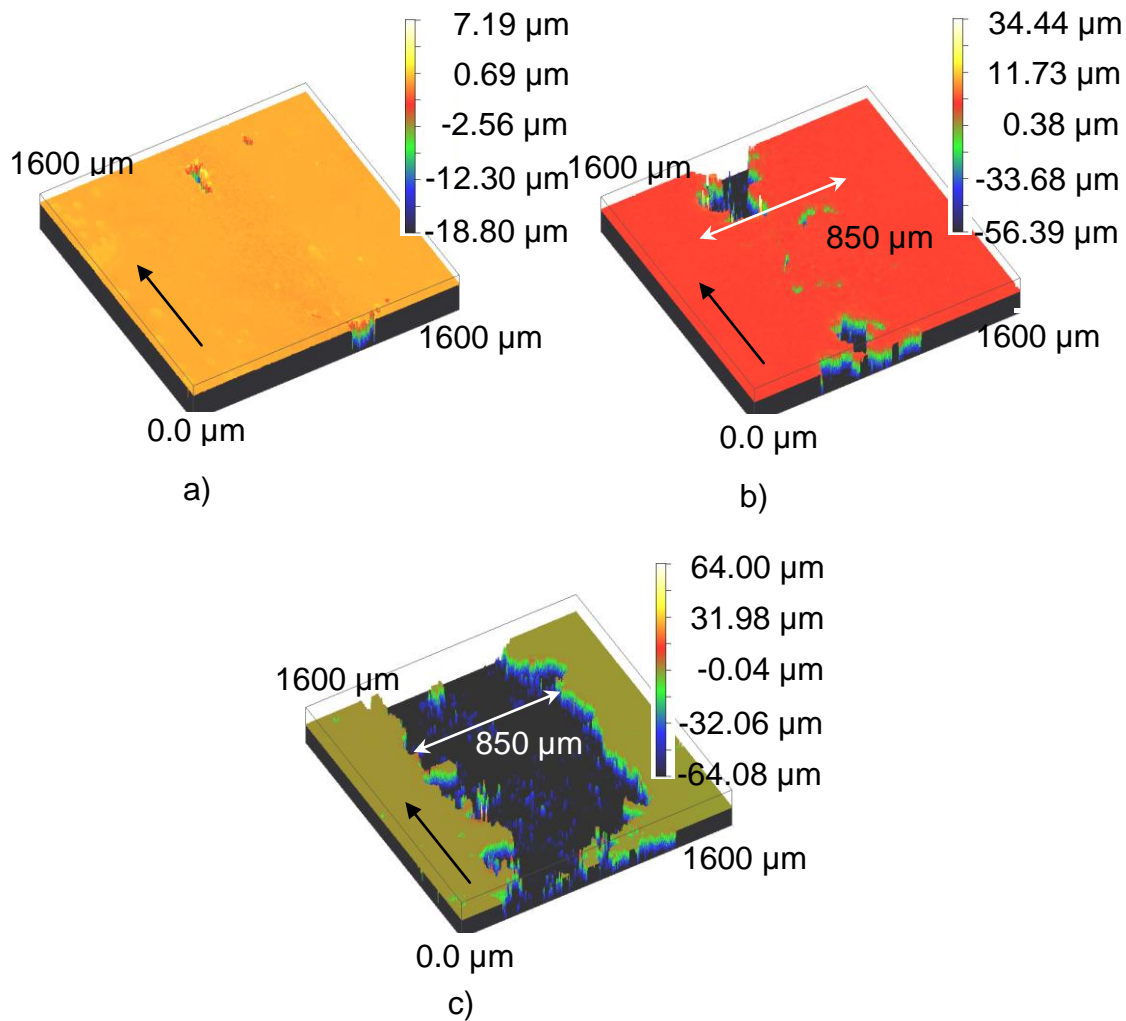


Fig. 5-19: 3D images of surface erosion at different pressures, a) 100 MPa, b) 200 MPa and c) 300 MPa, at a feedrate of 2000 mm/min, a number of jet passes of 4 and a standoff distance of 30 mm (black arrows indicate the traverse direction of the nozzle)

3D images of the surface structures for the same specimens treated at different standoff distances are shown in [Fig. 5-20](#). The images were taken on the same erosion tracks as presented in [Fig. 5-16](#). However, only the 3D images with the highest erosion (i.e. at standoff distances of 60, 90 and 120 mm) are presented here since there was little difference in the characteristics of the eroded surfaces from previously presented 3D images. A similar feature of the erosion tracks in 3D was

observed from previously characterized images by SEM. The erosion was noticed the most at a standoff distance of 90 mm as shown in [Fig. 5-20](#) (b) with the deepest valley.

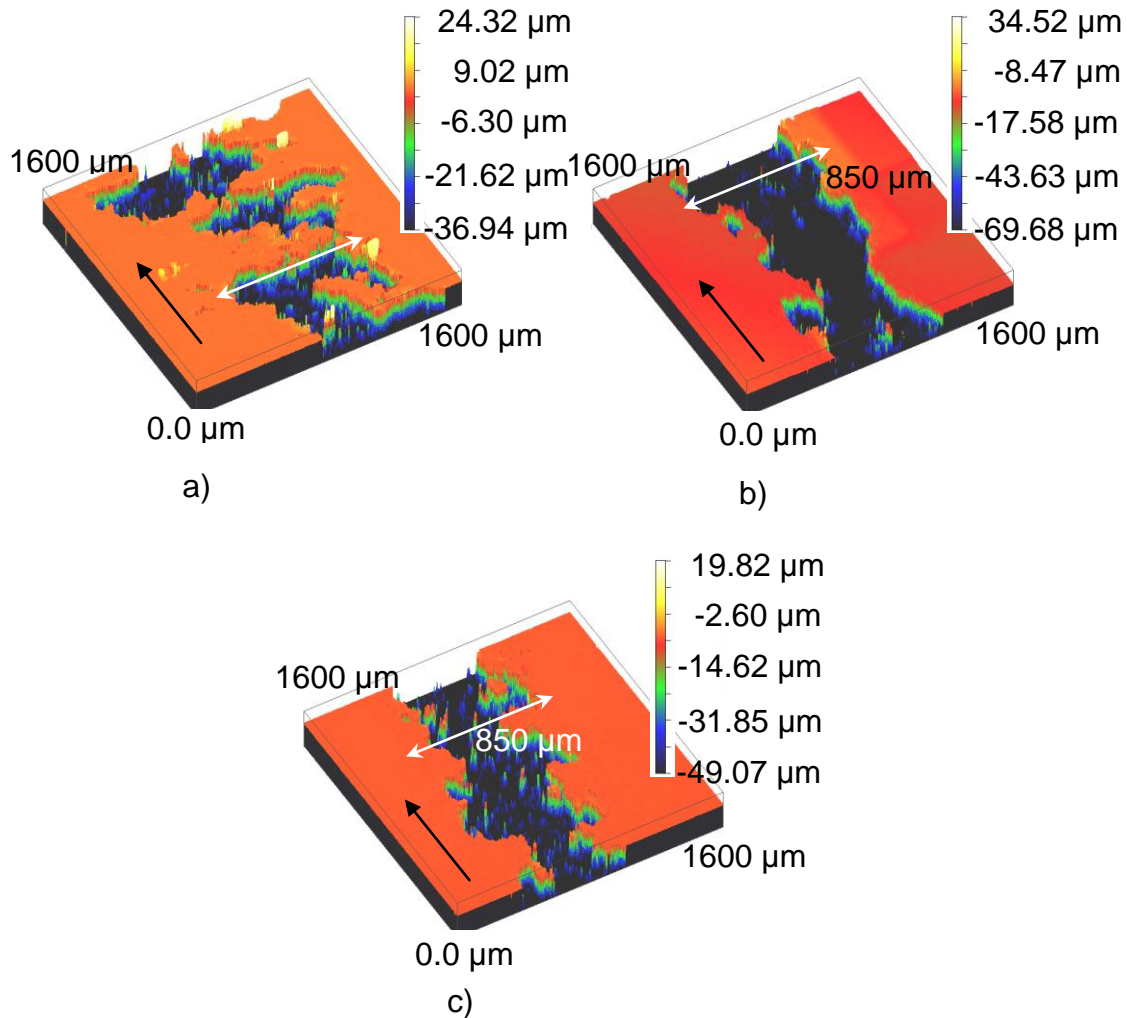


Fig. 5-20: 3D images of surface erosion at different standoff distances, a) 60 mm, b) 90 mm and c) 120 mm, at a pressure of 200 MPa, a number of jet passes of 4 and a feedrate of 2000 mm/min (black arrows indicate the traverse direction of the nozzle)

It is also interesting to discuss about the effect of the number of jet passes on the erosion track width. On macro-scale erosion as seen above, some of the eroded surfaces do not display a clear erosion track width since it happened as a small pocket. However, the width of the erosion track can be clearly seen on the treated surfaces that display a continuous removal of the material especially in the specimens treated with a higher number of jet passes. An almost constant erosion track width of approximately 850 µm was produced in those treated jet specimens. In the present case, it can be expected that the effective coverage area from the jet with a nozzle diameter of 0.3 mm is about 850 µm. Likewise, it can be seen that the

traces of the surface erosion such as craters are also located within this width in the specimens treated with a lower number of jet passes. This shows that the material removal on the surface under the waterjet impingement only happens within the effective coverage area. It is believed that the erosion track will not appreciably get wider with even more jet passes but certainly the erosion track depth will notably get deeper. Also, the randomly formed craters on the surface during previous jet passes may easily combine to form larger craters at subsequent jet passes. As a result, uniform erosion with full removal of materials is developed over the surface within the jet effective coverage area.

5.1.3 Comparisons of surface effects between both materials

It is good to compare about the results of surface roughness and erosion for both materials (i.e. stainless steel 304 and carbon steel 1045) studied in the present work. It is known that the material properties (i.e. strength, hardness, ductility, fatigue resistance, etc.) affect the surface erosion of a material. Krella and Czyniewski [120] commented that an increase in the material strength and hardness tend to increase the cavitation erosion resistance. However, they also noted that there was no straight correlation between the material hardness and the incubation period. In case of the present study, a similar conclusion can be made where there is no clear correlation between the incubation period and the hardness of the materials. It is to note that the stainless steel 304 has a higher hardness than the carbon steel 1045 (i.e. 230 HV_{0.01} versus 145 HV_{0.01}). however, it can be seen from [Fig. 5-2](#) and [Fig. 5-3](#) that both materials show a relatively similar behaviour in regard to the incubation period at about 2 – 4 jet passes.

In general, carbon steel 1045 has produced a higher value of surface roughness than stainless steel 304 as shown in [Fig. 5-1](#), [Fig. 5-2](#) and [Fig. 5-3](#). This can be expected since the carbon steel has a lower hardness than the stainless steel. Therefore, it has a lower erosion resistance thus producing a higher roughness of the surface. Interestingly, the increase of roughness in the carbon steel 1045 can be considered moderate in comparison to the stainless steel 304 within the same parametric conditions although the hardness of the former is slightly more than half of the latter. Also, the degree of erosion observed in the carbon steel 1045 is only slightly more severe with a continuous erosion surface particularly at a higher pressure and more

number of jet passes as shown in [Fig. 5-15 \(b\)](#) and [Fig. 5-15 \(c\)](#) than in the stainless steel 304 as shown in [Fig. 5-12 \(b\)](#) and [Fig. 5-12 \(c\)](#). Possibly, since the carbon steel 1045 has a lower original roughness than stainless steel 304 (i.e. 0.07 μm versus 0.15 μm) this results in a lower increase of roughness after the waterjet treatment. It is known that an initially smooth surface is favourable to the erosion resistance [121].

However, the erosion behaviour of the material surface under the waterjet impact is very complex. A lot of factors may influence its behaviour. It can be said that a lower material hardness is no guarantee to a lower erosion resistance. Additionally, there is no simple relation between the amount of material loss during cavitation erosion and the mechanical properties of a material, such as hardness, strength and toughness [122]. In contrast, Lee [123] found a relationship between the materials' hardness and the erosion rate. The erosion rate decreased with an increase in the material hardness. However, the same author pointed out that the erosion rate for a simple two-phase alloy system is strongly related to the amount of primary ferrite in the microstructure rather than its hardness. While, Mann and Arya [124] commented that the hardness of coatings played a crucial role in improving the erosion resistance especially during the incubation period for coated materials.

Richman and McNaughton [125] suggested that material removal rates are correlated with cyclic deformation parameters, a strong indication that the damage in the cavitation erosion is a fatigue process. They established the relationship between the erosion behaviour with the fatigue strength coefficient. The fatigue strength coefficient is inversely proportional to the erosion depth. Based on the database of cyclic deformation parameters for various metals, the stainless steel 304 displays a higher value of the fatigue strength coefficient than carbon steel, thus it has a higher erosion resistance [125]. Furthermore, Feller and Kharrazi [126] reported that the erosion resistance strongly influenced by the binding energy and the crystal structure of the base material. They explained that single phase alloys had high erosion resistance due to high covalent bonding and low stacking fault energy. The predominant mode of deformation is thus planar slip due to the low stacking fault energy which prevents recombination of partial dislocations necessary for cross-slip [127]. In other words, the surface distortion is largely confined to the grain-boundary regions, thereby limiting the area susceptible to erosion [128].

While, the second-phase particles in multi-phase alloys were preferentially removed because of the initiation of deformation and cracks at the particle-matrix interfaces. Also according to Preece and Macmillan [128], the material in these alloys is removed by lateral growth of flat-bottomed pits that develops because of the large numbers of dislocation sources. This results in the near-surface highly localized stress concentrations which lead to the initiation of cracks. This may explain why more erosion had occurred in the carbon steel 1045 than the stainless steel 304. It is to note that the former consists of multi-phases (i.e. ferrite and pearlite phases) while the latter consists of a single austenite phase. Furthermore, Heathcock et al. [127] attributed the low erosion resistance of ferritic steels to the strain rate sensitivity of the body-centered cubic lattice structure. The high strain rates generated from waterjet peening treatment may result in a rapid brittle fracture along both transgranular and intergranular paths [127].

Another possible reason of good erosion resistance of the stainless steel 304 is due to the phase transformation that may occur during waterjet treatment [120, 127]. It is known that the phase transformation needs energy which typically occurs during heating resulted from highly localized impact of water droplets [120]. The energy generated will be absorbed or dissipated by the solid material to change its dislocation structure and transform its austenite into martensite phase [120, 127, 129]. As a result of a high work-hardening rate of the stainless steel 304, it is thus expected to have a higher erosion resistance. In general, the alteration of phase and dislocation structure may finally change the material properties and change the erosion resistance of the material. The details discussions on the erosion mechanisms for both materials are reported in the following section.

5.2 Erosion mechanisms

A further investigation of SEM images at a higher magnification gives details of the erosion nature. Since, the erosion features under the microscopic observation for different surfaces displayed relatively similar characteristics; only several magnified images at selected locations are presented here. Nevertheless, various surface damage mechanisms can be clearly seen from these images. In general, the erosion mechanisms for both materials (i.e. austenitic stainless steel 304 and carbon steel 1045) show quite similar features since both materials are ductile metals. As

explained by Hancox and Brunton [57], yielding in ductile metals can be expected to begin locally at average impact pressures appreciably below the average flow stress for the metals. The regions which are yielded previously were further deformed and pitted by the liquid flow. As a result, the material removal from the surface happens by the impingement of the liquid flow against the edges of the surface fractures [57]. The detail discussions on the erosion mechanisms will be presented with the help of SEM images at higher magnifications. The SEM Images for both materials are used interchangeably throughout this section.

Several magnified SEM images of the stainless steel 304 were captured at different locations of the erosion tracks. The images represent the effect of different waterjet peening parameters as shown in [Fig. 5-4](#) to [Fig. 5-6](#). The magnified images are shown in [Fig. 5-21](#) to [Fig. 5-24](#) respectively for different numbers of jet passes, feedrates, pressures and standoff distances. Clearly, severe erosion happens particularly at the highest number of jet passes, the lowest feedrate, the highest pressure and the standoff distance of 90 mm as displayed in [Fig. 5-21](#) (c), [Fig. 5-22](#) (a), [Fig. 5-23](#) (c) and [Fig. 5-24](#) (b) respectively where the original surfaces are no longer present as evidenced by a larger size of the pit with more undercuts. A similar observation was noticed by Barriuso et al. [78] in roughening of metallic biomaterials using abrasiveless waterjet peening where they observed a large number of pits with undercuts as well as some larger intrusions, which are more abundant and larger as in those treated with the lower feedrate. Besides, erosion of material was observed appearing like hills and valleys as well as some parts of relatively flat indentations and rolled-up grains around the crater as similarly observed by Oka et al. [76] in waterjet treatment of aluminium alloy. It can be anticipated that increasing the number of jet passes causes the removal of the material tip repetitively thus eroding the surface further. Furthermore, decreasing the feedrate allows additional overlap of the waterjet action and more water molecules to impinge on the surface hence resulting in severe erosion. Moreover, it implies smaller impingement time of the waterjet on the same point of the specimen. Whereas, a higher pressure generates a higher kinetic energy of water molecules hence eroding the surfaces more efficiently.

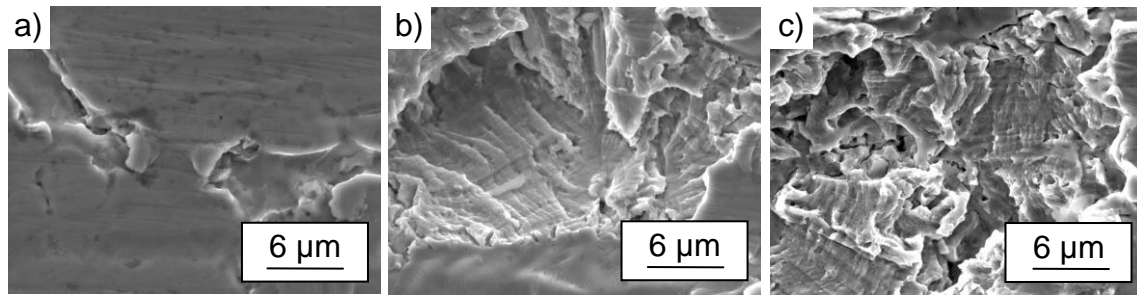


Fig. 5-21: Details of surface erosion for different number of jet passes a pressure of 200 MPa, a feedrate of 2000 mm/min, and a standoff distance of 30 mm, a) 2 jet passes, b) 4 jet passes, and c) 6 jet passes

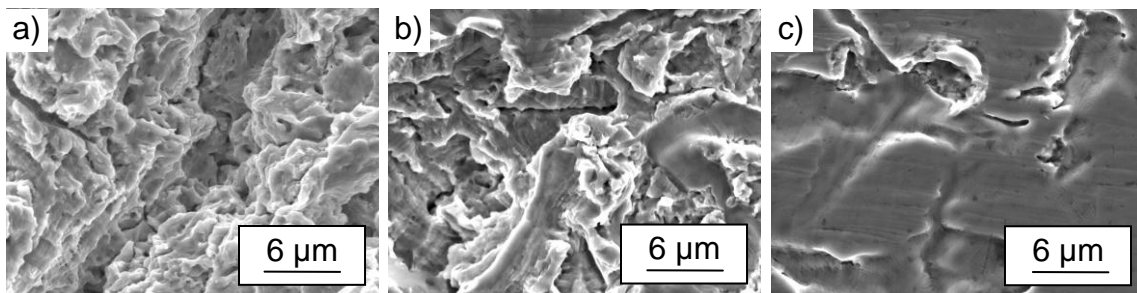


Fig. 5-22: Details of surface erosion for different feedrates at a pressure of 200 MPa, a number of jet passes of 4 and a standoff distance of 30 mm, a) 1000 mm/min, b) 2000 mm/min, and c) 3000 mm/min

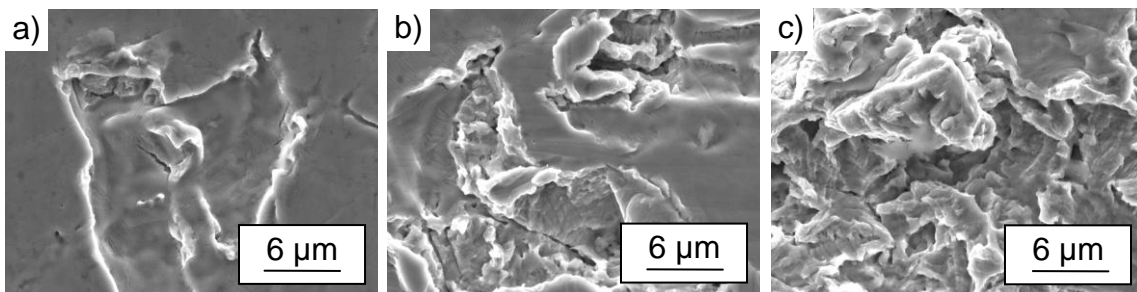


Fig. 5-23: Details of surface erosion for different pressures at a feedrate of 2000 mm/min, a number of jet passes of 4 and a standoff distance of 30 mm, a) 100 MPa, b) 200 MPa, and c) 300 MPa

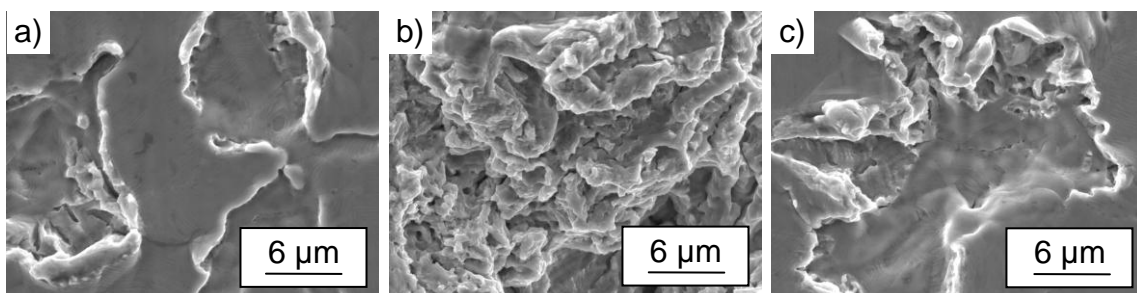


Fig. 5-24: Details of surface erosion for different standoff distances at a pressure of 200 MPa, a feedrate of 2000 mm/min and a number of jet passes of 2, a) 60 mm, b) 90 mm, and c) 120 mm

It is also interesting to discuss about the effect of the waterjet parameters on the micro-scale erosion pattern. Generally, all surfaces experience a certain degree of erosion during the waterjet impingement at different parameters. The surfaces with severe erosion show a similarity where the original surface is no longer present. However, the eroded surfaces treated with different numbers of jet passes display a relatively different pattern. A shape like a mountain hill terrace was produced and it became clearly visible especially at a higher number of jet passes as illustrated in [Fig. 5-21 \(b\)](#) and [Fig. 5-21 \(c\)](#). Comparing these figures, it seems that the latter shows a deeper slope of terrace due to the additional erosion from more waterjet passes. This specific pattern is not found on the other eroded surfaces treated with different parameters as shown in [Fig. 5-22](#) to [Fig. 5-24](#). This is a strong indication that the erosion mechanism during the waterjet impingement process is somehow like a fatigue process especially under the multiple jet passes treatment [128, 130]. This will be further discussed in the next paragraphs.

As discussed above, during subsequent jet passes with more water impacts, old cracks are further propagated thus forming a network of cracks as well as the initiation of new cracks. Adler and Hooker [131] suggested that the hydraulic penetration mode of fracture dominates the subsequent erosion process. This damage is due to the hydraulic stresses generated by the penetration of the water during the subsequent impacts into the enlarged impact zone. The most favourable structure for the hydraulic penetration effect is the original sites of the lateral outflow fracture and pitting [131]. This leads to crack propagation and eventually pitting as well as material removal. As shown in [Fig. 5-21 \(b\)](#), with more water impacts at a higher jet passes, the previously formed small craters may easily combine to form a larger crater. As a result, a bigger crater is developed with full removal of materials over the surface. With even further jet passes, more fractures can be expected with full removal of the material fragments as shown in [Fig. 5-21 \(c\)](#).

In general, the material removal occurs at two levels, i.e., initial and evolved damage [74, 81]. Due to the highly stochastic nature of the plastic deformation in material surfaces, it is hard to capture its initial damage perfectly. However, a possibly initial damage image was captured on a surface treated with the lowest jet pass number as indicated in [Fig. 5-25](#) and [Fig. 5-26](#) respectively for the stainless steel 304 and the carbon steel 1045. The images were captured on the treated surface (i.e. [Fig. 5-4 \(a\)](#)

and Fig. 5-15 (a) respectively) with no noticeable erosion traces. The deformation starts when high-velocity droplets hit the impact zone as shown in Fig. 5-25 (a) as well as Fig. 5-26 (a). As a result, a small central depression crater is formed due to the impact pressure. Also some cracks initiate and propagate from the impact zone. Some grains are also deformed due to the impact pressure as well as the generated stress waves. Strain gradients are set up across the grain boundaries because of the different strains in the neighbouring grains eventually leading to grain boundary fractures [123]. The water droplets hit within a certain area thus forming many impact craters with various extended crack lines and deformed grains as shown in Fig. 5-25 (b) as well as Fig. 5-26 (b). Later, the liquid outward flow results in lateral shear stresses which may further fracture the solid particles in the impact zone and its surrounding areas.

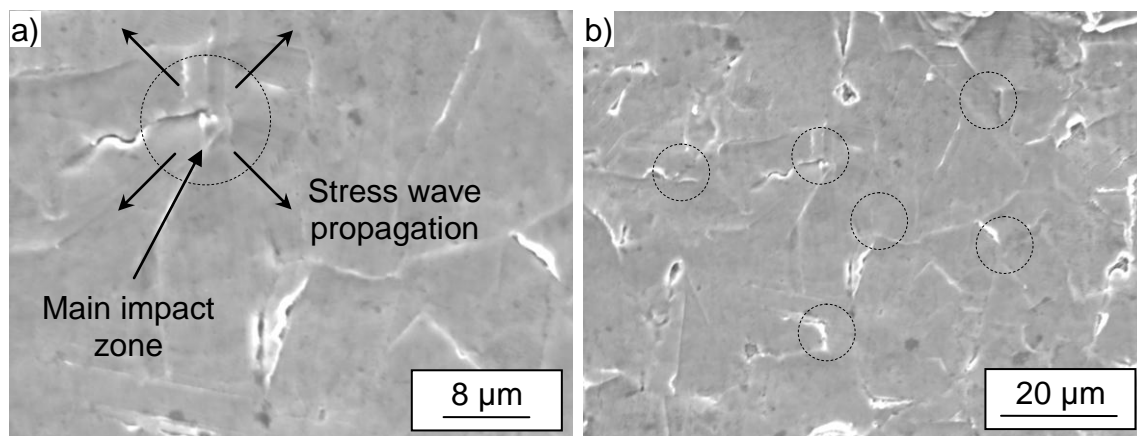


Fig. 5-25: Example of the initial damage on the stainless steel surface, a) a single impact zone, b) many impact zones (circles indicate the main impact zones)

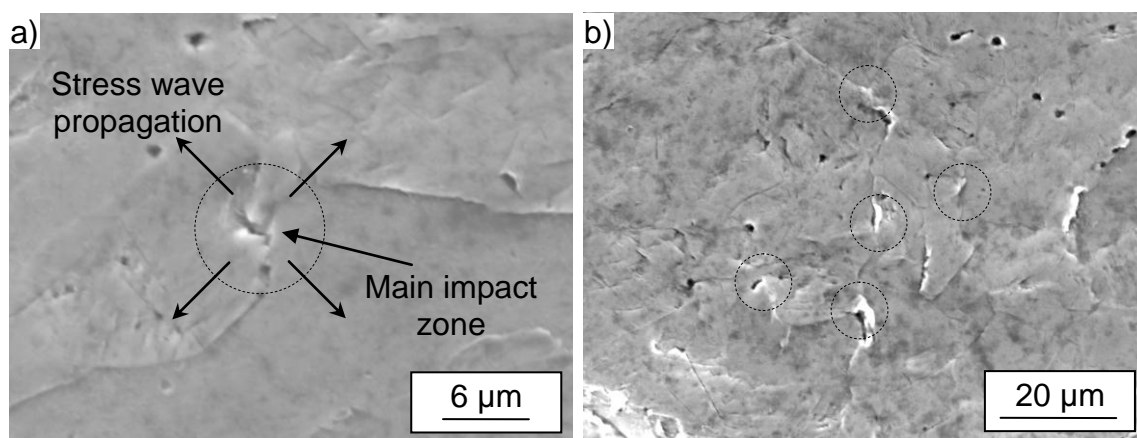


Fig. 5-26: Example of the initial damage on the carbon steel surface, a) a single impact zone, b) many impact zones (circles indicate the main impact zones)

The examples of the evolved damage surface are shown in [Fig. 5-27](#). The images were captured on various locations of the eroded surfaces of the carbon steel 1045. Various surface damage mechanisms can be seen from these images. Deep cavities are formed when the pits from the individual fractures are combined together as shown in [Fig. 5-27](#) (a) and (b). Besides, the surface erosion was observed appearing like hills and valleys as well as some parts of relatively flat indentations and rolled-up grains around the crater as shown in [Fig. 5-27](#) (c). The surface cracks are possibly propagated mainly along the grain boundaries as evidenced by tilting of a grain as indicated in [Fig. 5-27](#) (d).

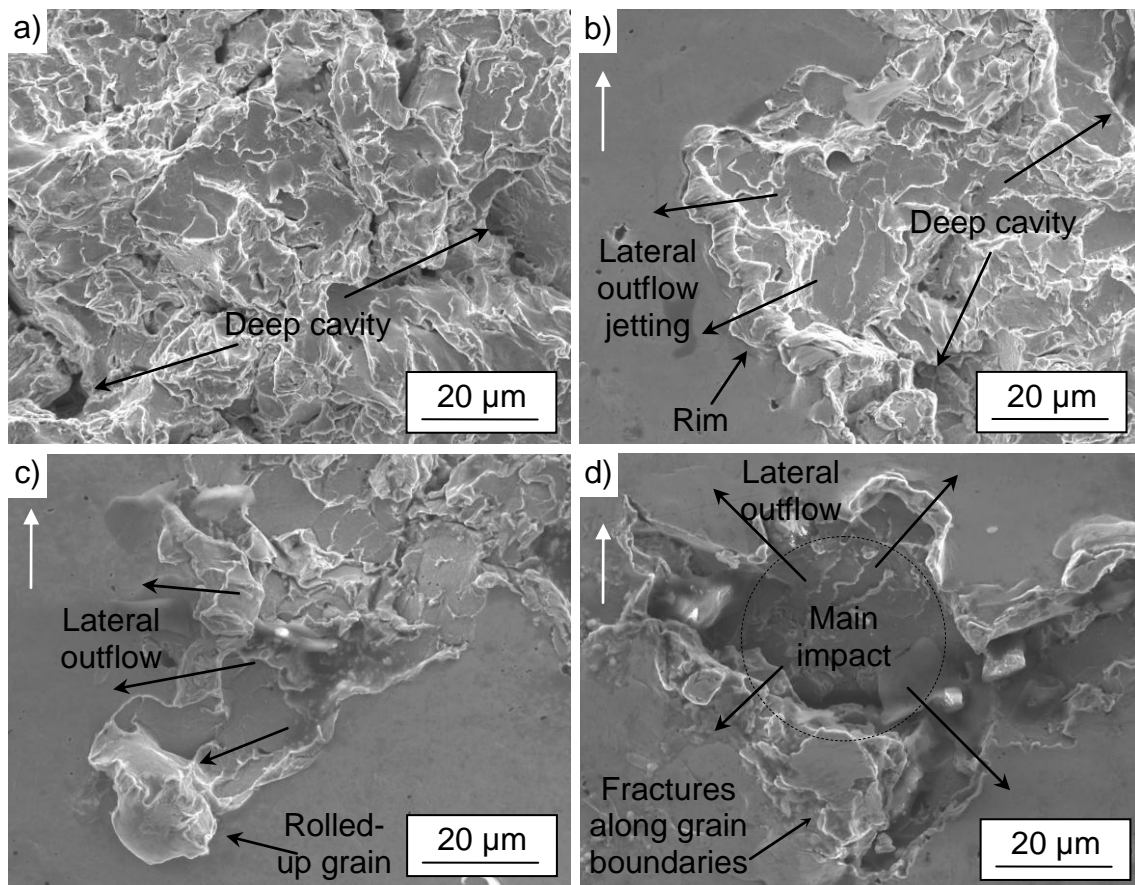


Fig. 5-27: Example of the evolved damage on the carbon steel surface, a) full removal of material with deep cavities, b) lateral outflow jetting, c) rolled-up grains, and d) fractures along grain boundaries

It is also important to discuss about the effect of lateral outflow jetting in characterizing the erosion track. As discussed above, there are shear forces due to the outward flow impinging against projections in the impact surface which may result in local shear fractures [57]. It can be clearly seen that the surface outside the deep fractures (i.e. edges of the erosion track) is increasingly broken by a pitting action as

shown in [Fig. 5-27](#) (b) to (d). Also, the circumferential rims on the edges of the erosion track were plastically deformed and slightly raised by a ploughing action due to an outward acting shear stress arising from the liquid flow across the surface. It is known that the outward stress wave propagates circumferentially from the impact zone [56]. This can be seen in those figures where there exist some parts of circular bands in the edges due to the lateral outflow jetting. However, the band waves appear to propagate only in the direction of the erosion track edges (i.e. to the left or right sides of the erosion track) as indicated in [Fig. 5-27](#) (b) and (c). The possible reason is that the traces of bands in the nozzle traverse direction were eventually removed by subsequent jet passes.

Hancox and Brunton [57] assumed the maximum outward flow stress (shear stress) to be approximately one-tenth of the impact pressure if a cylindrical indenter was used. This shear stress can be considered too small to cause significant damage to the surface. However, in most cases the surface experiences some degree of damage (e.g. cracks and fractures) from the initial impact pressure. Therefore, the shear stress is normally large enough to cause local shear fractures on the already weakened surface [57]. Still, the lateral outflow jetting does not significantly contribute to the widening of the erosion track outside the effective coverage area of the jet. However, it may further deform and pitted the regions which were initially yielded.

It is interesting to discuss about the fracture mode of the eroded surfaces for both materials. The fracture surfaces were carefully examined. For the stainless steel 304 as shown in [Fig. 5-28](#) (a), the erosion mode involves a highly ductile fracture mechanism as indicated by the appearance of the fracture surface to be dull and fibrous. The observed mode of erosion agrees with that reported previously in the cavitation erosion test of a similar material [127]. On the other hand, all the eroded specimens of the carbon steel 1045 showed a mixture of brittle–ductile erosion mode. A typical fracture surface is shown in [Fig. 5-28](#) (b). A brittle fracture region can be clearly seen as indicated by nearly flat surfaces with river patterns typical of cleavage fracture. This happens since the material consists of both ferrite and pearlite phases. It is suggested that pearlitic flaws are responsible as cleavage initiators [132]. The cementite plates of a pearlitic colony are broken in two when they cannot accommodate the slip deformation of ferrite due to their much higher

stiffness. As a result, the slip proceeds inside the pearlitic colony and act as a void nucleation mechanism for the discontinuities produced by the breakage of cementite. Finally, the voids grow assisted by plastic deformation and become pearlitic flaws to trigger the cleavage damage. Since pearlite is randomly distributed within the microstructure, therefore, the cleavage induced by such a constituent in these microstructures must also be a random phenomenon [133]. Furthermore, ferritic steels are sensitive to the strain rate due to its body centred cubic (BCC) lattice crystal structure [127]. The waterjet impingement produces high strain rates thus resulting in rapid brittle fracture along both transgranular and intergranular paths for ferritic-pearlitic steel as the material removal mechanism. Therefore, the erosion mechanism shows a predominant mode of brittle fracture. Likewise, Heathcock et al. [127] noticed the mode of material removal of the sample in the fully ferritic steel was almost entirely by the brittle fracture while for the samples in the duplex state, the erosion mechanism showed an increasing proportion of ductile fracture.

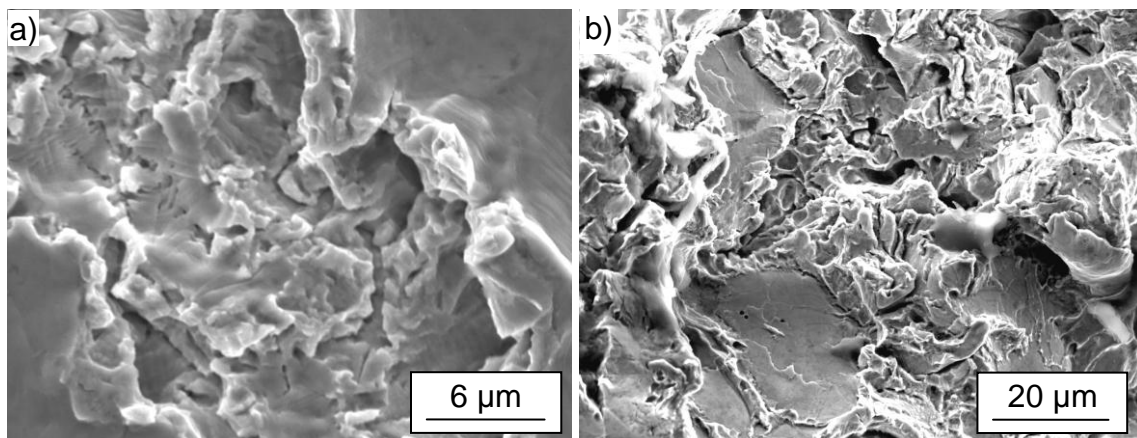


Fig. 5-28: The typical fracture surfaces showing, a) a ductile erosion mode in stainless steel 304, and b) a ductile-brittle erosion mode in carbon steel 1045

It is interesting to note that the erosion under waterjet impingement is somehow like a fatigue process especially with a higher number of jet passes. The erosion does not occur in a single impact; rather, it is produced by multiple impacts and assumed to be cumulative as a form of fatigue failure [128]. Furthermore, Richman and McNaughton [125] found good correlations between material removal rates in a cavitation erosion process and cyclic deformation parameters. They concluded that it was a strong indication that the damage in cavitation erosion was a fatigue process. As the bubbles collapse incessantly and randomly in the cavitation process, the impact stress thus exerting on the material surface can be considered to act in a way very

similar to that of low cycle strain fatigue [122]. In other word, at low impact energy, the average stress may be too low to cause general fractures, but some deformation is produced by each impact in regions of stress concentration [57]. The amount of deformation is accumulated and after certain number of impacts the fractures can be detected. Together with the effect of jet outward flow, striation marks can be observed especially at the rims of the impact craters as shown in [Fig. 5-29](#). Kamkar et al. [134] suggested that the striation marks confirm the transgranular nature of crack propagation mechanism. It indicates the intrinsic cyclic damaging mechanism associated with water droplets impingement erosion.

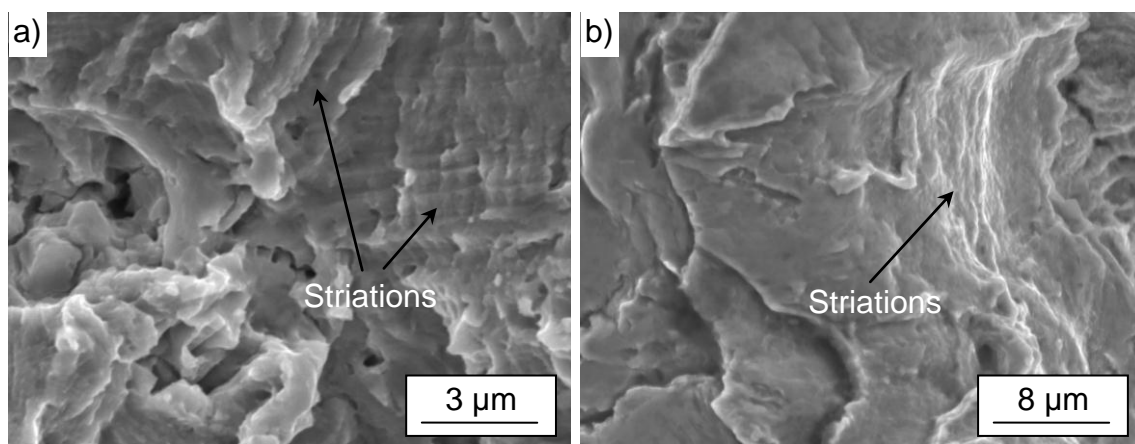


Fig. 5-29: Striation marks indicating cyclic ductile propagation mode of, a) stainless steel 304, and b) carbon steel 1045

In order to get further information about the grain erosion, some of the eroded surfaces of the carbon steel 1045 were mildly etched for about 15 seconds with 3% Nital. The SEM images of etched specimen in the middle and at the edge of erosion track are shown in [Fig. 5-30](#) (a) and (b), respectively. It is clear that the water impact produces deformation in the grains. However, the cracks are more concentrated at the ferritic-pearlitic grain boundaries as indicated as bold black arrows in [Fig. 5-30](#) (a) and (b). Also, it can be noticed that some cracks also occur within the ferrite grains. With further water impact, damage continues by a tunnelling mechanism until complete ferrite grains are removed thus leaving the harder pearlite grains [123]. With even further water impact, tunnelling is extensive enough to remove the surface pearlite colonies thus leaving a completely eroded surface.

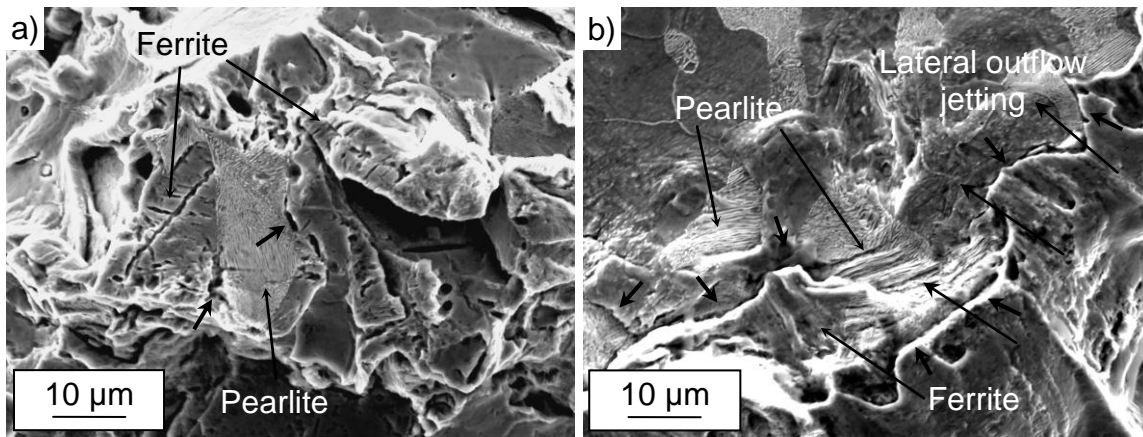


Fig. 5-30: a) uneroded grains in the middle of erosion track, and b) deformed grains at the edge of erosion track

It is also interesting to examine the structure underneath the eroded surface. The treated specimens were cross-sectioned and mounted. The specimens were sectioned randomly over the erosion tracks. Only the treated surfaces that show visible erosion with respects to the initial and evolved damage are discussed here. Examples of early cross-sectional damage of the eroded surface are shown in [Fig. 5-31](#). The initial damage characteristics show small and isolated pockets of erosion with some cracks beneath it as shown in [Fig. 5-31](#) (a). The surface cracks seem to propagate within the grains (i.e. ferrite grains). Also, there exist sub-surface transgranular cracks as indicated as white arrows in [Fig. 5-31](#) (a) which are considered as simply nucleated and not as the result of crack propagation in the out-of-plane direction [134]. However, it is also possible that the cracks as indicated as white arrows might have direct contact to the eroded area in another cross section. Since ferrite is the weaker phase, more surface and sub-surface cracks were identified to originate within the ferrite than pearlite grains. However, the major damage occurred at the grain boundaries. [Fig. 5-31](#) (b) was captured on the surface treated with the highest jet passes but at the lowest pressure of 100 MPa. Although the surface was treated with repeated water impacts, however, it experienced very little erosion. The surface can be considered in the early stage of damage since the pressure used is below the threshold limit.

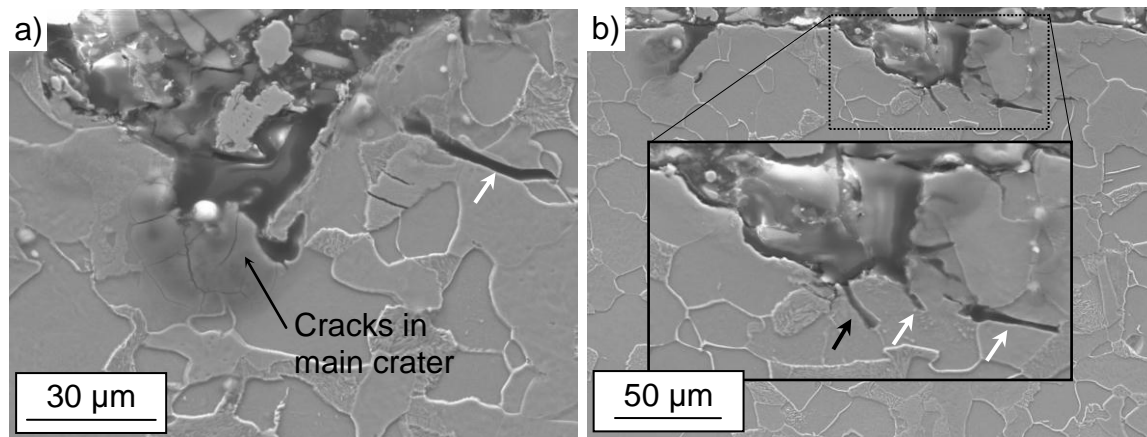


Fig. 5-31: Cross-sectioned images of erosion tracks taken from figures, a) Fig. 5-15 (a), and b) Fig. 5-13 (c)

Additionally, more cross-sectional images were captured at different erosion tracks as shown in [Fig. 5-32](#). The damage features at these locations show somehow the typical evolved damage characteristics under the waterjet treatment. Overall, the cross-sectional views show a similar damage characteristic as discussed above where the erosion tracks are deeper and wider for the specimens treated at a higher jet passes and higher pressure. The cross-sectional views of the erosion tracks treated with different jet passes are shown in [Fig. 5-32](#) (a) and (b). Increasing the number of jet passes, the erosion tracks were widened and deepened as shown in [Fig. 5-32](#) (a) with the width and depth of about 480 and 60 µm respectively. Also, there exist two main craters which are separated by unbroken fragments as indicated in the inset of [Fig. 5-32](#) (a). A major portion of the unbroken fragments are made up of pearlite grains since they appear to be a more resistant constituent and less prone to be damaged by the cavitation erosion process [117]. With further jet passes, the unbroken fragments will probably be removed because cracks propagate beneath them in ferrite grains or at grain boundaries and the craters be joined thus forming a larger crater. This can be seen in the erosion track treated at the highest jet passes with a width and depth about 750 µm and 125 µm, respectively, as indicated in [Fig. 5-32](#) (b). A further examination of the damage features as indicated in the inset of [Fig. 5-32](#) (b) shows various damage mechanisms including cracks along the grain boundaries (indicated black arrow) as well as within the grains (indicated white arrows). However, the pictures seem to suggest that the damage is concentrated along the grain boundaries. As damage progresses, the primary ferrites were eroded before the pearlite. This comes as no surprise since the grain boundaries are zones

of weakness and they act as initiation sites in the damage of the primary ferrite phase in the hypoeutectoid steels [123].

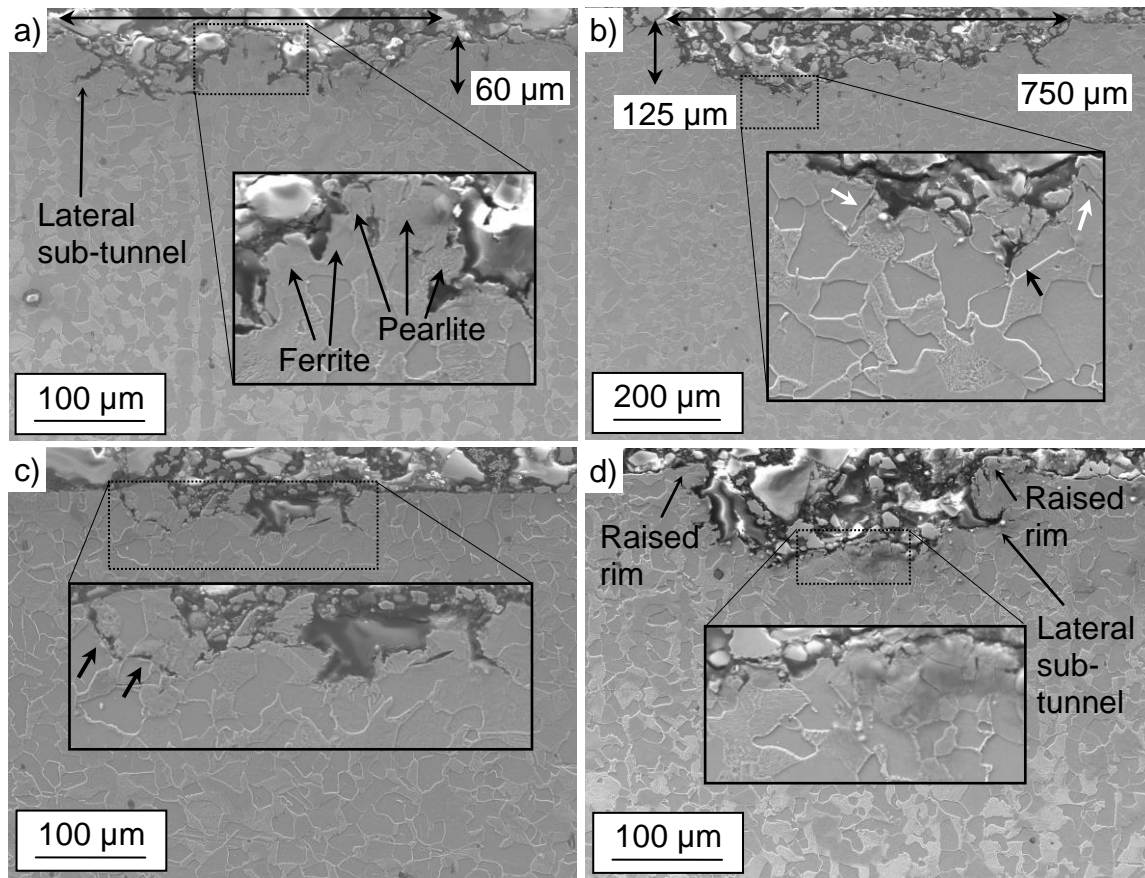


Fig. 5-32: Cross-sectioned images of erosion tracks taken from figures, a) Fig. 5-15 (b), b) Fig. 5-15 (c), c) Fig. 5-14 (b), and d) Fig. 5-14 (c)

Fig. 5-32 (c) shows an example of sub-surface cracks merging together and leads to the detachment of a larger fragment of the material. It is indicated as black arrows in the inset of Fig. 5-32 (c). It seems that the cracks mainly propagated along the grain boundaries although some propagated through the grains. With further water impacts, the cracks or the tunnels are extensive enough to remove the whole fragment of the material. The tunnelling mechanism thus produces more intense pressures within them leading to damage propagation on a larger scale than unmerged cracks [134]. Fig. 5-32 (d) shows the typical effect of the jet lateral flow. The shearing force from the lateral flow raises the circumferential rim as shown in Fig. 5-32 (d). Also, the shearing force creates lateral cracks and sub-tunnels within the rim. In the subsequent jet passes, the shearing force may further raise the rim as well as propagate the cracks and sub-tunnels. Since the sub-tunnels run parallel to

the eroded surface, further propagation of the cracks and tunnels may lead to the removal of sizeable fragments of the rims [134].

It is also interesting to examine the structure underneath the eroded surface of stainless steel 304. Again, the specimens were sectioned randomly over the erosion tracks. Only the treated surfaces that show visible erosion will be discussed here. The cross-sectional microstructures of the eroded surface of stainless steel 304 are shown in [Fig. 5-33](#). As explained above, the high erosion resistance of this alloy is attributed to its deformation characteristics. The material removal initiates at, and propagates from, protruding slip bands and/or twin boundary steps and grain boundaries [127]. These various damage initiations can clearly be seen from [Fig. 5-33](#) (a). However, in most cases, the surface erosion was observed to initiate and propagate from protruding slip bands as shown in [Fig. 5-33](#) (b). This is in contrast with Kwok et al. [135] who found that the cavitation erosion of a similar material was first initiated at the twin boundaries rather than at the grain boundaries. Anyway, it is to note that the cracks initiate and propagate in a three-dimensional direction and the cross-sectional views only give partial information. Nonetheless, the non-random feature of the crack distribution gives a strong trend in how the microstructure may influence the crack propagation and also the induced erosion.

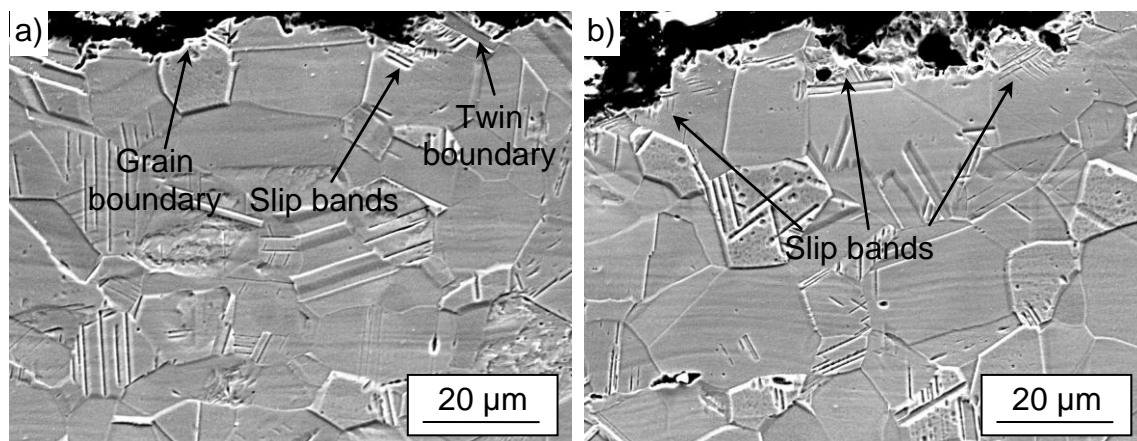


Fig. 5-33: Cross-sectioned images of erosion tracks of stainless steel 304 showing, a) various damage initiations, and b) most damage initiated from slip bands

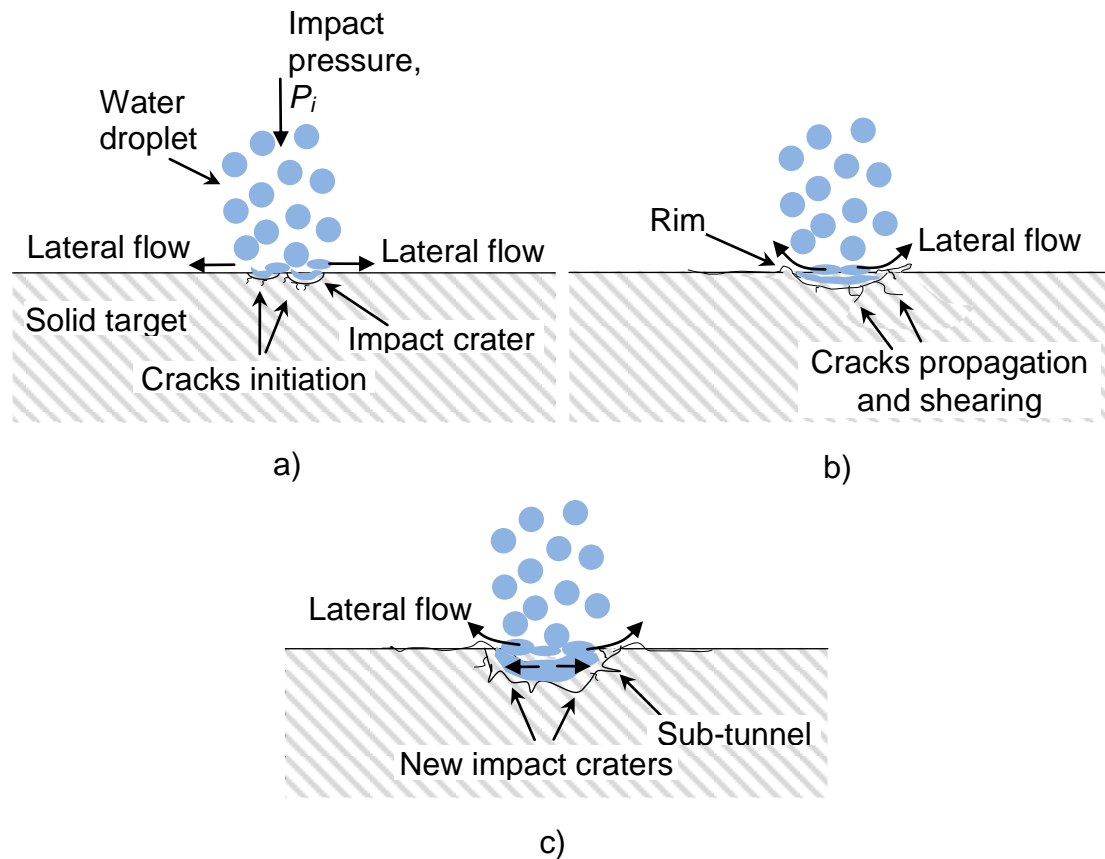


Fig. 5-34: Overview of water erosion mechanism under repeated impacts, a) during initial jet passes, small central depression craters are created as well cracks and fractures due to impact pressure and lateral flow of droplets, b) during subsequent jet passes, more fractures happen by pitting and ploughing action in which the previously formed craters may combine to form a larger crater, c) with even more jet passes, more fractures can be expected hence introducing new craters as well as deepening the erosion craters

It is obvious that the erosion mechanism of metals particularly plain carbon steel under multiple passes treatment of waterjet peening is very complex. It consists of various stages of material removal mechanisms including the deformation of the impact crater, the initiation and propagation of cracks with possible tunnelling to remove large fragments of the material. These stages of material removal mechanism can be summarized as in [Fig. 5-34](#). In general, during earlier jet passes, the high impact pressure of water droplets produces many small central depression craters in the material surface as illustrated in [Fig. 5-34](#) (a). As a result, the material beneath it experiences a larger plastic deformation as well as some initiation of cracks. Later, the lateral outward flow of the droplets may result in local shear fractures in the material surface by a pitting action. In the subsequent jet passes, old cracks are further propagated and also new cracks are initiated. The cracks may

easily propagate to form a network of cracks thus fracturing the grains and/or sub-grains. Also, the circumferential rims on the edges of the erosion track were plastically deformed and slightly raised by a ploughing action from the droplet outward flow. As a result, a bigger crater is developed to form uniform erosion with full removal of materials over the surface as shown in [Fig. 5-34 \(b\)](#). If the eroded surface is subjected to further jet passes, more fractures can be expected hence introducing new craters as well as deepening the main erosion craters as shown in [Fig. 5-34 \(c\)](#).

As a summary, the material removal mechanism occurs at two levels, i.e. initial damage and evolved damage [81]. An example of initial damage surface is shown in [Fig. 5-35](#). Impact zone occurs when high-frequent impact of water strikes onto the solid surface. High impact of water droplet creates compressible stresses, which act on both the solid surface and the water droplet forming a shock envelope [55]. The liquid behind the envelope is compressed and the solid surface beneath this area is subjected to a high pressure, which consequently tends to deform the target material. Due to repeated impact of water droplets during peening, the contact wall was subjected to severe shear force because of the outward flow (i.e., lateral jetting) of water across the surface [136]. The shear stresses exerted by the radial flow of water from subsequent impact breaks the solid particles. Hence, cracking and eroding of solid particles happen particularly in the impact zone and its surrounding area. The cracks in the impact zone join together and results in material removal and the formation of micropits [81].

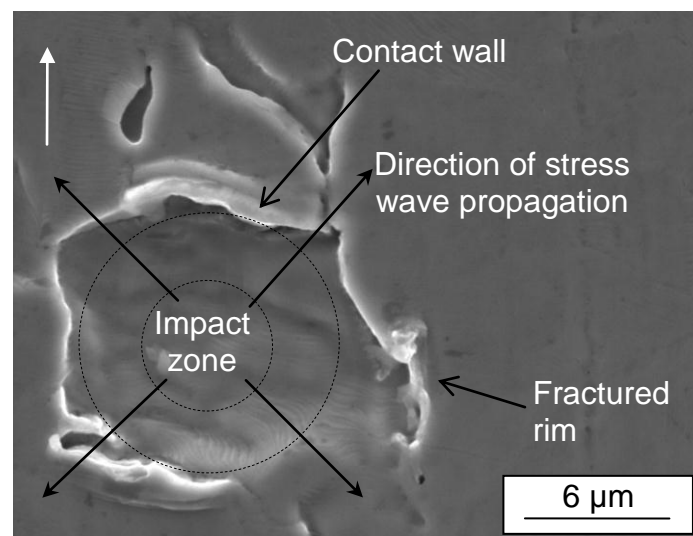


Fig. 5-35: An example of initial damage surface

The cracks and fractures of material at later damage stage i.e. evolved damage, are shown in [Fig. 5-36](#). The material has a grain size of approximately between 10 to 40 μm . It can be speculated that the cracks and fractures occur along the grain boundaries as well as inside the grains. This phenomenon is more noticeable during peening with a higher number of jet passes. Also as shown in previous surface microstructures, materials were removed in a higher quantity during treatment with a higher pressure or a lower feedrate. It can be concluded that at a higher jet passes and pressure and also a lower feedrate, the energy was high enough to create tremendous fractures and more continual erosion along the grain boundaries and within the grains.

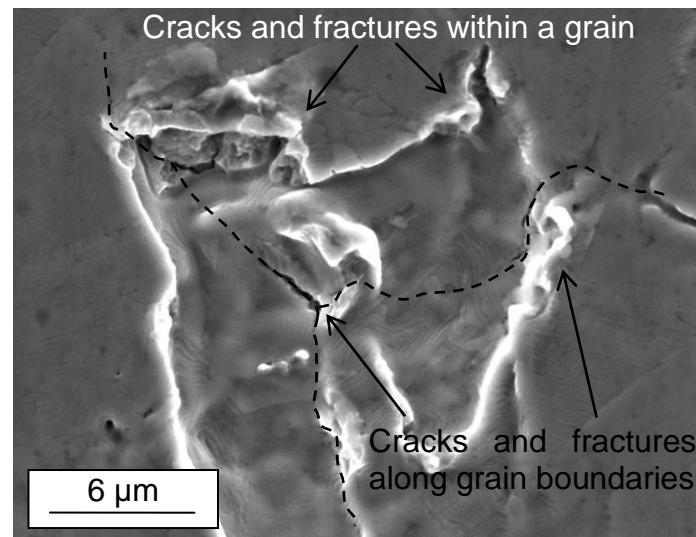


Fig. 5-36: An example of evolved damage surface

5.3 Effect of waterjet peening on the sub-surface

5.3.1 Hardness

The subsurface hardness was measured on the cross-sections of the specimens at different depths starting from 20 μm beneath the jet impinged surface until a far distance of 1000 μm . The result for the effect of the different number of passes on surface hardening is shown in [Fig. 5-37](#). For stainless steel 304, there are generally significant changes in hardness values up to a depth of approximately 100 μm with an exception of a specimen treated with the lowest number of passes where the hardening layer depth is less than 100 μm . However, based on outlying lines of power graphs, the hardening layer may extend slightly up to a depth of 150 μm

especially in the case of the highest number of passes (i.e. 6 passes). The average maximum hardnesses were recorded to be 258, 263 and 280 HV_{0.01} for 2, 4 and 6 number of passes respectively. These constitute to an increase in hardness of about 12, 14 and 22% respectively with respect to the base material which has an average hardness of approximately 230 HV_{0.01}.

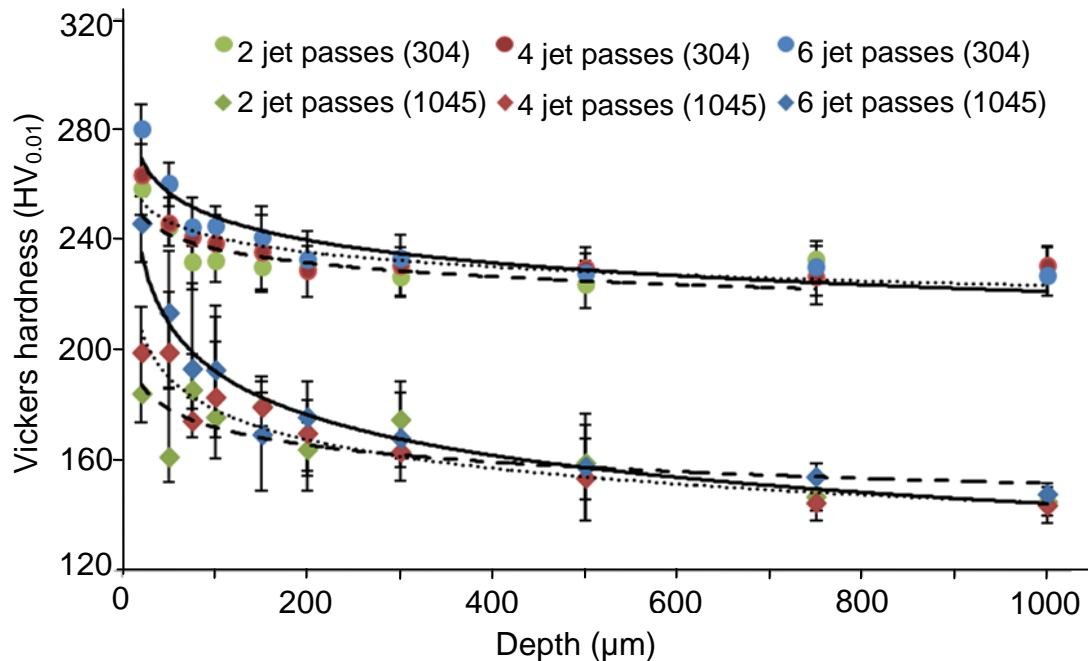


Fig. 5-37: Effect of number of passes on Vickers hardness as a function of depth below eroded surface at a pressure of 200 MPa, a feedrate of 2000 mm/min and a standoff distance of 30 mm.

While for carbon steel 1045, overall there are significant changes in hardness values up to a depth of approximately 300 μm. Beyond that, the hardness is about the same as the material's original hardness of about 145 HV_{0.01}. Generally, it shows a very similar trend as previous case where the hardness decreases gradually from the surface. Also, the specimen treated with a higher jet passes displayed a higher increase in hardness as shown in [Fig. 5-37](#). The average maximum hardnesses were recorded to be 184, 199 and 246 HV_{0.01} for 2, 4 and 6 number of passes respectively. These constitute to an increase in hardness of about 27, 37 and 70% respectively with respect to the hardness of base material. This clearly shows that treating the surface with the higher number of passes produces a higher increase of hardness as well as a deeper hardening layer. Obviously, the increase in hardness and thickness of hardening layer is the result of repeated water droplet impacts on the material surface after the multiple jet passes treatment.

It is interesting to relate the effect of work hardening in the material erosion resistance. Obviously, the surface has been hardened after early jet passes as discussed above. This increase in hardness may contribute to the initial erosion resistance of the material. Duraiselvam et al. [137] suggested that after long exposure periods, a material loss could be promoted due to the removal of the work hardened layer by brittle fracture. As a result, the erosion increased with an increase in the number of jet passes which results in a higher exposure time as discussed above. The surface hardness had also increased with an increase in the number of jet passes. However, it is believed that the hardened layer was not completely removed at the subsequent jet passes. Furthermore, a new hardened layer was introduced and resulted in a higher increase in the surface hardness.

The effect of feedrate on Vickers hardness as a function of depth below eroded surface is shown in [Fig. 5-38](#). Generally, a similar trend is also noticed with hardness decreasing gradually from the surface. Also, a higher hardness gradient is found in a specimen treated with a lower feedrate. For stainless steel 304, the data shows that there is an increase in average maximum hardness of about 27, 14 and 12% for feedrates of 1000, 2000 and 3000 mm/min respectively as compared to the base material. In contrast, the average increases of maximum hardness are about 50, 37 and 22 % respectively for carbon steel 1045. The hardness gradient has a similar depth profile like the previous ones. The hardness gradient for the specimens treated with the slowest feedrate of 1000 mm/min shows higher depth of about 300 and 400 μm for stainless steel 304 and carbon steel 1045 respectively. Interestingly for stainless steel 304, samples treated with 2000 and 3000 mm/min show a similar hardness gradient trend in which their graph lines are almost overlapping. As discussed above, the feedrate of over 2000 mm/min is beyond its threshold limit where its effectiveness in treating the material is very much reduced. As a result, the hardness profiles do not differ significantly between feedrates of 2000 and 3000 mm/min. In addition, decreasing the traverse rate allows more water molecules to impinge on the surface, therefore, introducing higher amount of compressive residual stresses and leading to a higher hardness.

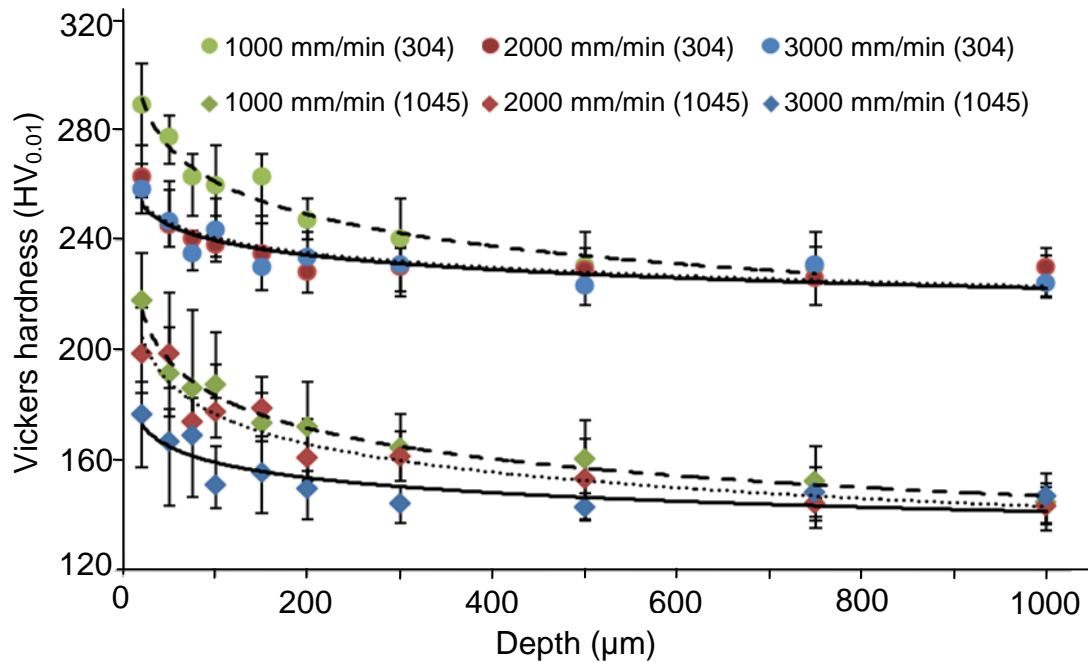


Fig. 5-38: Effect of feedrate on Vickers hardness as a function of depth below eroded surface at a pressure of 200 MPa, a number of jet passes of 4 and a standoff distance of 30 mm.

The effect of pressure on Vickers hardness as a function of depth below eroded surface is shown in [Fig. 5-39](#). Again, for both materials, a similar trend with hardness decreasing gradually from the surface is noticed. Furthermore, a higher hardness gradient is found in a specimen treated with a higher pressure. For stainless steel 304, the graph shows that there is an increase in average maximum hardness of about 16, 27 and 31% for pressures of 100, 200 and 300 MPa respectively as compared to the base material. The depth of the hardened layer is extended up to 250 μm . While, for carbon steel 1045, there is an increase in hardness up to a depth of 300 μm . The average increases in maximum hardness are about 21, 35 and 70% for pressures of 100, 200 and 300 MPa respectively as compared to the base material. Likewise, the specimens treated with a higher pressure also displayed a higher increase in hardness. Possibly, a higher pressure generates a higher kinetic energy of water molecules thus inducing a higher magnitude of residual stress over the surface [74]. Interestingly for carbon steel 1045, the hardness profiles do not differ significantly between the specimens treated with the lowest pressure and the original specimen. Perhaps as discussed above, at the lowest pressure, the water droplets do not carry enough impact energy to plastically deform the material at the surface in order to increase its hardness.

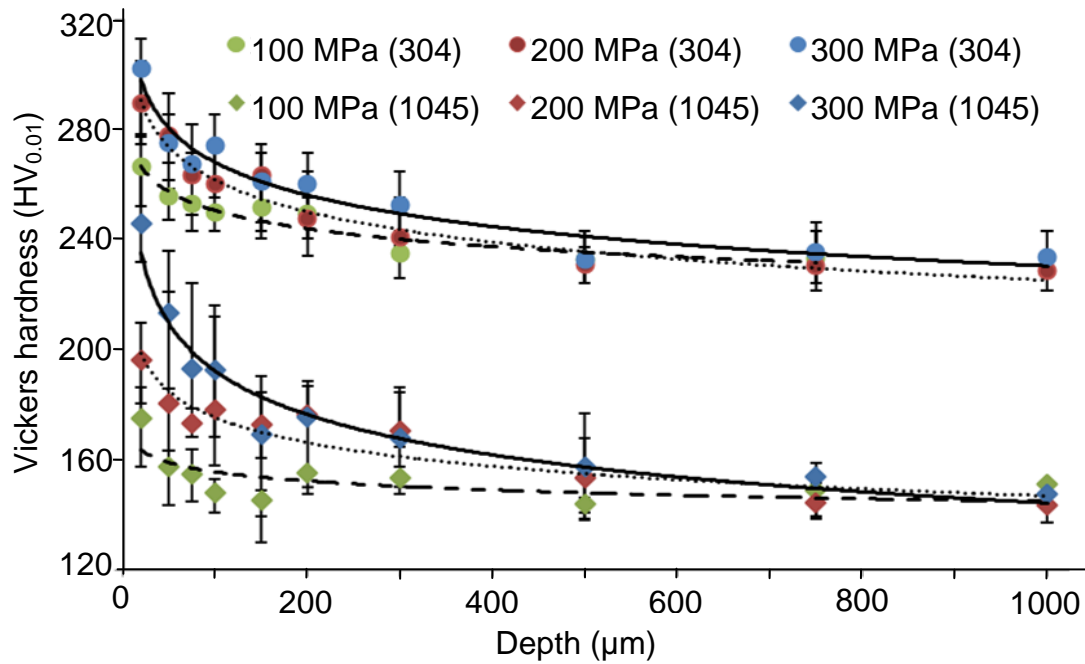


Fig. 5-39: Effect of pressure on Vickers hardness as a function of depth below eroded surface at a feedrate of 2000 mm/min, a number of jet passes of 4 and a standoff distance of 30 mm.

The effect of standoff distance on Vickers hardness as a function of depth below eroded surface is shown in Fig. 5-40. A similar trend with hardness decreasing gradually from the surface can be noticed. For stainless steel 304, there is an increase in average maximum hardness of about 13, 21 and 18% for standoff distances of 60, 90 and 120 mm respectively as compared to the base material. The depth of hardened layer is less than 200 μm . While, for carbon steel 1045, there is an increase in hardness up to a depth of 300 μm . The average increases in maximum hardness are about 34, 60 and 37% for standoff distances of 60, 90 and 120 mm respectively as compared to the base material. For both specimens, a standoff distance of 90 mm resulted in the highest increase in hardness. As expected, this standoff distance is believed to carry the highest impact pressure thus deforming the surface the most.

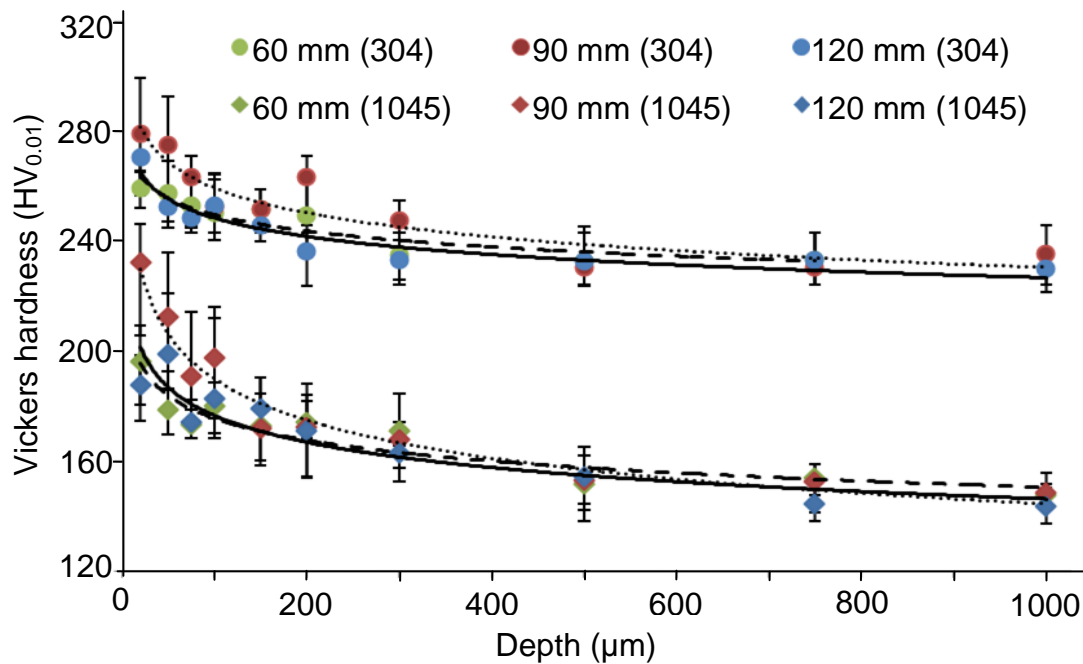


Fig. 5-40: Effect of standoff distance on Vickers hardness as a function of depth below eroded surface at a pressure of 200 MPa, a feedrate of 2000 mm/min and a number of jet passes of 4.

It is interesting to discuss the percentage increase of hardness for both materials. It is obvious that within the same treatment parameters, the carbon steel 1045 generally shows a higher percentage of hardness increase than stainless steel 304. The maximum percentage increase of the carbon steel 1045 was 70% meanwhile the stainless steel 304 only produced a maximum hardness increase of 31%. This is possibly due to the different hardness values of the original surface. As mentioned above, the average original hardness of the stainless steel 304 is significantly higher than the carbon steel 1045 (i.e. 230 HV_{0.01} versus 145 HV_{0.01}). Since the latter is softer than the former, amount of plastic deformation in this material is larger compared to the stainless steel 304 [138]. As a result, this induces more cold work giving in a higher hardness increase compared to its core hardness. In other words, according to Nikitin and Besel [139], the hard surface regions have lower plastic flow (i.e. less dislocation movement). As a result, the work hardening state of the surfaces shows only little changes. Therefore, the hard surface experiences very little plastic deformation thus limiting the increase in hardness upon the impact of waterjet.

Another interesting point to discuss is about the hardness increase variation for both materials. It can be seen from [Fig. 5-37](#) to [Fig. 5-40](#) that the hardness measurements of carbon steel 1045 show a wide margin of errors. While, the stainless steel 304

shows a relatively small margin of errors. It seems that the changes in the microstructures (residual stress, work hardening) of the stainless steel 304 are more stable thus leading to a small variation in hardness measurements. As reported by Nikitin and Besel [139], a hard microstructure results in a stable residual state. As discussed above, the austenite phase in the stainless steel 304 may transform into the martensite phase under the work hardening process [87, 88, 89]. According to Lee et al. [19], for the carbon steel 1045, the cementite phase in the pearlitic microstructure is spheroidized and dissolved into the ferrite thus refining the ferrite grains. It is known that amongst them, the martensite is the hardest phases [140]. Therefore, it is possible that the stainless steel 304 achieves a stable work hardening state due to a harder martensite phase. Another possible reason of high variation in hardness measurement of carbon steel 1045 is due to its multiple phases microstructure. The ferrite phase is softer than pearlite/ spheroidite phase [141]. Therefore, the hardness measurement on different phases of carbon steel 1045 microstructures (i.e. ferrite, pearlite/ spheroidite) may result in quite significant variation of hardness values especially using a small load of Vickers indenter. Similarly, Autenrieth et al. [142] found a wide range of scatter in the hardness data during a micro cutting process of the same material which was attributed to the influence of variations in the phase composition and different grain orientations within the sampled volume of the material.

Furthermore, it is also interesting to compare the performance of the same materials but treated with other peening processes. In shot peening of austenitic stainless steel S30432, there was an increase in hardness of more than 50% of the substrates' value with a depth of hardening layer of 250 μm [143]. While, in hammer peening of stainless steel 304L, the hardness increased about 78% of the original hardness with a depth of hardening layer of 500 μm [144]. Whereas, in shot peening of steel with carbon content of 0.45%, the surface hardness increased about 76% after the treatment [19]. While, in laser shock peening of AISI 1045 steel, the hardness increased by more than double of the original hardness with a hardening layer depth of 100 – 150 μm [145]. It seems that from literatures, carbon steel 1045 experienced a higher percentage of hardness increase than stainless steel 304 under peening processes. This is in agreement with the present study where carbon steel 1045 displayed a higher degree of hardness increase than stainless steel 304. However,

the hardness increase in both materials used in the present study is relatively lower than other peening processes.

5.3.2 Microstructures

The subsurface microstructures were acquired using scanning electron microscope (SEM) from cross-sectioned specimens of stainless steel 304. The cross-sectional microstructures were captured up to a depth of approximately 350 μm . Additionally, the magnified pictures at just below the eroded surface ($\approx 50 \mu\text{m}$), at a depth approximately 150 μm and at a depth approximately 250 μm were also captured. These depths were selected based on the analysis of hardness profiles as presented above. The locations of magnified pictures were selected randomly as to show appropriate features of grains as well as to avoid some artifacts in the microstructures.

The subsurface morphologies of peened samples for the different numbers of jet passes are shown in [Fig. 5-41](#). Cross-sectional microstructures of all samples indicate that the substrate experienced a certain degree of plastic deformation. The density and quantity of deformed grains decrease gradually with increasing layer depth from the treated surface. It is evidenced as shown in the top inset pictures where more grains suffered significant deformation through different systems of slip bands as compared to the middle and bottom inset pictures. Similar observation was made in shot peening of the same material. The outmost layer of the substrate suffered severe deformation and the grain boundary became obscure [34]. Amounts of slip bands are more abundant and severe in the specimen treated with the higher number of passes as illustrated in [Fig. 5-41](#) (c) as compared to the specimens treated with a lower jet passes as shown in [Fig. 5-41](#) (a) and (b). Also the deformation of grains is extended up to a depth of 150 μm as shown in the middle inset picture with a small amount of slip bands. There is no noticeable deformation beyond that depth since there is an absence of slip bands as shown in the bottom inset picture. This is in agreement with the subsurface hardness measurement which show the gradient of hardness up to a depth of 150 μm for the specimen treated with 6 jet passes. The specimens treated with 2 and 4 jet passes show a significant deformation only just below the eroded surfaces as shown in the top inset pictures of [Fig. 5-41](#) (a) and (b) respectively with little slip bands. This shows that the thickness

of hardened layer is limited to just below the eroded surface when it is treated with lower jet passes.

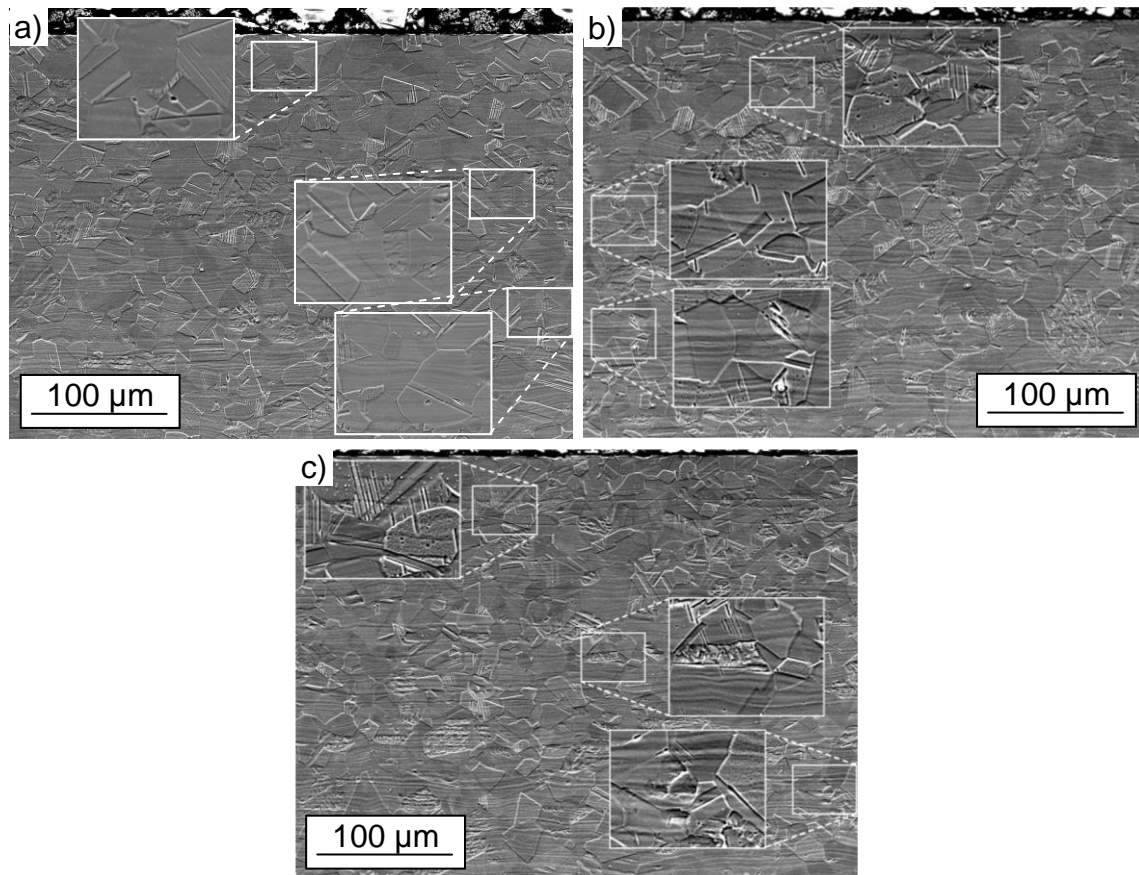


Fig. 5-41: Subsurface microstructures for different number of jet passes at a pressure of 200 MPa, a feedrate of 2000 mm/min and a standoff distance of 30 mm, a) 2 passes, b) 4 passes and c) 6 passes, (The insets show the magnified pictures at just below the eroded surface (top), at a depth of approximately 150 μm (middle) and at a depth approximately of 250 μm (bottom))

Subsurface microstructures for different feedrates are shown in [Fig. 5-42](#). Basically the microstructures show a similar pattern where slip bands can be clearly seen in the deformed grains especially near the eroded surface as shown in the top insets of Figure 15. However, some slip bands still can be seen in the deformed grains away from the surface in the specimen treated with the lowest feedrate as shown in the [Fig. 5-42 \(a\)](#). This is just to confirm the earlier hardness profile analysis where the hardness gradient is extended up to 250-350 μm for the specimen treated with the lowest feedrate. In contrast, there is an absence of slip bands in the grains away from the surface in the specimens treated with feedrates of 2000 and 3000 mm/min as illustrated in [Fig. 5-42 \(b\) and \(c\)](#) respectively. Again, this shows that the

deformation of grains is limited up to 100 μm close to the surface as discussed above where the depth of hardening layers for those specimens is about 100 μm . Overall, this is in agreement with Ju and Han [45] in water cavitation peening (WCP) of pure titanium where they found the density and quantity of deformed grains increase gradually with increasing WCP duration and decrease gradually with increasing layer depth from the treated surface. It is to note that a higher feedrate implies smaller impingement duration of the waterjet on the same point of the specimen. Therefore, less deformed grains are found in the specimens treated with higher feedrates.

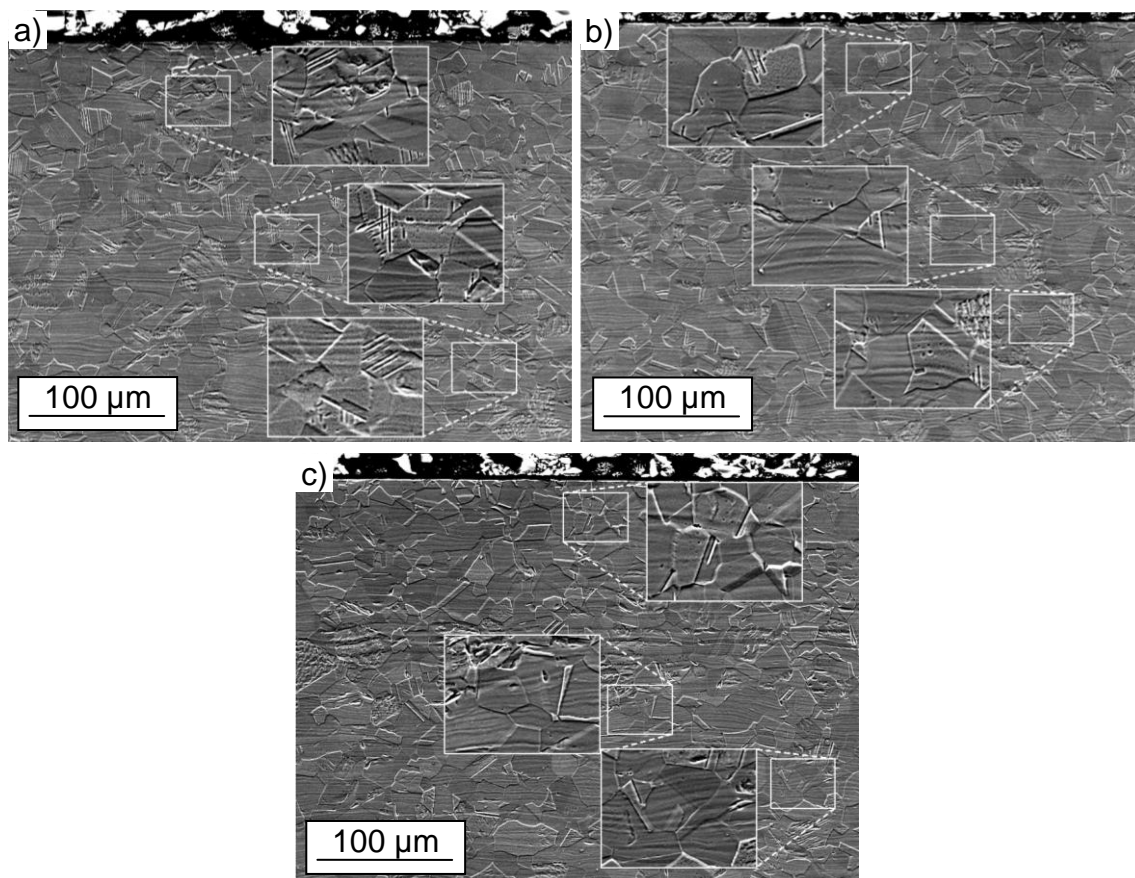


Fig. 5-42: Subsurface microstructures for different feedrates at a pressure of 200 MPa, a number of jet passes of 4 and a standoff distance of 30 mm, a) 1000 mm/min, b) 2000 mm/min and c) 3000 mm/min, (The insets show the magnified pictures at just below the eroded surface (top), at a depth of approximately 150 μm (middle) and at a depth of approximately 250 μm (bottom))

The subsurface morphologies of peened samples for the different pressures are shown in [Fig. 5-43](#). Cross-sectional microstructures of all samples indicate that the substrate experienced a certain degree of plastic deformation even up to a depth of 250 μm as shown in the bottom insets of [Fig. 5-43](#). Generally, this is in agreement

with the hardness gradient analysis above which shows the depth of hardening layer is extended up to 200 μm . Amounts of slip bands in the deformed grains are more abundant and severe in the specimen treated with the higher pressures as illustrated in [Fig. 5-43](#) (b) and (c) as compared to the specimens treated with a lower pressure as shown in [Fig. 5-43](#) (a).

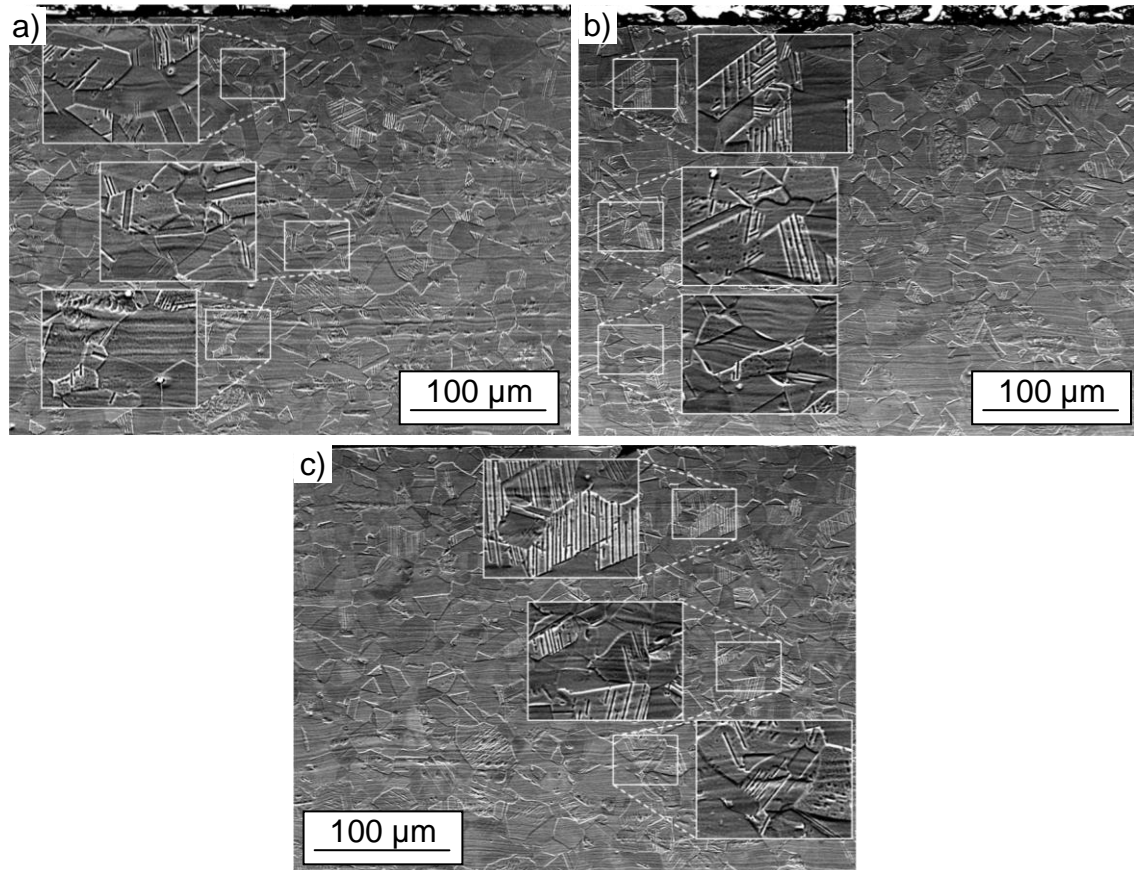


Fig. 5-43: Subsurface microstructures for different pressures at a feedrate of 2000 mm/min, a number of jet passes of 4 and a standoff distance of 30 mm, a) 100 MPa, b) 200 MPa and c) 300 MPa, (The insets show the magnified pictures at just below the eroded surface (top), at a depth of approximately 150 μm (middle) and at a depth of approximately 250 μm (bottom))

Also there is a considerable amount of slip bands in the deformed grains at a depth of 250 μm for the specimen treated with the highest pressure of 300 MPa as shown in the bottom inset picture of [Fig. 5-43](#) (c). Therefore, it can be speculated that the grains would be deformed beyond the depth of 250 μm . Moreover, as shown in [Fig. 5-39](#), the depth of hardening layer is extended up to 400 μm in the specimen treated with the highest pressure of 300 MPa. Again, this is due to the fact that a higher kinetic energy of water molecules at higher pressures induces higher amount

of compressive stresses hence plastically deforming the grains more and to a higher depth.

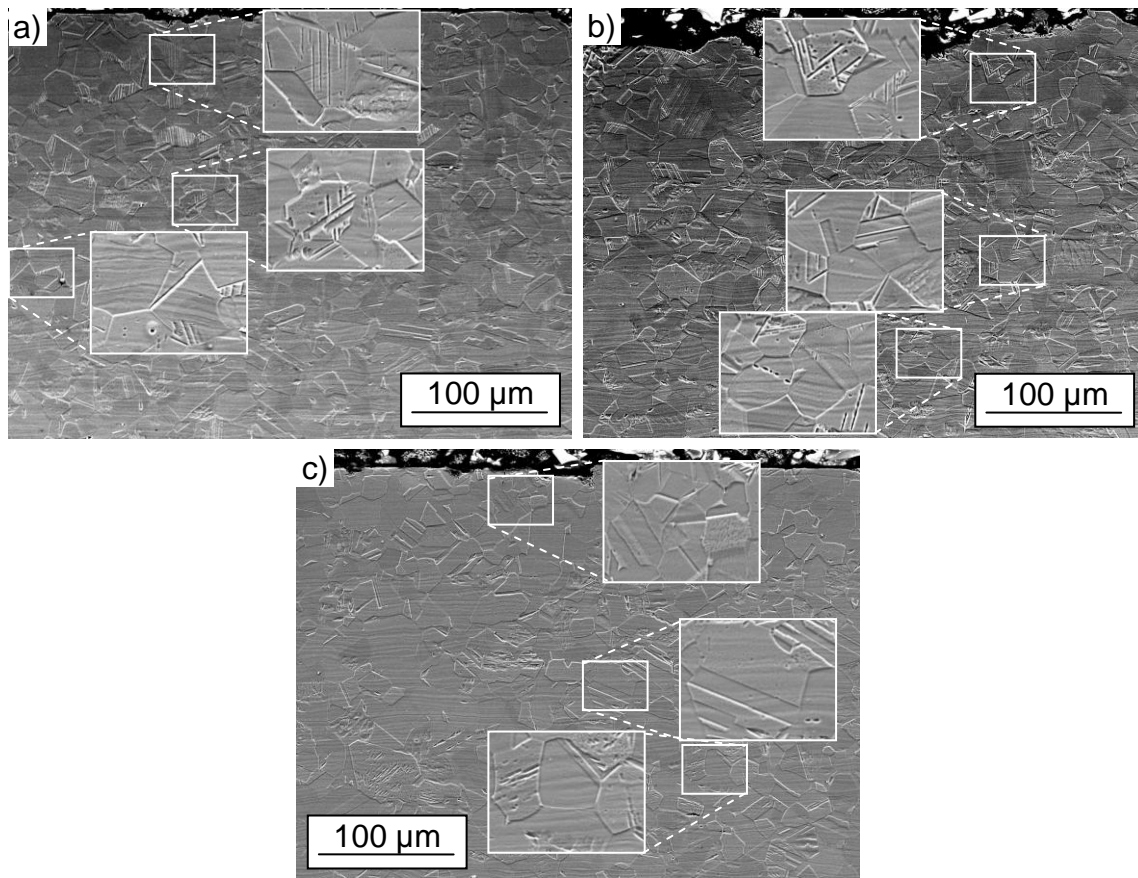


Fig. 5-44: Subsurface microstructures for different standoff distances at a pressure of 200 MPa, a feedrate of 2000 mm/min and a number of jet passes of 4, a) 60 mm, b) 90 mm and c) 120 mm, (The insets show the magnified pictures at just below the eroded surface (top), at a depth of approximately 150 μm (middle) and at a depth of approximately 250 μm (bottom))

The subsurface morphologies of peened samples for the different standoff distances are shown in [Fig. 5-44](#). Cross-sectional microstructures of the sample treated at a standoff distance of 90 mm indicate that the substrate experienced a certain degree of plastic deformation up to a depth of 250 μm as shown in [Fig. 5-44](#). This is somehow in agreement with the hardness gradient analysis above which shows the depth of hardening layer is extended beyond 200 μm . Also, amounts of slip bands in the deformed grains are more abundant and severe as compared to the specimens treated at standoff distances of 60 mm and 120 mm as illustrated in [Fig. 5-44](#) (a) and (c) respectively. This can be expected since the standoff distance of 90 mm resulted

in the highest increase in hardness thus plastically deforming the grains most and to a higher depth.

It is good to discuss about the changes in the microstructures of the carbon steel 1045. Unlike, the stainless steels which showed slipbands or twinings in the grains indicating the plastic deformation, a similar form of deformation cannot be seen in the carbon steels. Evidence of plastic deformation is hardly observed in the cross-sectional microstructures. Fig. 5-45 shows a typical cross-sectional view of the eroded surfaces captured using an optical microscope. It can be expected that the material experiences a certain degree of plastic deformation just below the eroded surface as shown in Fig. 5-45 (a). At the rim of the erosion crater, the grains are heavily plastically deformed due to the effect of the jet lateral outflow as indicated in Fig. 5-45 (b).

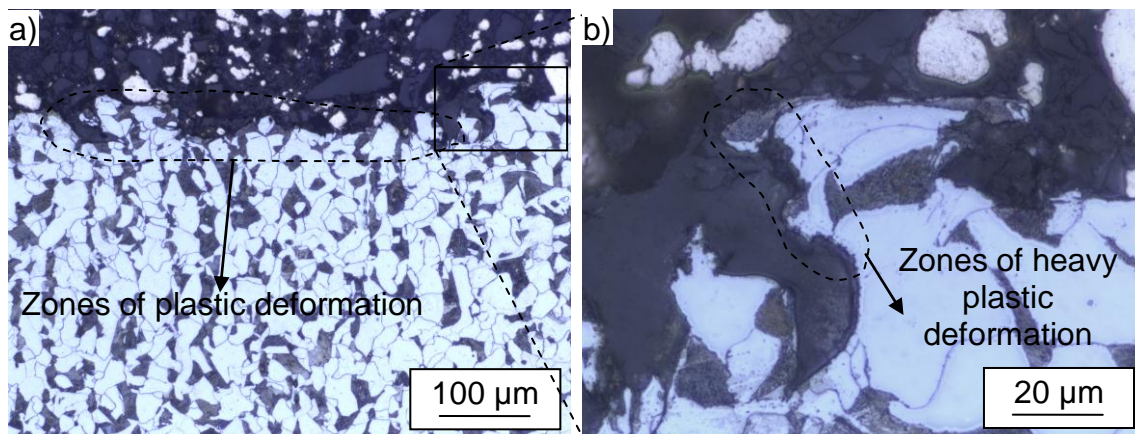


Fig. 5-45: a) typical eroded surface showing the plastic deformation zone, and b) enlarged image showing the zone of heavily plasticially deformed grains

The eroded surfaces were further characterized using a SEM. An example of plastically deformed grains is shown in Fig. 5-46. This image is randomly captured in one of the erosion craters. Due to the high pressure of the waterjet, the material experiences large plastic deformation especially in the main impact zones. As a result, some grains are distorted as shown in Fig. 5-46 (a). Upon a closer look as shown in Fig. 5-46 (b), part of the grains seems to be stretched to the sides. This possibly happens due to the jet lateral outflow which exerts high tensile stresses to the material surface. Of course, this happens after repeated impact of the water droplets onto the surface.

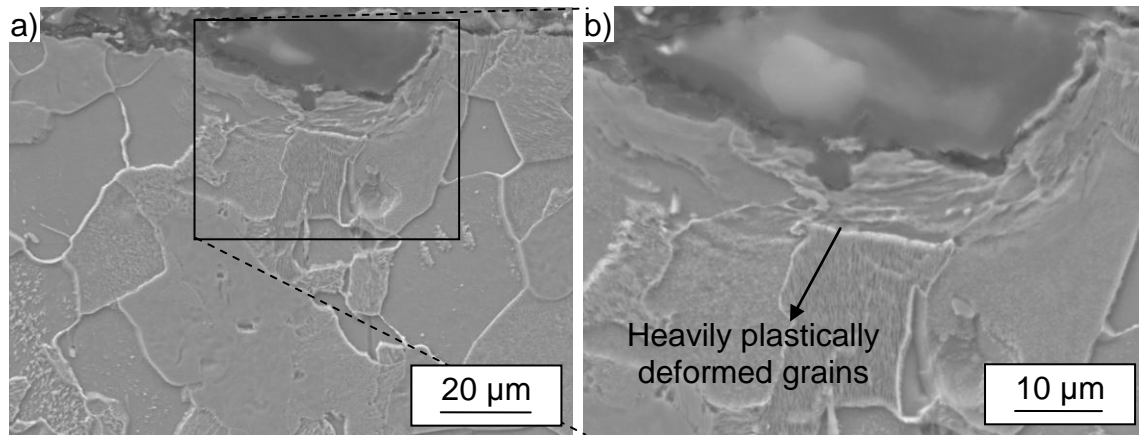


Fig. 5-46: a) typical eroded surface in the main impact crater, and b) enlarged image showing the zone of heavily plastically deformed grains

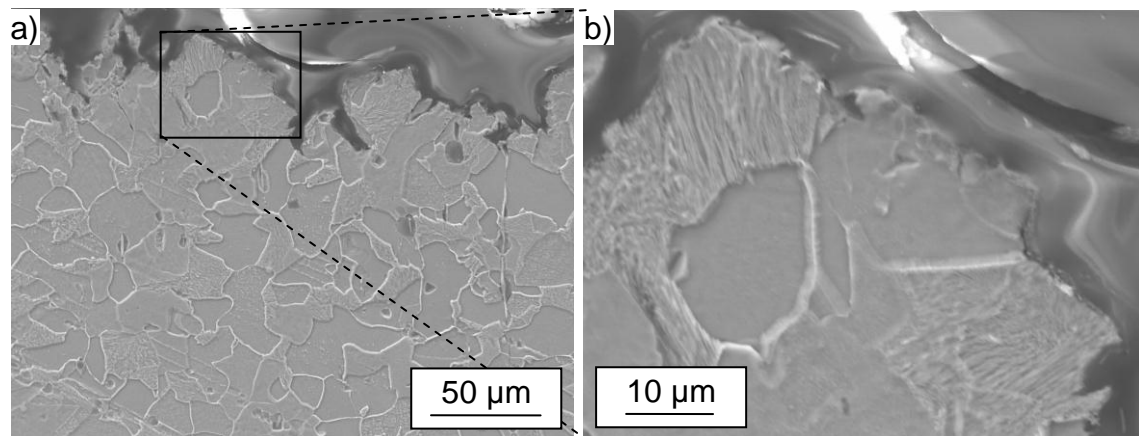


Fig. 5-47: a) typical eroded surface, and b) enlarged image showing a possible grain refinement zone

Other images of the eroded surface are shown in [Fig. 5-47](#). It is believed that the grains at the surface layer are heavily deformed due to the intensive plastic deformation as indicated in [Fig. 5-47](#) (a). However, from the image it is hard to tell the change in the microstructures of ferrite or pearlite in the carbon steel 1045. But, it is widely reported in the literatures that in this type of steel, there is a formation of nanocrystalline structures in the surface during severe plastic deformation [19, 146, 147, 148, 149]. [Fig. 5-47](#) (b) possibly shows an example of the zone where the grain refinement takes place. Of course, it is pretty much difficult to see the nanostructures using SEM. A transmission electron microscope (TEM) is commonly used to better understand the variation of the grain refinement. Unfortunately, in the present study, TEM has not been used due to some constraints. Perhaps, it would be used in the future research. However, the hardening mechanisms involving this alloy in other cold-working processes are discussed.

It is known that most nanocrystalline materials possess high strength and hardness [148]. Therefore, the mechanical properties of most material can be enhanced by refining their microstructures. It has been reported that the strengthening mechanism in peening processes such as shot peening is due to the work-hardening and the surface grain refinement [19, 147]. Grain refinement is regionally homogeneous and the grain size progressively increases with the distance from the peened surface [147, 148]. Zhou et al. [150] reported that the plastic deformation induces substantial grain refinement of both ferrite and cementite in a steel with spheroidal cementite. Ferrite grains are plastically deformed first in which most dislocations are found to be nucleated at the cementite/ ferrite interfaces. The refinement process of ferrite is significantly facilitated by the presence of dispersed cementite particles. The coarse-grained ferrite phase is subdivided by plenty of sub-grain boundaries and grain boundaries into submicron-sized grains [148]. Plastic deformation occurs in cementite particles through gliding of edge dislocations after the refinement of ferrite grains [150]. Due to accumulation of multiple gliding, the cementite refines into nano-sized cementite particles mixed within ferrite nano-grains in the top surface layer [150].

Zhou et al. [150] noticed a decreasing volume fraction of cementite with decreasing depth of in the top deformed layer thus indicating of dissolution of cementite induced by increasing plastic straining. Furthermore, in a shot peening process of carbon steels, Lee et al. [19] reported that cementite in the pearlite colony is spheroidized and dissolved into the ferrite under a very large plastic deformation. Initially, the cementite acts as an initiation site for dislocation and is finally spheroidized. Then, it is dissolved into the ferrite thus creating subgrain boundaries. As a result, the ferrite grains are appreciably refined. The spheroidized cementite acts a precipitation, and together with the grain refinement lead to the strengthening of the carbon steel [19].

5.4 Effect of waterjet peening on fatigue life

5.4.1 Fatigue life performance

The specimens (stainless steel 304) were treated with three different waterjet peening conditions designated with W1 (2 jet passes), W2 (4 jet passes) and W3 (6 jet passes). The other parameters were kept constant, i.e. a pressure of 200 MPa, a

feedrate of 2000 mm/min and a standoff distance of 30 mm. The different treatment conditions resulted in average surface roughnesses of 0.86, 2.20 and 3.43 μm for the specimens of W1, W2 and W3 respectively as summarized in [Table 5-1](#).

Table 5-1: Average surface roughness of treated and non-treated specimens

Specimens	Surface roughness, Ra (μm)	Surface hardness, HV _{0.01} (% increase)
Original	0.14 – 0.16	224 – 243
W1	0.78 – 0.94	249 – 265 (12%)
W2	1.60 – 2.62	255 – 275 (14%)
W3	2.34 – 4.86	275 – 289 (22%)

It is to note that the original specimen has an average surface roughness of 0.15 μm . The treated surfaces are shown in [Fig. 5-48](#). It can be seen that the waterjet treatment covers the whole regions uniformly with the highest erosion for specimen W3 followed by W2 and W1. It was also found that the maximum increases of hardness in the surface were about 12%, 14% and 22% with respect to the base material for the specimens of W1, W2 and W3 respectively [74].

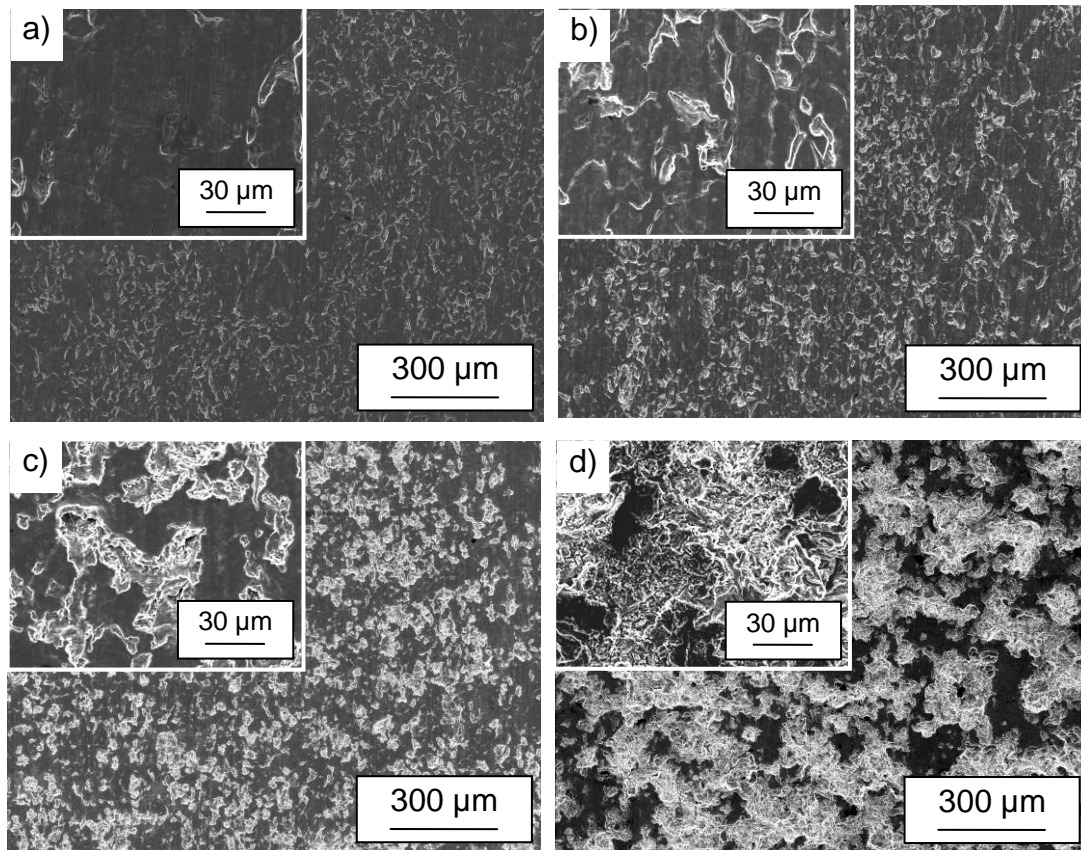


Fig. 5-48: Surfaces of fatigue specimens, a) original, b) W1, c) W2 and d) W3. (Insets are magnified images)

The results of the fatigue tests are plotted as the stress amplitudes versus N (number of cycles). The S-N curves are shown in Fig. 5-49. Overall, the waterjet treated specimens show a lower fatigue strength than the original specimens. Specimens with the highest increase in hardness and also surface roughness (i.e. specimen W3) resulted in the largest decrease in fatigue strength. This was followed by specimens W2. It is interesting to note that, the specimens W1 do not show a decrease in fatigue strength as compared to the original ones. Perhaps, it demonstrates a very marginal increase in the fatigue strength. However, the increase in the fatigue strength could not be conclusively said since only a limited number of specimens were tested. In comparison with Arola et al. [91] in abrasive waterjet peening of the same material, an increase in the fatigue strength of the treated specimen was discored. However, the increase in the fatigue strength was rather limited less than 10% with respect to the untreated specimen. In contrast, no noticeable increase in the fatigue strength was observed in the present study. Possibly, the amount of compressive residual stress introduced over the specimen surface was very much lower than Arola et al. [91]. This is to be expected since no abrasive particles were used in the present study unlike Arola et al. [91]. It is known that using abrasive particles in the waterjet peening might introduce a higher compressive residual stress than a pure waterjet [68].

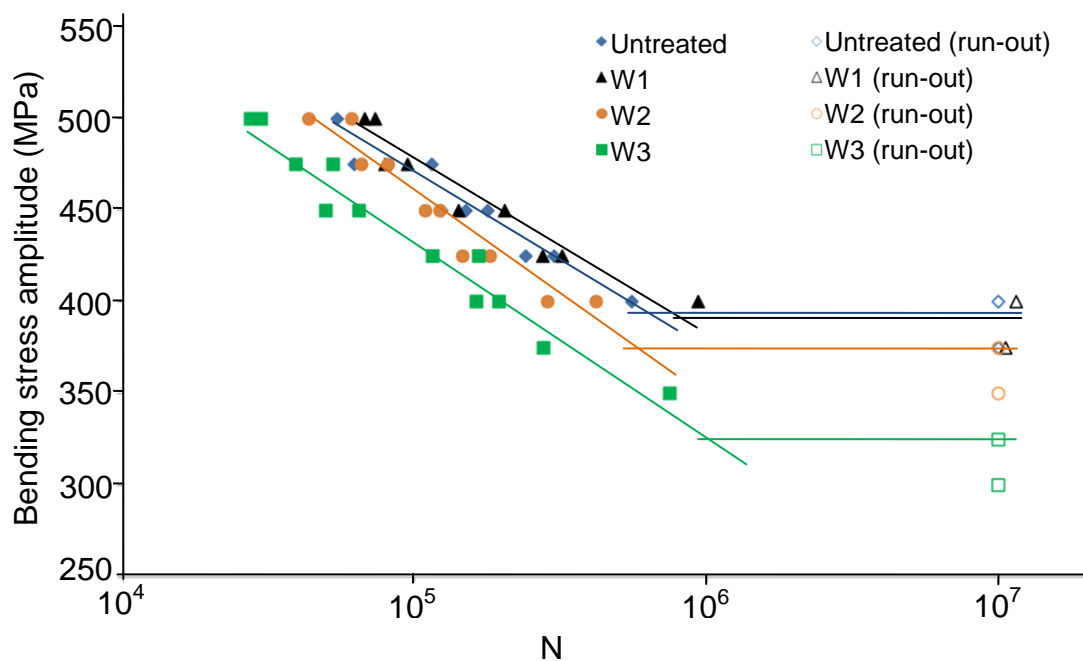


Fig. 5-49: Stress versus N diagrams for stainless steel 304

The results seem to suggest that the influence of the surface roughness is more prominent than the increase in hardness in determining the fatigue strength. However, it comes as no surprise since rougher surfaces are expected to encourage fatigue crack initiation [93]. In fatigue testing of mild carbon steel with different surface finishes produced by polishing which resulted in surface roughness between 1.78 to 5.48 μm , Alang et al. [151] found that the fatigue strength increased with a decrease in the surface roughness. Furthermore, Aviles et al. [145] found a lower fatigue resistance of laser peened specimens than the original specimens of medium carbon steel. They noticed that the laser peened specimen displayed an increase in micro-hardness up to double than its original with a hardening layer of about 100-150 μm . However, the surface roughness also increased to 0.30-0.35 μm from 0.04-0.08 μm . Upon further examination of laser peened surfaces, they found some micro-cracks and the inclusions which were the main cause of the reduction in fatigue life.

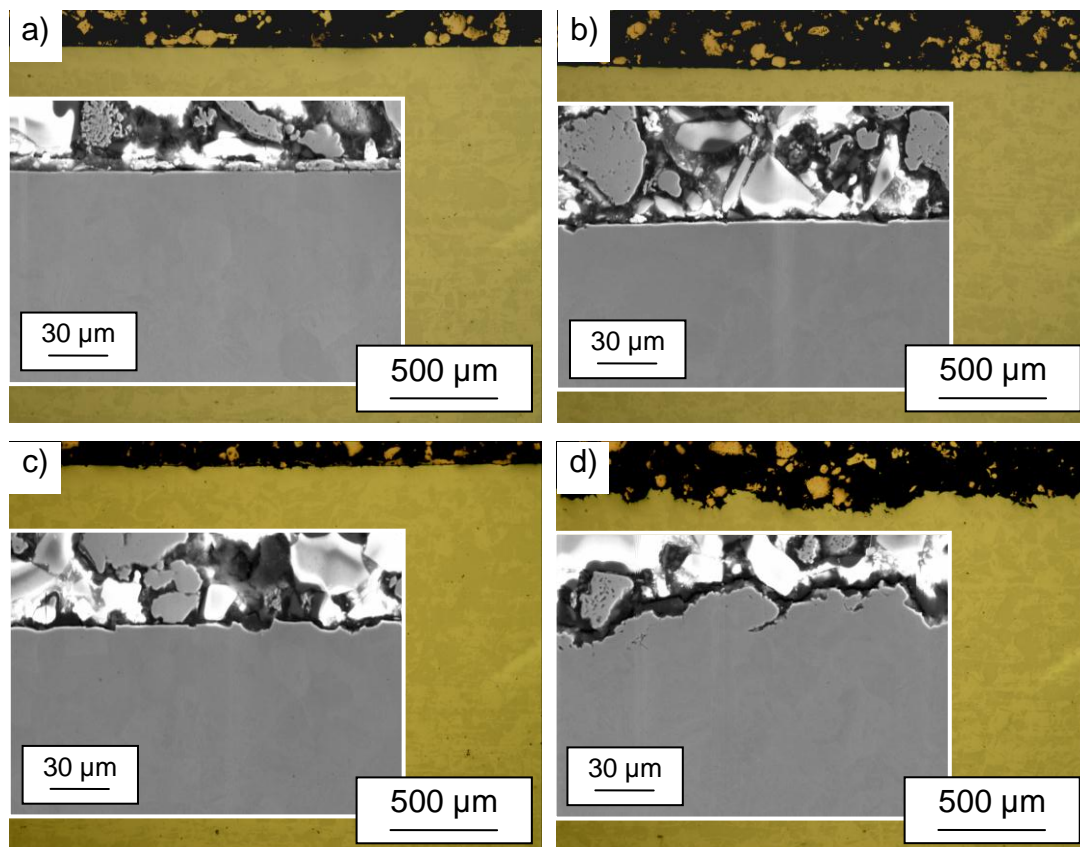


Fig. 5-50: Cross-sectional view of the fatigue specimens, a) Original, b) W1, c) W2 and d) W3. (Insets are magnified images)

A similar observation was also found in the present study. Upon further examination of the fatigue specimens, some cracks and notches were observed in the specimens

as shown in [Fig. 5-48](#) as well as [Fig. 5-50](#). It is clear that with increasing number of jet passes, the number of surface defects increased significantly. As a result, the higher roughness of the surface decreases the fatigue time for crack initiation.

It is also to note that no measurements of residual stresses were conducted for the peened fatigue specimens in the present study. Therefore, the relationship between the induced residual stresses and the fatigue strength cannot be established. However, it is expected that the compressive residual stress is also introduced the most in the specimens that displays the highest increase in the hardness (i.e. specimen W3) as similarly observed in [32, 145, 152]. Also, this specimen produced the highest amount of surface defects as shown in [Fig. 5-48](#) (d) and [Fig. 5-50](#) (d). The initiation of cracks in peened specimens is dependent on the positive effect of compressive residual stresses and the negative effect of surface defects [153]. In the present case, the benefit of compressive residual stresses was possibly defeated by the negative effect of surface defects thus leading to the overpeening effect. The high amount of microcracks in the surface may just act as the crack initiation and easily propagate during the fatigue test. Similar results were also found in shot peening process [32, 152, 154] as well as laser shock peening process [145].

5.4.2 Surface fracture analysis

The broken specimens were later examined using SEM to determine the crack initiation mechanisms. Since broken surfaces for different specimens tested at different loads displayed little difference, only selected SEM images of the broken specimens will be reported and discussed. The fractured surfaces of W1 specimen are shown in [Fig. 5-51](#). It can be seen that the crack initiations started mainly at both upper and lower corners as shown in [Fig. 5-51](#) (b) since these were the areas with the highest stress concentrations. Similarly, the fatigue test of the untreated specimens revealed that the cracks initiated at only these areas. However, it can also be noticed that the cracks also initiated at the surface as shown in [Fig. 5-51](#) (c). As expected, this was possible since the surface experienced slight erosion due to the waterjet treatment. Therefore, the notches on the surface act as the sites for the cracks initiation. The residual fracture surface in the middle of the specimen shows a typical ductile fracture mode with fatigue striation patterns as shown in [Fig. 5-51](#) (d).

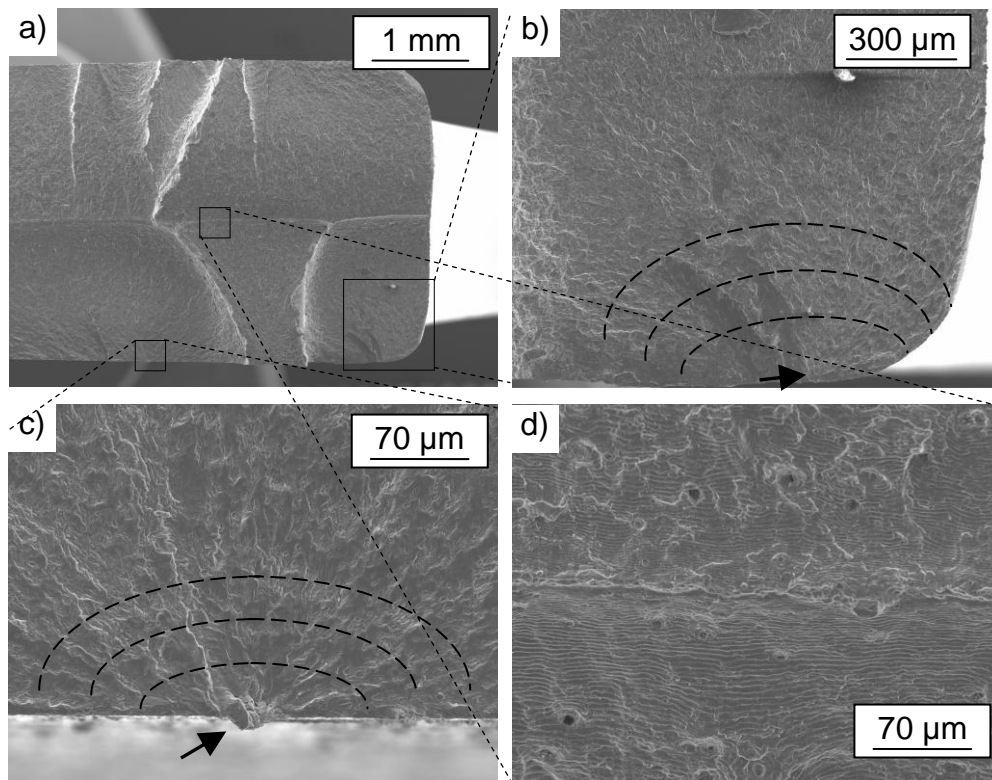


Fig. 5-51: SEM images of W1 fractured specimen, a) overview at a stress amplitude of 450 MPa, b) crack initiation at the corner, c) crack initiation at the surface and d) striation in the middle (arrows indicate crack initiation sites)

While, the fractured surfaces of W2 specimen at applied loads of 450 and 500 MPa are shown in [Fig. 5-52](#). Clearly, more cracks were initiated and propagated at the surface flaws as shown in [Fig. 5-52](#) (a) and [Fig. 5-52](#) (b). The residual fracture surface in the middle of the specimen shows a typical ductile fracture mode with fatigue striation patterns as shown in [Fig. 5-52](#) (d).

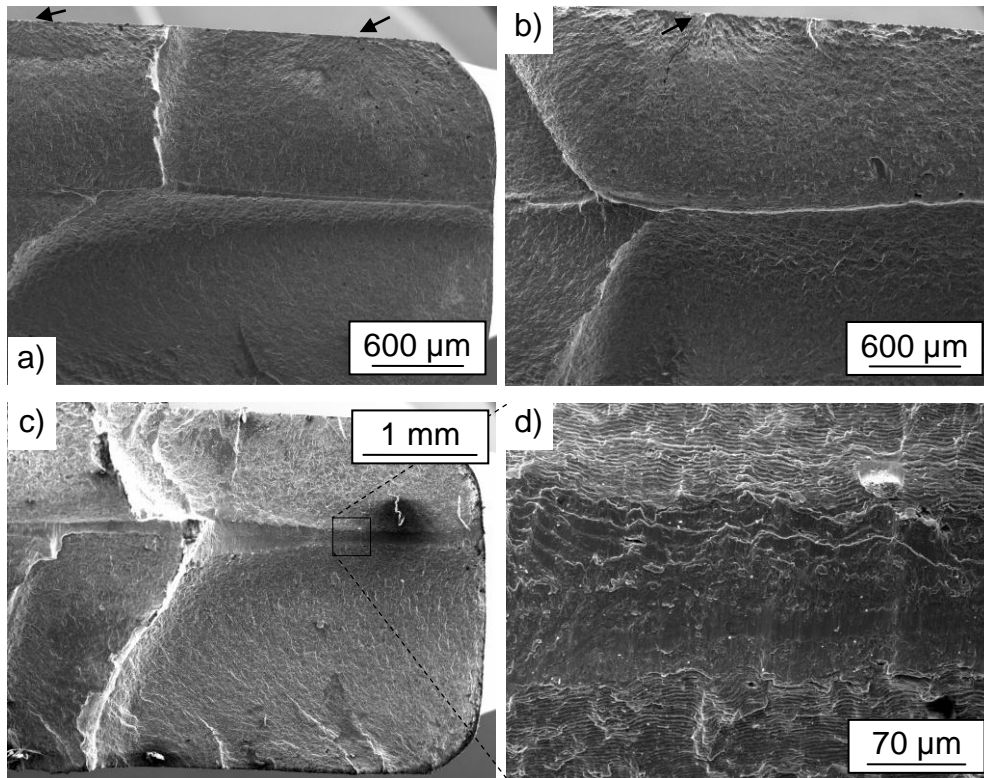


Fig. 5-52: SEM images of W2 fractured specimen, a) in the corner, b) in the middle at a stress amplitude of 450 MPa, c) overview at a stress amplitude of 500 MPa crack initiation, and d) striation in the middle (arrows indicate crack initiation sites)

While, the fractured surfaces of W3 specimen are shown in [Fig. 5-53](#). Again, it can be seen that the crack initiations started at corners of the specimen as shown in the [Fig. 5-53](#) (b) since these were the areas with the highest stress concentrations. However, more cracks were probably initiated at the surface due to a higher extent of the surface defects as shown in [Fig. 5-53](#) (d). These surface defects may simply act as the crack initiation sources. Although, the hardness increase was recorded the highest in these specimens, but the negative effect of surface defects generated by waterjet peening was more favourable. The higher surface roughness decreases the fatigue time for crack initiation eventually breaking the specimens faster. This leads to the overpeening effect where there is a pronounced drop in the fatigue life at higher jet passes. The residual fracture surface in the middle of the specimen shows a typical ductile fracture mode with fatigue striation patterns as shown in [Fig. 5-53](#) (c). Comparing the fatigue striation patterns for the specimens W2 and W3 at the same applied load of 500 MPa as shown in [Fig. 5-52](#) (d) and [Fig. 5-53](#) (c), it seems that the striation spacing is more in the latter specimen. This indicates the faster fatigue crack growth rate [84].

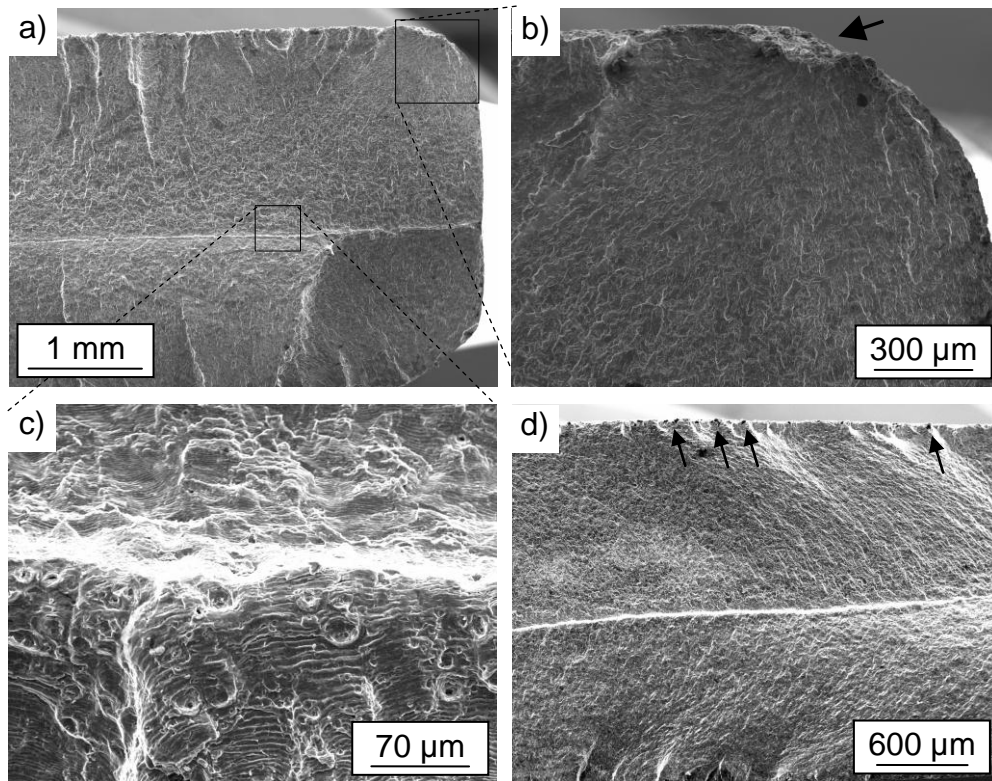


Fig. 5-53: SEM images of W3 fractured specimen, a) overview at a stress amplitude of 500 MPa, b) crack initiation at the corner, c) crack initiation at the surface and d) overview at a stress amplitude of 350 MPa (arrows indicate crack initiation sites)

It is obvious that the fatigue strength under waterjet peening treatment is directly related to the surface quality of the peened specimens as well as the location of these defects. The surface defects act as stress concentration sites which magnify the applied stresses according to the severity of the surface flaws, unlike bulk defects which are more shielded by the surrounding materials [155]. This severity depends on the size and shape of the surface defects. Sharper and deeper surface defects may increase the concentration of stress at their crack tips that are more likely to act as crack initiation sites [156]. A similar conclusion can be drawn as shown in the present study where surfaces with more and severe defects result in higher crack initiation sources thus lowering the fatigue strength of the material.

6 Optimization of the waterjet peening process

This chapter discusses the usage of a method to optimize the waterjet peening process. The aluminium alloy 5005 was used as an example specimen. For a robust process design, there is a need to focus on the optimization of parameters by reducing the measured variation of quality characteristics. Therefore, a design of experiment based on the response surface methodology can be utilized for the process optimization. These collections of mathematical and statistical techniques are useful for modelling and analysis in applications where a response of interest is influenced by several factors and the objective is to optimize this response [157].

6.1 Design of experiment

Design of experiments (DOE) was first introduced by Fisher in the early 1920s intended to study the effects of multiple variables simultaneously and most economically using a statistical technique [158]. The process of DOE is carried out for quality improvement purposes. Using DOE, all combinations of the factors included in an experimental study are able to be laid out for investigation purposes. If the number of possible combinations is too large, then a fraction of the total possibilities is conducted such that all factors will be evenly present. Fisher devised the first method that made it possible to analyze the effect of more than one factor at a time [158]. The combinations are created using a matrix, which allows each factor an equal number of test conditions. Statistical calculations such as mean and ANalysis Of VAriance (ANOVA) are used to analyze the results of such experiments. By studying the effects of individual factors on the results, the best factor combination can be determined. When applied to product or process design, the method helps to seek out the best design among the many alternatives.

The various methods of DOE can be used to solve scientific problems which involve determining a proper combination of factors, ingredients, parameters and variables rather than innovations or a single identifiable cause. In general, it is applicable to any situation that depends on many influencing factors. It is a method that scientifically gives the best option when facing with many possibilities. It is possible to investigate one factor at a time to determine the effect of the factor but it is not necessarily true since factors are interacting with each other in real-life application.

Real behaviour of the factors can be studied when the influences of all factors have an equal opportunity to be present. Therefore, it is recommended to apply the DOE technique to capture such effects. The number of necessary experiments depends on the number of factors and their levels. Generally, the larger the number of factors, the bigger is the reduction from the total possibilities in a full factorial experiment.

There are very few studies on waterjet peening that have explored on finding the optimal conditions for various waterjet peening parameters affecting the quality characteristics. Macodiyo and Soyama [96] investigated the effects of fatigue strength of carburized chrome-molybdenum steel subjected to surface treatment by cavitation peening. They used a design of experiment (DOE) based on the response surface methodology (RSM) to model optimal conditions for the critical factors such as processing times and cavitation number affecting fatigue strength. They found that the cavitation number yielded better results in improving the fatigue strength of chrome-molybdenum steel and the models used in the DOE were in agreement with the experiments performed. Furthermore, Rajesh and Babu [97] established empirical models of waterjet peening of aluminium alloy based on Taguchi's experimental design. They noticed only a slight deviation in the results predicted with the models compared to the results obtained from the experiments.

6.2 Response surface methodology

In the present work, the response surface methodology (RSM) was selected as the method for the experimental design. It is an empirical modelling approach for determining the relationship between various processing parameters and responses [159]. The Box–Behnken design is a widely used experimental design for RSM due to its simplicity [160]. It requires only parameters at three different levels and it is based on the combination of the factorial with incomplete block designs for each independent parameter. Therefore, this design gives desirable statistical properties and most importantly with only a fraction of the experiments required for three-level factorials [160].

A statistical method known as multiple linear regression is widely used in building the empirical models in RSM. It is a statistical technique for investigating and modelling the relationship between variables, where an equation is established to relate the

independent variables or commonly known as the predictor or regressor variables and the dependent variables or commonly known as the response variables [157]. In other words, in the multiple linear regression models, the values of the regressor variables can be fixed and the corresponding value of the response variables will be observed. In almost all applications of regression, the regression equation is just an approximation to the actual functional relationship between the variables of interest. These regression models can be termed as mechanistic or empirical models since these functional relationships are based on knowledge of underlying the mechanisms of physical, chemical, or other engineering or scientific theory [157]. In the present work, the waterjet peening process involves a number of defined dependent factors or parameters, k . Thus, the functional relationship between the response, y and independent variables, x can be represented by the second order polynomial model with interaction as shown in Eq. (6-1) [157].

$$y(x) = \beta_0 + \sum_{i=1}^k \beta_i x_i + \sum_{i=1}^k \beta_{ii} x_i^2 + \sum_{i=1}^{k-1} \sum_{j=2}^k \beta_{ij} x_i x_j + \varepsilon \quad (6-1)$$

where β and ε are the coefficients and error, respectively.

In WJP, there are a vast number of parameters affecting the quality of the results. Therefore, only a few parameters were selected to ensure the feasibility of the multipass treatment and its influence can be properly assessed. The machining parameters and their respective ranges were carefully selected based on preliminary trial runs as well as in literature reviews [43, 44, 45, 47, 68, 74]. The effect of WJP treatment was clearly observed within these ranges of parameters. The machining parameters and their ranges are shown in Table 6-1.

Table 6-1: Waterjet peening parameters and their respective ranges

No.	Waterjet Peening parameters	Range		
		Low	Medium	High
1.	Number of jet passes, n_j	1	2	3
2.	Pressure, p_o (MPa)	50	100	150
3.	Feedrate, v_n (mm/min)	500	1000	1500
4.	Standoff distance, h (mm)	20	40	60

In a linear regression analysis, a complete set of data is essential in ensuring a more simplified and applicable model to be established. Therefore, it is important to have a

good method of data collection. The best way of collecting data is using a designed experiment where a set of parameters or factors and their levels can be manipulated. In the present study, the Box-Behnken experimental design was used to create a sufficient set of data.

The total number of experiments is based on the number of parameters and their levels [157]. Since in the present case, there is a total of four parameters with each at three levels, therefore a total number of 29 experiments is required based on the Box-Behnken experimental design. In determining the total number of experiments, the experimental design is divided into blocks representing the number of interactions between any 2 parameters. In each block, a certain number of parameters are put through all combinations for the factorial design, while the other parameters are kept at the central values. For instance, the Box-Behnken design for 4 parameters involves six blocks, in each of which 2 parameters are varied through the 4 possible combinations of high and low. This gives the total number of experiments of 24 (i.e. 6 blocks multiply with 4 possible combinations in each block). With additional of 5 experimental runs at a centre point, the total number of experiments becomes 29.

A centre point (i.e. in which all factors are at their central values) was included in the experimental design. The experimental run at the centre point is included as to improve the accuracy and repeatability of the experimental design. The experimental runs for the centre point were repeated 5 times (i.e. at experimental runs number 1, 10, 14, 15 and 19). A software for design of experiments, Design-Expert®, was used for analyzing the experimental results based on the response surface methodology approach. A total of 29 experimental runs were carried out in the present study as shown in Table 6-2.

Table 6-2: Experimental runs and their results based on Box-Behnken experimental design

Exp. No.	Waterjet peening parameters				Responses	
	n_j	p_o (MPa)	v_n (mm/min)	h (mm)	R_a (μm)	Hardness ($\text{HV}_{0.01}$)
1	2	100	1000	40	8.25	59.20
2	2	150	500	40	15.93	61.30
3	1	150	1000	40	14.28	58.67
4	2	100	500	60	16.41	59.00
5	2	100	1500	20	0.54	57.57
6	3	100	1000	60	14.04	60.70
7	3	100	1000	20	0.55	60.00
8	3	100	1500	40	5.14	55.83
9	1	50	1000	40	0.54	54.60
10	2	100	1000	40	8.18	57.77
11	3	50	1000	40	0.69	56.10
12	2	100	500	20	0.73	56.70
13	2	50	1000	60	0.57	55.00
14	2	100	1000	40	5.85	58.20
15	2	100	1000	40	5.83	58.90
16	2	150	1500	40	13.01	59.07
17	1	100	1500	40	0.56	54.80
18	2	50	1000	20	0.51	55.10
19	2	100	1000	40	6.50	58.50
20	2	50	500	40	0.54	55.07
21	3	100	500	40	13.44	59.73
22	1	100	500	40	6.78	57.90
23	2	100	1500	60	4.11	57.23
24	1	100	1000	60	1.85	57.00
25	2	150	1000	20	10.55	58.27
26	1	100	1000	20	0.53	56.80
27	3	150	1000	40	15.25	59.60
28	2	150	1000	60	16.00	59.83
29	2	50	1500	40	0.56	54.50

Exp. No. Experimental number

6.3 Analysis of results

Table 6-2 above shows the experimental results for both roughness and hardness based on the Box-Behnken experimental design.

6.3.1 Roughness

It is to note that the average original surface roughness is about $0.49 \mu\text{m}$. In the present study, the roughnesses after the peening treatment were obtained between

0.51 to 16.42 μm . Based on the roughness level of all experimental runs, the results can be divided into three different groups. The first group consists of experimental runs with a low roughness below 1 μm . The experimental runs in the second group have a range of roughness between 1 to 10 μm . Finally, the third group refers to the experimental runs which have a high roughness of more than 10 μm .

About 11 experimental runs produce roughnesses below 1 μm . An example of a 3D image of the surface structure in this group is shown in [Fig. 6-1](#). The erosion on the surfaces are hardly to be observed and they are comparable to the original surface. The amount of removed material is nearly zero. A further analysis for experimental run number 5 shows that the maximum depth of the pit was 2.90 μm . In comparison, the original surface has the maximum depth of the pit about 2.79 μm . Nevertheless, the maximum depth of the pit within this group varies from 2.80 to 4.50 μm .

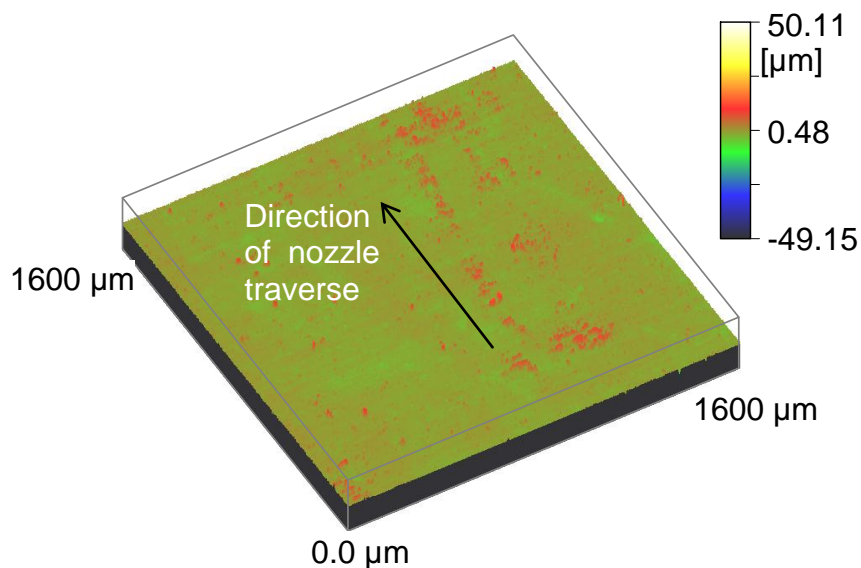


Fig. 6-1: 3D images of surface structures for experimental run number 5 ($R_a = 0.54 \mu\text{m}$)

About 9 experimental runs have roughnesses between 1 to 10 μm . An example of 3D image of surface structure in this group is shown in [Fig. 6-2](#) for the experimental run number 22. In this group, there is significant erosion over the surfaces. However, the erosion track is not continuous as shown in [Fig. 6-2](#). Furthermore, no constant width of erosion track is produced on the surface. There is a moderate removal of material with high values of the valley-to-peak between 34.50 to 73.67 μm .

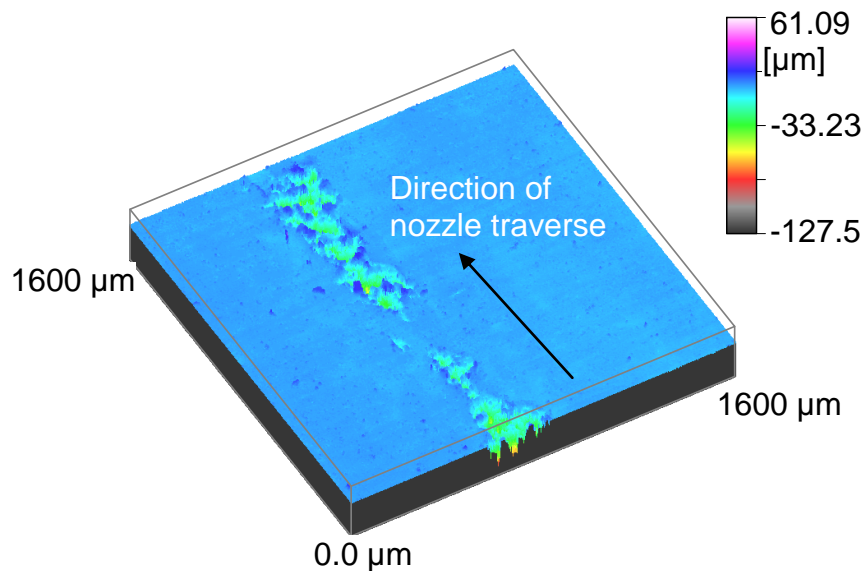


Fig. 6-2: 3D images of surface structures for experimental run number 22 ($R_a = 6.78 \mu\text{m}$)

There are another 9 experimental runs that produce roughnesses above $10 \mu\text{m}$. Fig. 6-3 shows the example of the 3D image of the surface structure for the experimental run number 16. All experimental runs in this group show severe erosion to the surfaces. There is a high amount of removed material with an almost constant width of erosion track. The erosion continues along the track without interruption with very high values of valley-to-peak in a range between 69.92 to $105.66 \mu\text{m}$.

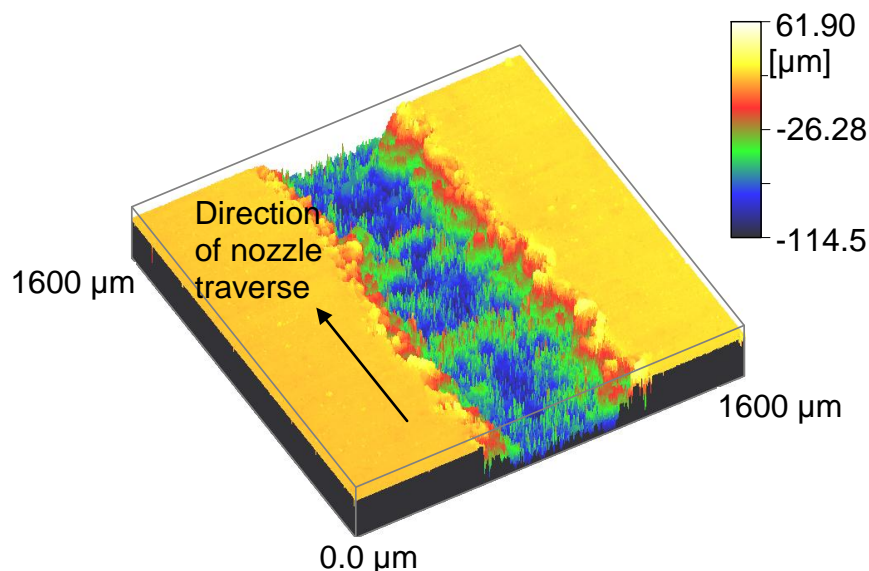


Fig. 6-3: 3D images of surface structures for experimental run number 16 ($R_a = 13.78 \mu\text{m}$)

It is interesting to further discuss about the erosion nature of the aluminium alloy 5005 under the waterjet impingement process. The eroded surfaces were examined using SEM at different magnifications. Since, the erosion features for different surfaces displayed relatively similar characteristics, only several SEM images at selected erosion tracks are presented here. Nevertheless, the overall surface damage mechanism can be clearly seen from these images. Fig. 6-4 shows an example of the eroded surface at different magnifications. The surface displays uniform erosion with full removal of the material over the erosion track width as shown in Fig. 6-4 (a). Upon a closer look at a higher magnification as shown in Fig 6-4 (b), the erosion is characterized by ductile removal of the material with undulated appearance of the surface as well as lots of large pits.

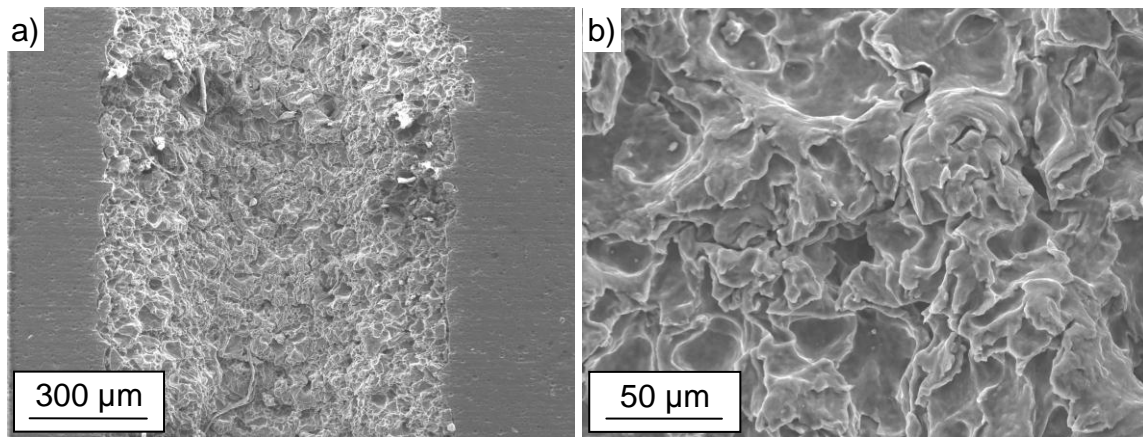


Fig. 6-4: Example of eroded surface for the experimental number 16 at a magnification of, a) 66x, and b) 515x

Fig. 6-5 shows the effect of four different peening parameters on the surface roughnesses of the peened specimens. It can be seen that increasing the number of passes produces a higher surface roughness as shown in Fig. 6-5 (a). Also, the surface roughness increases with an increase in pressure as shown in Fig. 6-5 (b). Furthermore, rougher surfaces were also produced at lower feedrates as shown in Fig. 6-5 (c). In addition, the surface roughness increases with an increase in standoff distance as shown in Fig. 6-5 (d).

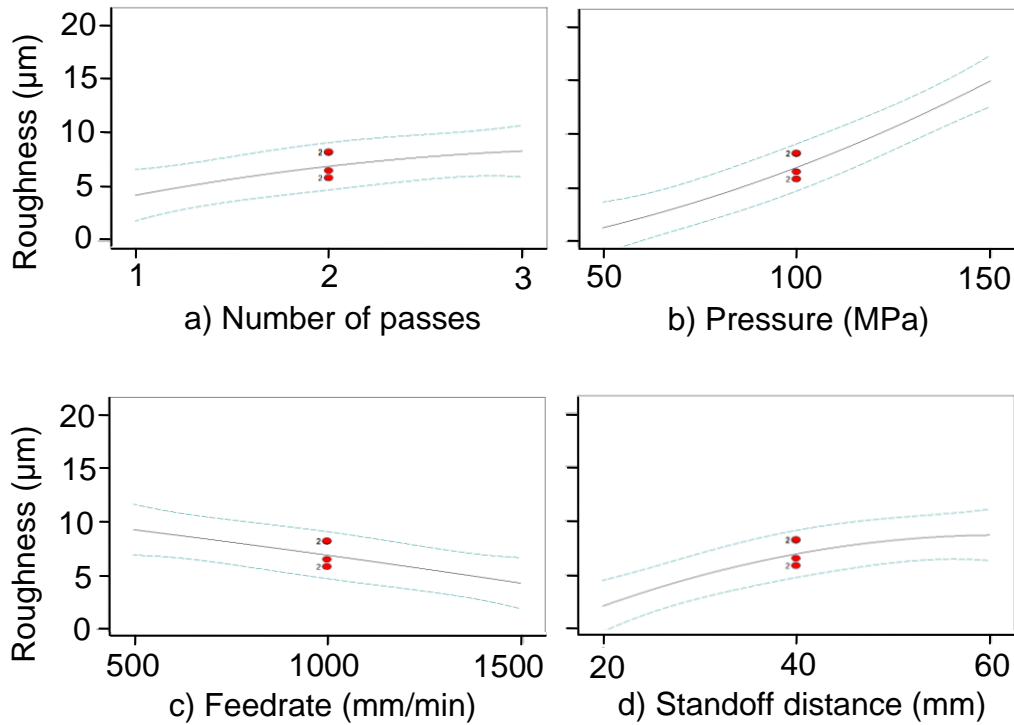


Fig. 6-5: Effect of, a) number of passes, b) pressure, c) feedrate, and d) standoff distance on R_a

6.3.2 Hardness

On the basis of the three different groups as discussed above, the effect of surface roughness on hardness was analyzed. It is to note that the base material has an average hardness of approximately 53.58 $\text{HV}_{0.01}$. The change in hardness as a function of the depth below the eroded surface for a few experimental runs which produced roughnesses below 1 μm is shown in Fig. 6-6. The roughnesses for trial 13, 18 and 20 are 0.57, 051 and 054 μm , respectively. Overall, there are almost no changes in hardness values along the depth. It may seem to be a very small change of hardness gradients near to the surface. But, the error bars are quite long to strongly suggest that there is any change in hardness gradients in the present study.

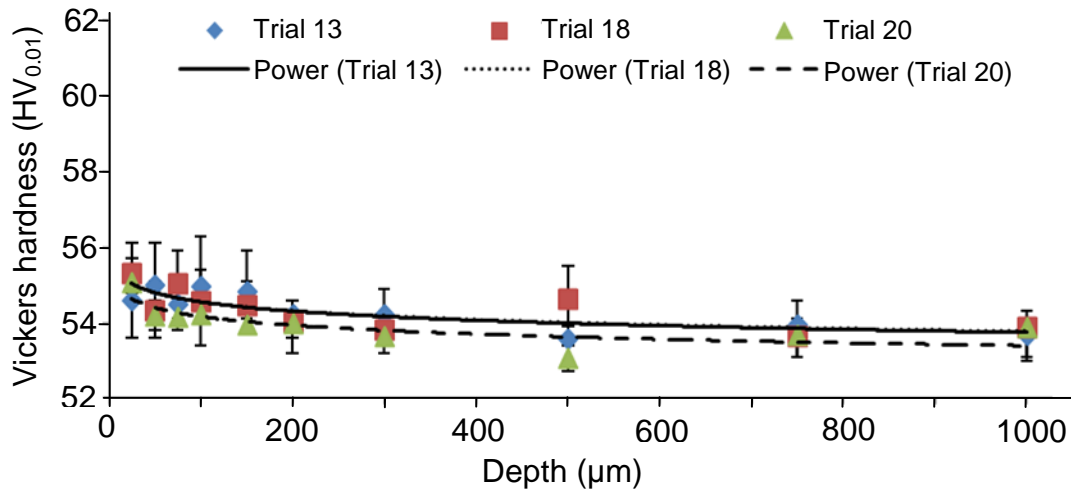


Fig. 6-6: Hardness as a function of depth for experimental runs with low R_a

The changes of hardness gradients for experimental runs which have intermediate roughnesses (between 1 to 10 μm) are shown in Fig. 6-7. The roughnesses for trial 8, 22 and 23 are 5.14, 6.78 and 4.11 μm , respectively. The magnitude of hardness is high at the surface and decreases with increasing depth from the surface. There are significant changes in hardness values up to a depth of approximately 200 μm . Beyond this depth, the hardness is about the same as the original hardness at the surface.

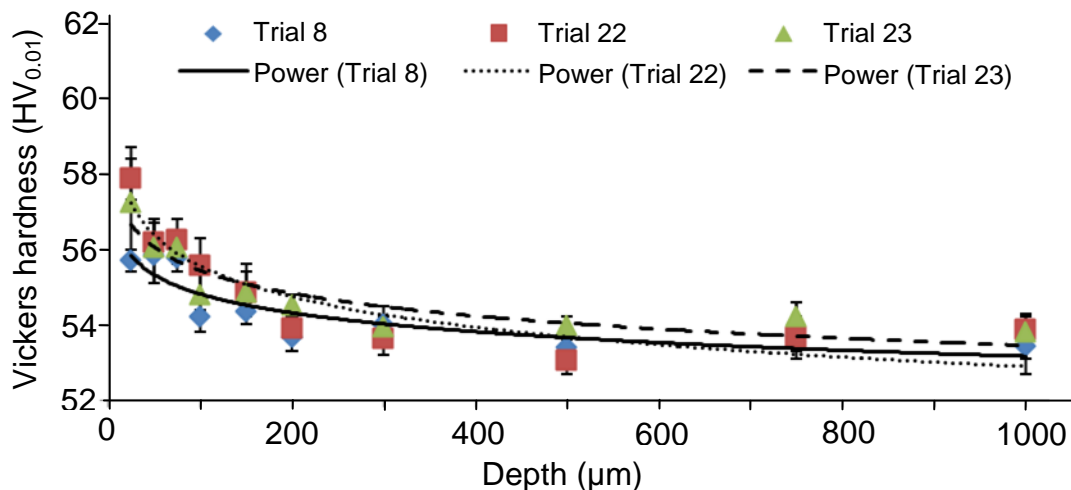


Fig. 6-7: Hardness as a function of depth for experimental runs with intermediate R_a

The changes of hardness gradients for the experimental runs which produced high roughnesses (above 10 μm) are shown in Fig. 6-8. The roughnesses for trial 16, 27 and 28 are 13.01, 15.25 and 16.00 μm , respectively. There are significant changes in hardness values up to a depth of approximately 300 μm . It is more interesting to note

that the maximum increase in hardness is not located just below the eroded surface. The maximum increase in hardnesses was recorded at a depth of approximately 80 – 120 μm . Further analysis of the material structures below the eroded surfaces show some cracks as can be seen in [Fig. 6-9](#). The low strength of aluminium alloy makes it possible for the occurrence of cracks especially at very high impact energy of injected water used within this experiment. The crack propagation extends up to a depth of about 50 - 80 μm . Therefore, the measurement of hardness within these depths shows a low value as shown in [Fig. 6-8](#).

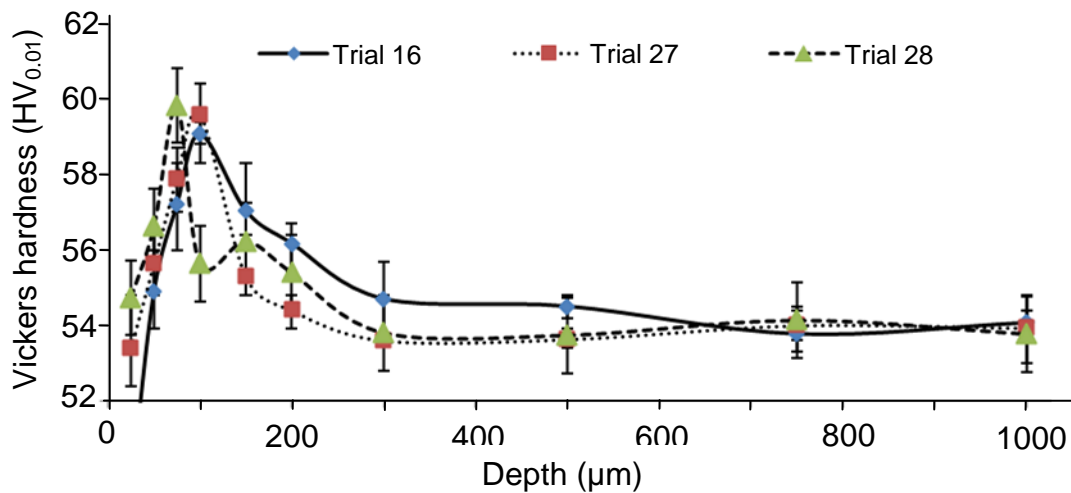


Fig. 6-8: Hardness as a function of depth for experimental runs with high R_a

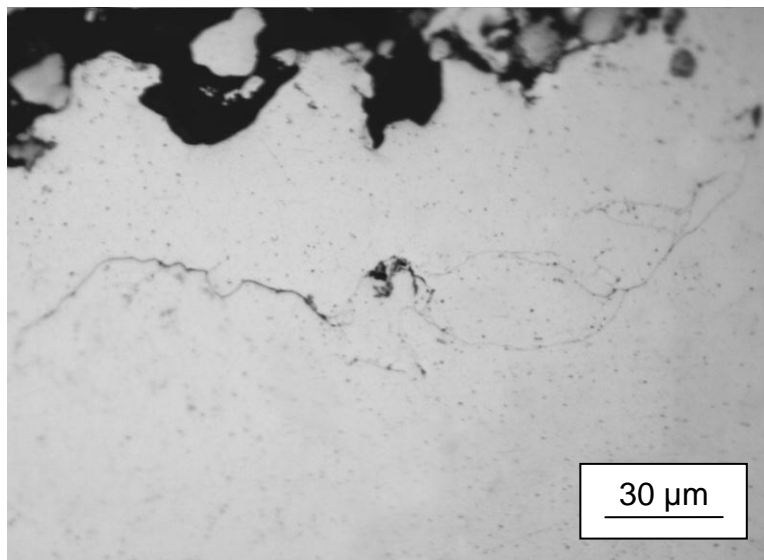


Fig. 6-9: Cracks below the eroded surface (Experimental run 27)

The effect of different peening parameters on hardness is shown in [Fig. 6-10](#). Overall, there is a change in maximum hardness with an increasing number of

passes as shown in [Fig. 6-10 \(a\)](#). The increase in hardness is the result of the introduction of compressive stresses from repeated waterjet impact forces at a higher number of passes [74]. The effect of pressure on the Vickers hardness is shown in [Fig. 6-10 \(b\)](#). A higher hardness gradient is found in a specimen treated with a higher pressure. This is due to the fact that a higher kinetic energy of water droplets at higher pressures induces a higher amount of compressive stresses hence, increasing the hardness. The effect of the feedrate on the hardness is shown in [Fig. 6-10 \(c\)](#). Increasing the traverse rate allows less water droplets to impinge on the surface. Therefore, it may induce a lower amount of compressive residual stresses and lead to a lower hardness. Besides, the effect of the standoff distance on the hardness is shown in [Fig. 6-10 \(d\)](#). There is a very small increase in hardness as the standoff distance increases. It is due to the same reason above that the impact energy of waterjet is low at a lower distance because of water column effect.

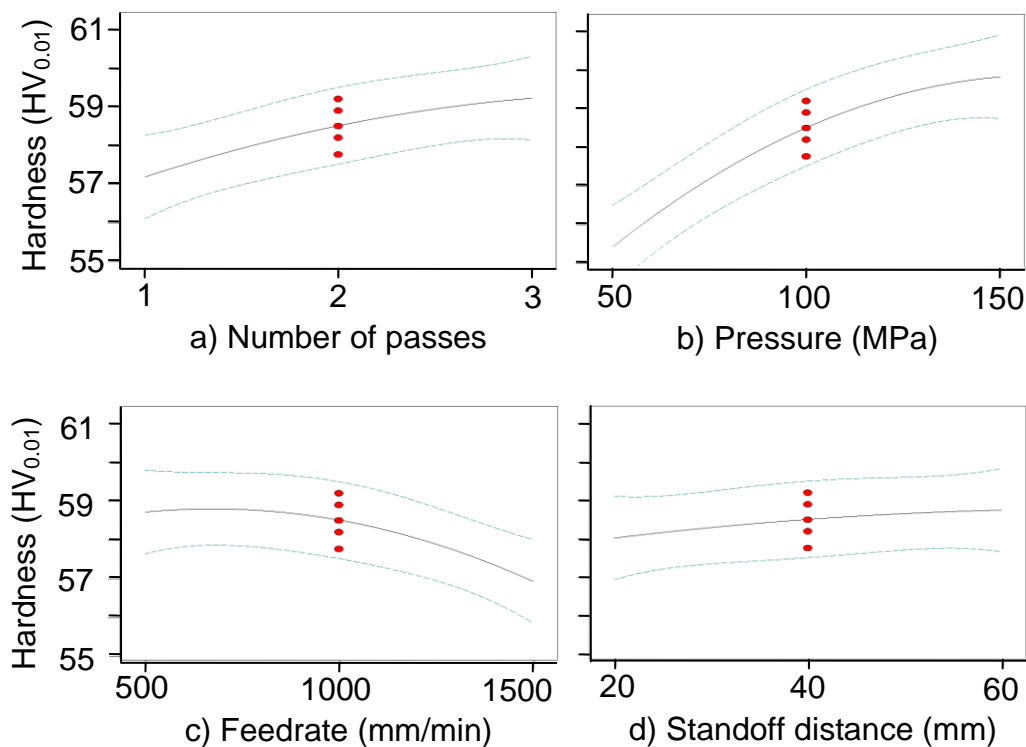


Fig. 6-10: Effect of, a) number of passes, b) pressure, c) feedrate, and d) standoff distance on hardness

Based on the changes of hardness and surface roughness, it is without a doubt that they are linearly related. The equivalent parametric trends show the increase in hardness is not possible without a corresponding increase in surface roughness. The relationship between the hardness and corresponding surface roughness of the

waterjet peened AA 5005 is shown in [Fig. 6-11](#). Similarly, a higher residual stress was found in the specimens with a higher surface roughness [91]. Unsurprisingly, the parametric combinations that give a high energy of waterjet (e.g. high pressure, etc) may induce a high degree of compressive residual stress and hardness. Also, due to the high energy of the waterjet, significant erosion of the surface may be occurred.

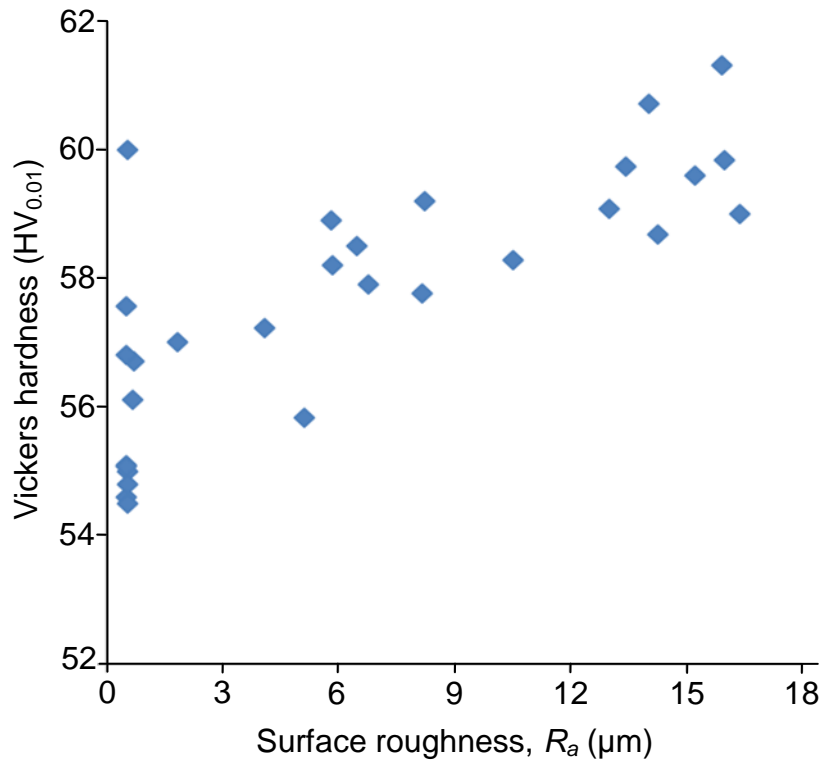


Fig. 6-11: Relationship between the average surface roughness and hardness resulting from waterjet peening of AA 5005

Based on the experimental data set in [Table 6-2](#), the surface roughness (R_a) and the hardness (HV) empirical models were developed. The R_a model describes the average roughness on the surface while the HV model shows the maximum of the hardness value below the surface. The hardness for every trial run was measured across the specimen depth. An average of at least four hardness data was recorded at every depth. Therefore, for the purpose of developing a model for hardness, only a single value of hardness is needed for every trial run. So only the maximum hardness (average) value at a certain depth for each trial run was recorded in [Table 6-2](#). Thus, the empirical model for hardness is capable to predict only the maximum hardness after the peening process regardless of the depth of hardening layer. The coefficients of regression were determined using the stepwise method of the Design Expert software. The two models were based on the 29 experimental runs conducted

according to the Box-Behnken experimental design. The second-order models for R_a (μm) and hardness ($HV_{0.01}$) in terms of waterjet peening parameters are shown in Eq. (6-2) and Eq. (6-3), respectively.

$$R_a[\mu\text{m}] = -12.774 - 4.038n_j + 1.360 \times 10^{-1}p_o + 7.130 \times 10^{-3}v_n + 1.634 \times 10^{-1}h + 1.521 \times 10^{-1}n_jh - 3.0 \times 10^{-4}v_nh \quad (6-2)$$

$$HV_{0.01} = 47.908 + 1.016n_j + 1.092 \times 10^{-1}p_o + 3.15 \times 10^{-3}v_n - 3.3 \times 10^{-4}p_o^2 - 2.5 \times 10^{-6}v_n^2 \quad (6-3)$$

where n_j is the number of jet passes, p_o is the pressure (MPa), v_n is the feedrate (mm/min) and h is the standoff distance (mm), respectively.

In order to accept the models for practical use, it is important to do some assessment to check their validity. The model validation is directed toward determining whether the model will function successfully in its intended operating environment for prediction purposes. A common way for checking the validity of a regression model is by evaluating the coefficients of determinations (R^2 and adjusted R^2) [157]. It is the proportion of variation explained by the regressor where values of that are close to 1 mean that most of the variability in response is explained by the regression model. Generally, if the model fits the data well, the overall value of R^2 and adjusted R^2 (R_{adj}^2) should be higher or equal to 0.70. For the case of surface roughness, the values of R^2 and R_{adj}^2 are 0.884 and 0.852, respectively. Whereas, the values of R^2 and R_{adj}^2 for hardness are 0.808 and 0.766, respectively. There are reasonable correlations between the measured and the predicted values for both R_a and hardness as shown in [Fig. 6-12](#). Therefore, the empirical models are useful in predicting the responses of R_a and hardness during waterjet peening of aluminium alloy 5005 within the ranges of the parameters in this study. A proper selection of the peening parameters can be formulated to be used in practical works.

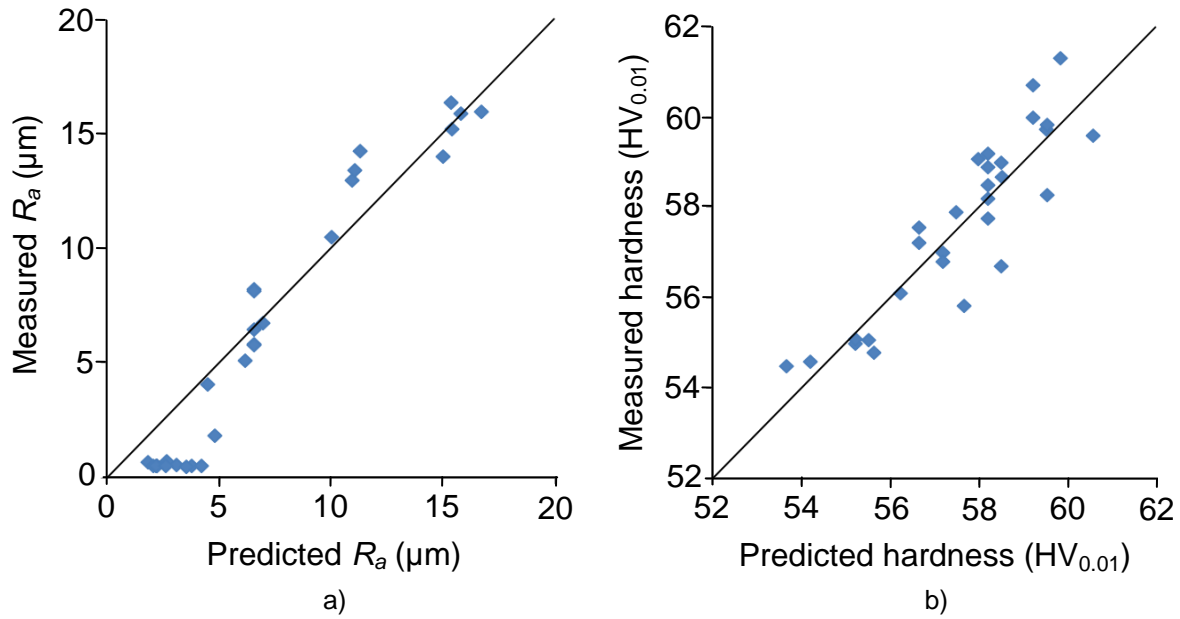


Fig. 6-12: Comparison of measured versus predicted values of, a) R_a , and b) hardness (line indicates an ideal case)

The significance of the models and their parameters were then investigated through the analysis of variance (ANOVA). ANOVA is a statistical technique conducted mainly to learn about the influence of various design parameters and to observe the degree of sensitivity of the result to different parameters affecting the quality characteristics [161]. Through ANOVA, the degree of variation of each control factor which causes relative to the total variation observed in the result can be seen clearly [158]. The F -ratio or the variance ratio is the ratio between the parameters effect variance (the mean square due to a parameter) and the experimental error variance (the mean square due to experimental error). This ratio is used to test for the significance of factor effects. A larger F -value indicates that there is a big change in the performance characteristic due to the variation of the process parameter. Also, if a p -value of any model and its terms is less than or equal to 0.05, the terms in the model have significant effect on the response. The ANOVA results for R_a and hardness are shown in [Table 6-3](#) and [Table 6-4](#) respectively. This analysis was carried out for a 95% confidence level. It was found that the respective p -values for both models are less than 0.05. It shows that both models are significant.

Table 6-3: ANOVA results for surface roughness (R_a)

Source	Sum of squares	Degree of freedom	Mean square	F-value	p value (Prob > F)
Model	884.046	6	147.341	27.826	< 0.0001
n	50.307	1	50.307	9.501	0.0054
p	555.016	1	555.016	104.816	< 0.0001
u	74.551	1	74.507	14.079	0.0011
h	130.482	1	130.482	24.641	< 0.0001
nh	37.027	1	37.027	6.992	0.0148
uh	36.663	1	36.663	6.923	0.0152
Residual	116.493	22	5.295	-	-
Lack of fit	110.627	18	6.146	4.191	0.0872
Pure error	5.866	4	1.466	-	-
Cor total	1000.539	28	-	-	-

Prob Probability, Cor total Corrected total

Corrected total=Total Sum of squares (SS) for the model terms + Residual SS and
Corrected total = Sum of degrees of freedom (df) of all the model terms + residual df

Based on the p -value for the R_a model as shown in [Table 6-3](#), all the model terms are significant with pressure having the highest degree of significance followed by standoff distance, feedrate and number of passes. Furthermore, the interactions either between the number of passes and the standoff distance as well as between the feedrate and the standoff distance are also significant but they have a low degree of significance on the surface roughness. It is also good to note that as discussed above, none of the experimental runs with roughnesses below 10 μm were treated with the highest pressure of 150 MPa. This simply confirms that the pressure is the most significant parameter in influencing the surface roughness in this experiment. Hence, treating the surfaces with the highest pressure will certainly produce extensively rougher surfaces.

The p -value of the lack of fit test is 0.08. It is insignificant since its value is more than 0.05 thus indicating that all the data in this study fit the model adequately. The individual influence of each parameter on R_a was discussed above. However, it is interesting to discuss about the significant interaction effects between the number of passes and the standoff distance as well as between the feedrate and the standoff distance. As shown in [Table 6-3](#), both interactions are significant as indicated by the p -values which are less than 0.05. The effect of interaction between the number of passes and the standoff distance on R_a is shown in [Fig. 6-13](#). It can be observed that at a lower number of passes, R_a shows only marginal changes at different levels of

the standoff distance. However, at the highest number of passes, R_a increases dramatically as the standoff distance increases from 20 to 60 mm. This indicates that in this study there exists a strong interaction between the number of passes and the standoff distance particularly at a higher level of jet passes.

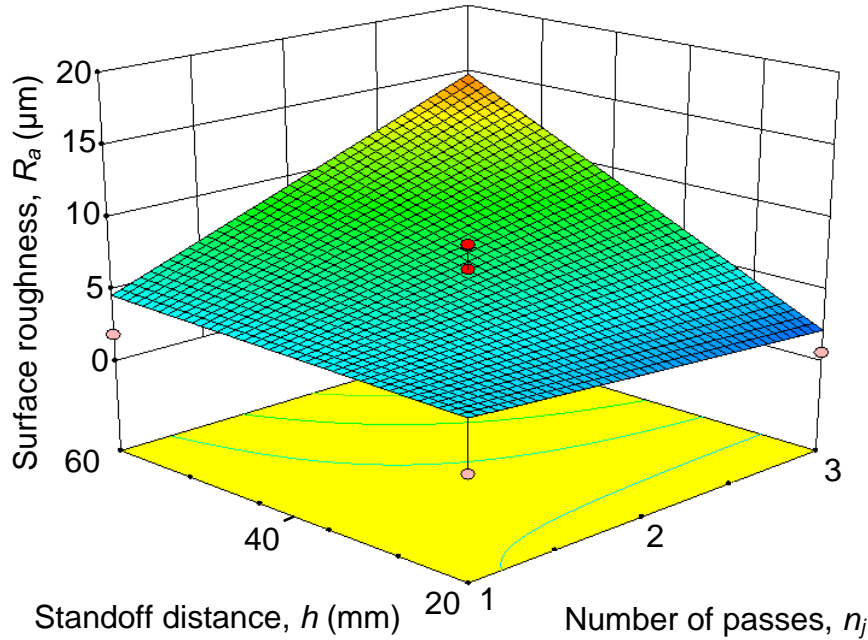


Fig. 6-13: Effect of interaction between number of passes and standoff distance on R_a

On the contrary, the interaction between the feedrate and the standoff distance shows a reverse effect on surface roughness as shown in Fig. 6-14. In other words, the effect of increasing the standoff distance on R_a is more profound at the lowest feedrate. R_a increases significantly while the standoff distance increases from 20 to 60 mm at the lowest feedrate. However, changing the standoff distance shows an almost no change in R_a at the highest feedrate of 1500 mm/min. Similarly, R_a does not change with increasing feedrate at the lowest standoff distance of 20 mm. This suggests that there is a strong interaction between the feedrate and the standoff distance in influencing the R_a .

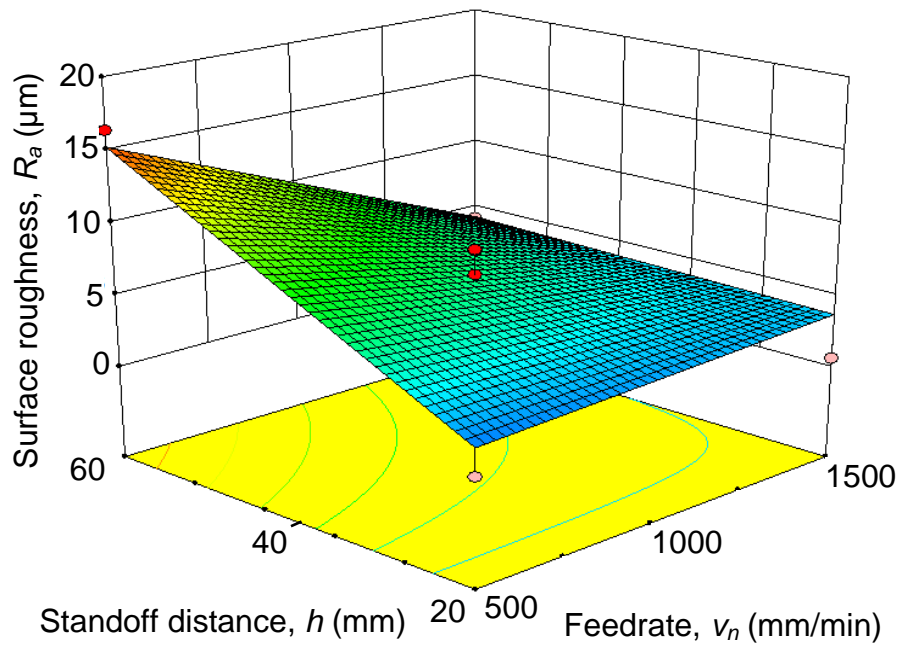


Fig. 6-14: Effect of interaction between feedrate and standoff distance on R_a

Whereas, based on the p-value for the HV model as shown in [Table 6-4](#), all the parameters are significant except the standoff distance. Again, the pressure has the highest degree of significance followed by the number of passes and the feedrate. As presented in [Table 6-2](#), the highest HV recorded was at the highest pressure of 150 MPa. Also, the values of HV were notably higher at the highest pressure. This simply confirms that the pressure is the most significant parameter in influencing the HV in this experiment.

The p -value of the lack of fit test is 0.13. It is insignificant since its value is more than 0.05 thus indicating that all the data fit the model adequately in this study. The individual influence of each parameter on HV has been explained above. However, it is interesting to discuss the insignificant effect of the standoff distance in influencing the HV . There is a possibility that the chosen range of standoff distance (i.e. 20 – 60 mm) in this study gives only a marginal effect to the HV . As found by Oka et al. [76] in waterjet treatment of aluminium alloy 5083, the value for the impingement force was constant at a standoff distance of less than 100 mm. Therefore, it gave an almost constant hardening effect to the surface of the material. Furthermore, Grinspan and Gnanamoorthy [82] found only a slight increase in HV for oil jet peened aluminium alloy 6063-T6 at different standoff distances between 25 and 40 mm. There was less than 4 % difference of the hardness increase from the original hardness.

Table 6-4: ANOVA results for hardness (HV)

Source	Sum of squares	Degree of freedom	Mean square	F-value	p-value (Prob > F)
Model	86.254	6	17.251	19.319	< 0.0001
<i>n</i>	12.383	1	12.383	13.867	0.0011
<i>p</i>	57.948	1	57.948	64.894	< 0.0001
<i>u</i>	9.541	1	9.541	10.684	0.0034
<i>h</i>	4.590	1	4.590	5.140	0.0331
<i>P</i> ²	2.625	1	2.625	2.940	0.0999
<i>u</i> ²	20.538	23	0.893	-	-
Residual	19.266	19	1.014	3.189	0.1347
Lack of Fit	1.272	4	0.318	-	-
Pure error	106.793	28	-	-	-
Cor total	86.254	6	17.251	19.319	< 0.0001

Prob Probability, *Cor total* Corrected total

Corrected total=Total Sum of squares (SS) for the model terms + Residual SS and
Corrected total = Sum of degrees of freedom (*df*) of all the model terms + residual *df*

6.3.3 Optimization

Based on the developed models, an analysis on multiple response optimizations was conducted to achieve optimum results. The target is to find the optimal set of parameters within the tested range in the present study that can produce a minimum surface roughness and a maximum hardness simultaneously. Different sets of optimal parameters were obtained using the desirability function approach in the Design Expert software for the optimization of multiple response processes. Different desirability functions were used based on different importance criteria of roughness and hardness. The criteria of the desirability function are intended to achieve different sets of optimal parameters that may produce roughnesses below 10 μm . A total of five experimental runs was selected and performed for optimal sets of parameters as shown in [Table 6-5](#). Furthermore, these different combinations of optimal parameters were used to validate the robustness of the developed empirical models. The results of optimization for actual and predicted R_a as well as HV based on different importance criteria for each response are shown in [Table 6-5](#). The predicted responses for both R_a and HV were calculated from the empirical models. From the Design Expert software, the minimum overall desirability function was found to be 82%. All responses were predicted to be within these desired limits. Overall, the predicted and actual responses for both R_a and HV are satisfactory with good reliability. It shows that the models are workable in predicting the responses of R_a and HV in the present research.

Table 6-5: Optimization runs and their results

Exp. No.	Waterjet peening parameters				Actual responses		Predicted responses	
	n_j	p_o (MPa)	v_n (mm/min)	h (mm)	R_a (μm)	Hardness ($\text{HV}_{0.01}$)	R_a (μm)	Hardness ($\text{HV}_{0.01}$)
1	3	103.0	826.61	20.0	0.77	57.67	2.45	59.60
2	3	108.1	818.67	20.0	1.39	58.23	3.14	59.81
3	3	114.0	806.18	20.0	2.30	58.67	3.93	60.03
4	3	122.1	784.58	20.0	4.53	58.33	5.00	60.30
5	3	130.0	735.14	24.7	8.90	59.50	7.91	60.54

Exp. No. Experimental number

From the multiple response optimization based on the desirability function approach, similar optimal parameters were selected to treat specimens for the fatigue test. Since, there is a little change in the hardness values at different optimal conditions, only two different sets of parameters were utilized for the fatigue test. The two different cases are the one that results in the lowest and the highest increase in the hardness. Of course, the lowest increase in the hardness also corresponds to the lowest increase in the roughness and vice versa. The two sets of optimal parameters are denoted as experiment number 1 and 5 respectively in the [Table 6-5](#). The bending fatigue specimens were treated at these two set of parameters in a similar manner as described in Chapter 4.4.

6.3.4 Fatigue results

The result of the fatigue test is shown in [Fig. 6-15](#). The results show that the treated specimens at optimal conditions produce lower fatigue strength than the untreated specimens. Almost all treated specimens had consistently failed at a lower number of cycles than the untreated specimens for almost all stress levels. Specimens with the highest increase in the hardness and also the surface roughness (exp. no. 5) resulted in the largest decrease in the fatigue strength. This was followed by other treated specimens (exp. no. 1). The fatigue strengths are approximately 220 MPa (untreated), 200 MPa (exp. no. 1) and 165 MPa (exp. no. 5). This should come as no surprise since the hardness increase at optimal conditions is very marginal with significant increase in the surface roughness. As discussed in Chapter 5.4, there is a stronger influence of the surface roughness than the hardness in determining the fatigue strength of a material.

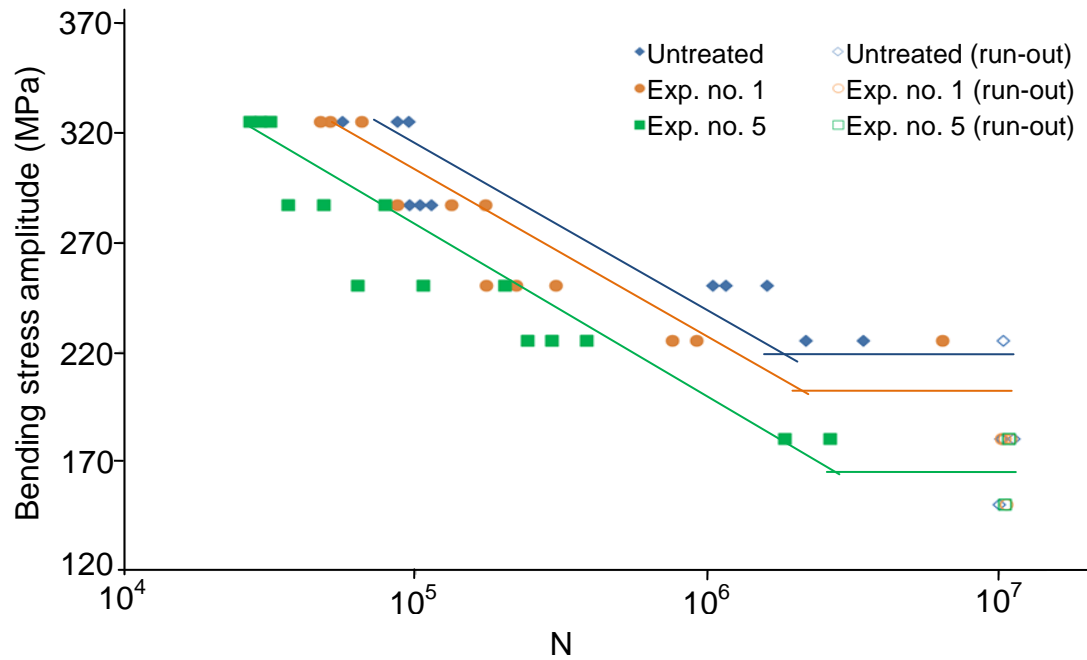


Fig. 6-15: Stress versus N diagrams for aluminium alloy 5005

Fig. 6-16 shows the untreated and treated surfaces of the fatigue specimens. The untreated specimen as shown in Fig. 6-16 (a) has an average surface roughness of about $0.5 \mu\text{m}$. The specimens treated at optimal conditions generate a noticeable amount of erosion with uniform erosion on the specimen with the highest roughness (exp. no. 5) as shown in Fig. 6-16 (c). While, another treated specimen (exp. no. 1) show a limited amount of erosion with few isolated craters as shown in Fig. 6-16 (b). Some cracks and notches can also be observed from the cross-sectional view of the treated specimens as shown in Fig. 6-17.

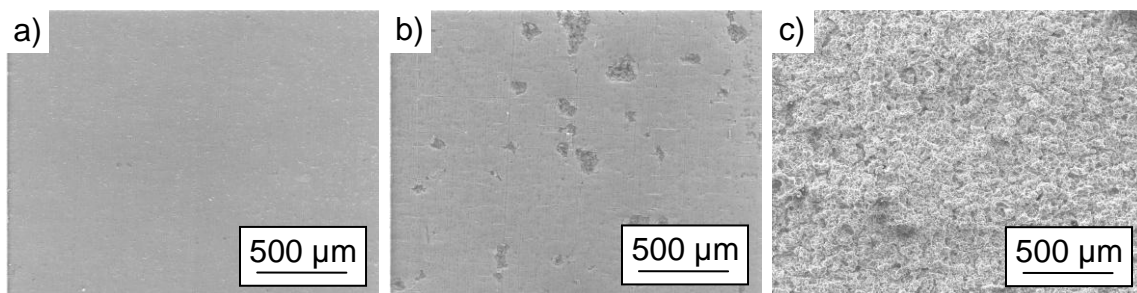


Fig. 6-16: Surface of fatigue specimens, a) untreated, b) exp. no. 1, and c) exp. no. 5

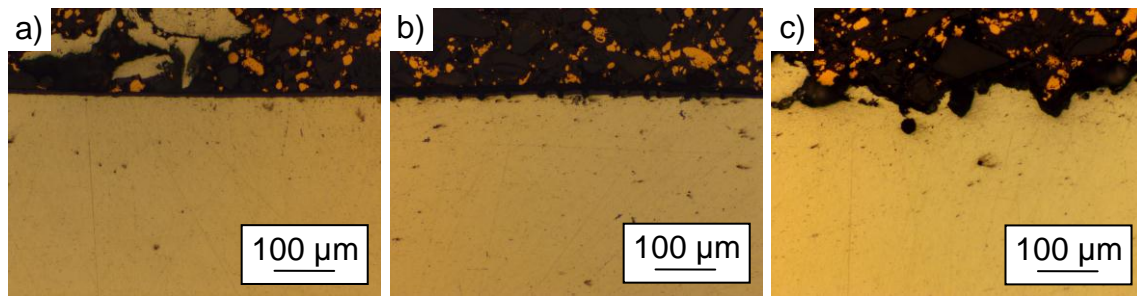


Fig. 6-17: Cross-sectional view of the fatigue specimens, a) untreated, b) exp. no. 1, and c) exp. no. 5

The broken specimens were later examined using SEM to determine the crack initiation mechanisms. Since broken surfaces for different specimens tested at different loads displayed little difference, only selected SEM images of the broken specimens are discussed. For standardization, fractured surfaces tested at a stress level of 287 MPa are presented here. A typical crack initiation site in the untreated specimen is shown in [Fig. 6-18](#).

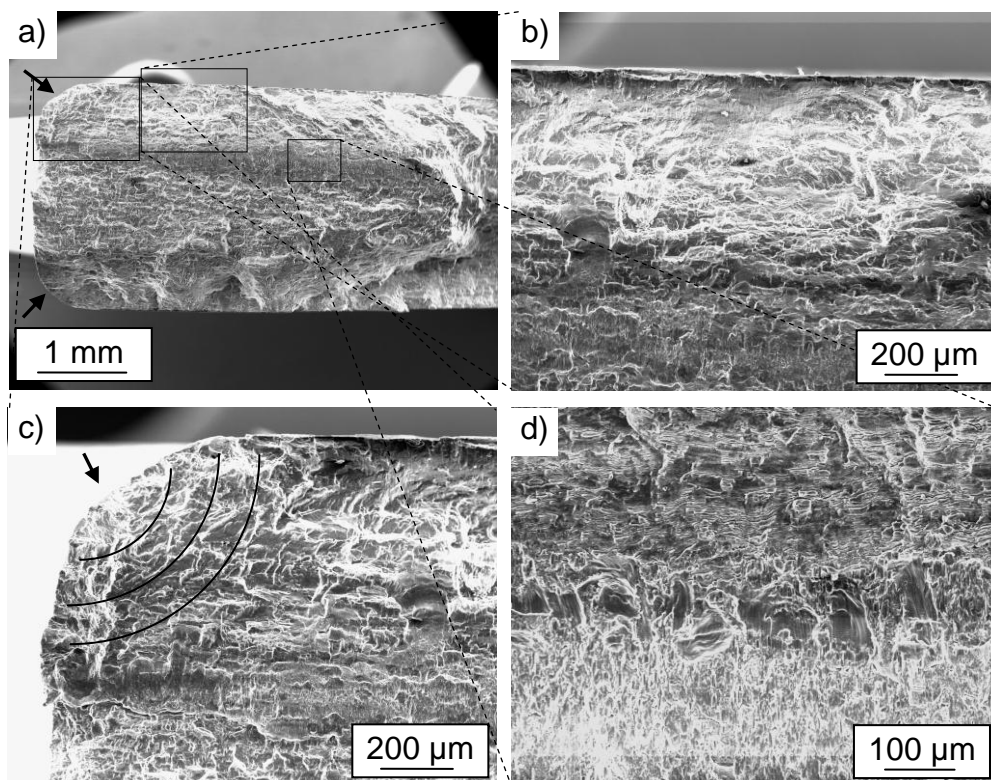


Fig. 6-18: SEM images of untreated fractured specimen, a) overview, b) surface, c) crack initiation at the corner, and d) fatigue striation in the middle (black arrows indicate crack initiation sites)

The surface experiences the maximum tensile stress during the bending test, as a result the fatigue crack is mostly initiated at the edge or corner of the specimens as

shown in [Fig. 6-18 \(a\)](#). The enlarged image of the corner is shown in [Fig. 6-18 \(c\)](#). No noticeable crack initiation sites have been found on the surface of the untreated specimen as shown in [Fig. 6-18 \(b\)](#). This is possibly due to the absence of defects on the surface. The residual fracture surface with fatigue striation is shown in [Fig. 6-18 \(d\)](#). Overall, the residual fracture surfaces indicate a dominant ductile fracture at all stress levels.

The fracture surface for the treated specimen (exp. no. 1) is shown in [Fig. 6-19](#). The crack initiations started mainly at the corners since these areas were subjected to the highest stress concentrations during the bending fatigue test. Also, some cracks randomly initiate from the surface as shown in [Fig. 6-19 \(b\)](#) because the existence of isolated pockets of erosion. Due to a higher degree of surface erosion at the top corner, the cracks easily initiate and propagate from it as shown in [Fig. 6-19 \(c\)](#). . The residual ductile fracture surface with fatigue striations is shown in [Fig. 6-19 \(d\)](#).

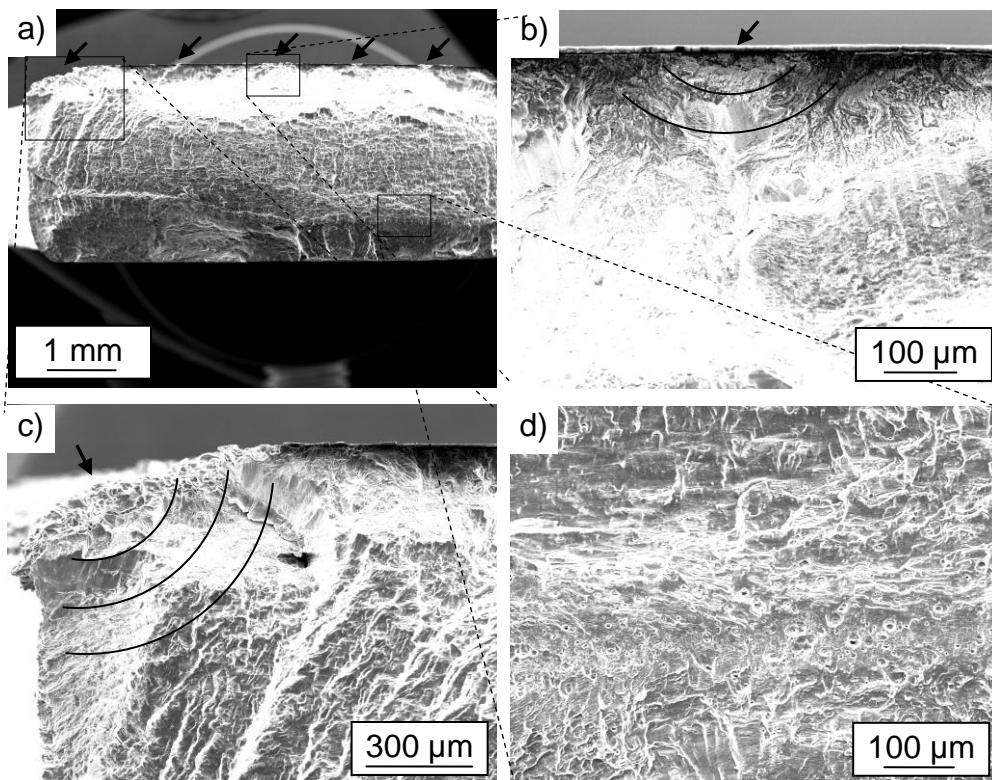


Fig. 6-19: SEM images of treated fractured specimen (exp. no. 1), a) overview, b) surface, c) crack initiation at the corner, and d) fatigue striation in the middle (black arrows indicate crack initiation sites)

[Fig. 6-20](#) shows the fractured surface for another treated specimen (exp. no. 5). Again, the crack initiations started mainly at the corners since these areas were

subjected to the highest stress concentrations during the bending fatigue test as illustrated in [Fig. 6-20 \(c\)](#). However, more cracks were probably initiated at the surface due to a higher extent of the surface defects as shown in [Fig. 6-20 \(b\)](#). The severe surface defects act as the crack initiation sources thus eventually breaking the specimens faster. The residual ductile fracture surface with fatigue striations is shown in [Fig. 6-20 \(d\)](#).

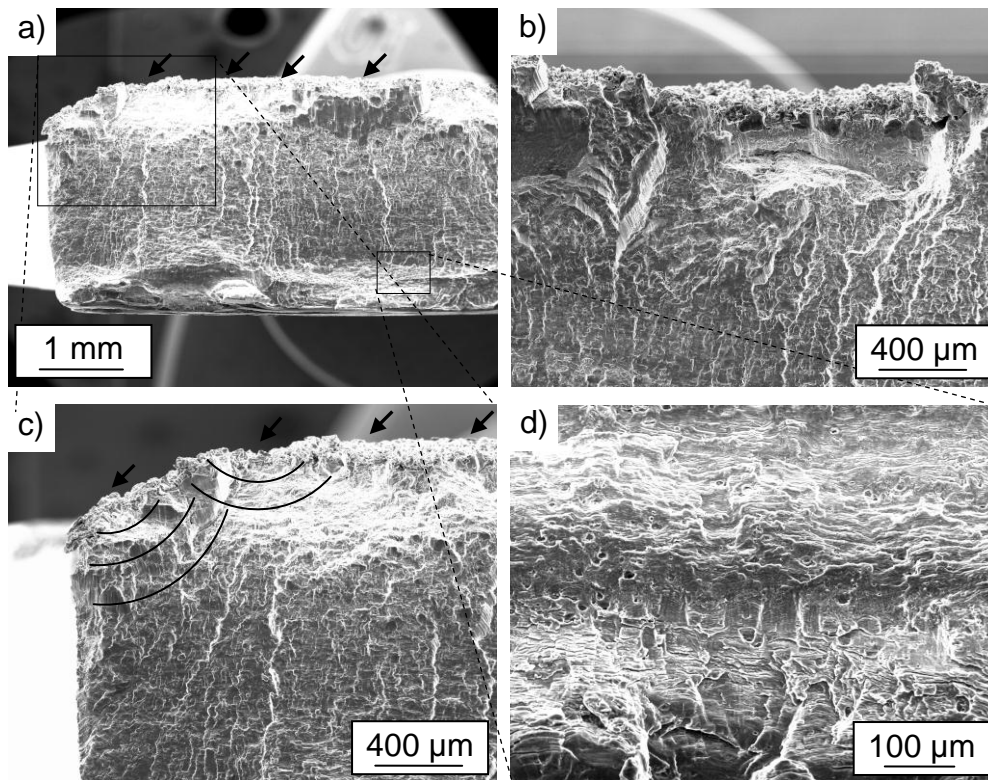


Fig. 6-20: SEM images of treated fractured specimen (exp. no. 5), a) overview, b) surface, c) crack initiation at the corner, and d) fatigue striation in the middle (black arrows indicate crack initiation sites)

7 Conclusions

7.1 Evaluation of surface effects

The surface roughness and erosion of austenitic steel 304 and carbon steel 1045 under waterjet peening process was investigated. Also, the effect of multiple jet passes treatment as well as other parameters such as feedrate, water pressure and standoff distance was examined. Based on the results, the following conclusions can be drawn.

- For both materials, increasing the number of jet passes produced a higher surface roughness as well as wider and deeper erosion tracks. Rougher surfaces and more erosion can be expected due to repeated bombardment of waterjet onto the surface. Furthermore, rougher surfaces were also produced at lower feedrates due to additional overlap machining action and more water molecules to impinge on the surface.
- Furthermore, the surface roughness and erosion increased with an increase in water supply pressure because of a higher kinetic energy of the water molecules thus enhancing their capability for material removal. Whereas, the standoff distance of about 90 mm produced the maximum surface roughness and erosion for both materials probably at this distance the jet structure consists of mainly water droplets.
- Generally, with carbon steel 1045, a higher value of surface roughness was observed than with stainless steel 304. This is possible due to a lower material hardness of the carbon steel 1045 thus lowering its erosion resistance.
- In general, the erosion mechanisms especially under multiple jet passes treatment happened in various stages. During earlier jet passes, the high impact pressure of water droplets produces many small central depression craters in the material surface thus initiating some cracks. Later, the lateral outward flow of the droplets further results in local shear fractures in the material surface by a pitting action. During subsequent jet passes, old cracks are further propagated and new cracks are initiated. The previously formed craters may easily combine to form a larger crater thus developing a bigger crater to form uniform erosion with full removal of materials over the surface.

7.2 Evaluation of sub-surface effects

The following conclusions can be drawn on the effect of various waterjet peening parameters on sub-surface of austenitic steel 304 and carbon steel 1045.

- For both materials, the hardness shows a general trend of decreasing gradually from the surface into the sub-surface. Also, the specimens treated with a higher jet passes displayed a higher increase in hardness as well as a deeper hardening layer. Similarly, a higher hardness gradient was also found in a specimen treated with a higher pressure. In contrast, a lower feedrate produced a higher increase in hardness gradient. As expected, a standoff distance of 90 mm resulted in the highest increase in hardness probably due to the highest impact pressure at this distance thus deforming the surface the most.
- The carbon steel 1045 showed a higher percentage of hardness increase than stainless steel 304. It is possible because of the higher hardness value of the original surface of stainless steel 304, it has a lower plastic flow thus restricting the dislocation movement.
- Also, the hardness increase variation in the stainless steel 304 had shown a relatively small margin of errors. This is probably due to a more stable work hardening state of stainless steel 304 during phase transformation.
- Cross-sectional microstructures of stainless steel 304 samples indicated that the substrate experienced a certain degree of plastic deformation. The density and quantity of slip bands in the deformed grains decreased gradually with increasing layer depth from the treated surface.

7.3 Evaluation of fatigue effects

The following conclusions can be drawn on the effect of the waterjet peening process on the fatigue life of austenitic steel 304 and aluminium alloy 5005.

- Overall, the waterjet treated specimens had shown lower fatigue strength than the original specimens. Specimens with the highest increase in hardness as well as surface roughness resulted in the largest decrease in the fatigue strength.
- The results suggested that the influence of the surface roughness was more prominent than the increase in hardness in determining the fatigue strength since

rougher surfaces are expected to encourage fatigue crack initiation. The specimens with more surface defects decreased the fatigue time for crack initiation.

- Based on the SEM images of the broken specimens, the crack initiations started mainly at both upper and lower corners of the specimens. However, more cracks were probably initiated at the surface due to a higher extent of the surface defects.
- Although, there was an increase in the hardness, but the fatigue life decreased due to the surface defects thus leading to the overpeening effect.

7.4 Optimization of waterjet peening process

Based on the Box-Behnken experimental design approach, the following conclusions on the effect of waterjet peening process of aluminium alloy 5005 can be drawn.

- The equivalent parametric trends show that the increase in hardness is not possible without a corresponding increase in surface roughness. The surface roughness and hardness are linearly related. Understandably, the parametric combinations that give a high energy of waterjet may induce a high degree of hardness as well as significant surface erosion.
- The developed empirical models for surface roughness (R_a) and hardness (HV) have reasonable correlations between the measured and predicted responses with acceptable R^2 and R_{adj}^2 . A proper selection of peening parameters can be formulated to be used in practical works.

Different sets of optimal parameters were generated based on different desirability functions for each response. The predicted and actual responses for optimized R_a and HV are satisfactory with good reliability. It shows that the models are workable in predicting the responses of R_a and HV in the present research.

8 Summary and outlook

The present study addresses the effect of multiple jet passes and other parameters such as feedrate, water pressure and standoff distance in waterjet peening (WJP) of metallic surfaces. An analysis of surface integrity in terms of surface roughness, erosion, hardness, microstructures and fatigue strength was used to evaluate the performance of different parameters in the WJP process. An increase in the number of jet passes as well as pressure leads to a higher roughness and more erosion of the surface and also to a higher hardness. However, the feedrate shows a reverse effect on surface roughness, erosion and hardness. For the standoff distance, there exists a specific distance that results in the maximum surface roughness, erosion and hardness. The surface microstructures show the mechanism of material removal process involving initial and evolved damages. Furthermore, the damage is more concentrated along the grain boundaries. The shearing force from the jet lateral flow raised the circumferential rims and created lateral cracks and sub-tunnels which might eventually be removed in the subsequent jet passes. The waterjet treated specimens had produced lower fatigue strength than the untreated specimens most probably due to the formation of a high degree of surface erosion. The influence of the surface roughness is more prominent than the increase in the hardness in determining the fatigue strength since rougher surfaces are expected to encourage fatigue crack initiation.

Also in the present study, the waterjet peening process is optimized using the design of experiment (DOE) approach. The DOE method is based on the response surface methodology utilizing the Box–Behnken experimental design approach. Workable empirical models were developed to predict the surface roughness and hardness. The developed empirical models show reasonable correlations between the measured and predicted responses with acceptable coefficients of determinations. A proper selection of WJP parameters can be formulated to be used in practical works.

Overall, the present study has shown some potential for future works especially in the application of multiple jet passes in the waterjet peening process. It has been shown that the treated surfaces with multiple jet passes may produce a smaller roughness and erosion compared to the abrasive waterjet and also the water

cavitation process. However, the surface hardness has somehow shown a limited increase compared to other waterjet peening processes. With a proper combination of other parameters and the number of jet passes, an optimum performance can be achieved. Furthermore, based on the fatigue result, the effect of surface erosion is more prominent than the increase in the hardness with multiple jet passes treatment. It would be interesting if the surface erosion can be minimized while achieving an optimum increase of hardness. Multiple jet passes can be conveniently applied by performing a polishing action on the surface with the subsequent passes. Firstly, the material surface is treated with sufficient kinetic energy during the initial jet passes so that an optimum compressive residual stress and hardness can be induced with suitable erosion. Finally, much lower kinetic energy of the jet is used during subsequent passes hence only unstable fragments of material introduced from previous erosion are removed. As a result, the surface can be smoothened while maintaining the initially hardened layer. Consequently, the smoother surface of the treated specimen may produce higher fatigue strength since fatigue crack initiation is discouraged with the formation of smoother surface.

Literature

- [1] FOLKES, J.: *Waterjet—An innovative tool for manufacturing*. Journal of Materials Processing Technology, 209 (2009), pp. 6181-6189.
- [2] HASHISH, M.; STEELE, D.E.; BOTHELL, D.H.: *Machining with super-pressure (690 MPa) waterjets*. International Journal of Machine Tools and Manufacture, 37 (1997), pp. 465-479.
- [3] DAOMING, G.; JIE, C.: *ANFIS for high-pressure waterjet cleaning prediction*. Surface and Coatings Technology, 201 (2006), pp. 1629-1634.
- [4] CUI, L.; AN, L.; GONG, W.; JIANG, H.: *A novel process for preparation of ultra-clean micronized coal by high pressure water jet comminution technique*. Fuel, 86 (2007), pp. 750-757.
- [5] TÖNSHOFF, H.K.; KROOS, F.; MARZENELL, C.: *High-pressure water peening—a new mechanical surface-strengthening process*. CIRP Annals-Manufacturing Technology, 46 (1997), pp. 113-116.
- [6] MOCHIZUKI, M.; ENOMOTO, K.; SAKATA, S.; KUROSAWA, K.; SAITO, H.; TSUJIMURA, H.; ICHIE, K.: *A study on residual stress improvement by water jet peening*. Proceedings of the 5th International Conference on Shot Peening, (1993), Oxford, pp. 247-256.
- [7] SCHINDLER, C.; SEVERIN, F.; WIND, M.: *CFD-Simulation von Flachstrahldüsenströmungen*, O+P Zeitschrift für Fluidtechnik, 4 (2007), pp. 178-182.
- [8] CADAVID-GIRALDO, R.: *Cutting with fluidjets of small diameter*, Dissertation, Fachbereich Maschinenbau und Verfahrenstechnik, Technische Universität Kaiserslautern, 2004.
- [9] CADAVID, R.; WÜSTENBERG, D.; LOUIS, H.; PUDE, F.; SENNE, T.: *Effect of helium atmospheres on abrasive suspension water jets*. International Journal of Advanced Manufacturing Technology, 26 (2005), pp. 1246-1254.
- [10] WEISS, M.: *Trennen von Faser-Nicht Faserverbunden mit hochdruckwasserstrahlen am Beispiel von Nadelvliesboden*, Dissertation, Fachbereich Maschinenbau und Verfahrenstechnik, Technische Universität Kaiserslautern, 2000.

-
- [11] WEISS, M.; WÜSTENBERG, D.; MOMBER, A.W.: *Hydro-erosive separation of plastic fibers from textile compounds*. Journal of Material Cycles and Waste Management, 5 (2003), pp. 84-88.
- [12] GROß, I.: *Schneiden der Hornhaut am Auge mit Wasserstrahl*, Dissertation, Fachbereich Maschinenbau und Verfahrenstechnik, Technische Universität Kaiserslautern, 2003.
- [13] LOOF, C.: *Entwicklung eines Hydrokeratoms für die LASIK-Chirurgie*, Fachbereich Maschinenbau und Verfahrenstechnik, Dissertation, Technische Universität Kaiserslautern, 2008.
- [14] LOOF, C.; SCHINDLER, C.: *Development of a microkeratome for LASIK-surgery based on high pressure water jet technology*. Proceedings of 6th Conference on Mechanical Engineering, (2008), Budapest, pp. 1-10.
- [15] SCHINDLER, C; LOOF, C.: *Hornhautschnitt mit Hochdruckwasserstrahl für die LASIK-OP*. Medizintechnik, 129 (2009), pp. 103-108.
- [16] KLOOS, K.E.; MACHERAUCH, E.: *Development Of Mechanical Surface Strengthening Processes From The Beginning Until Today*. Proceedings of 3rd International Conference on Shot Peening, (1987), Garmisch-Partenkirchen, pp. 3-27.
- [17] CALLISTER, W.D.: *Fundamentals of materials science and engineering: an integrated approach*. 5th edition, John Wiley & Sons, New York, 2001.
- [18] SCHULZE, V.: *Modern mechanical surface treatment*. Wiley-Vch, Weinheim, 2006.
- [19] LEE, W.; CHO, K.; KIM, K.; MOON, K.; LEE, Y.: *The effect of the cementite phase on the surface hardening of carbon steels by shot peening*. Materials Science and Engineering: A, 527, (2010), pp. 5852-5857.
- [20] SANJURJO, P.; RODRÍGUEZ, C.; PARIENTE, I.; BELZUNCE, F.; CANTELI, A.: *The influence of shot peening on the fatigue behaviour of duplex stainless steels*. Procedia Engineering, 2 (2010), pp. 1539-1546.
- [21] MIAO, H.; DEMERS, D.; LAROSE, S.; PERRON, C.; LÉVESQUE, M.: *Experimental study of shot peening and stress peen forming*. Journal of Materials Processing Technology, (2010), pp. 2089-2102.

-
- [22] BREUER, D.: *Vacuum/Surface Treatment Laser Peening- Advanced Residual Stress Technology*. Industrial Heating, 74 (2007), pp. 48-50.
- [23] WOHLFAHRT, H.: *The influence of peening conditions on the resulting distribution of residual stress*. Proceedings of the International Conference on Shot Peening, (1984), Chicago, pp. 316-331.
- [24] AL-OBAID, Y.F.: *A rudimentary analysis of improving fatigue life of metals by shot-peening*. Journal of applied mechanics, 57 (1990), pp. 307-312.
- [25] MIAO, H.Y.: *Numerical and theoritical study of shot peening and stress forming process*, University of Montreal, Dissertation, 2010.
- [26] WANG, S.; LI, Y.; YAO, M.; WANG, R.: *Compressive residual stress introduced by shot peening*. Journal of Materials Processing Technology, 73 (1998), pp. 64-73.
- [27] WILLIAM, S.: *Practical application of shot peening*. The shot peener, 5 (1992), pp. 1-4.
- [28] KIRK, D.: *Shot peening*. Aircraft Engineering and Aerospace Technology, 71 (1999), pp. 349-361.
- [29] GARIEPY, A.; LAROSE, S.; PERRON, C.; BOCHER, P.; LEVESQUE, M.: *On the effect of the peening trajectory in shot peen forming*. Finite Element in Analysis and Design, 69 (2013), pp. 48-61.
- [30] SINGH, L.; KHAN, R.A.; AGGARWAL, M.L.: *Effect of shot peening on hardening and surface roughness of nitrogen austenitic stainless steel*. International Journal of Engineering Science, 2 (2010), pp. 818-826.
- [31] TORRES, M.A.S.; VOORWALD, H.J.C.: *An evaluation of shot peening, residual stress and stress relaxation on the fatigue life of AISI 4340 steel*. International Journal of Fatigue, 24 (2002), pp. 877-886.
- [32] ZHANG, P.; LINDEMANN, J.; LEYENS, C.: *Shot peening on the high-strength wrought magnesium alloy AZ80—Effect of peening media*. Journal of Materials Processing Technology, 210 (2010), pp. 445-450.
- [33] LEE, H.; KIM, D.; JUNG, J.; PYOUN, Y.; SHIN, K.: *Influence of peening on the corrosion properties of AISI 304 stainless steel*. Corrosion Science, 51 (2009), pp. 2826-2830.

-
- [34] SHEN, L.; WANG, L.; WANG, Y.; WANG, C.: *Plasma nitriding of AISI 304 austenitic stainless steel with pre-shot peening*. Surface and Coatings Technology, 204 (2010), pp. 3222-3227.
- [35] HATAMLEH, O.A.: *Comprehensive investigation on the effects of laser and shot peening on fatigue crack growth in friction stir welded AA 2195 joints*. International Journal of Fatigue, 31 (2009), pp. 974-988.
- [36] SATHYAJITH, S.; KALAINATHAN, S.: *Effect of laser shot peening on precipitation hardened aluminum alloy 6061-T6 using low energy laser*. Optics and Lasers in Engineering, 50 (2011), pp. 345-348.
- [37] MONTROSS, C.; WEI, T.; YE, L.; CLARK, G.; MAI, Y.: *Laser shock processing and its effects on microstructure and properties of metal alloys: a review*. International Journal of Fatigue, 24 (2002), pp. 1021-1036.
- [38] GAO, Y.K.: *Improvement of fatigue property in 7050-T7451 aluminum alloy by laser peening and shot peening*. Materials Science and Engineering: A, 528 (2011), pp. 3823-3828.
- [39] MAAWAD, E.; SANO, Y.; WAGNER, L.; BROKMEIER, H.; GENZEL, C.: *Investigation of laser shock peening effects on residual stress state and fatigue performance of titanium alloys*. Materials Science and Engineering: A, 536 (2011), pp. 82-91.
- [40] SATHYAJITH, S.; KALAINATHAN, S.; SWAROOP, S.: *Laser peening without coating on aluminum alloy Al-6061-T6 using low energy Nd: YAG laser*. Optics & Laser Technology, 45 (2012), pp. 389-394.
- [41] LIM, H.; KIM, P.; JEONG, H.; JEONG, S.: *Enhancement of abrasion and corrosion resistance of duplex stainless steel by laser shock peening*. Journal of Materials Processing Technology, 212 (2012), pp. 1347-1354.
- [42] PEYRE, P.; SCHERPEREEL, X.; BERTHE, L.; CARBONI, C.; FABBRO, R.; BERANGER, G.; LEMAITRE, C.: *Surface modifications induced in 316L steel by laser peening and shot-peening. Influence on pitting corrosion resistance*. Materials Science and Engineering: A, 280 (2000), pp. 294-302.
- [43] CHILLMAN, A.; RAMULU, M.; HASHISH, M.: *Waterjet peening and surface preparation at 600 MPa: A preliminary experimental study*. Journal of Fluids Engineering, 129 (2007), pp. 485-490.

-
- [44] GRINSPAN, A.S.; GNANAMOORTHY, R.A.: *Novel surface modification technique for the introduction of compressive residual stress and preliminary studies on Al alloy AA6063*. Surface and Coatings Technology, 201 (2006), pp. 1768-1775.
- [45] JU, D.Y.; HAN, B.: *Investigation of water cavitation peening-induced microstructures in the near-surface layer of pure titanium*. Journal of Materials Processing Technology, 209 (2009), pp. 4789-4794.
- [46] QIN, M.; JU, D.Y.; OBA, R.: *Improvement on the process capability of water cavitation peening by aeration*. Surface and Coatings Technology, 200 (2006), pp. 5364-5369.
- [47] QIN, M.; JU, D.; OBA, R.: *Investigation of the influence of incidence angle on the process capability of water cavitation peening*. Surface and Coatings Technology, 201 (2006), pp. 1409-1413.
- [48] YANAIDA, K.; OHASHI, A.: *Flow characteristics of water jets*. Second International Symposium on Jet Cutting Technology, A2 (1974), Cranfield, pp. 19-32.
- [49] YANAIDA, K.; OHASHI, A.: *Flow characteristics of water jets in air*. Fifth International Symposium on Jet Cutting Technology, A3 (1980), Hannover, pp. 33-43.
- [50] SHIMIZU, S.: *Tribology in Water Jet Processes*. New Tribological Ways. InTech, Rijeka, 2011, pp. 153-164.
- [51] CHILLMAN, A.; RAMULU, M.; HASHISH, M.: *Waterjet and Water-Air Jet Surface Processing of a Titanium Alloy: A Parametric Evaluation*. Journal of Manufacturing Science and Engineering, 132 (2010), pp. 011012.
- [52] LESSER, M.B.; FIELD, J.E.: *The impact of compressible liquids*. Annual Review of Fluid Mechanics, 15 (1983), pp. 97-122.
- [53] HALLER, K.; POULIKAKOS, D.; VENTIKOS, Y.; MONKEWITZ, P.: *Shock wave formation in droplet impact on a rigid surface: lateral liquid motion and multiple wave structure in the contact line region*. Journal of Fluid Mechanics, 490 (2003), pp. 1-14.

-
- [54] REIN, M.: *Phenomena of liquid drop impact on solid and liquid surfaces*. Fluid Dynamics Research, 12 (1993), pp. 61-93.
- [55] FIELD, J.E.: *ELSI conference: invited lecture: Liquid impact: theory, experiment, applications*. Wear, 233 (1999), pp.1-12.
- [56] BOWDEN, F.P.; FIELD, J.E.: *The brittle fracture of solids by liquid impact, by solid impact, and by shock*. Proceedings of the Royal Society of London. Series A, Mathematical and Physical Sciences, 282 (1964), pp. 331-352.
- [57] HANCOX, N.L.; BRUNTON, J.H.: *The erosion of solids by the repeated impact of liquid drops*. Philosophical Transactions for the Royal Society of London. Series A, Mathematical and Physical Sciences, 260 (1966), pp. 121-139.
- [58] PREECE, C.M.; BRUNTON, J.H.: *A comparison of liquid impact erosion and cavitation erosion*. Wear, 60 (1980), pp. 269-284.
- [59] OBARA, T.; BOURNE, N.K.; FIELD, J.E.: *Liquid-jet impact on liquid and solid surfaces*. Wear, 186 (1995), pp. 388-394.
- [60] HEYMANN, F.J.: *High-speed impact between a liquid drop and a solid surface*. Journal of Applied Physics, 40 (1969), pp. 5113-5122.
- [61] COOK, S.S.: *Erosion by water-hammer*. Proceedings of the Royal Society A: Mathematical, Physical and Engineering Sciences, 119 (1928), pp. 481-488.
- [62] HUANG, L.; FOLKES, J.; KINNELL, P.; SHIPWAY, P: *Mechanisms of damage initiation in a titanium alloy subjected to water droplet impact during ultra-high pressure plain waterjet erosion*. Journal of Materials Processing Technology, 212 (2012), pp. 1906-1915.
- [63] ADLER, W.F.: *Liquid drop collisions on deformable media*. Journal of Materials Science, 12 (1977), pp. 1253-1271.
- [64] KENNEDY, C.F.; FIELD, J.E.: *Damage threshold velocities for liquid impact*. Journal of Materials Science, 35 (2000), pp. 5331-5339.
- [65] GEDEON, M.: *Strain hardening and strength*. Technical Tidbits, 17 (2010), pp. 1-2.
- [66] BLACK, J.T.; KOHSE, R.A.: *Degarmo's materials and processes in manufacturing*. 11th edition, John Wiley & Sons, Inc., New York, 2012.

-
- [67] ASKELAND, D.R.; FULAY, P.P.; WRIGHT, W.J.: *The science and engineering of materials*. 6th edition, Cengage Learning, Inc., Stamford, 2011.
- [68] AROLA, D.; MCCAIN, M.; KUNAPORN, S.; RAMULU, M.: *Waterjet and abrasive waterjet surface treatment of titanium: a comparison of surface texture and residual stress*. *Wear*, 249 (2002), pp. 943-950.
- [69] AROLA, D.; HALL, C.L.: *Parametric effects on particle deposition in abrasive waterjet surface treatments*. *Machining Science and Technology*, 8 (2004), pp. 171-192.
- [70] AROLA, D.; MCCAIN, M.L.: *Abrasive waterjet peening: a new method of surface preparation for metal orthopedic implants*. *Journal of Biomedical Materials Research*, 53 (2000), pp. 536-546.
- [71] KUNAPORN, S.; CHILLMAN, A.; RAMULU, M.; HASHISH, M.: *Effect of waterjet formation on surface preparation and profiling of aluminum alloy*. *Wear*, 265 (2008), pp. 176-185.
- [72] KUNAPORN, S.; RAMULU, M.; HASHISH, M.; HOPKINS, J.: *Ultra high pressure waterjet peening Part I: Surface texture*. *Proceedings of WJTA American Waterjet Conference*, (2001), Minnesota, Paper 25.
- [73] RAMULU, M.; KUNAPORN, S.; AROLA, D.; HASHISH, M.; HOPKINS, J.: *Waterjet machining and peening of metals*. *Journal of Pressure Vessel Technology*, 122 (2000), pp. 90-95.
- [74] AZHARI, A.; SCHINDLER, C.; KERSCHER, E.; GRAD, P.: *Improving surface hardness of austenitic stainless steel using waterjet peening process*. *The International Journal of Advanced Manufacturing Technology*, 63 (2012), pp. 1035-1046.
- [75] SADASIVAM, B.; HIZAL, A.; AROLA, D.: *Abrasive waterjet peening with elastic prestress: A parametric evaluation*. *International Journal of Machine Tools & Manufacture*, 49 (2009), pp. 134-141.
- [76] OKA, Y.I.; MIHARA, S.; MIYATA, H.: *Effective parameters for erosion caused by water droplet impingement and applications to surface treatment technology*. *Wear*, 263 (2007), pp. 386-394.

- [77] FOLDYNA, J.; SITEK, L.; ŠČUČKA, J.; MARTINEC, P.; VALÍČEK, J.; PÁLENÍKOVÁ, K.: *Effects of pulsating water jet impact on aluminium surface*. Journal of Materials Processing Technology, 209 (2009), pp. 6174-6180.
- [78] BARRIUSO, S.; LIEBLICH, M.; MULTIGNER, M.; ETXEBERRIA, I.; ALBERDI, A.; GONZÁLEZ-CARRASCO, J.: *Roughening of metallic biomaterials by abrasiveless waterjet peening: Characterization and viability*. Wear, 270 (2011), pp. 634-639.
- [79] TAYLOR, T.A.: *Surface roughening of metallic substrates by high pressure pure waterjet*. Surface and Coatings Technology, 76 (1995), pp. 95-100.
- [80] ISLAM, M.A.; FARHAT, Z.; BONNELL, J.: *High pressure water-jet technology for the surface treatment of Al-Si alloys and repercussion on tribological properties*. Journal of Surface Engineered Materials and Advanced Technology, 1 (2011), pp. 112-120.
- [81] KONG, M.C.; AXINTE, D.; VOICE, W.: *Aspects of material removal mechanism in plain waterjet milling on gamma titanium aluminide*. Journal of Materials Processing Technology, 210 (2010), pp. 573-584.
- [82] GRINSPAN, A.S.; GNANAMOORTHY, R.: *Surface modification by oil jet peening in Al alloys, AA6063-T6 and AA6061-T4: Residual stress and hardness*. Applied Surface Science, 253 (2006), pp. 989-996.
- [83] HIRANO, K.; ENOMOTO, K.; MOCHIZUKI, M.; HAYASHI, M.; HAYASHI, E.; SHIMIZU, S.: *Improvement of residual stress on material surface by water jet peening*. 14th International Conference on Structural Mechanics in Reactor Technology, 2 (1997), Lyon, pp. 361-368.
- [84] HAN, B.; JU, D.Y.; JIA, W.P.: *Influence of water cavitation peening with aeration on fatigue behaviour of SAE1045 steel*. Applied Surface Science, 253 (2007), pp. 9342-9346.
- [85] DANIEWICZ, S.R.; CUMMINGS, S.D.: *Characterization of a water peening process*. Journal of Engineering Materials and Technology, 121 (1999), pp. 336-340.
- [86] GRINSPAN, A.S.; GNANAMOORTHY, R.: *Effect of oil jet peening duration on surface modification and fatigue behavior of medium carbon steel AISI 1040*. Materials Science and Engineering: A, 456 (2007), pp. 210-217.

-
- [87] NI, Z.; WANG, X.; WANG, J.; WU, E.: *Characterization of the phase transformation in a nanostructured surface layer of 304 stainless steel induced by high-energy shot peening*. Physica B: Condensed Matter, 334 (2003), pp. 221-228.
- [88] WANG, T.; LU, B.; ZHANG, M.; HOU, R.; ZHANG, F.: *Nanocrystallization and α martensite formation in the surface layer of medium-manganese austenitic wear-resistant steel caused by shot peening*. Materials Science and Engineering: A, 458 (2007), pp. 249-252.
- [89] TSUJIKAWA, M.; EGAWA, M.; SONE, T.; UEDA, N.; OKANO, T.; HIGASHI, K.: *Modification of S phase on austenitic stainless steel using fine particle shot peening*. Surface and Coatings Technology, (2012).
- [90] CAMPBELL, F.C.: *Elements of metallurgy and engineering alloys*. ASM International, Inc., Ohio, 2008.
- [91] AROLA, D.; ALADE, A.E.; WEBER, W.: *Improving fatigue strength of metals using abrasive waterjet peening*. Machining science and technology, 10 (2006), pp. 197-218.
- [92] KUNAPORN, S.; RAMULU, M.; JENKINS, M.; HASHISH, M.; HOPKINS, J.: *Ultra high pressure waterjet peening, Part II: High cycle fatigue performance*. Proceedings of WJTA American Waterjet Conference, (2001), Minnesota, Paper 26.
- [93] TAYLOR, D.; CLANCY, O.M.: *The fatigue performance of machined surfaces*. Fatigue & Fracture of Engineering Materials & Structures, 14 (1991), pp. 329-336.
- [94] SOYAMA, H.: *Improvement of fatigue strength by using cavitating jets in air and water*. Journal of Materials Science, 42 (2007), pp. 6638-6641.
- [95] AZHARI, A.; SCHINDLER, C.; LI, B.: *Effect of waterjet peening on aluminium alloy 5005*. International Journal of Advanced Manufacturing Technology, 67 (2013), pp. 785-795.
- [96] MACODIYO, D.O.; SOYAMA, H.: *Optimization of cavitation peening parameters for fatigue performance of carburized steel using Taguchi methods*. Journal of Materials Processing Technology, 178 (2006), pp. 234-240.

-
- [97] RAJESH, N.; RAMESH, B.N.: *Empirical modelling of water-jet peening of 6063-T6 aluminium alloy*. Journal of Production Engineering, 86 (2005), pp. 22-26.
- [98] SCHEY, J.A.: *Introduction to manufacturing processes*. 3rd edition. McGraw-Hill, Inc., New York, 2000.
- [99] CRITCHLOW, G.W.; BREWIS, D.M.: *Review of surface pretreatments for titanium alloys*. International Journal of Adhesion and Adhesives, 15 (1995), pp. 161-172.
- [100] XIANGHUI, L.: *Recent advance in surface treatment and its applications in China*. Surface and Coatings Technology, 131 (2000), pp. 261-266.
- [101] ULUTAN, D.; OZEL, T.: *Machining induced surface integrity in titanium and nickel alloys: A review*. International Journal of Machine Tools and Manufacture, 51 (2011), pp. 250-280.
- [102] MEGUID, S.A.; SHAGAL, G.; STRANART, J.C.: *Finite element modelling of shot - peening residual stresses*. Journal of Materials Processing Technology, 92-93 (1999), pp. 401-404.
- [103] DING, K.; YE, L.: *Simulation of multiple laser shock peening of a 35CD4 steel alloy*. Journal of Materials Processing Technology, 178 (2006), pp. 162-169.
- [104] KARABELCHTCHIKOVA, O.; RIVERO, I.V.: *Variability of residual stresses and superposition effect in multipass grinding of high-carbon high-chromium steel*. Journal of Materials Engineering and Performance, 14 (2005), pp. 50-60.
- [105] ZHANG, B.; YANG, F.; WANG, J.; ZHU, Z.; MONAHAN, R.: *Stock removal rate and workpiece strength in multi-pass grinding of ceramics*. Journal of Materials Processing Technology, 104 (2000), pp. 178-184.
- [106] WANG, J.; GUO, D.M.: *The cutting performance in multipass abrasive waterjet machining of industrial ceramics*. Journal of Materials Processing Technology, 133 (2003), pp. 371-377.
- [107] BIGDELI KARIMI, M.; ARABI, H.; KHOSRAVANI, A.; SAMEI, J.: *Effect of rolling strain on transformation induced plasticity of austenite to martensite in a high-alloy austenitic steel*. Journal of Materials Processing Technology, 203 (2008), pp. 349-354.

- [108] BRINGAS, J.E.: *Handbook of comparative world steel standards*. ASM International, Inc., Massachusetts, 2004.
- [109] Seeberger GmbH & Co. KG: *Material data sheet 3.3315*. URL: http://www.seeberger.net/_assets/pdf/werkstoffe/aluminium/en/3.3315.pdf. (Accessed on 23/05/2012).
- [110] mejo Metall Josten GmbH & Co. KG: *Festigkeitseigenschaften Aluminium Bleche und Bänder*. URL: http://www.mejo.de/metalexikon_europaeische_normen_festigkeitseigenschaften_aluminium_bleche_und_baender.asp#L4. (Accessed on 23/05/2012).
- [111] Quick-Ohm Küpper & Co. GmbH: *Sapphire waterjet nozzles type 18*. URL: http://www.quick-ohm.com/sapphire_waterjet_nozzles/typ18.htm (Accessed on 20/01/2014).
- [112] Standard ISO 4287: 1997: *Geometrical Product Specifications (GPS) -- Surface texture: Profile method -- Terms, definitions and surface texture parameters*; International Organization for Standardization.
- [113] Buehler Ltd.: *The science behind Materials preparation: A guide to materials preparation and analysis*. United States of America, 2004.
- [114] AKAY, S.; YAZICI, M.; BAYRAM, A.; AVINC, A.: *Fatigue life behaviour of the dual-phase low carbon steel sheets*, Journal of Materials Processing Technology, 209 (2009), pp. 3358-3365.
- [115] BELINGARDI, G.; CAVATORTA, M.P.; FRASCA, C.: *Bending fatigue behavior of glass-carbon/epoxy hybrid composites*. Composites Science and Technology, 66 (2006), pp. 222-232.
- [116] AZMIR, M.A.; AHSAN, A.K.: *A study of abrasive water jet machining process on glass/epoxy composite laminate*. Journal of Materials Processing Technology, 209 (2009), pp. 6168-6173.
- [117] GODOY, C.; MANCOSU, R.; LIMA, M.; BRANDÃO, D.; HOUSDEN, J.; AVELAR-BATISTA, J.: *Influence of plasma nitriding and PAPVD Cr1-xNx coating on the cavitation erosion resistance of an AISI 1045 steel*. Surface Coating Technology, 200 (2006), pp. 5370-5378.

-
- [118] LEU, M.; MENG, P.; GESKIN, E.; TISMENESKIY, L.: *Mathematical modeling and experimental verification of stationary waterjet cleaning process*. Journal of Manufacturing Science and Engineering, 120 (1998), pp. 571-579.
- [119] SOHR, J.M.; THORPE, M.L.: *Stripping of thermal spray coatings with ultra high pressure water jet*. SAE Technical Paper, 101 (1992), pp. 51-59.
- [120] KRELLA, A.; CZYZNIEWSKI, A.: *Influence of the substrate hardness on the cavitation erosion resistance of TiN coating*. Wear, 263 (2007), pp. 395-401.
- [121] PREECE C.; DRAPER, C.: *The effect of laser quenching the surfaces on their cavitation erosion resistance*. Wear, 67 (1981), pp. 321-328.
- [122] ZHAO, K.; GU, C.; SHEN, F.; LOU, B.: *Study on mechanism of combined action of abrasion and cavitation erosion on some engineering steels*. Wear, 162-164 (1993), pp. 811-819.
- [123] LEE, G.M.C.: *The erosion resistance of plain carbon steels under water droplet impact conditions*. Wear, 141 (1990), pp. 185-201.
- [124] MANN, B.S.; ARYA, V.: *An experimental study to correlate water jet impingement erosion resistance and properties of metallic materials coatings*. Wear, 253 (2002), pp. 650-661.
- [125] RICHMAN, R.H.; MCNAUGHTON, W.P.: *Correlation of cavitation erosion behavior with mechanical properties of metals*. Wear, 140 (1990), pp. 63-82.
- [126] FELLER, H.G.; KHARRAZI, Y.: *Cavitation erosion of metals and alloys*. Wear, 93 (1984), pp. 249-260.
- [127] HEATHCOCK, C.J.; PROTHEROE, B.E.; BALL, A.: *Cavitation erosion of stainless steel*. Wear, 81 (1982), pp. 311-327.
- [128] PREECE, C.M.; MACMILLAN, N.H.: *Erosion*. Annual Review of Materials Science, 7 (1977), pp. 95-121.
- [129] KRELLA, A.: *Influence of cavitation intensity on X6CrNiTi18-10 stainless steel performance in the incubation period*. Wear, 258 (2005), pp. 1723-1731.
- [130] LUISET, B.; SANCHETTE, F.; BILLARD, A.; SCHUSTER, D.: *Mechanisms of stainless steels erosion by water droplets*. Wear, 303 (2013), pp. 459-464.
- [131] ADLER, W.F.; HOOKER S.V.: *Rain erosion behaviour of polymethylmethacrylate*. Journal of Material Science, 13 (1978), pp. 1015-1025.

-
- [132] MILLER, L.; SMITH, G.: *Tensile fracture in carbon steels*. Journal of Iron Steel Institute, 208 (1970), pp. 998-1005.
- [133] VALIENTE, A.; RUIZ, J.; ELICES, M.: *A probabilistic model for the pearlite-induced cleavage of a plain carbon structural steel*, Engineering Fracture Mechanics, 72 (2005), pp. 709-728.
- [134] KAMKAR, N.; BRIDIER, F.; BOCHER, P.; JEDRZEJOWSKI, P.: *Water droplet erosion mechanisms in rolled Ti-6Al-4V*. Wear, 301 (2013), pp. 442-448.
- [135] KWOK, C.T.; MAN, H.C.; CHENG, F.T.: *Cavitation erosion and damage mechanisms of alloys with duplex structures*. Materials Science and Engineering A, 242 (1998), pp. 108-120.
- [136] GRINSPAN, A.S.; GNANAMOORTHY, R.: *Surface modification by oil jet peening in Al alloys, AA6063-T6 and AA6061-T4, Part 2: Surface morphology, erosion, and mass loss*. Applied Surface Science, 253 (2006), pp. 997-1005.
- [137] DURAISELVAM, M.; GALUN, R.; WESLING, V.; MORDIKE, B.L.; REITER, R.; OLIGMÜLLER, J.; BUVANASKEHARAN, G.: *Cavitation erosion resistance of Ti6Al4V laser alloyed with TiC-reinforced dual phase intermetallic matrix composites*. Materials Science and Engineering A, 454-455 (2007), pp. 63-68.
- [138] MAHAGAONKAR, S.B.; BRAHMANKAR, P.K.; SEEMIKERI, C.Y.: *Effect of shot peening parameters on microhardness of AISI 1045 and 316L material: an analysis using design of experiment*. The International Journal of Advanced Manufacturing Technology, 38 (2008), pp. 563-574.
- [139] NIKITIN, I.; BESEL, M.: *Correlation between residual stress and plastic strain amplitude during low cycle fatigue of mechanically surface treated austenitic stainless steel AISI 304 and ferritic-pearlitic steel SAE 1045*. Material Science and Engineering A, 491 (2008), pp. 297-303.
- [140] KANG, S.H.; IM, Y.T.: *Three-dimensional thermo-elastic-plastic finite element modeling of quenching process of plain-carbon steel in couple with phase transformation*. International Journal of Mechanical Sciences, 49 (2007), pp. 423-439.
- [141] AL-ABBASI, F.: *Micromechanical modeling of ferrite-pearlite steels*. Materials Science and Engineering A, 527 (2010), pp. 6904-6916.

- [142] AUTENRIETH, H.; OKOLO, B.; SCHULZE, V.; WANNER, A.: *Surface workhardening and residual stresses induced by micro cutting processes*. Proceedings of the 8th International Conference on Residual Stresses, (2008), Denver, pp. 608-615.
- [143] ZHAN, K.; JIANG, C.H.; JI, V.: *Effect of prestress state on surface layer characteristic of S30432 austenitic stainless steel in shot peening process*. Materials and Design, 42 (2012), pp. 89-93.
- [144] HACINI, L.; LE, N.V.; BOCHER, P.: *Effect of impact energy on residual stresses induced by hammer peening of 304L plates*. Journal of Materials Processing Technology, 208 (2008), pp. 542-548.
- [145] AVILÉS, R.; ALBIZURI, J.; LAMIKIZ, A.; UKAR, E.; AVILÉS, A.: *Influence of laser polishing on the high cycle fatigue strength of medium carbon AISI 1045 steel*. International Journal of Fatigue, 33 (2011), pp. 1477-1489.
- [146] LIU, W.; ZHANG, C.; XIA, C.; YANG, Z.; WANG, P.; CHEN, J.: *Strain-induced refinement and thermal stability of a nanocrystalline steel produced by surface mechanical attrition treatment*. Materials Science & Engineering A, 568 (2013), pp. 176-183.
- [147] LIU, G.; WANG, S.; LOU, X.; LU, J.; LU, K.: *Low carbon steel with nanostructured surface layer induced by high-energy shot peening*. Scripta Materialia, 44 (2001), pp. 1791-1795.
- [148] TAO, N.; WANG, Z.; TONG, W.; SUI, M.; LU, J.; LU, K.: *An investigation of surface nanocrystallization mechanism in Fe induced by surface mechanical attrition treatment*. Acta Materialia, 50 (2002), pp. 4603-4616.
- [149] LIU, G.; LU, J.; LU, K.: *Surface nanocrystallization of 316L stainless steel induced by ultrasonic shot peening*. Materials Science and Engineering A, 286 (2000), pp. 91-95.
- [150] ZHOU, L.; LIU, G.; MA, X.L.; LU, K.: *Strain-induced refinement in a steel with spheroidal cementite subjected to surface mechanical attrition treatment*. Acta Materialia, 56 (2008), pp. 78-87.
- [151] ALANG, N.A.; RAZAK, N.A.; MISKUN, A.K.: *Effect of surface roughness on fatigue life of notched carbon steel*. International Journal of Engineering & Technology, 11 (2011), pp. 203-206.

-
- [152] ZHANG, P.; LINDEMANN, J.: *Influence of shot peening on high cycle fatigue properties of the high-strength wrought alloy AZ80*. Scripta Materialia, 52 (2005), pp. 485-490.
- [153] HUTMANN, P.: *The application of mechanical surface treatment in the passenger car industry*. Shot Peening, Wiley-VCH Verlag GmbH & Co., Weinheim, 2006, pp. 3-12.
- [154] WAGNER, L.: *Mechanical surface treatments on the titanium, aluminium and magnesium alloys*. Materials Science and Engineering A, 263 (1999), pp. 210-216.
- [155] KOSMAC, T.; OBLAK, C.; JEVNIKAR, P.; FUNDUK, N.; MARION, L.: *The effect of surface grinding and sandblasting on flexural strength and reliability of Y-TZP zirconia ceramic*. Dental Materials, 15 (1999), pp. 426-433.
- [156] SCHERRER, S.S.; DENRY, I.L.; WISKOTT, H.W.: *Comparison of three fracture toughness testing techniques using a dental glass and a dental ceramic*. Dental Materials, 14 (1998), pp. 246-255.
- [157] MONTGOMERY, D.C.; PECK, E.A.; VINING, G.G.: *Introduction to linear regression analysis*. John Wiley & Sons, Inc., New York, 2001.
- [158] ROY, R.K.: *Design of experiments using the Taguchi approach*. John Wiley & Sons, Inc., New York, 2001.
- [159] CHI, G.; HU, S.; YANG, Y.; CHEN, T.: *Response surface methodology with prediction uncertainty: A multi-objective optimisation approach*. Chemical Engineering Research and Design, 90 (2012), pp. 1235-1244.
- [160] ALAO, A.R.; KONNEH, M.: *Surface finish prediction models for precision grinding of silicon*. International Journal of Advanced Manufacturing Technology, 58 (2012), pp. 949-967.
- [161] FOWLKES, W.Y.; CREVELING, C.M.: *Engineering methods for robust product design: using Taguchi methods in technology and product development*. Prentice Hall, Inc., Massachusetts, 1995.

List of Publications

- [1] AZHARI, A.; SCHINDLER, C.; KERSCHER, E.; GRAD, P.: *Improving surface hardness of austenitic stainless steel using waterjet peening process*. The International Journal of Advanced Manufacturing Technology, 63 (2012), pp. 1035-1046.
- [2] AZHARI, A.; SCHINDLER, C.; LI, B.: *Effect of waterjet peening on aluminium alloy 5005*. International Journal of Advanced Manufacturing Technology, 67 (2013), pp. 785-795.
- [3] AZHARI, A.; SCHINDLER, C.; NKOUMBOU, J.; KERSCHER, E.: *Surface erosion of carbon steel 1045 during waterjet peening*. Journal of Materials Engineering and Performance 23 (2014), pp. 1870-1880.

List of Students' Projects

- [1] LI, B.: *The effect of waterjet peening on aluminium alloy 5005*. Studentarbeit Nr.: 675 (2012), Lehrstuhl für Konstruktion im Maschinen- und Apparatebau (KIMA), Technische Universität Kaiserslautern.
- [2] JHISLAIN, N.K.: *Waterjet treatment of ferritic steel (1045)*. Studentarbeit Nr.: 711 (2012), Lehrstuhl für Konstruktion im Maschinen- und Apparatebau (KIMA), Technische Universität Kaiserslautern.

Curriculum vitae

First name: Mohd Azmir

Last name: Mohd Azhari

Education

1986 – 1991 Seri Cempaka Primary School, Kampong Gajah, Perak

1992 – 1996 Izzuddin Shah Secondary School, Ipoh, Perak

April 1999 Matriculation certificate,
International Islamic University Malaysia

May 2003 Bachelor of Engineering in Manufacturing,
International Islamic University Malaysia

December 2006 Masters of Science in Manufacturing,
International Islamic University Malaysia

December 2013 PhD in Mechanical Engineering
Technische Universität Kaiserslautern

Work experience

Apr 2002 – Jun 2002 Industrial trainee, Lafarge Malayan Cement Ltd.

May 2003 – Dec 2003 Production executive, F&N Dairies Pvt. Ltd.

Dec 2005 – Dec 2006 Lecturer, School of Engineering and Technology,
INTI International College Subang

Dec 2006 – Dec 2009 Lecturer, Faculty of Manufacturing Engineering,
Universiti Malaysia Pahang

Dec 2009 – Dec 2013 PhD scholar, Chair of Design in Mechanical Engineering,
Technische Universität Kaiserslautern

Dec 2013 – Senior lecturer, Faculty of Manufacturing Engineering,
Universiti Malaysia Pahang

KIMA-Schriftenreihe

bereits veröffentlicht wurden

- 1 Cadavid-Giraldo, R.: Cutting with fluidjets of small diameter.
2004, ISBN 3-936890-46-3 € 30,-
- 2 Kasper, J.: Untersuchungen zur Schneidzerkleinerung von Aluminium.
2005, ISBN 3-936890-70-6 € 30,-
- 3 Theobald, U.: Untersuchung des Gewebeaufschlusses in Reißmaschinen
unter Betrachtung des Einzelbeanspruchungsvorganges.
2005, ISBN 3-936890-74-9 € 30,-
- 4 Loof, C.: Entwicklung eines Hydrokeratoms für die LASIK-Chirurgie.
2008, ISBN 978-3-939432-79-1 € 30,-
- 5 Thjunjoto: Entwicklung einer Apparatur zur Gewinnung von Proben
aus Bohrkernen unter in-situ Druck.
2009, ISBN 978-3-941438-07-1 € 30,-
- 6 Wind, M.: Numerische und experimentelle Analyse und Optimierung
der technischen Eigenschaften eines selbstexpandierenden Stents.
2011, ISBN 978-3-941438-75-0 € 30,-
- 7 Kleiner, O.: Numerische und experimentelle Untersuchung der
Rad/Schiene-Interaktion unter Berücksichtigung mechanischer
und thermomechanischer Effekte.
2011, ISBN 978-3-941438-88-0 € 30,-
- 8 Soffel, M.: Untersuchung des Lufteinzuges beim
Hochgeschwindigkeitswickeln von Kunststofffolien.
2013, ISBN 978-3-943995-32-9 € 40,-
- 9 Stephan, N. K.: Vorgehensmodell zur Unterstützung der interdisziplinären
und förderierten Zusammenarbeit in der frühen Phase der Produktentstehung
- am Beispiel der Nutzfahrzeugindustrie -
2013, ISBN 978-3-943995-37-4 € 40,-
- 10 Li, H.: Analysis of Off-Road Tire-Soil Interaction through
Analytical and Finite Element Methods
2013, ISBN 978-3-943995-42-8 € 40,-
- 11 Azhari M. A. M.: Effects of Waterjet Treatment on Surface
Integrity of Metals and its Optimization
2014, ISBN 978-3-943995-60-2 € 40,-